CRUSTAL CONTAMINATION, SULPHIDE MINERALIZATION, AND COMPACTION DURING FORMATION OF THE MARGINAL ZONE OF THE MUSKOX INTRUSION, NUNAVUT, AND IMPLICATIONS FOR THE EVOLUTION OF THE 1.27 Ga MACKENZIE MAGMATIC EVENT

by

ROBIN MACKIE

B.Sc.H. University of Manitoba, 2003

A THESIS SUBMITTED FOR PARTIAL FULFILMENT

OF THE REQUIREMENTS FOR THE DEGREE OF

MASTER OF SCIENCE

in

THE FACULTY OF GRADUATE STUDIES

(GEOLOGICAL SCIENCES)

THE UNIVERSITY OF BRITISH COLUMBIA

April 2006

ABSTRACT

The age, petrology, geochemistry, and Hf-Nd-S isotopic compositions of basal marginal rocks at two locations (West Pyrrhotite Lake and Far West Margin) along the western margin of the large Muskox layered mafic-ultramafic intrusion, Nunavut, are used (1) to constrain the petrogenesis of the marginal zone and associated sulphide mineralization, and (2) to evaluate the genetic relationship of the Muskox intrusion with the Mackenzie dikes and Coppermine River flood basalts during the 1.27 Ga Mackenzie magmatic event. The marginal zone (1269 ± 2 Ma; U-Pb baddeleyite) consists of a lower 10 m-thick gabbronorite and upper 100-150 m-thick peridotite subzone. A shift in incompatible trace element ratios and isotopic compositions at the transition from peridotite (low Th/Yb; high Nb/La; $\varepsilon_{Hf(t)}$ = -3 to +2; $\varepsilon_{Nd(t)}$ = -4 to 0; $\delta^{34}S$ = +6) to gabbronorite ($\varepsilon_{Hf(t)}$ = -5 to -15; $\varepsilon_{Nd(t)}$ = -1 to -13; $\delta^{34}S$ = +7 to +10) and the corresponding early crystallization of orthopyroxene and appearance of granophyre within the gabbronorite indicates that the effects of crustal contamination by the adjacent country rocks (high Th/Yb; low Nb/La; $\varepsilon_{Hf(t)}$ = -24 to -29; $\varepsilon_{Nd(t)}$ = -14 to -16; $\delta^{34}S$ = +7 to +11) is restricted to a thin (10 m) boundary zone along the contact. Silica and sulphur addition promoted local sulphide saturation within the contaminated magmas along the outer wall of the magma chamber. The low metal content of sulphides throughout the intrusion indicates that in general early solidification of this zone inhibited segregated sulphide liquid from interacting with subsequent pulses of magma (low R-factor). The overlying peridotites contain increasing proportions of postcumulus phases relative to cumulus olivine towards the base of the marginal zone, a feature that is related to the competing effects of compaction and rapid heat loss through the base of the intrusion. The marginal zone peridotites and overlying layered series rocks of Muskox intrusion and the lowermost Coppermine River basalts have the same range of Nd isotopic compositions, suggesting that they both were derived from a common relatively enriched mantle source and that this portion of the flood basalts were fed by magma that temporarily resided and fractionated within the Muskox magma chamber during their final ascent through the crust.

TABLE OF CONTENTS

LIST OF TABLES

LIST OF FIGURES

ACKNOWLEDGEMENTS

Many people have thoughtfully invested their time and energy in various parts of this thesis. Firstly, I would like to thank my advisors James Scoates and Dominique Weis for their constant encouragement and support, and for all that they have taught me since my first arrival at UBC. James has devoted countless hours to the betterment of this work, especially during the final stages in the preparation of this manuscript, and for that I am very appreciative. I thank all the staff and students of the Pacific Centre for Isotopic and Geochemical Research at UBC, including Gwen Williams, Diane Hanano, Rich Friedman, Wilma Pretorius, Jane Barling, Elisa Dietrich-Sainsaulieu and Bert Mueller, who all contributed to this work. Mati Raudsepp and Elisabetta Pani are thanked for their expertise in the SEM and electron microprobe facility at UBC, as well as, Claude Maerschalk for his assistance with column chemistry at ULB. I am appreciative for the assistance of Kelly Russell, Jon Scoates, Erik Scheel, and Steve Rowins who provided helpful reviews of this manuscript.

I am grateful for the financial and logistical support provided by Anglo American Exploration (Canada) Ltd. (AAEC) throughout this study. In particular, I would like to acknowledge Dave Peck and Gary DeSchutter. Dave is responsible for the initial commencement of this project and provided helpful reviews of various drafts of this manuscript. Dave will undoubtedly continue to be a mentor in the years to come. Gary is thanked for his support during the early stages of this project and his impeccable management of both summer and winter AAEC drill programs on the Muskox intrusion. I would also like to thank friends and co-workers at AAEC, Nathan Rand in particular, for their help with sample collection and core splitting, and for making my stay at McGregor Lake Camp an unforgettable experience.

My family has always supported my studies, and for that they deserve my gratitude and respect. Norm Halden is thanked for his continued encouragement and for inspiring my curiosity with many painful, yet satisfying, lectures on igneous petrology at the University of Manitoba. Caroline-Emmanuelle Morisset and Heidi Annell are thanked for their support throughout my time at UBC. Most importantly, my wife Tamara deserves my utmost appreciation and gratitude for her encouragement and patience throughout my years at university. Despite my countless absent-minded evenings and my more than occasional complete absence, Tamara has always supported my aspirations and goals and for that I am extremely grateful.

CHAPTER 1

Geologic and exploration context of the Marginal Zone of the Muskox intrusion

1.1 INTRODUCTION

This study focuses on the marginal rocks at the base of the Muskox layered mafic-ultramafic intrusion located approximately 60 km south of the Coronation Gulf on the Arctic Circle in Nunavut, Canada (Fig. 1.1). The Muskox intrusion is situated within metasedimentary, metaplutonic, and metavolcanic rocks of the 1.8-1.9 Ga Wopmay Orogen and an unconformably overlying supracrustal succession containing Hornby Bay sandstones, Dismal Lake carbonates, and Coppermine River flood basalts (Smith, 1962; Baragar & Donaldson, 1973; Hoffman, 1984). The intrusion was emplaced along with the Coppermine River flood basalts and Mackenzie dikes during the 1.27 Ga Mackenzie magmatic event. The Mackenzie magmatic event represents a period of extensive tholeiitic magmatism considered to reflect the emplacement of a mantle plume at the base of the lithosphere at the outset of continental rifting (Fig. 1.1) (Fahrig, 1987; LeCheminant & Heaman, 1989; Baragar et al., 1996; Stewart & DePaolo, 1996; Griselin et al. 1997). The Muskox intrusion has been the site of numerous scientific studies and Ni-Cu-PGE exploration programs, however relatively few studies have focused on providing a comprehensive geologic and geochemical context for rocks of the marginal zone, their relationship to the layered series, and the origin of associated sulphide mineralization.

The initial discovery of the intrusion (ca. 1956) was made by members of the Canadian Nickel Company (now INCO Ltd.) during aerial reconnaissance when two prominent ridges of gossan were recognized; these ridges delineated sulphide mineralization along the inward dipping walls of the intrusion (Irvine & Baragar, 1972). Numerous exploration companies have targeted this marginal zone sulphide – INCO Ltd. (ca. 1957-1959), Equinox Resources Ltd. and International Platinum Company (ca. late 1980s), Muskox Minerals Corporation (ca. 1995-present) and Anglo American Exploration (Canada) Ltd. (ca. 2003-2004). Over 240 exploration holes have been drilled on the Muskox intrusion, however no economic accumulations have been found to date (DeSchutter, 2003). Sulphides within the Muskox intrusion are mostly concentrated along the basal margin of the intrusion, and sulphide is also associated with chromitite within the upper part of the layered series (Chamberlain, 1967). The Muskox chromitite typically contains an order of magnitude less platinum group elements than analogous chromite-rich horizons from the Stillwater complex, Montana, and Bushveld complex, South Africa (Barnes & Francis, 1995). The basal sulphides are sporadically distributed and typically form relatively thin bands or layers with highly variable metal contents (Barnes & Francis, 1995). Sulphur isotopic compositions of sulphide show that sulphur was

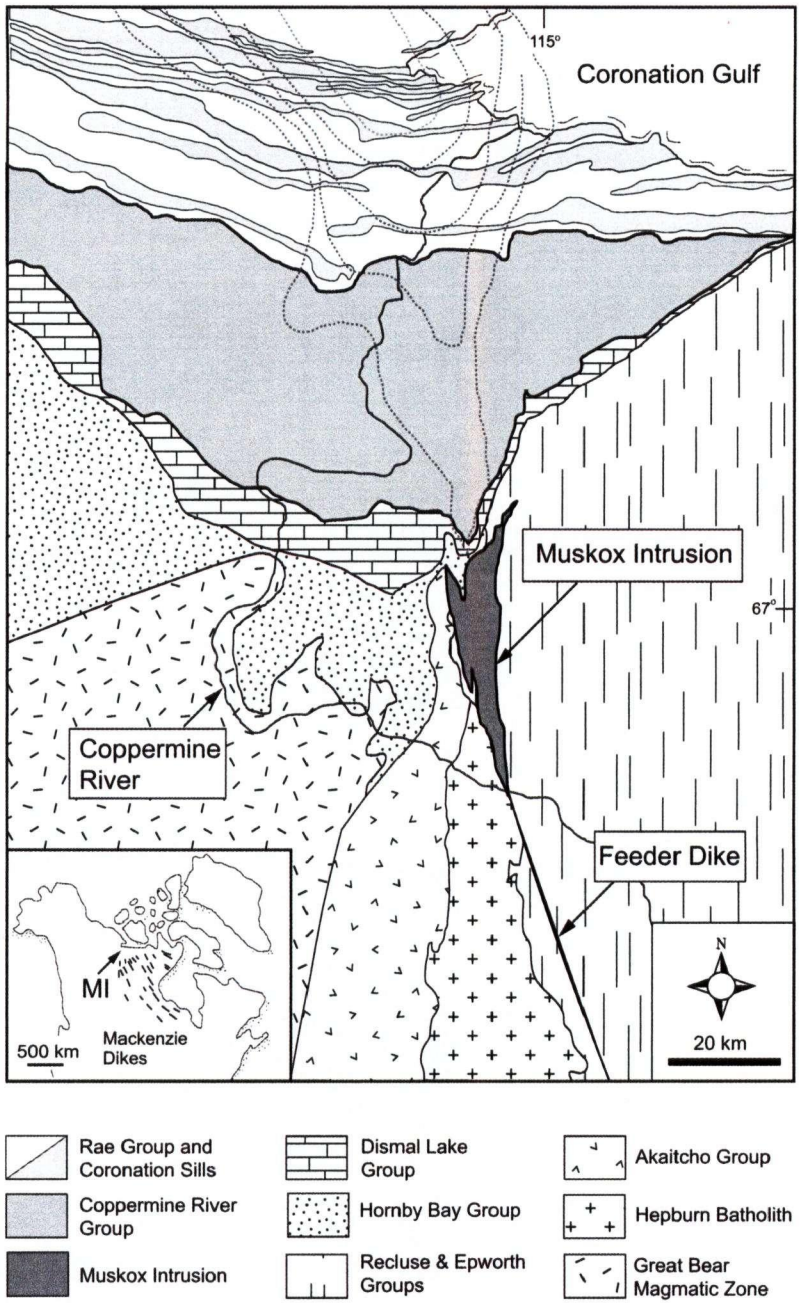

Fig. 1.1: Regional geologic and gravity map of the Coppermine region, Nunavut (adapted from Francis, 1994; geologic map compiled by Hoffman, 1984). Gravity contours (dotted lines, 10 mgl intervals) are from Irvine & Smith (1967) and are based on gravity data from Hornal (1963). The inset shows the distribution of the Mackenzie dikes (after Gibson et al., 1987), MI = Muskox intrusion. The Muskox intrusion and its underlying feeder dike are exposed for over 120 km within deformed rocks of the Wopmay orogen (Recluse, Epworth, and Akaitcho groups, Hepburn Batholith, and Great Bear Magmatic Zone) and beneath rocks of the Coppermine Homocline (Hornby Bay, Dismal Lakes, Coppermine River, and Rae groups). The Muskox intrusion plunges towards the north beneath the overlying supracrustal rocks and may, in part, be responsible for the gravity anomaly that extends northward towards the Coronation Gulf.

derived primarily from a crustal source indicating that interaction between the Muskox magmas and adjacent country rocks was an important factor in the formation of marginal zone sulphide (Sasaki, 1969; Barnes & Francis, 1995).

Mapping and deep drilling programs by the Geological Survey of Canada (Smith, 1962; Findlay & Smith, 1965) revealed that the intrusion is exposed for over 120 km from the basal feeder in the south to the upper roof zone in the north, and plunges shallowly northward (~5-10°) beneath the overlying volcano-sedimentary succession where it reaches a maximum thickness of ~2000 m (Fig. 1.2). The main body of the intrusion is divided into two marginal zones that trend parallel to the inward-dipping walls of the intrusion (20-50°; Smith, 1962), a layered series that contains numerous northward dipping dunite, pyroxenite, and gabbroic layers, and a granophyric roof zone that forms a heterogeneous region along the upper contact of the intrusion (Fig. 1.2 & 1.3). A characteristic feature of the marginal zone is that it becomes progressively more evolved in composition towards the base (i.e. from peridotite to gabbronorite). This trend is opposite from that observed in the overlying layered series and that expected during differentiation of the tholeiitic parental magmas to the intrusion (Smith, 1962; Irvine & Smith, 1967; Francis, 1994). The mechanism by which the marginal zone formed and its relationship to the layered series are not well constrained. The only other study that focused on the marginal rocks of the intrusion was completed by Francis (1994), who investigated the effects of crustal contamination within the feeder dike, marginal zone, and layered series rocks based on major and trace element compositions of outcrop samples. This study indicated that contamination within the marginal zone was restricted to a thin zone along the outer margin of the intrusion and involved the selective exchange of primarily the most incompatible elements (i.e. large ion lithophile and light rare earth elements) between mafic magmas within the Muskox chamber and adjacent crustal rocks.

The Muskox intrusion is considered to have formed by repeated injections of relatively undifferentiated (high MgO ~14 wt %; Irvine, 1977) basaltic magma and concurrent removal (eruption) of fractionated liquid (Irvine & Smith, 1967; Irvine, 1970). The cumulate rock layers within the intrusion record the order that minerals crystallized and accumulated from successive magma pulses. Irvine (1980) proposed that compaction of newly deposited cumulates was an important process by which fractionated interstitial melt was removed to produce the thick dunite layers (>90 vol % olivine) within the lower 2/3 of the intrusion. He also suggested that upward migrating fractionated liquid would react with cumulus minerals within the overlying cumulate pile, producing shifts in whole rock and mineral compositions. Tharp et al. (1998)

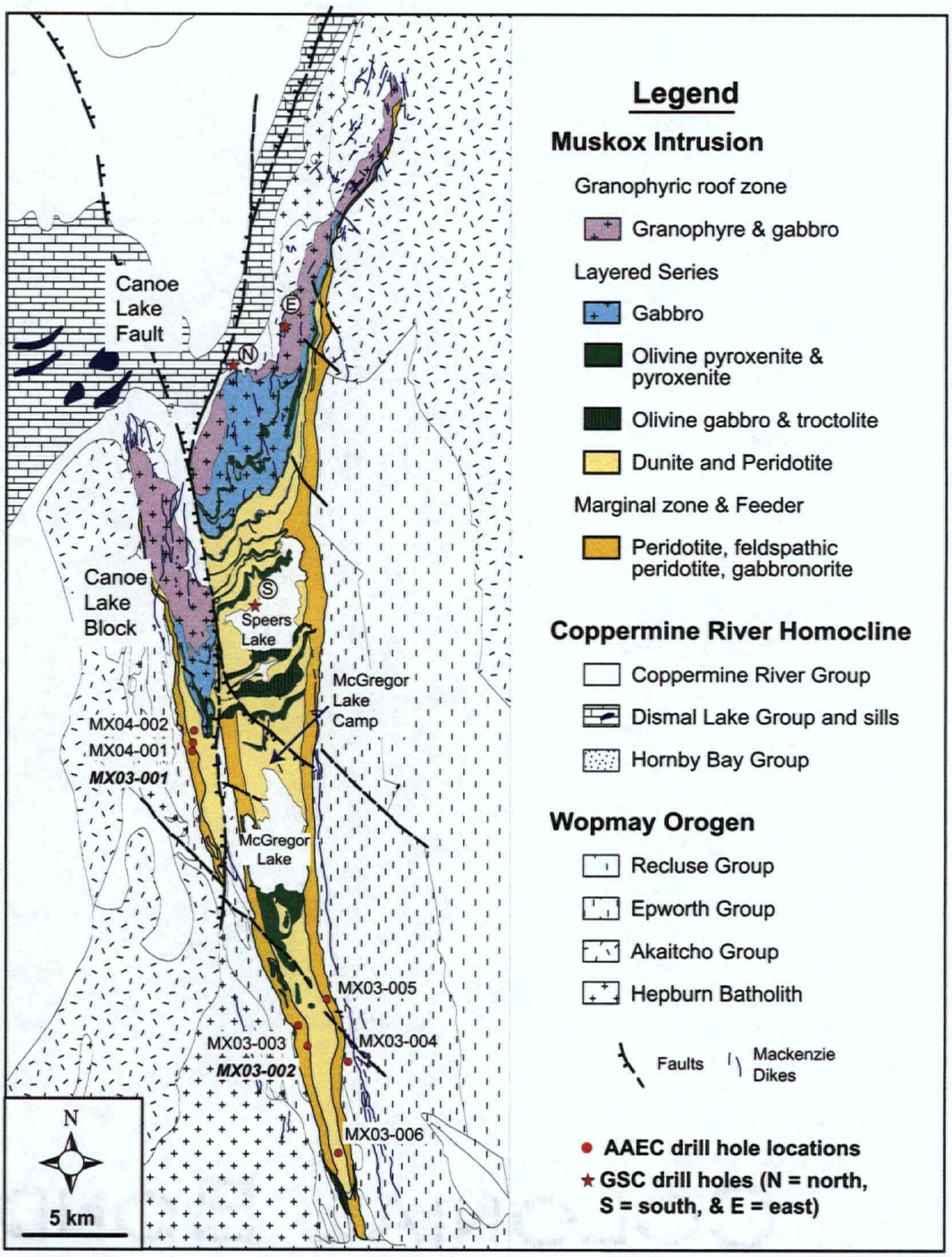

Fig. 1.2: Geologic map of the Muskox intrusion and surrounding area showing the locations of the Anglo American Exploration (Canada) Ltd. drill holes and the historic Geological Survey of Canada drill holes (after Hulbert, 2005; mapping by Smith, 1962). Water bodies have been omitted for clarity, with the exception of McGregor and Speers lakes. The feeder dike extends off the map toward the south. The intrusion is cut by the Canoe Lake fault, which separates the Canoe Lake Block from the main body of the intrusion. This study focuses on the marginal rocks and adjacent country rocks along the western margin of the intrusion that were intersected in drill holes MX03-002 (West Pyrrhotite Lake) and MX03-001 (Far West Margin).

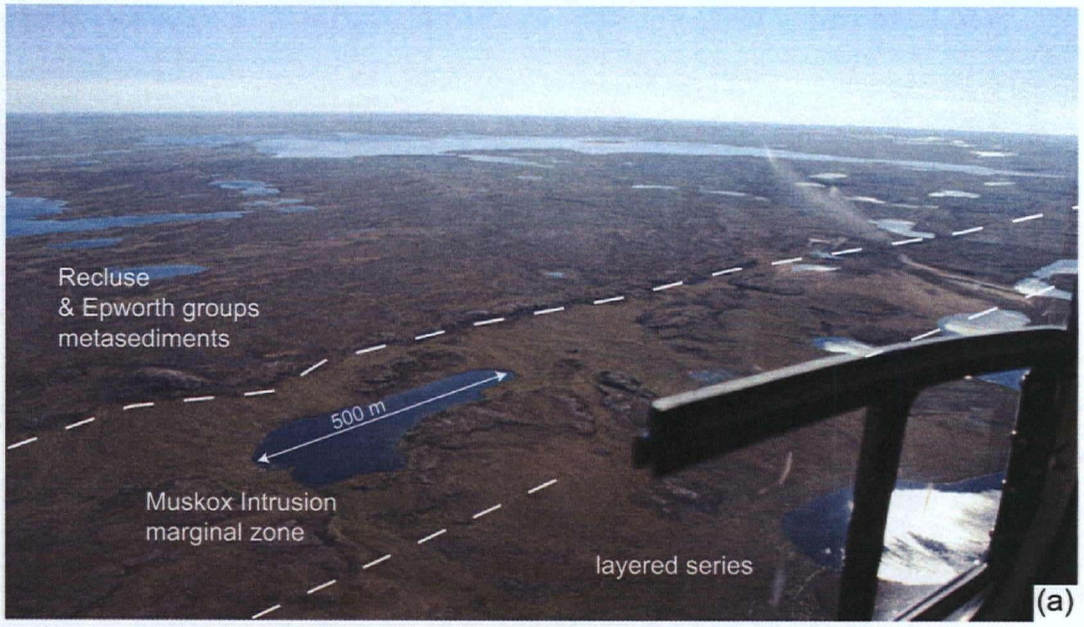

Fig. 1.3: (a) Aerial photograph of the eastern contact of the Muskox intrusion and the adjacent metasedimentary rocks between Speers Lake and McGregor Lake (looking southeast). (b) Photograph of oxidized, sulphide-bearing marginal rocks southeast of McGregor Lake (looking east).

modeled the compaction of olivine cumulates within the Muskox intrusion and proposed that conduction of heat through the floor of the intrusion likely played an important role in the formation of the marginal zone. Several studies have shown that compaction of igneous cumulates is an important process in the chemical and textural evolution of mafic-ultramafic bodies (Shirley, 1987; Meurer & Boudreau, 1998a; 1998b; Boudreau & Philpotts, 2002).

1.2 ANGLO AMERICAN EXPLORATION (CANADA) LTD. DRILL PROGRAM

Recent (ca. 2003-2004) Ni-Cu-PGE exploration activities within the Muskox intrusion provided a unique opportunity to investigate the marginal zone rocks of one of the world's largest known layered intrusions. Anglo American Exploration (Canada) Ltd. (joint venture with Muskox Minerals Corp. (now Prize Mining Corp.) completed eight exploration drill holes during the summer of 2003 and winter of 2004, which were designed to test conductive bodies delineated using a then proprietary Spectrem time-doman airborne electromagnetic system (Fig. 1.2) (DeSchutter, 2004; 2005). Operations were conducted from the McGregor Lake Camp on the north shore of McGregor Lake and included mainly ground-based geophysical surveys, soil sampling, and diamond drilling (~2000 m total). Drilling by AAEC intersected relatively thin zones (<0.5 m) of massive sulphide adjacent to and within host paragneiss at the base of the marginal zone within the Canoe Lake Block along the western margin of the intrusion. During employment with AAEC, the author was involved in various parts of the 6-week summer exploration during the 2003 program including prospecting, ground geophysical surveys, core logging, and sample collection. For the purposes of the present study drill core samples were collected every 6-10 m down-hole, providing exceptionally detailed chemical profiles (major element oxide and trace element concentrations) through the marginal zone rocks at different locations within the intrusion. This study focuses on two drill holes (MX03-002 and MX03-001) along the western margin of the intrusion (Fig. 1.2). Examination of petrographic and geochemical variations from other drill holes provided supplementary information. The West Pyrrhotite Lake and Far West Margin sections were chosen because of distinct mineralogical and chemical characteristics of the intrusive and country rocks at each location observed during core logging. In addition, these sections occur at different locations within the Muskox intrusion, allowing for a comparison of the character of the marginal zone at different stratigraphic heights within the intrusion.

1.3 OVERVIEW OF THE THESIS

This thesis contains three distinct and complimentary studies of the marginal rocks of the Muskox intrusion that are presented in Chapters 2, 3, and 4, respectively. This study provides the first combined mineralogical, chemical, isotopic, and geochronological investigation of marginal zone rocks within the Muskox intrusion. The objectives of this study are (1) to characterize the mineralogical and chemical variations of the marginal zone of the Muskox intrusion, (2) to provide constraints on the character and extent of crustal contamination along the base of the intrusion and its relationship to the formation of sulphide mineralization, (3) to generate a petrogenetic model for the formation of the marginal zone, and (4) to constrain the relationship between the Muskox intrusion and the other components of the Mackenzie magmatic event. Chapters 2 and 3 utilize drill core samples collected during the summer AAEC drill program at the West Pyrrhotite Lake and Far West Margin sections, whereas Chapter 4 employs a previously compiled dataset of sulphide-mineralized samples from various locations along the margin of the intrusion (provided by AAEC and Muskox Minerals Corporation). Chapters 2, 3, and 4 were prepared in a manuscript format appropriate for submission to international scientific journals. As such, there are some areas of overlap between the chapters mainly regarding introductory figures and background material, however each of the background sections is described within a context relevant to the individual chapter. Chapter 5 is a summary of the major findings of this thesis.

Chapter 2 involves a detailed characterization of the mineralogical, textural, and chemical variations of marginal rocks and adjacent country rocks at the West Pyrrhotite Lake and Far West Margin sections. Major and trace element results from 82 drill core samples combined with petrographic observations provide the framework for investigating the formation of the marginal zone of the Muskox intrusion. Sulphur isotopic compositions (23 samples) and trace element abundances of marginal zone rocks and adjacent wall rocks constrain the nature and extent of crustal contamination along the basal margin of the intrusion, which has important implications for the formation of marginal zone sulphide mineralization. Olivine compositions from peridotites (180 individual analyses from 10 samples) within the upper part of the marginal zone, although originally acquired to calculate parent magma compositions, appear to record varying degrees of re-equilibration with interstitial liquid. The IRIDIUM program (Boudreau, 2003) is used to model compaction of olivine cumulates within a thermal gradient to asses the role of compaction in producing the observed mineralogical and chemical variations within marginal zone rocks.

Chapter 3 evaluates the U-Pb geochronology of marginal zone rocks, and Hf and Nd isotopic compositions and trace element abundances of marginal rocks and the adjacent country rocks. U-Pb dating of baddeleyite from two peridotites and one gabbronorite at the two studied regions constrains the crystallization age of the marginal zone and confirms the temporal relationship between the Muskox intrusion and the Mackenzie dikes (1267 ± 2 Ma; LeCheminant & Heaman, 1989). The Hf and Nd isotopic compositions and high-precision trace element abundances of peridotites, gabbronorites and country rock gneisses (17 samples) not only constrain the spatial extent and degree of crustal contamination, but also provide a link between the marginal zone and layered series of the intrusion. A compilation of Nd isotopic compositions from this study and previous investigations of the Muskox intrusion (Stewart & DePaolo, 1992; 1996), Mackenzie dikes (Dundas & Peterson, 1992 (unpublished)), and Coppermine River basalts (Griselin et al. 1997) provide unique insights into the relationship between each of these bodies and the mantle source for the Mackenzie magmatic event.

Chapter 4 documents the compositional variations of sulphide within marginal rocks at various locations within the Muskox intrusion. Recalculation of whole rock Ni, Cu, Pd, and S values (330 samples) to 100% sulphide allows for comparison of the metal contents from samples with varying amounts of sulphide. The compositions of magmatic Ni-Cu-PGE sulphides are considered to reflect variations in the metal contents of the magma from which a sulphide liquid segregates, the mass of silicate magma with which the liquid equilibrates, and subsequent fractionation of the sulphide liquid during cooling (e.g. Campbell & Naldrett, 1979; Naldrett et al., 1997). Numerical modeling of the compositional variation produced by these effects help constrain the formation and relationship of sulphides at different locations within the intrusion.

Finally, the appendix contains tables summarizing: 1) the analytical methods and procedural duplicates for major and trace element results from ACME Analytical Laboratories Ltd., 2) complete olivine compositions by electron microprobe, 3) a comparison of the Ni abundance of olivine by different electron microprobe methods, 4) duplicate analyses of trace element abundances by high-resolution ICP-MS at the Pacific Centre for Isotopic and Geochemical Research (PCIGR), 5) a comparison of trace element abundances for USGS reference materials, and 6) a comparison of trace element results from PCIGR and ACME Ltd.

1.4 REFERENCES

Baragar, W.R.A. & Donaldson, J.A. (1973). Coppermine and Dismal Lakes map areas. *Geological Survey of Canada Paper* **71-39**, 20 pp.

Baragar, W.R.A., Ernst, R.E., Hulbert, L. & Peterson, T. (1996). Longitudinal petrochemical variation in the Mackenzie dike swarm, Northwestern Canadian Shield. *Journal of Petrology* **37-2**, 317–359.

Barnes, S.J. & Francis, D. (1995). The distribution of platinum-group elements, nickel, copper, and gold in the Muskox Layered Intrusion, Northwest Territories, Canada. *Economic Geology* **90**, 135–154.

Boudreau, A.E. (2003). IRIDIUM- a program to model reaction of silicate liquid infiltrating a porous solid assemblage. *Computers & Geosciences* **29**, 423–429.

Boudreau, A.E. & Philpotts, A.R. (2002). Quantitative modeling of compaction in the Holyoke flood basalt flow, Hartford Basin, Connecticut. *Contributions to Mineralogy and Petrology* **144**, 176-184.

Campbell, I.H. & Naldrett, A.J. (1979) The influence of silicate:sulfide ratios on the geochemistry of magmatic sulphides. *Economic Geology* **74**, 1503–1506.

Chamberlain, J.A. (1967). Sulfides in the Muskox intrusion. *Canadian Journal of Earth Sciences* **4**, 105–153.

DeSchutter, G. (2004). Muskox intrusion project, Kitikmeot Region, Nunavut. *Anglo American Exploration (Canada) Ltd. 2003 Work Report*, 52 pp.

DeSchutter, G. (2005). Muskox intrusion project, Kitikmeot Region, Nunavut. *Anglo American Exploration (Canada) Ltd. 2004 Work Report*, 52 pp.

Dudas, F.O. & Peterson, T.D. (1992). Nd isotopic composition of Mackenzie Dikes, Northwest Territories, Canada (Abstract). *EOS, Transactions of the American Geophysical Union, Spring Meeting Supplement* **339**.

Fahrig, W.F. (1987). The tectonic settings of continental mafic dyke swarms: Failed arm and early passive margins. *Geological Association of Canada Special Paper* **34**, 331–348.

Francis, D. (1994). Chemical interaction between picritic magmas and upper crust along the margins of the Muskox intrusion, Northwest Territories. *Geological Survey of Canada Paper* **92-12**, 94 pp.

Gibson, I.L., Sinah, M.N. & Fahrig, W.F. (1987). The geochemistry of the Mackenzie Dike Swarm, Canada. In: Halls, H.C. & Fahrig, W.F. (eds) *Mafic Dyke Swarms. Geological Association of Canada, Special Paper* **34**, 109–121.

Griselin, M., Arndt, N. & Baragar, W.R.A. (1997). Plume-lithosphere interaction and crustal contamination during formation of Coppermine River basalts, Northwest Territories, Canada. *Canadian Journal of Earth Sciences* **34**, 958–975.

Hoffman, P.F. (1984). Geology, Northern Internides of Wopmay Orogen, District of Mackenzie, Northwest Territories. *Geological Survey of Canada, Map* **1576A**.

Hornal, R.W. (1968). The gravity anomaly field in the Coppermine area of the Northwest Territories (Canada). *Dominion Observatory Gravity Map Series*, **45**.

Hulbert, L. (2005). Geology of the Muskox intrusion and associated Ni and Cu occurrences. *Geological Survey of Canada, Open File 4881, CD-ROM.*

Irvine, T.N. (1970). Crystallization sequences in the Muskox intrusion and other layered intrusions – I. Olivine-pyroxene-plagioclase relations. In: Visser, D.J.L. & Von Gruenewaldt, G. (eds) *Symposium on the Bushveld Igneous Complex and Other Layered Intrusions. Geological Society of South Africa, Special Publication* **1**, 441–476.

Irvine, T.N. (1977). Definition of primitive liquid compositions for basic magmas. *Carnegie Institute of Washington Year Book* **76**, 454–461.

Irvine, T.N. (1980). Magmatic infiltration metasomatism, double-diffusive fractional crystallization, and adcumulus growth in the Muskox intrusion and other layered intrusions. In: Hargraves, R.B. (ed.) *Physics of Magmatic Processes*. Princeton: Princeton University Press, pp. 325–383.

Irvine, T.N. & Smith, C.H. (1967). The ultramafic rocks of the Muskox intrusion, Northwest Territories, Canada. In: Wyllie, P.J. (ed.) *Ultramafic and Related Rocks*. New York: John Wiley & Sons, Inc., pp. 38–49.

Irvine, T.N. & Baragar, W.R.A. (1972). Muskox intrusion and Coppermine River lavas, Northwest Territories, Canada. *International Geological Congress Field Excursion* **A29**, 70 pp.

LeCheminant, A.N. & Heaman, L.M. (1989). Mackenzie igneous events, Canada: Middle Proterozoic hotspot magmatism associated with ocean opening. *Earth and Planetary Science Letters* **96**, 38–48.

Naldrett, A.J., Ebel, D.S., Asif, M., Morrison, G. & Moore, C.M. (1997). Fractional crystallization of sulfide melts as illustrated at Noril'sk and Sudbury. *European Journal of Mineralogy* **9**, 629–635.

Meurer, W.P. & Boudreau, A.E. (1998a). Compaction of igneous cumulates part I: geochemical consequences for cumulates and liquid fractionation trends. *Journal of Geology* **106**, 281–292.

Meurer, W.P. & Boudreau, A.E. (1998b). Compaction of igneous cumulates part II: compaction and the development of igneous foliations. *Journal of Geology* **106**, 293–304.

Sasaki, A. (1969). Sulphur isotope study of the Muskox intrusion, District of Mackenzie (86 J/13, O/3). *Geological Survey of Canada Paper* **68-46**, 68 pp.

Shirley, D.N. (1987). Differentiation and compaction in the Palisades sill, New Jersey. *Journal of Petrology* **28**, 835–865.

Smith, C.H. (1962). Notes on the Muskox Intrusion, Coppermine River area, District of Mackenzie. *Geological Survey of Canada Paper* **61-25**, 16 pp.

Smith, C.H. & Kapp, H.E. (1963). The Muskox intrusion, a recently discovered layered intrusion in the Coppermine River area, Northwest Territories, Canada. *Mineralogical Society of America, Special Paper* **1**, 30–35.

Tharp, T.M., Loucks, R.R. & Sack, R.O. (1998). Modeling compaction of olivine cumulates in the Muskox intrusion. *American Journal of Science* **298**, 758–790.

CHAPTER 2

Formation of the Marginal Zone in the 1.27 Ga Muskox intrusion, Nunavut: crustal contamination, sulphide mineralization, and compaction

2.1 INTRODUCTION

Basal marginal zones are an important subdivision of mafic-ultramafic intrusions that potentially provide information on the processes of magma emplacement, crustal contamination and cooling along the basal contacts and outer walls of magma chambers. These marginal zones, or border series, are observed in many differentiated mafic-ultramafic sills (e.g. Partridge River intrusion, Duluth complex, Minnesota, USA) and layered intrusions (e.g. Great Dyke, Zimbabwe; Stillwater Intrusion, Montana, USA) and are generally characterized by a downward differentiation trend in terms of whole rock and mineral chemistry (Wilson, 1982; Raedeke & McCallum, 1984; Page et al., 1985; Hoover, 1989; Grant & Chalokwu, 1992; Laytpov, 2003; Gibb & Henderson, 2006). This trend is typically opposite from that observed in the overlying rocks and from that expected during fractionation of basaltic magma. Previous studies on the Muskox intrusion, Nunavut, demonstrated that compaction of cumulates and migration of intercumulus liquid may have been an important differentiation mechanism in the development of the inverted character of the marginal zone (Irvine, 1980; Tharp et al., 1998).

The Muskox intrusion, one of the world's largest known mafic-ultramafic layered intrusions, contains a marginal zone that has been the focus of numerous Ni-Cu-PGE exploration programs since the discovery of the intrusion in 1956 by the Canadian Nickel Company (Smith & Kapp, 1963; Irvine, 1988). Over 240 exploration drill holes have targeted Ni-Cu-PGE-enriched sulphide mineralization along the basal margin of the intrusion, however to date no economic accumulations have been found (Chamberlain, 1967; Barnes & Francis, 1995). Despite this ongoing exploration interest, relatively few scientific studies have been completed on marginal zone rocks. Mapping and deep drilling (>3000 m combined) programs completed by the Geological Survey of Canada in the early 1960's provided an understanding of the morphology and internal structure of the intrusion and revealed that the marginal zone is a structurally distinct unit that extends throughout the entire stratigraphic height of the intrusion (Smith, 1962; Findlay & Smith, 1965; Smith, 1967). A study of the variations in the sulphur isotopic compositions from sulphides along the basal contact of the intrusion by Sasaki (1969) indicated that the sulphur was largely derived from the local crustal rocks. This led Barnes and Francis (1995) to suggest that the sporadic distribution of sulphide along the margin of the intrusion was the result of limited availibility of a local sulphur source. Francis (1994) evaluated compositional variations from a number of exposed sections of the marginal

zone rocks along mainly the eastern side of the intrusion and proposed that the interaction between the Muskox magmas and the adjacent crustal rocks, which is recorded in only the outer few metres of the intrusion, was a selective process involving mainly the most incompatible trace elements (large ion lithophile and light rare earth elements).

In this study we examine new drill core samples collected at two different regions along the western margin of the intrusion (West Pyrrhotite Lake and Far West Margin) during a recent Anglo American Exploration (Canada) Ltd. (AAEC) drill program. Detailed petrographic observations combined with an evaluation of major and trace element abundances, olivine chemistry, and sulphur isotopic compositional variations provide a framework for investigating the origin and evolution of the marginal zone of the Muskox intrusion. The main goals of the study are (1) to classify the mineralogical, textural, and chemical variations that define the marginal zone at different locations within the intrusion, (2) to determine the character and spatial extent of contamination along the basal margin of the intrusion and its relationship to observed sulphide mineralization, (3) to develop a conceptual and a quantitative model for the formation of the marginal zone of the Muskox intrusion. We demonstrate that local crustal contamination is restricted to a very thin zone of gabbronoritic rocks at the base of the marginal zone, and that the downward differentiation trend in the marginal zone of the Muskox intrusion corresponds mainly to an overall downward increase in the proportion of intercumulus phases within overlying peridotites. Sulphides at the base of the marginal zone formed as a result of local addition of crustal sulphur and silicate material derived from the directly adjacent wall rocks. Comparison of the mineralogical and chemical characteristics of marginal rocks at the different sections indicates that their character changes at different locations within the intrusion, which indicates that the marginal zone likely formed at different stages during the evolution and growth of the Muskox magma chamber. Finally, using the IRIDUM software (Boudreau, 2003), we show that the mineralogical and chemical variation observed within the peridotites can be readily explained by crystallization of varying amounts of intercumulus liquid during compaction of a cumulate pile within a thermal gradient at the base of the intrusion, supporting the original proposals of Irvine (1980) and Tharp et al. (1998).

2.2 GEOLOGY AND EMPLACMENT OF THE MUSKOX INTRUSION

The Muskox intrusion (1270 ± 4 Ma, U-Pb baddeleyite/zircon; LeCheminant & Heaman, 1989) is located ~60 km south of the Coronation Gulf in the Coppermine region of Nunavut, Canada (Fig. 2.1). The main body of the intrusion and underlying feeder dike are exposed for over 120 km within early Proterozoic rocks of the Wopmay orogen and an overlying late Proterozoic supracrustal succession containing the Hornby Bay sandstones, Dismal Lake carbonates, and Coppermine River flood basalts (Hoffman, 1980; Hoffman, 1984; Hoffman & Bowring, 1984; Hoffman & Hall, 1993). Based on gravity data, the exposed part of the intrusion may only represent a portion of a much larger body that extends northward beneath the overlying supracrustal rocks (Irvine, 1970). The Muskox intrusion, along with the Mackenzie dike swarm and Coppermine River basalts, was emplaced during the 1.27 Ga Mackenzie magmatic event, which represents a period of extensive tholeiitic magmatism considered to be related to the emplacement of a mantle plume (Baragar, 1969; Fahrig, 1987; LeCheminant & Heaman, 1989; Dupuy et al., 1992; Baragar et al., 1996; Stewart & DePaolo, 1996; Griselin et al., 1997).

The intrusion has been divided into a feeder dike, marginal zone, layered series, and granophyric roof zone (Fig. 2.2 & 2.3; Smith, 1962; Smith & Kapp, 1963; Findlay & Smith, 1965). The feeder is exposed south of the Coppermine River (Fig. 2.1) and consists of a ~100-150 m wide, steeply-dipping, gabbronorite and norite dike that is considered to represent part of the conduit through which the initial magmas entered the chamber; later influxes may have been injected from the north (Irvine, 1980). The 100-200 m thick marginal zone trends parallel to the inward-dipping walls of the intrusion and is discordant to the layering within the layered series (Smith, 1962). The overlying 1800 m-thick layered series contains numerous rock layers that are composed of principally olivine-chromite and olivine-clinopyroxene cumulates within the lower 1300 m of the intrusion, and pyroxene and plagioclase cumulates within the upper 600 m (Fig. 2.3; Findlay & Smith, 1965; Irvine & Smith, 1967; Bédard & Taner, 1992; DesRoches, 1992). The granophyric roof zone consists of granophyric gabbro and granophyre with abundant roof rock xenoliths and is considered to represent a layer of low-density, SiO_2-rich liquid that was produced during partial melting of the overlying wall rocks (Stewart & DePaolo, 1992).

Petrologic investigations of layered series rocks from the Muskox intrusion (Irvine & Smith, 1967; Irvine, 1970; 1975; 1977a) have shown that the intrusion formed through

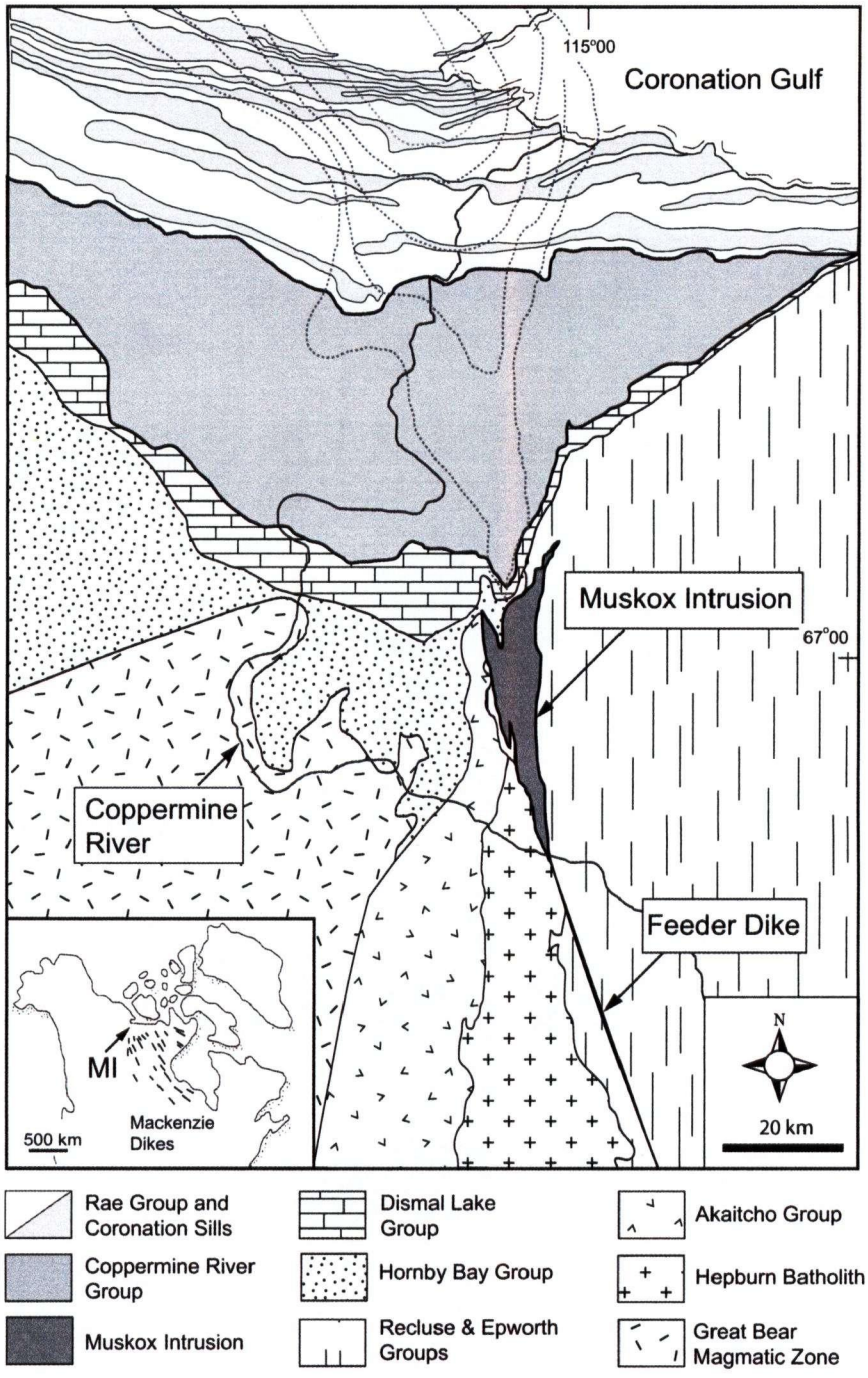

Fig. 2.1: Regional geologic and gravity map of the Coppermine region, Nunavut (adapted from Francis, 1994). Gravity contours (dotted lines, 10 mgl intervals) are from Irvine & Smith (1967) and are based on gravity data from Hornal (1963). The inset shows the distribution of the Mackenzie dikes (after Gibson et al., 1987), MI = Muskox intruison. The Muskox intrusion was emplaced below an unconformity at the base of Hornby Bay and Dismal Lake group sediments, and along the boundary between metasedimentary and granitic rocks of Wopmay orogen (Irvine, 1970; 1980).

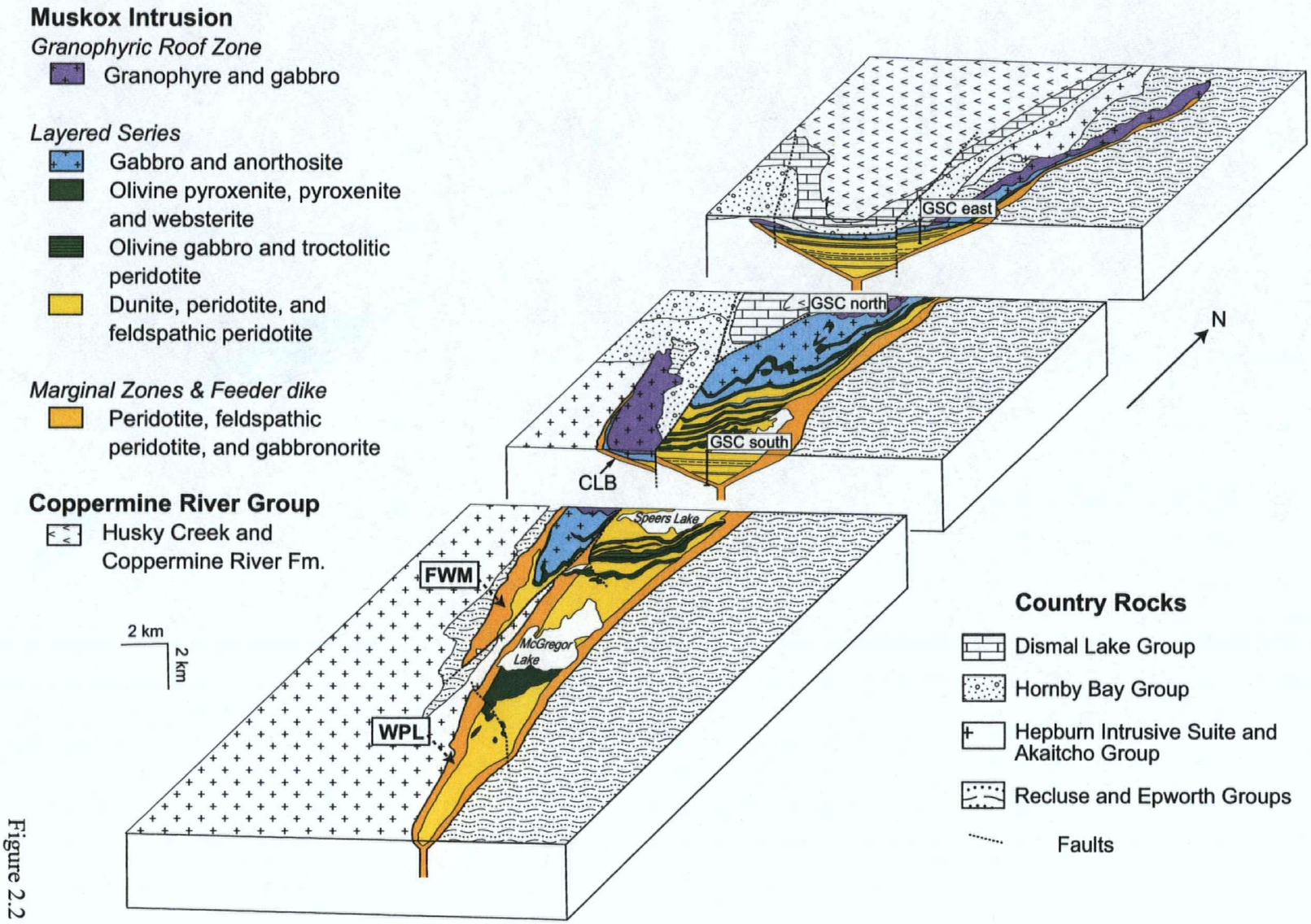
Muskox Intrusion
Granophyric Roof Zone
Granophyre and gabbro
Layered Series
Gabbro and anorthosite
Olivine pyroxenite, pyroxenite and websterite
Olivine gabbro and troctolitic peridotite
Dunite, peridotite, and feldspathic peridotite
Marginal Zones & Feeder dike
Peridotite, feldspathic peridotite, and gabbronorite
Coppermine River Group
Husky Creek and Coppermine River Fm.
2 km
2 km
GSC east
GSC north
GSC south
CLB
N
Speers Lake
FWM
McGregor Lake
WPL
Country Rocks
Dismal Lake Group
Hornby Bay Group
Hepburn Intrusive Suite and Akaitcho Group
Recluse and Epworth Groups
Faults

Figure 2.2

Fig. 2.2: Interpreted 3-dimensional geology map of the main body of the Muskox intrusion (after Irvine, 1980; based on mapping by Smith, 1962 and drill core descriptions by Findlay & Smith, 1965). The intrusion forms an elongate funnel-shaped body that plunges towards the north beneath the Hornby Bay and Dismal Lake Group sediments. A major north-trending fault, the Canoe Lake Fault, displaces the Canoe Lake Block (CBL) southward along the western margin of the intrusion. The feeder dike, which is exposed off the map to the south, is projected beneath the main body of the intrusion. Note the location of the two study regions (WPL = West Pyrrhotite Lake; FWM = Far West Margin) and the historic Geological Survey of Canada drill holes (GSC south, north, and east).

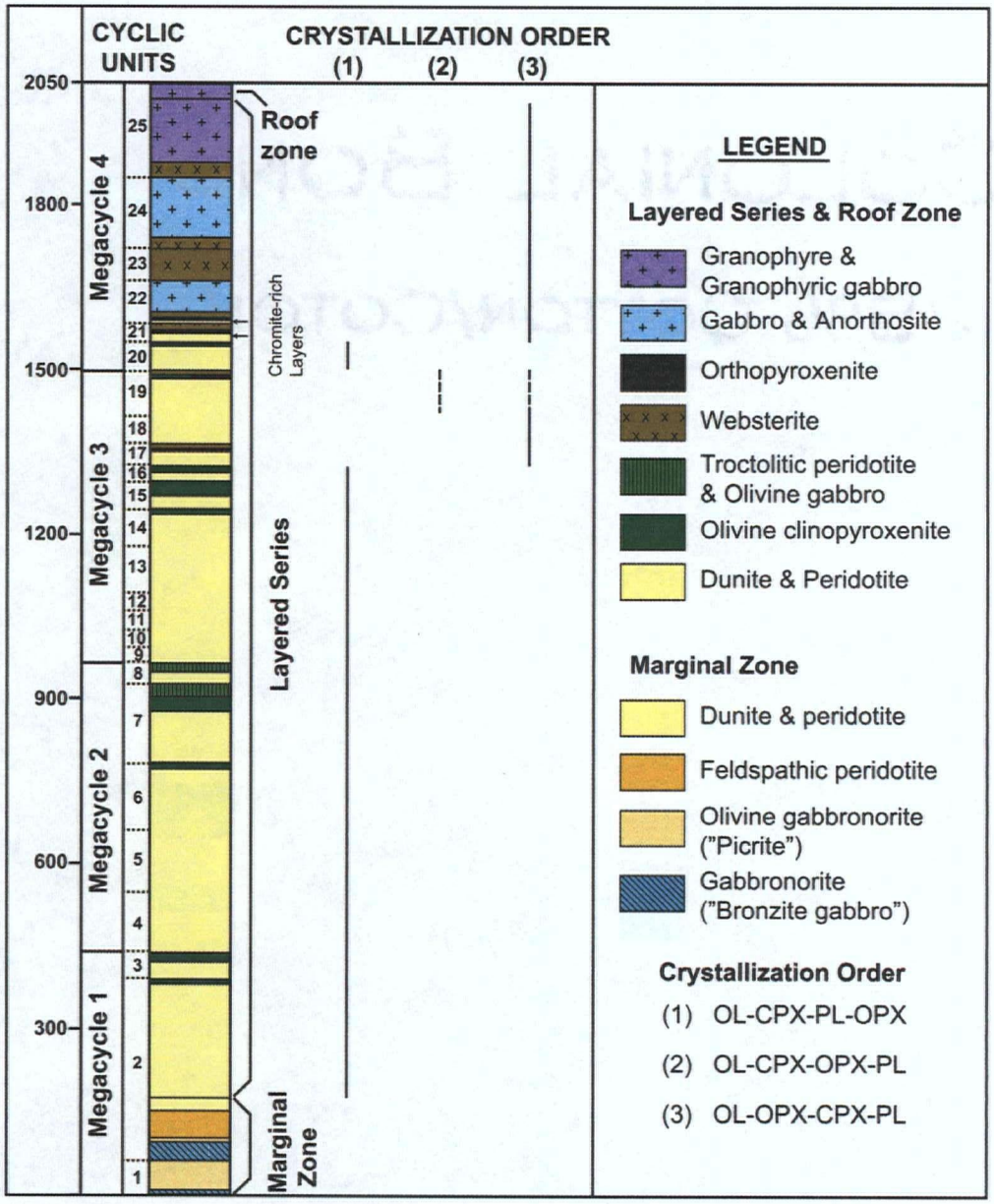

Fig. 2.3: Stratigraphic column of the Muskox intrusion based on Geological Survey of Canada drill holes (Findlay & Smith, 1965) showing the variations in the crystallization order for each cyclic unit defined by Irvine & Smith (1967). The division of the layered series into four megacycles (Francis, 1994) reflects larger-scale changes in the evolution of the Muskox magma chamber. Cyclic units are defined by both shifts to less differentiated compositions in the accumulating mineral assemblage and cryptic chemical variations within thick dunitic sections (Irvine & Smith, 1967). There is an overall progression to more evolved compositions upwards with dunite, peridotite, and feldspathic peridotite, and olivine clinopyroxenite forming most of the lower 1500 metres; and websterite, orthopyroxenite, and gabbro forming the upper 500 metres of stratigraphy. The marginal zone shows the opposite trend and becomes more evolved in composition towards the base, as described in detail in the text. This downward trend in differentiation is observed in both cyclic unit 1 (feldspathic peridotite to gabbronorite) and the lower part of cyclic unit 2 (peridotite to gabbronorite) which indicates that locally the marginal zone contains multiple sequences.

numerous injections of basaltic magma and concurrent removal (eruption) of fractionated residual liquid. Irvine and Smith (1967) grouped the cumulate rock layers within the intrusion into 25 cyclic units, each of which represents the minerals removed and deposited from a single magma batch (Fig. 2.3). The rocks within a cyclic unit become more evolved in composition with increasing stratigraphic height. The transition from relatively evolved cumulates at the top of one cyclic unit to less differentiated cumulates at the base of the overlying cyclic unit is considered to record the influx of higher temperature, less fractionated magma and removal of fractionated residual magma (Irvine, 1970). A change in the order of crystallization within the upper part of the intrusion (i.e. advanced crystallization of orthopyroxene) reflects a change to a more SiO_2-rich magma, potentially as a result of mixing relatively evolved and primitive magmas within the chamber (Irvine & Smith, 1967; Irvine, 1970; Stewart & DePaolo, 1992; 1996). A similar mechanism was proposed for the formation of two chromitite seams that occur within peridotite at the base of cyclic units 21 and 22 (Irvine, 1975; 1977a; Roach et al., 1998). Irvine (1980) and Tharp et al. (1998) proposed that crystals accumulated at the base of the Muskox chamber would compact under their own weight, such that much intercumulus liquid was continuously recycled into the overlying magma column. Thus, the rocks within the intrusion are considered to have formed through the initial accumulation of minerals at the base of the magma chamber, and concurrent removal of intercumulus liquid during compaction of the cumulate pile.

2.3 MARGINAL ZONE ROCKS FROM THE WESTERN MARGIN OF THE MUSKOX INTRUSION

The two regions studied represent sections across the marginal zone at stratigraphically low (West Pyrrhotite Lake) and high (Far West Margin) positions along the western margin of the Muskox intrusion (Fig. 2.2). The following is a detailed description of the mineralogical and textural variations of marginal zone rocks and adjacent country rocks from drill holes MX03-002 (total depth = 200 m) for the West Pyrrhotite Lake section and MX03-001 (total depth = 175 m) for the Far West Margin section (Fig. 2.4). Observations from two additional drill holes located 400 m (MX04-001) and 1000 m (MX04-002) north of the Far West Margin section provide supplementary information and indicate that the lithologic units described below can be traced along strike for >1 km north of the Far West Margin section. As described by Irvine (1970) the rocks within the Muskox intrusion are mainly cumulates,

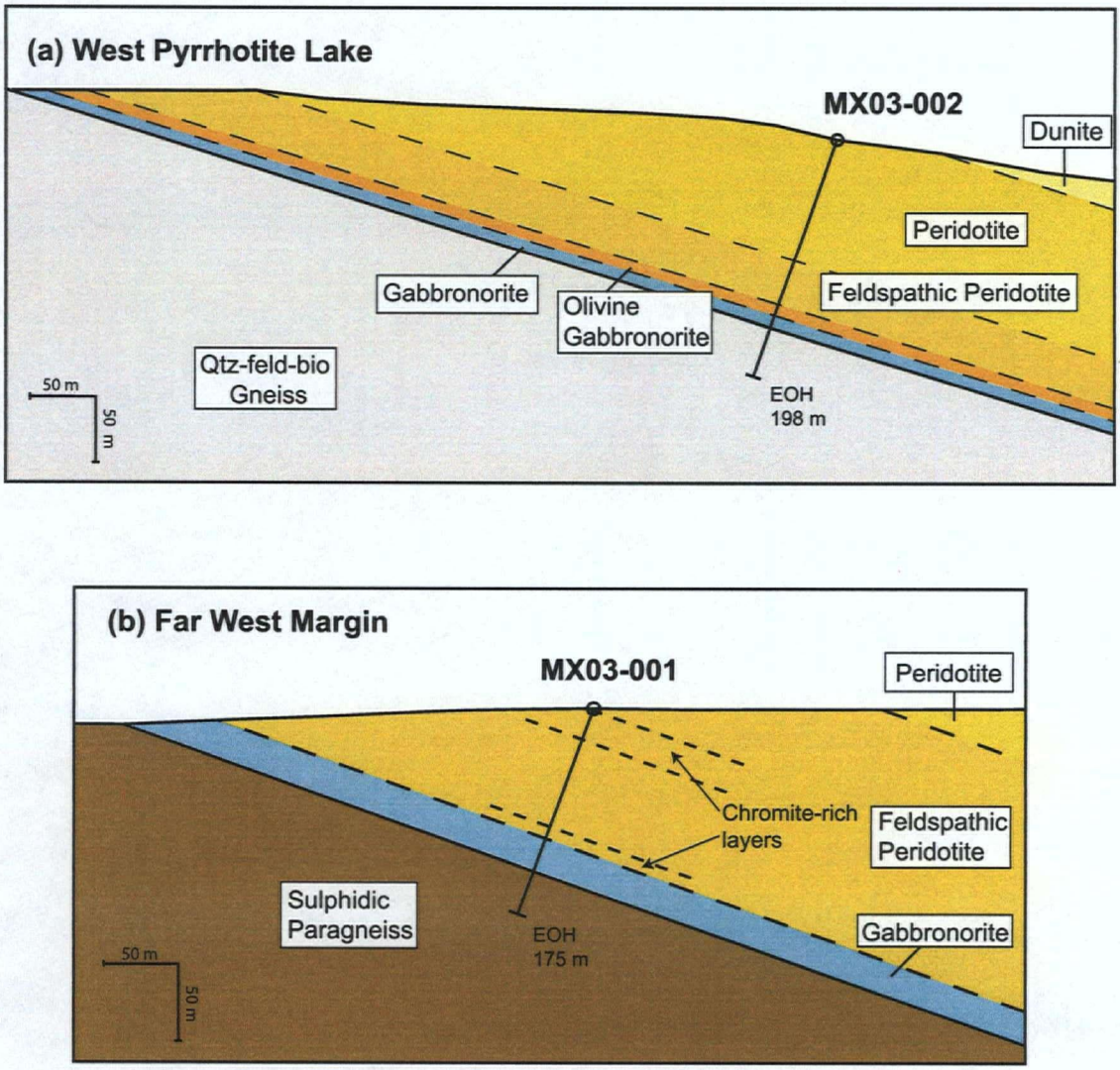

Fig. 2.4: Interpreted geologic cross-sections of the (a) West Pyrrhotite Lake (drill hole MX03-002; Az. 270/70°) and (b) Far West Margin (drill hole MX03-001; Az. 279/70°) sections. Geologic contacts are based on petrographic and chemical variations observed in drill core and are extended to the surface from mapping by Smith (1962). The West Pyrrhotite Lake section contains the typical marginal zone sequence, grading from peridotite at the innermost part, to feldspathic peridotite, olivine gabbronorite, and gabbronorite at the outer contact. The Far West Margin section is distinct and consists of chromite-rich peridotite, feldspathic peridotite, and gabbronorite. EOH = end of hole, referring to the termination of each diamond drill hole.

composed of early-forming cumulus minerals that are enveloped by late-forming postcumulus minerals. The cumulate terminology is used here to describe the mineralogy and texture of the marginal rocks and does not imply any specific mechanism of formation.

2.3.1 West Pyrrhotite Lake section

The marginal zone rocks at West Pyrrhotite Lake grade downwards from peridotite to feldspathic peridotite, olivine gabbronorite, gabbronorite, and granophyre-bearing gabbronorite (Fig. 2.4a). This succession is consistent with that of the typical marginal zone sequence as mapped by Smith (1962) throughout most of the length of the intrusion and that described by Francis (1994) along the eastern margin of the intrusion (Fig. 2.2). Representative photomicrographs of the textural and mineralogical variations within the West Pyrrhotite Lake section are shown in Fig. 2.5.

The uppermost unit of the marginal zone at West Pyrrhotite Lake consists of an 80 m-thick homogeneous peridotite unit that is composed of closely-packed 0.5-0.8 mm cumulus olivine (70-80 vol %) and <0.1 mm chromite (~1 vol %) that are enclosed within 0.3-0.8 cm orthopyroxene and clinopyroxene (20-30 vol %), plagioclase (<5 vol %), and phlogopite (2-3 vol %) oikocrysts (Fig. 2.5a). Ilmenite, pyrrhotite, apatite, and trace monazite are accessory minerals that are associated with phlogopite in the interstitial regions between cumulus olivine grains. Individual olivine grains are typically 50-100% altered to serpentine and magnetite, although clusters of unaltered olivine commonly occur within orthopyroxene oikocrysts (Fig. 2.5a). Plagioclase is completely altered, but can be distinguished because of prominent internal fracturing and rarely preserved albite twinning. A progressive increase in the amount of postcumulus plagioclase marks the transition (over 5-10 m) from peridotite to feldspathic peridotite.

The feldspathic peridotite unit (~60 m thick) consists of 0.5-0.8 mm closely-packed cumulus olivine (50-70 vol %) that is enclosed within plagioclase (5-20 vol %) and clinopyroxene oikocrysts (10-20 vol %) (Fig. 2.5b). The plagioclase content within this unit increases towards the base where it becomes the dominant interstitial phase over pyroxene. Orthopyroxene (~10-20 vol %) rarely encloses olivine and has sharp grain boundaries with plagioclase. A further increase in the amount and grain size of plagioclase and a significant decrease in the amount of olivine marks the transition to olivine gabbronorite.

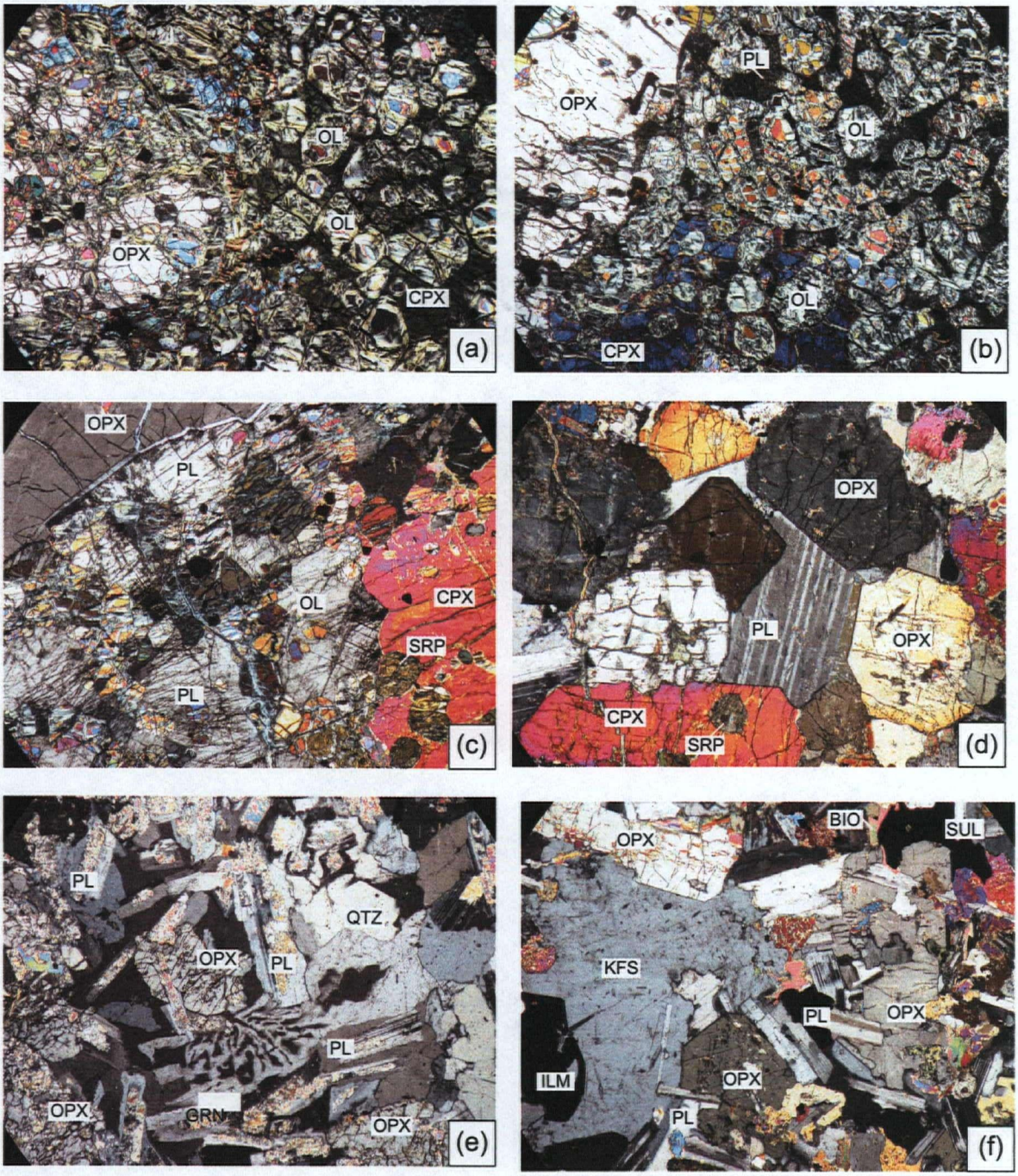
OL
OL
OPX
CPX
(a)
PL
OPX
OL
OL
CPX
(b)
OPX
PL
OL
CPX
SRP
PL
(c)
OPX
PL
OPX
CPX
SRP
(d)
PL
QTZ
OPX
PL
PL
OPX
GRN
OPX
(e)
BIO
SUL
OPX
KFS
PL
OPX
ILM
OPX
PL
(f)

Figure 2.5

Fig. 2.5: Representative photomicrographs (crossed polars) of marginal zone rocks at the West Pyrrhotite Lake section. The field of view is 5 mm for each photomicrograph. OL = olivine; OPX = orthopyroxene; CPX = clinopyroxene; PL = plagioclase; CHR = chromite; PHL = phlogopite; BIO = biotite; SUL = sulphide; ILM = ilmenite; GRN = granophyre; KFS = alkali feldspar; QTZ = quartz. (a) Peridotite (Sample: RMX02-4). Euhedral to round serpentinized olivine crystals enclosed within an orthopyroxene oikocryst (white to grey) and several clinopyroxene oikocrysts (green and blue) in the left and right side of the photo, respectively. (b) Feldspathic peridotite (Sample: RMX02-5). Partially serpentinized olivine enclosed within altered plagioclase (black to brown) and a single clinopyroxene oikocryst (blue to purple). A large (2-4 mm) subhedral orthopyroxene grain occupies the upper left corner and is nearly devoid of olivine. (c) Olivine gabbronorite (Sample: RMX02-8). Loosely-packed, euhedral to round olivine crystals enclosed within mainly plagioclase oikocrysts (heavily fractured; rare albite twinning) and to a lesser extent within clinopyroxene (red to yellow). Olivine is preserved within plagioclase, but completely altered to serpentine within clinopyroxene. A large (2-4 mm) subhedral orthopyroxene crystal occupies the upper left corner of the photo. (d) Gabbronorite (Sample: 71138). An equigranular-textured rock with euhedral orthopyroxene and clinopyroxene, and interstitial plagioclase. Rare ovoid-shaped serpentine grains within a clinopyroxene crystal at the bottom of the slide likely represent early-formed olivine. (e) Granophyre-bearing gabbronorite (Sample: 71139). Subophitic-textured rock containing sericitized plagioclase laths that are partially enclosed within orthopyroxene. Anhedral masses of quartz, alkali feldspar, and granophyre enclose plagioclase and orthopyroxene. (f) Granophyre-bearing gabbronorite (Sample: RMX02-9). Large (4-5 mm) composite alkali feldspar (with apatite inclusions) and ilmenite clot surrounded by a finer-grained portion composed of mainly subhedral plagioclase laths that are partially enclosed within subhedral orthopyroxene (grey to white) and clinopyroxene (purple to blue). Phlogopite (orange to green) and associated sulphide form clots within the finer grained region.

The olivine gabbronorite unit (~15 m thick) consists of 0.5-0.8 mm cumulus olivine (40-50 vol %) enclosed within 2-4 mm plagioclase oikocrysts (20-30 vol %) and to a lesser extent within 2-3 mm clinopyroxene oikocrysts (10-15 vol %) (Fig. 2.5c). Orthopyroxene (20-30 vol %) forms large (3-8 mm), irregular-shaped to subhedral grains that only rarely enclose cumulus olivine. This unit is considered to be equivalent to the "picrite" described by Smith (1962). In accordance with IUGS classification, and to avoid confusion with chemical and volcanological terminology, the term olivine gabbronorite is used throughout this paper for this rock type. The transition to gabbronorite occurs within ~8 m from the contact with the country rocks, and is marked by a sharp decrease (over a 1 m interval) in the amount of olivine.

The gabbronorite unit (~8 m thick) is distinctly more equigranular that the overlying olivine-rich units and is composed of 1-2 mm cumulus orthopyroxene (40 vol %) and clinopyroxene (10-20 vol %), and 1-2 mm postcumulus plagioclase (20-30 vol %) and phlogopite (5-10 vol %) (Fig. 2.5d). Olivine is rare (<5 vol %) and occurs exclusively as serpentine pseudomorphs within pyroxene. The gabbronorite unit also marks the first appearance of quartz, alkali feldspar, and minor granophyre (2-3 vol %), which occur interstitial to cumulus pyroxene. This unit is considered to be analogous to the "bronzite gabbro" unit of Smith (1962). A distinct change in texture and an increase in the abundance of granophyre marks the transition from gabbronorite to granophyre-bearing gabbronorite within 4 m of the contact (Fig. 2.5e & 2.5f).

The granophyre-bearing gabbronorite (~1 m thick) has a subophitic to ophitic texture where 1-2 mm plagioclase laths (40 vol %) are partially or completely enclosed within 0.8-1.2 mm subhedral orthopyroxene (30 vol %) and clinopyroxene (~10 vol %). Granophyre, quartz, and alkali feldspar are abundant (10-30 vol %) and form large clots up to 10 mm in diameter (Fig. 2.6). These large clots also contain blocky ilmenite, abundant needle-shaped apatite, and minor euhedral and hopper-textured zircon crystals (Fig. 2.6). Phlogopite (5 vol %) forms anhedral grains and is intergrown with blades of ilmenite. Directly adjacent to the contact (within 0.5 m) the gabbronorite contains 2-5 cm ellipsoid fragments of the adjacent country rocks. Sulphides occur as rare 2-10 mm blebs that are composed of mainly pyrrhotite and minor chalcopyrite.

The country rock at West Pyrrhotite Lake consists of variably contact metamorphosed quartz-feldspar-biotite gneiss. Near the contact with the intrusion the host rock has a

Figure 2.6

Fig. 2.6: Photomicrograph of a large granophyre-alkali feldspar-quartz clot within subophitic-textured gabbronorite from the West Pyrrhotite Lake section (Sample 71139). These clots are abundant within the outer 4 m of the intrusion at this location. Granophyre (intergrowths of alkali feldspar and quartz) forms 2/3 of the clot and individual anhedral grains of alkali feldspar and quartz form the remaining 1/3. The clot contains abundant acicular apatite and minor hopper-textured (skeletal) zircon, which are shown in backscatter electron images in insets B and C. The red box outlines the area show in B (rotated 45°). Apatite occurs in both granophyre and granular regions and commonly transects grain boundaries. The hopper-textured zircons form equant crystals about 60-70 microns in length. The outer boundary of the clot is curvilinear and is rimmed, in places, by sericitized plagioclase laths that separate it from the subophitic intergrowths of orthopyroxene and plagioclase. The clot appears to represent a partial melt of the adjacent crust incorporated into the marginal zone that did not mix with the mafic melt.

heterogeneous texture and banding is not well-developed. It is composed of 2-3 mm anhedral quartz (40-50 vol %), 2-3 mm anhedral alkali feldspar (30-40 vol %), and 1-2 mm subhedral clinopyroxene (10-15 vol %). Accessory phases include rare granophyric patches, acicular ilmenite, and euhedral apatite and zircon. Away from the contact (>20 m), the gneiss is strongly banded and composed of alternating biotite-rich (30 vol %) and biotite-poor (<5 vol %) bands. The gneiss is composed of 2-3 mm anhedral quartz and subhedral feldspar (40-60 vol %), which occur as discrete individual grains as well as granophyric intergrowths, and 1-2 mm subhedral biotite (5-30 vol %). Pyrrhotite, chalcopyrite, and acicular ilmenite occur as accessory phases within the biotite-rich bands. The granophyre likely represents pockets of partial melt that formed as a result of heating during the emplacement of the Muskox intrusion. The lack of biotite and granophyre within the country rocks directly adjacent to the intrusion could be the result of dehydration and melt extraction during the emplacement of the intrusion.

2.3.2 Far West Margin section

The marginal zone rocks at the Far West Margin (Drill hole: MX03-001, 175 m) are distinct from those at the West Pyrrhotite Lake section and consist of variably sulphide-mineralized feldspathic peridotite, chromite-rich peridotite, and gabbronorite (Fig. 2.4b). Representative photomicrographs of the textural and mineralogical variations within the Far West Margin section are shown in Fig. 2.7. The peridotites at Far West Margin contain coarse-grained olivine (1.0-1.5 mm) that is not observed at West Pyrrhotite Lake and has only been documented in the upper parts of the layered series (Irvine & Smith, 1969), which is broadly consistent with relative stratigraphic position of the Far West Margin section (Fig. 2.2).

The chromite-rich peridotite horizons consist of 0.8-1.2 mm cumulus olivine (50-60 vol %) and 0.1 mm chromite (2-10 vol %) that are enclosed within 0.8-1.5 cm orthopyroxene (20 vol %) and clinopyroxene (10 vol %) oikocrysts, and anhedral plagioclase (10 vol %) (Fig. 2.7a & 2.7b). Pyroxene is commonly altered to biotite (and chlorite) along fractures and grain boundaries. Chromite grains occur in clusters within orthopyroxene and plagioclase, and rarely phlogopite. The clusters form ellipsoidal outlines that may have originally rimmed olivine grains and which were subsequently replaced by orthopyroxene (Irvine & Smith, 1969). Phlogopite is abundant (8-10 vol %) and forms 2-3 mm postcumulus crystals associated with ilmenite and sulphide (pyrrhotite and minor chalcopyrite). Olivine is 50-100% altered to serpentine and magnetite. Plagioclase is completely altered, but can be distinguished

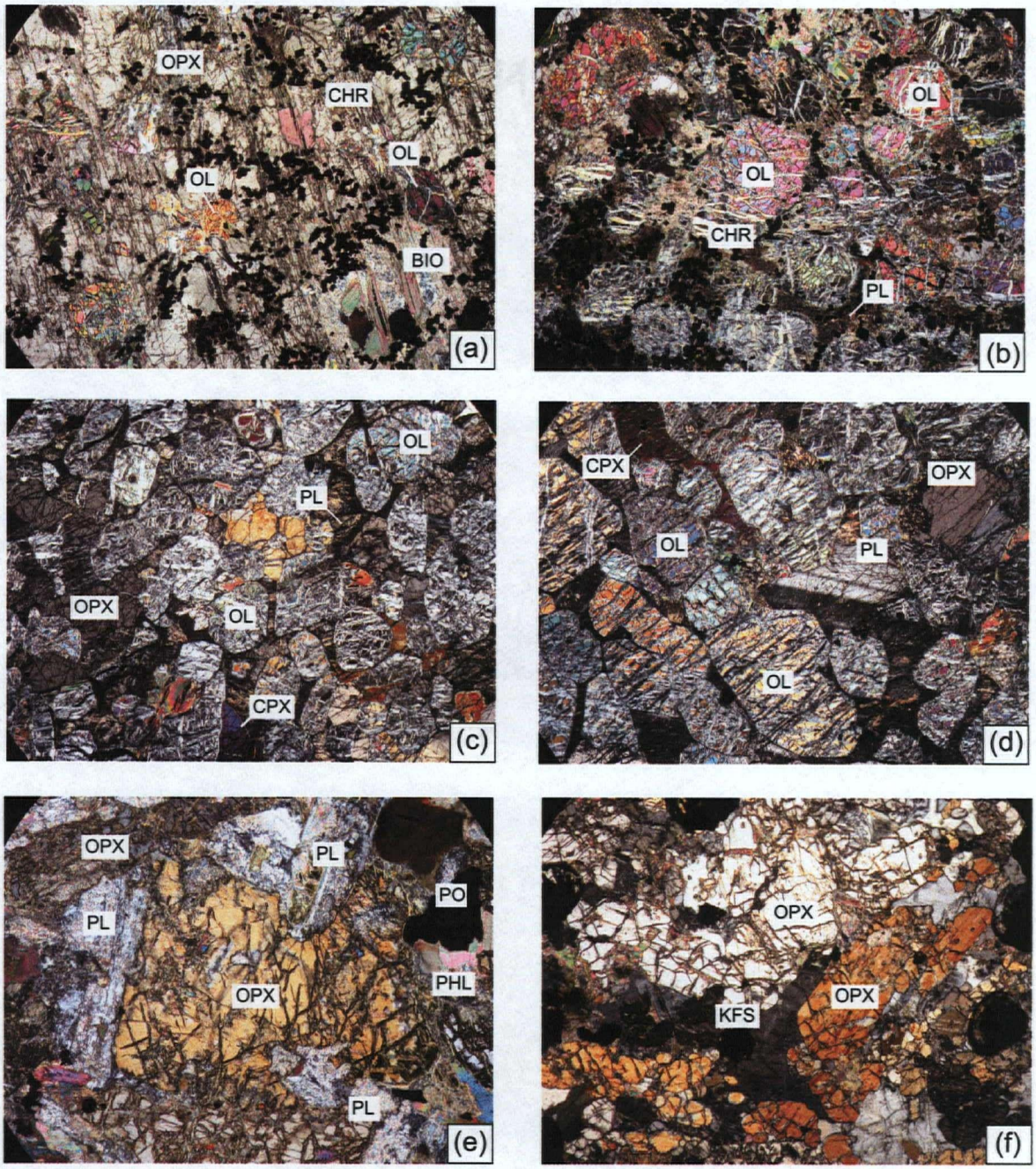
OPX
CHR
OL
OL
BIO
(a)
OL
OL
CHR
PL
(b)
OL
PL
OPX
OL
CPX
(c)
CPX
OPX
OL
PL
OL
(d)
OPX
PL
PO
PL
PHL
OPX
PL
(e)
OPX
OPX
KFS
(f)

Figure 2.7

Fig. 2.7: Representative photomicrographs (crossed polars) of marginal zone rocks for the Far West Margin section. Field of view is 10 mm for a-d and 5 mm for e-f. Abbreviations as in Fig. 2.5. (a) Chromite-rich peridotite (sample: RMX01-1). Olivine and clusters of chromite crystals enclosed within a single orthopyroxene oikocryst that occupies the entire field of view (10 mm). Secondary biotite occurs along fractures within pyroxene. (b) Chromite-rich peridotite (sample: RMX01-1). Large (1.5 mm) partially serpentinized olivine crystals surrounded by heavily fractured and sericitized plagioclase. Clusters of chromite crystals occur within interstitial plagioclase. (c) Feldspathic peridotite (sample: RMX01-4). Plagioclase, the most abundant interstitial phase, has well-developed albite twining and a heavily fractured appearance, and separates closely-packed serpentinized olivine crystals in the upper and right side of the view. Orthopyroxene is also interstitial and contains relatively few olivine crystals as shown in the left side of view. Clinopyroxene forms a minor wedge-shaped interstitial phase at the bottom of the photomicrograph. (d) Feldspathic peridotite (sample: RMX01-5). Anhedral plagioclase (white and dark grey) and clinopyroxene (red to purple) occurs in between closely-packed partially serpentinized olivine. (e) Gabbronorite (sample: RMX01-8). Subhedral sericitized plagioclase laths partially enclosed within an anhedral orthopyroxene crystal. Phlogopite is anhedral and associated with sulphide blebs within the upper right corner of the view. (f) Gabbronorite (sample: 71088). Alkali feldspar (dark grey) is interstitial to cumulus orthopyroxene.

by its heavily fractured appearance and rarely preserved albite twinning as noted within the West Pyrrhotite Lake section above. The abundance of chromite (2-8 vol %) and the coarseness of orthopyroxene oikocrysts (up to 1.5 cm) are distinguishing features of this unit. The chromite-rich horizons have been traced for over 1 km to the north in other drill holes. A sharp decrease in the abundance of chromite and a progressive increase in the abundance of feldspar mark the transition to feldspathic peridotite.

The feldspathic peridotite consists of 1.0-1.5 mm cumulus olivine (60-70 vol %) that is partially enclosed within 1.5-3.0 mm orthopyroxene (10-20 vol %) and clinopyroxene (5-10 vol %), and 1.5-2.0 mm plagioclase (10-30 vol %) (Fig. 2.7c & 2.7d). The abundance of plagioclase increases towards the base of the unit, where it forms equant subhedral crystals that are interstitial to olivine (Fig. 2.7d). This plagioclase-rich zone (30 vol %) likely is analogous to the "picrite" unit mapped on surface (Smith, 1962). Underlying the feldspathic peridotite is a second chromite-rich horizon that is comparable to the upper chromite-rich horizon and also contains secondary biotite. At ~9 m from the contact, there is a sharp change in lithology at a thin (<30 cm) breccia zone that contains ellipsoid gabbronoritic and granitic fragments (~10 cm in diameter).

Gabbronorite forms the contact phase at the Far West Margin and has an intergranular to subophitic texture with 1.0-2.0 mm subhedral calcic-plagioclase laths (20-30 vol %) and 1-4 mm subhedral orthopyroxene (30-40 vol %) (Fig. 2.7e & 2.7f). Interstitial to orthopyroxene and plagioclase are 1-4 mm anhedral phlogopite (5-10 vol %), sulphide (10-15 vol %), and rare sodic feldspar. Olivine (<5 vol %) occurs within plagioclase and orthopyroxene and is completely altered to serpentine and chlorite. Analogous to that observed at West Pyrrhotite Lake, the gabbronorite at the Far West Margin contains blebs of granophyre, quartz, and alkali feldspar (~10 vol % combined) that fill interstitial regions between orthopyroxene (Fig. 2.7f). The gabbronorite is not mapped at surface at the Far West Margin, likely due to poor exposure. This unit is not intersected 1000 m north of the Far West Margin section (DDH MX03-002), which is consistent with the observations of Smith (1962), who noted that the gabbronorite is not typically found north of Speers Lake.

Sulphide mineralization occurs throughout the Far West Margin section and is concentrated within the gabbronorite and the adjacent country rocks. The peridotites are variably mineralized, containing <1-5 vol % sulphide, which consists of 1-3 mm composite grains of pyrrhotite and pentlandite that are interstitial to olivine. Pentlandite forms globules

within the outer portions of pyrrhotite blebs and is associated with magnetite. The gabbronorite contains 5-15% sulphide, which occurs as 0.5-1.0 cm blebs and 1-3 mm anhedral clots of pyrrhotite and chalcopyrite, and minor pentlandite. Pyrrhotite forms the core of most blebs, whereas chalcopyrite occurs along the outer edge. Pentlandite within the gabbronorite occurs as exsolution lamellae within pyrrhotite, and rarely forms sub-millimetre blebs associated with chalcopyrite. Massive sulphide occurs as thin (30 cm) layers or lenses within gabbronorite and within the country rocks and was intersected in drill hole MX03-001 and 400 m towards the north in drill hole MX04-001. At the contact, massive sulphide consists of 1-4 mm polygonal pyrrhotite grains (70-80 vol %), which are rarely separated by lens-shaped chalcopyrite (15-20 vol %) and associated <1 mm equant pentlandite grains (<5 vol %). Sulphide also occurs as 5-10 mm wide veins within the matrix of a brecciated, biotite-rich section of the footwall rocks 15-20 m from the intrusive contact. The matrix consists of quartz-feldspar-(granophyre)-sulphide veins that contain a relatively high abundance of pentlandite and chalcopyrite and likely represent the remobilization of sulphide during hydrothermal fluid circulation within the wall rocks during the emplacement of the intrusion.

The country rocks at the Far West Margin are lithologically variable and typically consist of fine-grained hornfels with lenses of granitic material adjacent to the contact, and banded sulphidic metasediments and biotite-garnet-quartz schists further from the contact (as observed in drill holes MX03-002, MX04-001, and MX04-002). This is consistent with surface mapping, which indicates that the wall rocks in this region are biotite-rich paragneiss of the Recluse and Epworth groups (Smith, 1962). Directly adjacent to the intrusion the host rock is a fine-grained and intensely altered hornfels, consisting mainly of secondary mica and acicular ilmenite enclosed within pyroxene, quartz, and biotite poikiloblasts. The granitic lenses, which likely represent veins of partial melt formed during emplacement of the intrusion, are composed predominantly of 0.5-1.5 mm anhedral quartz (40-50 vol %) and alkali feldspar (30-40 vol %) that form individual grains and granophyric intergrowths, and anhedral biotite (10 vol %) and sulphide (2-3 vol %). A contact metamorphosed and altered gabbro was intersected within the footwall only in drill hole MX03-001 and consists of equant feldspar enclosed within poikiloblastic pyroxene and biotite. The extent of this gabbroic unit is unknown as it was not observed in other drill holes. Further from the contact (>20 m), the host rocks have a well-defined, but variably oriented fabric. These rocks consist mainly of equant quartz (40-50 vol %), altered plagioclase (30 vol %), varying amounts of anhedral

biotite (25-30 vol %) and granular pyrrhotite and chalcopyrite (2-5 vol %). Several metre-thick biotite-rich zones contain 0.5-0.8 cm garnet porphyroblasts, which occur 20-30 metres from the contact. As will be discussed below, these sulphidic sediments likely played an important role in the formation of sulphide mineralization at the Far West Margin section of the Muskox intrusion.

2.4 ANALYTICAL TECHNIQUES

2.4.1 Major element oxides and trace element concentrations

Major element oxides and trace element concentrations of 82 samples were determined at ACME Analytical Laboratories Ltd., Vancouver. Each sample represents a 0.5-1.5 m interval of split drill core collected during an Anglo American Exploration (Canada) Ltd. diamond drilling program on the Muskox intrusion in 2003. Samples were crushed to 70% passing 2 mm mesh using a TM Engineering Rhino Jaw Crusher with chrome-steel plates; and a 250 g sub-sample was subsequently powdered to 95% passing 100 micron mesh using a TM Engineering TM/G ring pulverizer with case-hardened steel bowl. The ACME analytical procedures are summarized in Appendix I. Major element oxides and trace elements were analyzed by ICP-ES following $LiBO_4$ fusion and digestion of 200 mg of sample in 5% HNO_3. Loss-on-ignition was determined from the weight difference after ignition at 1000°C and total sulphur was determined by Leco analysis. Relative errors (1σ) based on five duplicate digestions are typically less than 5% for major elements. Low contents of Na_2O and P_2O_5 in peridotite samples gave larger relative errors of 8% and 12%, respectively. Transition metals (including Cu, Pt, and Pd) were determined by ICP-MS following digestion of 30 grams of sample in HNO_3, HCl, and H_2O (2:2:2). Total nickel concentration was determined by ICP-ES following digestion of 500 mg of sample in H_2O, HF, $HClO_4$ and HNO_3 (18:10:3:6). Analytical reproducibility is estimated from five procedural duplicates, which give relative errors of <10% for most rare earth elements (REE) and high field strength elements, and 10-20% for Cs, Th, Nb, and Gd (Appendix II). Relative errors (1σ) for copper, nickel, cobalt, and chromium are less than 7%, and for platinum and palladium are less than 17%. Multiple analyses of an internal basalt standard (BAS2) are within error (2σ) of the accepted value. Raw data is shown in Table 2.1, and all diagrams use results after recalculation on an anhydrous basis.

Table 2.1a : Major and trace element abundances for the West Pyrrhotite Lake section (DDH # MX03-002)

Rock type	Peridotite	Peridotite	Peridotite	Peridotite	Altered Peridotite	Altered Peridotite	Peridotite	Peridotite	Peridotite	Peridotite	Peridotite	Peridotite	Peridotite	Peridotite	Feldspathic Peridotite
Sample ID	71104	71105	71106	71107	71108	71111	71112	71113	71114	71115	71116	71117	71118	71119	71120
From (m)	16.6	23.5	30.8	38.0	43.5	49.2	53.7	58.9	66.2	72.5	76.9	82.6	88.4	95.6	101.4
To (m)	17.6	24.5	31.8	39.0	44.5	50.2	54.7	59.9	67.2	73.5	77.9	83.6	89.4	96.6	102.4
Distance (m)	160.4	153.5	146.2	139.0	133.5	127.9	123.3	118.1	110.8	104.5	100.2	94.4	88.6	81.4	75.6
Major elements (wt%)															
SiO_2	35.23	35.41	35.61	35.97	34.69	35.55	35.76	35.63	36.42	36.62	36.76	36.41	36.76	36.58	37.64
TiO_2	0.29	0.32	0.33	0.34	0.36	0.35	0.35	0.35	0.39	0.38	0.38	0.39	0.39	0.41	0.40
Al_2O_3	2.59	2.57	2.65	2.80	2.88	2.86	2.96	2.92	3.06	3.20	3.18	3.15	3.12	3.21	3.55
Fe_2O_3*	14.93	14.96	14.80	14.66	13.68	13.93	14.29	14.34	14.41	14.62	14.50	14.62	14.88	14.28	14.63
MnO	0.15	0.17	0.16	0.17	0.16	0.17	0.16	0.16	0.16	0.16	0.16	0.16	0.16	0.17	0.16
MgO	32.83	32.75	33.08	32.48	32.80	32.82	31.85	32.02	31.45	31.16	31.29	31.74	32.16	31.24	31.23
CaO	0.69	1.29	1.57	1.51	0.62	1.03	1.98	1.86	2.30	2.50	2.49	2.24	2.37	2.33	2.69
Na_2O	0.02	0.08	0.02	0.02	0.02	0.03	0.02	0.07	0.02	0.01	0.02	0.10	0.05	0.12	0.06
K_2O	0.08	0.10	0.09	0.15	0.17	0.17	0.11	0.10	0.12	0.12	0.12	0.13	0.13	0.13	0.13
P_2O_5	0.05	0.08	0.09	0.08	0.06	0.06	0.06	0.06	0.05	0.08	0.07	0.07	0.09	0.07	0.10
Cr_2O_3	0.46	0.48	0.48	0.49	0.52	0.53	0.51	0.51	0.54	0.55	0.51	0.52	0.57	0.57	0.56
LOI[1]	12.2	10.8	10.4	11.1	12.6	12.0	10.8	10.9	10.5	10.1	9.7	9.4	8.7	9.9	8.6
S	0.07	0.03	0.03	0.02	0.08	0.04	0.03	0.03	0.06	0.02	0.02	0.02	0.01	0.04	0.04
Total	99.75	99.24	99.5	100.0	98.79	99.72	99.08	99.16	99.66	99.73	99.41	99.17	99.62	99.25	99.99
mg-number[2]	0.813	0.813	0.816	0.814	0.826	0.824	0.815	0.816	0.812	0.809	0.810	0.811	0.811	0.813	0.809
FeO**	13.43	13.46	13.32	13.19	12.31	12.53	12.86	12.90	12.97	13.16	13.05	13.16	13.39	12.85	13.16
Chalcophile elements (ppm)															
Cu	60	61	61	46	148	8	27	56	320	40	43	61	54	83	75
Ni	1842	1758	1714	1752	1775	1689	1780	1823	1878	1782	1782	1817	1864	1919	1852
Co	115	102	103	102	126	104	99	98	103	95	97	104	99	103	102
Pd (ppb)	12	17	44	44	41	19	11	51	96	10	41	29	12	25	20
Pt (ppb)	15	16	44	26	21	11	7	23	28	6	31	10	6	9	5
Au (ppb)	0.9	1.0	1.3	2.4	1.4	0.6	0.4	1.0	6.1	0.4	2.0	1.5	0.4	1.2	<.2

Table 2.1b (continued):

Rock type	Peridotite	Peridotite	Peridotite	Peridotite	Altered Peridotite	Altered Peridotite	Peridotite	Peridotite	Peridotite	Peridotite	Peridotite	Peridotite	Peridotite	Peridotite	Feldspathic Peridotite
Sample ID	71104	71105	71106	71107	71108	71111	71112	71113	71114	71115	71116	71117	71118	71119	71120
From (m)	16.6	23.5	30.8	38.0	43.5	49.2	53.7	58.9	66.2	72.5	76.9	82.6	88.4	95.6	101.4
To (m)	17.6	24.5	31.8	39.0	44.5	50.2	54.7	59.9	67.2	73.5	77.9	83.6	89.4	96.6	102.4
Distance (m)	160.4	153.5	146.2	139.0	133.5	127.9	123.3	118.1	110.8	104.5	100.2	94.4	88.6	81.4	75.6
Trace elements (ppm)															
Sc	7	5	5	5	10	7	5	6	5	4	5	5	4	5	4
V	101	102	98	102	115	102	105	109	117	114	108	114	114	118	128
Cr	334	217	204	283	660	445	248	272	238	187	201	214	211	281	193
Se	0.4	0.3	0.2	0.2	0.3	0.3	0.2	0.3	0.5	0.2	0.3	0.3	0.3	0.4	0.3
Rb	4	5	4	6	6	6	5	5	5	5	5	6	6	6	6
Sr	9	10	10	11	7	7	9	8	11	14	15	21	25	18	35
Y	4.2	4.2	4.4	4.4	4.9	4.5	4.7	4.5	5.6	5.2	5.1	5.7	5.5	5.3	5.5
Zr	20	19	21	23	24	20	23	21	31	24	25	27	25	29	25
Nb	1.3	1.7	1.6	1.8	1.8	1.7	1.6	1.5	2.0	1.9	2.0	2.0	2.0	2.0	2.0
Cs	0.2	0.3	0.2	0.4	0.3	0.6	0.3	0.3	0.3	0.3	0.3	0.3	0.4	0.4	0.2
Ba	18	22	20	37	44	29	34	27	25	27	33	36	38	24	43
La	2.3	2.6	2.6	2.9	2.4	2.3	3.1	3.1	3.7	3.5	3.4	3.3	3.3	3.5	3.6
Ce	5.4	6.2	5.8	6.8	6.0	5.0	6.8	6.7	7.7	7.4	7.2	7.4	7.4	7.5	7.7
Pr	0.69	0.73	0.71	0.83	0.82	0.70	0.88	0.85	1.03	0.97	0.96	1.00	0.92	0.96	0.96
Nd	3.3	3.6	4.0	4.5	3.8	3.4	4.3	3.4	5.0	5.3	4.7	5.0	4.3	4.9	4.0
Sm	0.9	0.8	0.9	0.8	1.0	0.9	1.1	1.1	1.0	1.1	1.0	1.0	1.0	1.1	1.1
Eu	0.22	0.24	0.24	0.32	0.28	0.23	0.27	0.30	0.34	0.34	0.27	0.33	0.37	0.33	0.35
Gd	0.90	0.84	0.85	1.16	0.84	0.90	1.02	1.06	1.05	0.89	1.21	1.15	1.09	1.24	1.22
Tb	0.13	0.14	0.13	0.17	0.20	0.17	0.19	0.17	0.19	0.20	0.17	0.19	0.17	0.16	0.17
Dy	0.72	0.72	0.70	0.83	0.92	0.78	0.89	0.89	1.06	1.05	0.90	0.85	0.96	1.07	0.93
Ho	0.13	0.15	0.13	0.18	0.17	0.17	0.17	0.19	0.21	0.19	0.17	0.21	0.19	0.19	0.20
Er	0.39	0.41	0.45	0.45	0.55	0.48	0.50	0.41	0.50	0.53	0.47	0.52	0.45	0.50	0.56
Tm	<.05	0.06	0.06	0.09	0.07	0.06	0.07	0.07	0.08	0.09	0.08	0.07	0.08	0.07	0.07
Yb	0.34	0.37	0.36	0.45	0.47	0.44	0.46	0.48	0.46	0.44	0.47	0.58	0.41	0.58	0.48
Lu	0.05	0.06	0.06	0.07	0.08	0.05	0.07	0.07	0.07	0.08	0.06	0.08	0.06	0.07	0.09
Hf	0.5	0.6	0.6	0.5	0.8	0.7	0.6	0.8	0.8	0.8	0.7	0.8	0.7	0.8	1.0
Ta	0.1	<.1	<.1	0.1	<.1	0.1	0.1	0.1	0.1	<.1	<.1	0.1	0.1	0.1	0.1
Th	0.2	0.2	0.5	0.9	0.4	0.6	0.6	0.2	0.7	0.3	0.8	0.7	0.7	0.7	0.7

Ol Gbnr = olivine gabbronorite; Qtz-feld-bio = quartz feldspar biotite; * Total Fe as Fe2O3;** Total Fe as FeO; [1]LOI = loss on ignition; [2]mg-number = $Mg/(Mg+Fe^{2+})$; < = below detection limit

Table 2.1a (continued): Major and trace element abundances for the West Pyrrhotite Lake section (DDH # MX03-002)

Rock type	Feldspathic Peridotite	Feldspathic Peridotite	Feldspathic Peridotite	Feldspathic Peridotite	Feldspathic Peridotite	Feldspathic Peridotite	Feldspathic Peridotite	Feldspathic Peridotite	Ol-Gbnr	Ol-Gbnr	Ol-Gbnr	Ol-Gbnr	Gouge	Gouge
Sample ID	71121	71122	71123	71124	71125	71126	71127	71128	71131	71132	71133	71134	71135	71136
From (m)	107.0	113.0	118.8	124.7	130.8	136.9	142.6	148.3	154.5	158.5	162.8	165.9	169.5	171.7
To (m)	108.0	114.0	119.8	125.7	131.8	137.8	143.0	149.3	155.5	159.5	163.3	166.9	171.0	172.1
Distance (m)	70.0	64.0	58.2	52.3	46.2	40.2	35.0	28.7	22.5	18.5	14.7	11.1	7.0	5.9
Major elements (wt%)														
SiO_2	37.07	37.90	38.15	38.98	39.97	39.34	39.60	40.78	40.74	42.88	43.72	44.20	39.71	41.17
TiO_2	0.46	0.45	0.49	0.50	0.58	0.64	0.65	0.72	0.80	0.89	0.99	1.07	0.95	0.75
Al_2O_3	3.29	3.82	4.01	4.16	4.77	4.90	5.11	5.85	6.26	7.18	7.77	8.29	8.43	7.36
Fe_2O_3*	15.17	14.67	14.46	14.35	14.27	14.53	14.66	14.78	14.57	14.90	14.51	14.23	14.30	13.58
MnO	0.16	0.17	0.18	0.16	0.16	0.17	0.17	0.17	0.17	0.17	0.16	0.15	0.12	0.12
MgO	30.71	30.23	29.25	28.28	26.94	26.11	26.05	25.24	24.35	22.75	21.66	20.89	24.99	24.23
CaO	2.42	3.10	2.55	3.07	3.65	3.83	3.05	4.08	4.12	5.19	5.40	5.35	0.84	1.56
Na_2O	0.11	0.12	0.04	0.13	0.19	0.23	0.39	0.52	0.56	0.67	0.91	0.83	0.18	0.27
K_2O	0.18	0.15	0.16	0.17	0.22	0.27	0.29	0.37	0.41	0.55	0.59	0.55	0.42	0.41
P_2O_5	0.12	0.07	0.07	0.10	0.09	0.08	0.08	0.09	0.13	0.13	0.15	0.15	0.13	0.13
Cr_2O_3	0.54	0.53	0.53	0.48	0.50	0.46	0.36	0.34	0.30	0.30	0.29	0.28	0.34	0.36
LOI[1]	8.8	8.5	9.8	8.6	8.5	8.0	8.4	6.7	7.5	4.2	3.7	4.0	9.2	9.2
S	0.13	0.09	0.04	0.06	0.03	0.15	0.19	0.02	0.02	0.02	0.03	0.07	0.19	0.18
Total	99.30	99.95	99.90	99.20	100.0	98.79	99.02	99.80	100.1	99.97	100.0	100.2	99.79	99.32
mg-number[2]	0.800	0.803	0.800	0.796	0.789	0.781	0.779	0.772	0.768	0.752	0.747	0.744	0.776	0.780
FeO**	13.65	13.20	13.01	12.91	12.84	13.07	13.19	13.30	13.11	13.41	13.06	12.80	12.87	12.22
Chalcophile elements (ppm)														
Cu	577	324	86	255	83	636	636	95	154	160	103	311	898	665
Ni	2066	1942	1676	1701	1579	1701	1586	1200	1203	1144	1055	1059	1376	1262
Co	105	99	95	92	84	92	95	90	82	80	71	69	100	96
Pd (ppb)	75	53	25	30	30	57	92	20	59	70	17	32	152	82
Pt (ppb)	13	8	6	9	8	13	15	9	20	14	5	4	7	5
Au (ppb)	6.8	3.3	1.3	2.1	1.5	5.0	6.7	1.2	3.7	3.0	2.0	2.1	6.4	5.3

Table 2.1b (continued):

Rock type	Feldspathic Peridotite	Feldspathic Peridotite	Feldspathic Peridotite	Feldspathic Peridotite	Feldspathic Peridotite	Feldspathic Peridotite	Feldspathic Peridotite	Feldspathic Peridotite	Ol-Gbnr	Ol-Gbnr	Ol-Gbnr	Ol-Gbnr	Gouge	Gouge
Sample ID	71121	71122	71123	71124	71125	71126	71127	71128	71131	71132	71133	71134	71135	71136
From (m)	107.0	113.0	118.8	124.7	130.8	136.9	142.6	148.3	154.5	158.5	162.8	165.9	169.5	171.7
To (m)	108.0	114.0	119.8	125.7	131.8	137.8	143.0	149.3	155.5	159.5	163.3	166.9	171.0	172.1
Distance (m)	70.0	64.0	58.2	52.3	46.2	40.2	35.0	28.7	22.5	18.5	14.7	11.1	7.0	5.9
Trace elements (ppm)														
Sc	5	5	5	4	4	4	5	4	4	3	3	5	16	13
V	120	117	123	129	139	149	144	165	168	182	200	214	202	175
Cr	223	199	213	184	207	236	303	239	275	223	259	366	1313	1100
Se	0.6	0.4	0.3	0.4	0.2	0.6	0.6	0.2	0.2	0.2	0.1	0.3	0.7	0.5
Rb	8	6	7	7	8	9	8	11	13	15	16	16	17	15
Sr	36	35	24	34	43	48	80	117	112	125	150	134	30	51
Y	6.5	6.2	6.3	6.9	7.1	8.9	8.2	10.5	11.5	12.5	14.4	15.9	12.2	12.2
Zr	36	27	31	32	35	45	44	48	56	62	73	74	65	53
Nb	2.4	2.0	2.4	2.3	3.0	3.1	3.3	3.5	4.3	4.6	5.0	6.0	5.5	4.5
Cs	0.5	0.3	0.5	0.7	0.6	0.8	1.1	1.3	1.3	2.5	2.5	1.2	1.0	1.5
Ba	57	47	47	58	62	92	94	107	129	129	162	191	90	143
La	4.6	3.7	3.9	4.2	4.9	5.4	5.2	6.4	7.0	7.6	8.8	9.2	7.3	8.9
Ce	10.1	7.9	9.1	9.2	11.3	12.9	12.0	13.9	16.1	17.3	19.4	20.9	16.9	17.7
Pr	1.37	1.02	1.21	1.28	1.52	1.59	1.57	1.81	1.97	2.29	2.60	2.76	2.27	2.25
Nd	6.5	5.1	5.3	5.9	7.7	8.1	7.2	8.5	10.4	10.3	12.4	12.4	9.4	10.7
Sm	1.2	1.2	1.2	1.4	1.6	1.9	1.7	2.1	2.5	2.5	2.7	3.0	2.5	2.4
Eu	0.33	0.37	0.40	0.46	0.51	0.53	0.58	0.56	0.67	0.72	0.77	0.86	0.52	0.52
Gd	1.21	1.29	1.19	1.3	1.77	2.03	1.83	1.92	2.34	2.44	2.6	3.21	2.48	2.65
Tb	0.23	0.19	0.22	0.23	0.29	0.32	0.31	0.33	0.32	0.36	0.45	0.49	0.37	0.39
Dy	1.14	1.14	1.15	1.27	1.43	1.62	1.61	2.10	2.10	2.24	2.66	2.75	2.29	2.20
Ho	0.23	0.21	0.25	0.25	0.29	0.32	0.33	0.34	0.44	0.40	0.51	0.54	0.43	0.37
Er	0.64	0.56	0.53	0.63	0.70	0.85	0.78	1.03	1.03	1.27	1.32	1.47	1.14	1.14
Tm	0.09	0.09	0.09	0.11	0.13	0.13	0.13	0.13	0.15	0.15	0.17	0.20	0.18	0.16
Yb	0.49	0.48	0.62	0.55	0.70	0.85	0.76	1.03	1.05	1.14	1.31	1.27	1.33	1.09
Lu	0.10	0.06	0.09	0.09	0.10	0.10	0.12	0.13	0.15	0.17	0.18	0.19	0.16	0.15
Hf	1.1	0.7	1.0	0.7	1.2	1.5	1.4	1.3	1.9	1.9	2.2	2.4	2.1	1.7
Ta	0.1	0.1	0.1	0.1	0.2	0.2	0.2	0.3	0.3	0.3	0.3	0.4	0.4	0.3
Th	1.3	0.7	0.4	0.9	1.2	0.8	1.1	1.0	1.1	1.6	1.6	1.8	1.6	1.1

Ol Gbnr = olivine gabbronorite; Qtz-feld-bio = quartz feldspar biotite; * Total Fe as Fe2O3;** Total Fe as FeO; [1]LOI = loss on ignition; [2]mg-number = $Mg/(Mg+Fe^{2+})$; < = below detection limit

Table 2.1a (continued): Major and trace element abundances for the West Pyrrhotite Lake section (DDH # MX03-002)

Rock type	Gabbro-norite	Gabbro-norite	Gabbro-norite	Qtz-feld-bio Gneiss	Qtz-feld-bio Gneiss	Qtz-feld-bio Gneiss	Qtz-feld-bio Gneiss	Qtz-feld-bio Gneiss	Qtz-feld-bio Gneiss	Qtz-feld-bio Gneiss	Qtz-feld-bio Gneiss	Qtz-feld-bio Gneiss	Qtz-feld-bio Gneiss
Sample ID	71137	71138	71139	71140	71141	71151	71142	71143	71144	71145	71146	71148	71147
From (m)	172.1	173.6	174.8	178.0	179.3	181.5	182.7	183.8	187.1	187.9	191.9	202.2	200.9
To (m)	173.6	174.8	175.8	179.0	180.3	182.5	183.2	185.4	187.9	188.9	192.9	202.9	201.9
Distance (m)	4.4	3.2	2.2	-1.0	-2.3	-4.5	-5.2	-7.4	-9.8	-10.9	-14.9	-24.9	-23.9
Major elements (wt%)													
SiO_2	43.86	47.92	50.49	67.23	69.13	70.28	69.20	58.72	36.76	56.70	58.49	65.86	65.53
TiO_2	0.80	0.76	0.47	0.36	0.35	0.30	0.21	0.61	0.39	0.41	0.58	0.52	0.56
Al_2O_3	9.68	8.94	10.19	8.89	11.60	10.57	13.93	15.88	9.93	12.46	15.57	15.41	15.38
Fe_2O_3*	14.78	17.77	18.32	11.37	5.62	5.86	3.53	8.93	38.60	17.27	10.47	4.89	4.86
MnO	0.15	0.34	0.49	0.13	0.13	0.11	0.06	0.08	0.10	0.07	0.04	0.08	0.04
MgO	17.43	15.00	11.90	3.89	2.60	3.02	1.55	3.35	1.69	2.28	2.91	2.69	2.51
CaO	6.13	2.73	2.26	1.79	2.59	1.66	1.25	1.20	0.90	1.13	0.45	0.74	0.47
Na_2O	0.74	0.58	0.89	1.21	2.33	1.68	2.47	2.45	1.54	1.64	1.00	2.93	2.00
K_2O	0.91	1.75	2.54	2.13	2.91	3.21	5.82	4.90	3.19	3.72	5.80	4.30	5.50
P_2O_5	0.13	0.11	0.10	0.05	0.07	0.06	0.19	0.07	0.08	0.06	0.06	0.06	0.06
Cr_2O_3	0.25	0.14	0.09	0.02	0.00	0.01	0.01	0.01	0.01	0.01	0.01	0.01	0.01
LOI[1]	4.0	2.9	2.0	2.8	2.6	2.8	1.7	3.5	6.2	4.2	4.4	2.7	3.1
S	1.18	1.06	1.58	3.45	1.42	1.27	0.98	2.45	12.51	5.54	3.3	0.63	0.81
Total	99.08	99.11	99.86	100.0	100.1	99.65	100.1	99.90	100.1	100.3	100.0	100.3	100.1
mg-number[2]	0.700	0.626	0.563	0.404	0.478	0.505	0.465	0.426	0.080	0.207	0.355	0.522	0.506
FeO**	13.30	15.99	16.48	10.23	5.06	5.27	3.18	8.04	34.73	15.54	9.42	4.40	4.37
Chalcophile elements (ppm)													
Cu	2002	1199	1045	1507	2312	829	1510	1310	8284	6188	2437	43	46
Ni	1465	945	655	878	975	438	616	749	4623	1820	1039	43	49
Co	115	82	59	106	54	38	28	76	554	197	87	12	13
Pd (ppb)	164	129	32	<10	159	39	136	<10	327	121	104	<10	<10
Pt (ppb)	5	3	3	2	9	2	6	2	18	8	3	<2	<2
Au (ppb)	10.8	5.7	3.0	3.5	12.4	2.9	6.5	4.0	19.8	8.2	4.4	1.2	0.4

Table 2.1b (continued):

Rock type	Gabbro-norite	Gabbro-norite	Gabbro-norite	Qtz-feld-bio Gneiss	Qtz-feld-bio Gneiss	Qtz-feld-bio Gneiss	Qtz-feld-bio Gneiss	Qtz-feld-bio Gneiss	Qtz-feld-bio Gneiss	Qtz-feld-bio Gneiss	Qtz-feld-bio Gneiss	Qtz-feld-bio Gneiss	Qtz-feld-bio Gneiss
Sample ID	71137	71138	71139	71140	71141	71151	71142	71143	71144	71145	71146	71148	71147
From (m)	172.1	173.6	174.8	178.0	179.3	181.5	182.7	183.8	187.1	187.9	191.9	202.2	200.9
To (m)	173.6	174.8	175.8	179.0	180.3	182.5	183.2	185.4	187.9	188.9	192.9	202.9	201.9
Distance (m)	4.4	3.2	2.2	-1.0	-2.3	-4.5	-5.2	-7.4	-9.8	-10.9	-14.9	-24.9	-23.9
Trace elements (ppm)													
Sc	5	9	6	3	2	4	5	9	6	6	9	8	8
V	208	371	280	73	34	46	26	108	87	59	112	83	88
Cr	368	418	228	83	31	47	32	97	37	48	74	70	68
Se	1.6	1.5	1.9	3.4	2.2	1.4	1.4	2.7	28.4	9.8	4.8	1.0	0.9
Rb	26	54	69	73	73	84	140	144	92	120	198	158	182
Sr	139	179	183	143	203	201	302	261	128	154	116	134	100
Y	13.2	12.3	11.6	13.4	16.8	13.1	13.6	19.5	12.8	15.5	21.3	23.1	17.5
Zr	60	67	73	213	285	222	189	222	127	181	160	287	249
Nb	4.5	5.2	4.9	5.7	7.4	6.3	6.0	11.4	7.8	8.8	10.9	11.5	10.3
Cs	1.9	2.1	2.7	3.4	2.0	2.6	2.5	4.5	2.4	3.1	5.1	4.8	4.8
Ba	301	394	409	420	435	338	1031	924	724	919	753	661	594
La	8.9	10.7	15.4	23.9	28.6	28.3	24.3	49.9	32.7	32.2	45.1	36.9	35.0
Ce	18.9	22.4	29.9	45.0	53.5	52.2	44.5	90.6	62.7	59.7	87.8	75.5	69.7
Pr	2.47	2.61	3.37	4.73	5.77	5.24	4.60	9.43	6.55	6.42	9.51	8.25	7.70
Nd	11.0	10.9	12.6	17.3	20.5	18.7	16.9	31.8	22.6	22.9	34.1	29.1	30.6
Sm	2.5	2.5	2.4	3.3	3.9	3.2	3.1	5.7	3.7	4.0	6.3	5.6	5.0
Eu	0.89	0.70	0.65	0.73	1.12	1.08	1.30	1.63	1.00	0.91	1.29	1.04	0.98
Gd	2.41	2.03	1.88	2.41	2.68	2.41	1.99	3.75	2.86	3.17	4.12	4.45	3.79
Tb	0.43	0.39	0.36	0.34	0.46	0.38	0.35	0.62	0.45	0.48	0.62	0.74	0.53
Dy	2.28	2.17	1.99	2.20	2.39	2.17	2.07	3.19	2.08	2.38	3.74	3.58	2.88
Ho	0.44	0.40	0.36	0.41	0.49	0.41	0.43	0.63	0.40	0.45	0.66	0.70	0.59
Er	1.21	1.18	1.19	1.21	1.53	1.15	1.30	1.91	1.20	1.39	1.83	2.18	1.53
Tm	0.17	0.17	0.15	0.16	0.20	0.17	0.24	0.27	0.16	0.19	0.26	0.29	0.23
Yb	1.16	1.14	1.22	1.31	1.48	1.48	1.53	1.82	1.18	1.41	1.55	1.97	1.53
Lu	0.17	0.19	0.19	0.20	0.25	0.21	0.27	0.29	0.18	0.21	0.27	0.33	0.25
Hf	1.7	1.8	2.4	5.8	8.0	6.5	5.5	6.6	4.1	5.2	4.7	8.3	7.6
Ta	0.4	0.4	0.4	0.4	0.6	0.7	0.7	1.0	0.6	0.7	0.9	1.1	1.0
Th	2.1	3.0	4.2	8.8	15.0	9.3	9.5	19.5	11.5	13.6	17.8	17.6	14.6

Ol Gbnr = olivine gabbronorite; Qtz-feld-bio = quartz feldspar biotite; * Total Fe as Fe2O3;** Total Fe as FeO; [1]LOI = loss on ignition; [2]mg-number = $Mg/(Mg+Fe^{2+})$; < = below detection limit

Table 2.1b: Major and trace element abundances for the Far West Margin section (DDH # MX03-001)

Rock type	Chr. Peridotite	Chr. Peridotite	Chr. Peridotite	Chr. Peridotite	Chr. Peridotite	Chr. Peridotite	Feldspathic peridotite	Feldspathic peridotite	Feldspathic peridotite	Feldspathic peridotite	Feldspathic peridotite	Feldspathic peridotite
Sample ID	71061	71062	71063	71064	71065	71066	71067	71068	71071	71072	71073	71074
From (m)	11.7	19.8	25.1	28.7	32.3	38.5	45.9	48.9	51.9	58.9	66.2	71.0
To (m)	10.7	18.8	24.2	27.7	31.3	37.5	44.8	47.4	50.9	57.8	65.2	70.0
Distance (m)	106.3	98.2	92.9	89.3	85.7	79.5	72.2	69.6	66.1	59.2	51.9	47.0
Major elements (wt%)												
SiO_2	35.43	38.35	36.95	36.80	36.14	38.41	37.32	38.13	38.92	38.50	39.19	39.14
TiO_2	0.56	0.54	0.31	0.29	0.37	0.34	0.39	0.42	0.31	0.41	0.41	0.41
Al_2O_3	5.22	5.23	3.71	3.90	3.83	3.81	3.99	4.13	4.20	4.00	4.27	4.74
Fe_2O_3*	14.85	11.96	13.39	15.11	14.06	11.59	10.91	11.15	10.67	10.93	10.55	11.36
MnO	0.10	0.15	0.11	0.13	0.12	0.13	0.13	0.13	0.13	0.13	0.14	0.13
MgO	30.49	29.81	32.20	30.67	31.92	32.99	33.17	32.21	32.23	32.31	31.53	29.84
CaO	0.82	3.08	1.51	1.79	1.39	2.70	2.08	2.73	2.90	2.87	2.82	3.06
Na_2O	0.10	0.23	0.07	0.07	0.01	0.05	0.11	0.13	0.12	0.09	0.18	0.21
K_2O	1.33	0.70	0.90	0.94	0.68	0.53	0.29	0.28	0.31	0.23	0.20	0.27
P_2O_5	0.10	0.12	0.08	0.10	0.09	0.08	0.09	0.08	0.09	0.06	0.09	0.06
Cr_2O_3	3.98	1.17	2.01	1.28	1.46	0.52	0.38	0.32	0.32	0.29	0.35	0.34
LOI[1]	7.0	8.5	8.7	8.8	9.8	9.0	10.8	10.2	9.8	9.9	10.2	10.2
S	0.18	0.19	0.89	1.47	0.88	0.30	0.47	0.37	0.04	0.07	0.05	0.46
Total	100.2	100.1	100.2	100.2	100.2	100.4	99.97	100.2	100.3	99.95	100.2	100.0
mg-number[2]	0.803	0.832	0.827	0.801	0.818	0.849	0.858	0.851	0.857	0.854	0.856	0.839
FeO**	13.36	10.76	12.05	13.60	12.65	10.43	9.82	10.03	9.60	9.83	9.49	10.22
Chalcophile elements (ppm)												
Cu	50	180	328	1121	350	142	532	265	31	21	18	433
Ni	1623	1583	2254	2024	2605	2044	2376	2086	1781	1783	1803	1990
Co	84	101	129	177	155	110	127	115	96	96	89	110
Pd (ppb)	23	19	41	131	71	29	39	14	<10	<10	<10	51
Pt (ppb)	2	<2	<2	<2	3	3	12	2	4	<2	<2	6
Au (ppb)	2.6	2.8	2.3	7.3	3.3	2.3	4.8	2.3	1.5	<.2	<.2	3.3

Table 2.1b (continued):

Rock type	Chr. Peridotite	Chr. Peridotite	Chr. Peridotite	Chr. Peridotite	Chr. Peridotite	Chr. Peridotite	Feldspathic peridotite	Feldspathic peridotite	Feldspathic peridotite	Feldspathic peridotite	Feldspathic peridotite	Feldspathic peridotite
Sample ID	71061	71062	71063	71064	71065	71066	71067	71068	71071	71072	71073	71074
From (m)	11.7	19.8	25.1	28.7	32.3	38.5	45.9	48.9	51.9	58.9	66.2	71.0
To (m)	10.7	18.8	24.2	27.7	31.3	37.5	44.8	47.4	50.9	57.8	65.2	70.0
Distance (m)	106.3	98.2	92.9	89.3	85.7	79.5	72.2	69.6	66.1	59.2	51.9	47.0
Trace elements (ppm)												
Sc	9	6	6	6	8	6	7	6	6	6	6	8
V	218	145	127	121	133	88	102	107	101	108	118	116
Cr	1131	541	916	882	772	594	530	400	396	391	395	481
Se	0.5	0.5	1.0	2.0	1.1	0.7	1.0	0.6	0.2	0.3	0.2	0.7
Rb	48	20	36	38	23	20	9	9	11	8	7	8
Sr	29	100	19	28	19	24	42	64	61	50	70	85
Y	4.4	8.6	5.7	5.8	5.7	6.4	6.4	5.9	4.2	6.4	6.9	6.6
Zr	33	39	24	22	23	24	22	21	12	23	28	27
Nb	2.1	2.7	1.7	1.6	1.6	1.7	1.9	1.4	1.0	1.8	2.0	2.0
Cs	1.5	1.0	1.6	2.2	1.1	1.1	1.2	0.8	0.9	0.8	1.0	1.0
Ba	147	213	96	124	128	114	144	126	103	91	153	126
La	1.2	4.8	1.6	2.6	1.7	2.8	4.3	3.4	2.3	3.5	4.2	3.6
Ce	2.7	10.7	4.1	6.2	4.3	6.6	7.5	6.1	4.2	7.9	8.9	8.3
Pr	0.41	1.42	0.66	0.88	0.70	0.91	0.99	0.68	0.56	0.87	1.07	1.00
Nd	2.2	5.5	4.0	4.6	3.2	4.5	4.8	3.0	2.1	4.5	4.6	4.7
Sm	0.6	1.5	1.0	1.1	1.0	1.2	1.0	0.9	0.7	1.1	1.1	1.0
Eu	0.08	0.48	0.16	0.27	0.22	0.30	0.49	0.37	0.34	0.40	0.33	0.46
Gd	0.73	1.52	1.05	1.16	0.86	1.30	1.10	0.90	0.76	1.04	1.37	1.32
Tb	0.10	0.24	0.19	0.17	0.16	0.19	0.20	0.16	0.15	0.20	0.20	0.19
Dy	0.78	1.60	1.10	1.11	1.03	1.03	1.22	1.01	0.76	1.04	1.37	1.13
Ho	0.14	0.28	0.18	0.19	0.19	0.21	0.19	0.17	0.18	0.23	0.24	0.24
Er	0.40	0.70	0.55	0.53	0.52	0.66	0.51	0.52	0.44	0.58	0.65	0.66
Tm	0.07	0.15	0.08	0.09	0.07	0.10	0.08	0.09	0.07	0.13	0.12	0.10
Yb	0.40	0.66	0.48	0.62	0.60	0.51	0.59	0.42	0.45	0.61	0.65	0.67
Lu	0.10	0.10	0.07	0.07	0.09	0.08	0.08	0.08	0.06	0.08	0.09	0.08
Hf	0.8	1.1	0.8	0.7	0.8	0.6	0.6	0.7	0.5	0.9	0.9	0.8
Ta	0.1	0.1	0.1	0.1	0.1	0.1	0.1	0.1	<.1	0.2	0.1	0.1
Th	1.1	1.1	1.2	1.3	0.4	0.7	0.5	0.6	0.6	0.5	0.5	0.4

Chr = chromite-rich; * Total Fe as Fe2O3;** Total Fe as FeO; [1]LOI = loss on ignition; [2]mg-number = $Mg/(Mg+Fe^{2+})$;< = below detection limit

Table 2.1b (continued): Major and trace element abundances for the Far West Margin section (DDH # MX03-001)

Rock type	Feldspathic peridotite	Feldspathic peridotite	Chr. Peridotite	Chr. Peridotite	Chr. Peridotite	Chr. Peridotite	Chr. Peridotite	Gabbro-norite	Gabbro-norite	Gabbro-norite	Gabbro-norite	Massive Sulphide	Gouge	Gabbro-norite
Sample ID	71075	71076	71077	71078	71079	71080	71081	71082	71083	71084	71085	71086	71087	71088
From (m)	74.0	81.4	88.7	94.7	98.0	101.5	105.5	109.1	110.3	111.8	112.5	112.8	115.3	116.5
To (m)	72.5	79.8	87.7	93.2	96.9	100.0	101.5	107.6	109.1	110.3	111.8	112.5	113.7	115.3
Distance (m)	44.5	37.2	29.4	23.8	20.1	17.1	15.6	9.4	7.9	6.7	5.2	4.5	3.3	1.8
Major elements (wt%)														
SiO_2	39.28	40.38	40.08	38.77	38.11	38.79	40.93	46.62	42.83	43.93	38.42	10.44	47.04	46.33
TiO_2	0.48	0.48	0.47	0.43	0.39	0.47	0.63	0.44	0.38	0.50	0.37	0.14	0.38	0.36
Al_2O_3	4.98	5.45	5.16	4.74	4.40	5.08	5.68	7.37	5.42	6.96	6.02	2.43	5.26	6.95
Fe_2O_3*	12.68	13.38	12.18	12.60	13.49	13.37	13.05	15.21	17.53	20.37	26.88	68.37	18.31	23.36
MnO	0.14	0.15	0.15	0.14	0.14	0.13	0.14	0.10	0.10	0.15	0.09	0.03	0.09	0.10
MgO	28.19	26.49	27.95	29.41	29.34	28.10	26.26	20.61	23.58	19.03	17.33	4.75	20.31	13.77
CaO	3.69	4.13	3.68	2.62	2.55	2.38	3.91	1.33	1.54	2.33	0.75	0.23	0.55	0.91
Na_2O	0.27	0.33	0.13	0.05	0.03	0.13	0.41	0.61	0.24	0.28	0.27	0.15	0.26	0.76
K_2O	0.30	0.42	0.78	0.98	0.77	0.73	0.63	1.50	1.68	1.99	1.73	0.40	1.30	2.09
P_2O_5	0.09	0.09	0.08	0.08	0.07	0.09	0.10	0.07	0.10	0.08	0.07	0.04	0.05	0.05
Cr_2O_3	0.31	0.47	0.86	1.10	0.81	0.62	0.32	0.11	0.30	0.12	0.11	0.07	0.15	0.08
LOI[1]	9.2	8.1	8.4	8.9	9.8	9.5	7.4	5.9	6.3	4.2	7.7	12.7	6.1	4.6
S	1.12	0.78	0.18	0.40	0.82	1.21	0.97	1.80	2.33	3.15	7.53	30.90	2.92	6.19
Total	99.97	100.1	100.2	100.1	100.2	99.77	99.83	100.0	100.2	100.1	99.94	100.3	100.0	99.63
mg-number[2]	0.815	0.797	0.820	0.822	0.812	0.806	0.799	0.729	0.727	0.649	0.561	0.121	0.687	0.539
FeO**	11.41	12.04	10.96	11.34	12.14	12.03	11.74	13.69	15.77	18.33	24.19	61.52	16.48	21.02
Chalcophile elements (ppm)														
Cu	1198	309	166	174	380	971	898	961	852	846	1511	5721	1064	2147
Ni	2626	1379	1763	2163	2498	2828	2784	953	1284	1049	1266	4623	1361	1778
Co	139	112	93	111	123	136	116	110	173	161	225	834	155	223
Pd (ppb)	142	22	21	50	112	144	140	46	57	40	22	106	53	48
Pt (ppb)	25	5	<2	4	5	3	10	2	3	<2	<2	<2	3	3
Au (ppb)	9.1	2.8	1.9	3.4	3.8	9.7	9.1	3.8	4.0	2.6	2.8	5.7	5.3	5.5

Table 2.1b (continued):

Rock type	Feldspathic peridotite	Feldspathic peridotite	Chr. Peridotite	Chr. Peridotite	Chr. Peridotite	Chr. Peridotite	Chr. Peridotite	Gabbro-norite	Gabbro-norite	Gabbro-norite	Gabbro-norite	Msv. Sulphide	Gouge	Gabbro-norite
Sample ID	71075	71076	71077	71078	71079	71080	71081	71082	71083	71084	71085	71086	71087	71088
From (m)	74.0	81.4	88.7	94.7	98.0	101.5	105.5	109.1	110.3	111.8	112.5	112.8	115.3	116.5
To (m)	72.5	79.8	87.7	93.2	96.9	100.0	101.5	107.6	109.1	110.3	111.8	112.5	113.7	115.3
Distance (m)	44.5	37.2	29.4	23.8	20.1	17.1	15.6	9.4	7.9	6.7	5.2	4.5	3.3	1.8
Trace elements (ppm)														
Sc	7	6	6	8	8	10	6	8	6	5	11	4	11	7
V	127	148	145	141	140	79	155	145	125	141	145	145	69	81
Cr	404	448	696	819	790	834	537	483	745	424	594	182	713	365
Se	1.4	0.7	0.4	0.8	1.3	1.6	1.2	1.8	2.2	2.8	5.6	21.4	3.1	5.3
Rb	9	13	26	35	27	23	21	50	62	73	70	16	49	66
Sr	107	115	77	50	34	64	102	124	50	75	53	31	67	99
Y	7.7	7.4	8.4	7.5	6.8	8.2	10.3	16.6	13.5	16.0	17.2	5.8	24.7	19.2
Zr	33	28	35	24	33	28	50	83	91	88	107	34	110	110
Nb	2.4	2.0	2.2	1.8	1.7	1.8	3.5	6.8	8.0	8.0	8.5	3.2	10.0	8.1
Cs	1.0	1.3	1.7	1.8	1.7	1.5	1.6	2.7	3.6	3.8	4.1	1.1	2.4	3.1
Ba	175	169	197	171	165	161	177	284	194	313	281	55	231	427
La	5.1	4.2	5.1	2.2	2.4	4.2	8.1	18.9	9.2	19.2	25.3	8.4	25.0	19.8
Ce	10.1	9.4	11.2	5.8	6.0	9.8	16.4	38.8	21.0	39.3	51.6	16.2	48.4	38.0
Pr	1.18	1.12	1.43	0.94	0.95	1.31	2.01	4.56	2.70	4.72	5.80	1.75	5.53	4.46
Nd	5.6	4.8	7.3	4.2	4.7	5.8	7.8	16.4	12.1	16.9	21.1	5.8	20.8	14.7
Sm	1.2	1.1	1.5	1.3	1.3	1.6	1.9	3.5	2.9	3.6	3.9	1.2	4.1	3.6
Eu	0.53	0.48	0.31	0.24	0.25	0.42	0.62	0.65	0.42	0.59	0.56	0.15	0.64	0.68
Gd	1.30	1.30	1.25	1.32	1.44	1.48	2.21	3.19	2.85	3.65	3.55	0.88	3.92	2.98
Tb	0.25	0.21	0.24	0.19	0.19	0.26	0.33	0.43	0.41	0.53	0.54	0.15	0.69	0.50
Dy	1.48	1.41	1.54	1.30	1.38	1.41	1.86	2.93	2.32	2.80	3.13	0.87	4.17	2.87
Ho	0.28	0.28	0.31	0.25	0.27	0.30	0.36	0.59	0.47	0.57	0.60	0.20	0.89	0.65
Er	0.77	0.69	0.85	0.65	0.78	0.81	1.03	1.81	1.28	1.45	1.67	0.53	2.59	2.06
Tm	0.12	0.13	0.14	0.13	0.10	0.13	0.13	0.25	0.17	0.22	0.24	0.11	0.41	0.31
Yb	0.68	0.70	0.83	0.68	0.64	0.77	1.03	1.72	1.26	1.47	1.77	0.49	3.27	2.25
Lu	0.09	0.10	0.11	0.10	0.07	0.12	0.15	0.26	0.19	0.17	0.27	0.09	0.51	0.32
Hf	1.0	1.1	1.0	0.7	0.8	0.7	1.6	2.4	2.5	2.4	2.9	0.9	2.8	3.2
Ta	0.1	0.1	0.2	0.2	0.2	0.1	0.2	0.5	0.5	0.5	0.5	0.2	0.6	0.5
Th	0.8	0.5	1.0	0.9	1.1	1.2	1.6	5.1	5.7	6.6	6.1	1.8	5.0	6.2

Chr = chromite-rich; * Total Fe as Fe2O3;** Total Fe as FeO; [1]LOI = loss on ignition; [2]mg-number = $Mg/(Mg+Fe^{2+})$;< = below detection limit

Table 2.1b (continued): Major and trace element abundances for the Far West Margin section (DDH # MX03-001)

Rock type	Gabbro-norite	Massive Sulphide	Hornfelsed paragneiss	Hornfelsed paragneiss	Massive Sulphide	Granitic pod	Granitic pod	Meta-gabbro	Meta-gabbro	Meta-gabbro	Meta-gabbro	Meta-gabbro	Sulphide Breccia
Sample ID	71091	71092	71093	71094	71095	71096	71097	71098	71099	71100	71101	71102	71103
From (m)	117.0	117.5	119.0	120.1	120.3	120.8	121.8	126.0	127.7	128.1	128.6	133.2	133.9
To (m)	116.5	117.0	117.5	119.0	120.1	120.3	120.8	125.7	127.3	127.7	128.3	132.8	133.3
Distance (m)	0.5	0.0	-0.5	-2.0	-3.1	-3.3	-3.8	-8.7	-10.3	-10.7	-11.3	-15.8	-16.3
Major elements (wt%)													
SiO_2	48.81	9.08	45.72	54.23	10.58	52.87	67.41	48.30	49.76	53.14	59.67	40.01	43.41
TiO_2	0.40	0.09	0.82	0.91	0.07	0.29	0.32	2.04	1.41	1.21	0.64	1.94	1.30
Al_2O_3	7.73	1.87	15.91	14.19	2.60	11.86	11.49	12.54	14.10	14.90	10.84	15.59	10.18
Fe_2O_3*	23.75	73.28	15.54	13.76	72.67	20.02	6.82	17.74	15.57	11.70	11.85	18.54	22.81
MnO	0.09	0.02	0.10	0.12	0.02	0.05	0.05	0.22	0.17	0.13	0.10	0.17	0.16
MgO	8.73	2.66	8.05	5.44	0.94	3.05	3.09	5.62	5.59	5.42	7.47	7.84	7.32
CaO	0.62	0.12	2.16	2.49	0.36	1.47	1.43	7.26	6.85	5.08	1.88	3.63	4.22
Na_2O	0.88	0.10	1.16	1.47	0.32	2.13	2.13	2.10	2.47	2.66	1.65	1.08	1.01
K_2O	2.99	0.25	3.68	3.09	0.61	3.21	4.00	1.82	1.36	2.75	1.39	4.58	2.52
P_2O_5	0.07	0.02	0.09	0.07	0.02	0.06	0.06	0.23	0.16	0.12	0.06	0.20	0.15
Cr_2O_3	0.07	0.04	0.02	0.01	0.04	0.03	0.02	0.00	0.01	0.01	0.01	0.01	0.01
LOI[1]	5.1	12.5	6.0	3.5	11.6	3.9	2.3	1.0	1.4	2.0	3.8	4.7	5.9
S	6.89	31.10	3.24	2.47	29.55	6.56	0.86	1.06	1.68	0.63	0.35	3.37	5.92
Total	99.52	100.9	99.37	99.41	101.2	99.34	99.24	99.08	99.14	99.29	99.44	99.21	100.4
mg-number[2]	0.421	0.067	0.507	0.439	0.025	0.232	0.473	0.386	0.416	0.479	0.555	0.456	0.389
FeO**	21.37	65.94	13.98	12.38	65.39	18.01	6.14	15.96	14.01	10.53	10.66	16.68	20.52
Chalcophile elements (ppm)													
Cu	2026	8362	1335	829.3	8016	2072	394.2	1732	1311	1111	1097	10189	7460
Ni	1672	6624	697	647	10278	2447	284	1187	2067	912	524	6568	10672
Co	221	793	113	80	996	206	33	63	85	38	28	145	224
Pd (ppb)	55	251	59	47	449	79	<10	142	135	111	88	1836	1247
Pt (ppb)	2	13	7	6	36	<2	<2	6	3	5	2	152	105
Au (ppb)	6.9	40.9	3.9	6.9	55.3	12.0	1.3	22.6	27.7	37.0	34.3	203.9	296.0

Table 2.1b (continued):

Rock type	Gabbro-norite	Msv. Sulphide	Hornfelsed paragneiss	Hornfelsed paragneiss	Msv. Sulphide	Granitic pod	Granitic pod	Meta-gabbro	Meta-gabbro	Meta-gabbro	Meta-gabbro	Meta-gabbro	Sul. Breccia
Sample ID	71091	71092	71093	71094	71095	71096	71097	71098	71099	71100	71101	71102	71103
From (m)	117.0	117.5	119.0	120.1	120.3	120.8	121.8	126.0	127.7	128.1	128.6	133.2	133.9
To (m)	116.5	117.0	117.5	119.0	120.1	120.3	120.8	125.7	127.3	127.7	128.3	132.8	133.3
Distance (m)	0.5	0.0	-0.5	-2.0	-3.1	-3.3	-3.8	-8.7	-10.3	-10.7	-11.3	-15.8	-16.3
Trace elements (ppm)													
Sc	12	5	15	8	3	9	7	5	6	6	9	15	14
V	158	141	342	244	129	94	77	389	301	236	118	367	244
Cr	386	177	88	58	64	108	97	7	25	32	34	66	39
Se	8.5	28.4	3.5	2.4	33.6	8.3	1.4	1.9	3.5	1.2	0.8	9.4	15.6
Rb	85	9	113	89	15	70	96	62	46	76	28	162	89
Sr	127	17	245	216	38	234	263	263	223	289	71	240	167
Y	21.1	4.7	23.0	27.9	2.6	15.9	23.1	37.7	32.0	23.9	18.8	31.9	23.0
Zr	126	18	111	156	17	70	148	111	73	85	72	123	83
Nb	8.8	1.9	10.5	13.5	0.9	5.2	6.4	15.9	10.3	11.7	7.6	12.9	7.9
Cs	3.0	0.5	2.9	2.9	0.6	2.1	2.2	3.0	2.3	2.6	1.0	6.0	1.9
Ba	578	27	274	384	130	784	740	504	251	493	99	761	393
La	30.7	4.3	28.1	53.3	4.3	17.9	29.8	19.4	9.6	12.1	8.1	16.1	15.5
Ce	59.0	8.0	52.6	98.6	7.2	29.2	53.2	40.1	21.9	24.7	16.0	35.2	33.9
Pr	6.56	0.94	6.30	11.25	0.77	3.22	5.93	4.74	2.93	2.89	1.81	4.49	4.09
Nd	24.3	3.4	23.3	35.7	2.7	10.8	20.0	22.4	15.1	13.5	7.8	20.0	18.1
Sm	4.7	0.7	4.7	6.0	0.5	2.1	4.1	5.5	4.3	3.1	2.2	5.3	4.2
Eu	0.8	0.1	1.2	1.4	0.2	1.2	1.0	2.0	1.4	1.4	0.9	1.4	1.2
Gd	3.68	0.73	4.26	5.58	0.49	2.52	3.65	6.36	5.26	3.92	2.29	5.74	4.75
Tb	0.58	0.14	0.69	0.89	0.09	0.45	0.67	1.24	0.95	0.67	0.54	1.08	0.72
Dy	3.92	0.85	4.09	4.70	0.37	2.63	4.08	6.86	5.16	3.89	2.94	5.87	3.88
Ho	0.77	0.16	0.73	0.84	0.07	0.58	0.79	1.42	1.09	0.78	0.65	1.16	0.85
Er	2.27	0.50	2.19	2.68	0.29	1.45	2.44	3.87	3.16	2.30	1.77	3.08	2.22
Tm	0.37	0.08	0.33	0.34	0.05	0.24	0.41	0.58	0.57	0.35	0.33	0.53	0.37
Yb	2.71	0.50	2.33	2.56	0.25	1.55	2.52	3.54	3.30	2.28	2.11	2.84	2.13
Lu	0.35	0.08	0.35	0.36	0.05	0.26	0.40	0.53	0.55	0.34	0.25	0.42	0.31
Hf	3.1	0.7	3.2	4.7	0.6	1.9	4.4	3.2	1.9	2.3	2.2	3.6	2.4
Ta	0.6	0.1	0.8	0.8	<.1	0.6	1.0	1.1	0.9	1.0	0.6	0.7	0.5
Th	7.9	1.1	7.7	10.5	0.9	4.7	11.9	1.9	1.4	2.3	3.4	2.3	3.0

Chr = chromite-rich; * Total Fe as Fe2O3;** Total Fe as FeO; [1]LOI = loss on ignition; [2]mg-number = $Mg/(Mg+Fe^{2+})$;< = below detection limit

2.4.2 Olivine compositions

Olivine compositions from 10 samples were determined by wavelength-dispersion spectrometry (WDS) using the Cameca SX50 Electron Microprobe at the University of British Columbia. The olivine compositions were measured with an accelerating voltage of 15 KeV, a beam current of 20 nA, and a beam size of 5 μm. Counting times for peak and background were 20 and 10 seconds, respectively. In order to precisely determine nickel contents, each analysis was repeated using the fixed-matrix mode and a beam current and counting time of 100 nA and 100 seconds, respectively. Natural and synthetic standards were used for calibration and procedural set-up. The "PAP" $\Phi(\rho Z)$ data reduction procedure of Pouchou & Pichoir (1991) was applied to all analyses. Relative errors (1σ) for SiO_2 and MgO, and for FeO are less than 1% and 2.5%, respectively. Low abundances of MnO and NiO gave higher relative errors of 10-30% using the standard method. CaO, Cr_2O_3, and TiO_2 abundances were at or below detection limits. Using the higher beam current and counting times, as described above, the analytical error on nickel analyses was reduced to <5% relative.

Olivine in the studied samples is strongly serpentinized (20-80 vol %); analyzed grains were chosen within clusters of relatively unaltered olivine. Each grain was analyzed in the core, in an intermediate spot, and on the rim, unless one of these areas was serpentinized, in which case only two analyses were determined. The olivine grains were not visibly zoned and all analyses from an individual grain are within error, with the exception of two samples from the Far West Margin that were clearly zoned. Two to four grains were measured in each cluster and 2-3 clusters were measured on each thin section for a total of 185 measurements. Representative core analyses are summarized in Table 2.2 and all data are reported in Appendix III. All analyses reported are consistent with mineral stoichiometry. Comparison of the two methods described above for Ni determination is shown in Appendix IV.

2.4.3 Sulphur isotopic compositions

Sulphur isotopic compositions were measured for 23 samples and 3 duplicates (71092, 71095 and 71145) at the Queen's Facility for Isotopic Research (QFIR) in the Department of Geological Sciences and Geological Engineering at Queen's University in Kingston, Ontario. The analyses were completed on a Finnigan MAT 252 isotope-ratio mass spectrometer using continuous-flow technology and online sulphur extraction. The measured sulphur isotopic compositions are reported in Table 2.3. All values were corrected using the NIST 8556

Table 2.2a: Representative olivine compositions from the West Pyrrhotite Lake section[1].

Region / Drillhole	West Pyrrhotite Lake / MX03-002									
Rock type[2]	Peridotite		Peridotite		F. Peridotite		F. Peridotite		Ol-Gbnr	
Thin Section	RMX02-3A		RMX02-4		RMX02-5		RMX02-6		RMX02-8	
Sample no.	71112		71115		71123		71127		71133	
Site	rim	mid	interm	rim	core	mid	mid	mid	mid	core
Oxide wt %										
SiO_2	39.22	39.11	39.08	39.36	39.27	38.97	38.61	38.48	38.32	38.51
TiO_2	0.07	0.01	0.03	0.04	0.04	0.03	0.04	0.04	0.02	0.02
FeO	17.75	16.95	18.01	17.42	18.97	18.29	20.31	19.12	22.78	21.03
MnO	0.19	0.27	0.27	0.26	0.27	0.30	0.26	0.27	0.32	0.28
MgO	42.76	43.10	43.15	43.27	42.20	42.49	40.75	41.52	39.07	40.09
CaO	0.02	0.08	0.05	0.04	0.05	0.04	0.07	0.02	0.07	0.07
Cr_2O_3	0.02	0.11	0.00	0.00	0.12	0.00	0.08	0.04	0.00	0.03
NiO	0.30	0.31	0.31	0.33	0.30	0.29	0.29	0.32	0.26	0.25
total	100.35	99.93	100.90	100.71	101.22	100.41	100.42	99.82	100.84	100.28
Cation (p.f.u.)										
Si	0.995	0.993	0.989	0.994	0.993	0.992	0.991	0.990	0.992	0.994
Ti	0.001	0.000	0.001	0.001	0.001	0.001	0.001	0.001	0.000	0.000
Fe^{2+}	0.377	0.360	0.381	0.368	0.401	0.389	0.436	0.411	0.493	0.454
Mn	0.004	0.006	0.006	0.006	0.006	0.006	0.006	0.006	0.007	0.006
Mg	1.618	1.631	1.627	1.629	1.590	1.612	1.560	1.592	1.508	1.542
Ca	0.001	0.002	0.001	0.001	0.001	0.001	0.002	0.001	0.002	0.002
Cr	0.001	0.005	0.000	0.000	0.006	0.000	0.004	0.002	0.000	0.002
Ni	0.006	0.006	0.006	0.007	0.006	0.006	0.006	0.007	0.005	0.005
Sum	3.003	3.004	3.011	3.005	3.004	3.007	3.006	3.009	3.008	3.005
Endmembers %										
Fo	81.1	81.9	81.0	81.6	79.9	80.6	78.2	79.5	75.4	77.3
Fa	18.9	18.1	19.0	18.4	20.1	19.4	21.8	20.5	24.6	22.7

[1] Reported values are for minimum and maximum forsterite contents in each thin section.

[2] F.Peridotite = Feldspathic peridotite; Ol-Gbnr = olivine gabbronorite; Cr. Peridotite = chromite-rich peridotite

Table 2.2b: Representative olivine compositions from the Far West Margin section [1].

Region / Drillhole	Far West Margin / MX03-001									
Rock type	Cr. Peridotite		Cr. Peridotite		Peridotite		F. Peridotite		Cr. Peridotite	
Thin Section	RMX01-1		RMX01-3		RMX01-4		RMX01-5		RMX01-6	
Sample no.	71061		71063		71072		71075		71078	
Site	rim	mid	core	rim	rim	core	rim	mid	core	rim
Oxide wt %										
SiO_2	39.28	40.59	40.01	40.24	40.01	39.50	39.51	39.72	39.86	39.67
TiO_2	0.01	0.01	0.03	0.00	0.02	0.04	0.02	0.01	0.06	0.01
FeO	18.54	11.69	13.04	12.17	14.80	14.26	17.01	15.54	14.79	13.89
MnO	0.14	0.18	0.17	0.17	0.21	0.22	0.24	0.26	0.14	0.25
MgO	42.33	47.85	46.20	47.22	45.41	45.19	43.81	43.96	45.89	45.80
CaO	0.01	0.05	0.11	0.04	0.08	0.07	0.08	0.13	0.07	0.06
Cr_2O_3	0.13	0.04	0.05	0.05	0.04	0.00	0.03	0.07	0.03	0.05
NiO	0.17	0.30	0.16	0.15	0.33	0.35	0.25	0.26	0.26	0.24
total	100.62	100.71	99.76	100.04	100.90	99.63	100.95	99.94	101.10	99.97
Cation (p.f.u.)										
Si	0.996	0.997	0.998	0.997	0.996	0.994	0.993	1.001	0.990	0.993
Ti	0.000	0.000	0.001	0.000	0.000	0.001	0.000	0.000	0.001	0.000
Fe^{2+}	0.393	0.240	0.272	0.252	0.308	0.300	0.357	0.327	0.307	0.291
Mn	0.003	0.004	0.004	0.004	0.004	0.005	0.005	0.006	0.003	0.005
Mg	1.599	1.752	1.718	1.744	1.684	1.696	1.641	1.651	1.699	1.708
Ca	0.000	0.001	0.003	0.001	0.002	0.002	0.002	0.004	0.002	0.002
Cr	0.006	0.002	0.002	0.002	0.002	0.000	0.001	0.003	0.001	0.002
Ni	0.003	0.006	0.003	0.003	0.007	0.007	0.005	0.005	0.005	0.005
Sum	3.001	3.002	3.000	3.002	3.003	3.005	3.006	2.997	3.008	3.006
Endmembers %										
Fo	80.3	87.9	86.3	87.4	84.5	85.0	82.1	83.5	84.7	85.5
Fa	19.7	12.1	13.7	12.6	15.5	15.0	17.9	16.5	15.3	14.5

[1] Reported values are for minimum and maximum forsterite contents in each thin section.

[2] F.Peridotite = Feldspathic peridotite; Ol-Gbnr = olivine gabbronorite; Cr. Peridotite = chromite-rich peridotite

Table 2.3: Sulphur isotopic compositions in marginal rocks of the Muskox intrusion

Host rock	Sample no.[1]	Drilled depth (m)	Distance (m)[2]	Mineralogy[3]	Texture/grain size[4]	Whole rock S (wt%)	$\delta^{34}S$ (CDT)[5]
Far West Margin (DDH # MX03-001)							
Chr. Peridotite	71064	28.7	88.4	po	D, BL	1.47	6.5
F. Peridotite	71067	45.9	71.2	po	D	0.47	6.4
F. Peridotite	71076	81.4	35.7	po	BL	0.78	6.3
Chr. Peridotite	71080	101.5	15.6	po	D, BL	1.21	7.9
Gabbronorite	71085a	112.5	4.6	po	BL, NT	7.53	9.1
Gabbronorite	71085b	112.5	4.6	po	BL / 0.8 cm	7.53	7.9
Gabbronorite	71088	116.5	0.5	po	D, BL	6.19	7.2
Gabbronorite	71092a	117.5	-0.5	po	MSV	31.1	7.9
Gabbronorite	71092b	117.5	-0.5	po	MSV	31.1	7.9
Paragneiss	71095a	120.3	-3.3	po	MSV	29.6	8.7
Paragneiss	71095b	120.3	-3.3	po	MSV	29.6	8.5
Paragneiss	71096	120.6	-3.6	po	BL / 0.8 cm	6.56	11.6
Paragneiss	GD 04-03	120.9	-3.9	po	MSV vein	-	9.4
Breccia	71103	133.9	-16.9	po,cpy	MSV vein	5.92	7.8
Paragneiss	141	141	-24.0	po	D	-	7.5
Paragneiss	149.2	149.2	-32.2	po	D	-	7.9
West Pyrrhotite Lake (DDH # MX03-002)							
Gabbronorite	71138	174.8	3.2	po	BL / 0.5 cm	1.06	6.7
Gabbronorite	71139	175.8	2.2	po	BL / 0.5 cm	1.58	6.1
Feld-Bio-Qtz Gneiss	71141	180.2	-2.2	po,cpy	D	1.42	7.6
Pegmatite Vein	RM02-10	182.7	-4.7	cpy,po	BL / 0.5 cm	-	7.3
Feld-Bio-Qtz Gneiss	71145	188.8	-10.8	po,cpy	MSV, 3.5 cm wide vein	5.54	7.0
Feld-Bio-Qtz Gneiss	71145b	188.8	-10.8	po,cpy	MSV, 3.5 cm wide vein	5.54	7.4
Feld-Bio-Qtz Gneiss	71146	192.9	-14.9	po,cpy	STR, 0.5 cm, along foliation	3.30	7.7

F. Peridotite = feldspathic peridoite; Chr. Peridotite = chromite-rich peridotite; Feld = feldspar; Bio = biotite; Qtz = quartz.

[1]Procedural duplicates are denoted "a" and "b"; with the exception of sample 71085 in which two distinct textured grains were analyzed.

[2]Drilled distance from the outer intrusive contact.

[3]po = pyrrhotite; cpy = chalcopyrite

[4]D = disseminated; BL = blebby; NT = net-textured; MSV = massive; STR = stringer

[5]CDT = Canyon Diablo Troilite

standard and are reported relative to Canyon Diablo Troilite (CDT). Analytical precision is ± 0.3‰ and results from the three procedural duplicates are within 0.5‰ (Table 2.3).

2.5 GEOCHEMISTRY OF THE MARGINAL ROCKS

The following section summarizes stratigraphic variations at the West Pyrrhotite Lake and Far West Margin sections in (1) major and trace element abundances, which primarily record changes in the modal abundance of cumulus and postcumulus phases; (2) olivine composition, which in the case of the Muskox marginal samples records mainly varying degrees of re-equilibration with intercumulus liquid during cooling (e.g. Barnes, 1986); (3) chalcophile elements, which are typically controlled by the distribution of sulphide minerals owing to their high partition coefficients between sulphide and silicate liquids (e.g. Rajamani & Naldrett, 1978; Fleet et al., 1991; Peach et al., 1994); (4) primitive mantle-normalized trace element diagrams; and (5) incompatible trace element ratios and sulphur isotopic compositions, which provide an index of contamination along the basal margin of the intrusion (Fig. 2.8-2.13). Select major elements are also plotted against MgO to compare results from the two sections with those of a previously studied section along the eastern margin of the intrusion (Francis, 1994; Pyrrhotite Lake section) and of an additional drill hole north of the Far West Margin (MX04-001).

2.5.1 West Pyrrhotite Lake

The peridotites (peridotite, feldspathic peridotite, and olivine gabbronorite) become progressively lower in MgO (38 to 22 wt %) and Cr_2O_3 (0.5 to 0.3 wt %), and higher in CaO (0.8 to 5.6 wt %), and Al_2O_3 (3.2 to 8.6 wt %) towards the contact with the country rocks (Fig. 2.8a). Stratigraphic trends of SiO_2, TiO_2, K_2O, Na_2O, and incompatible trace elements correlate with Al_2O_3 and progressively increase towards the margin, which corresponds to a progressive decrease in olivine abundance and increase in postcumulus pyroxene, plagioclase, and phlogopite abundances. The trend of decreasing whole-rock MgO contents correlates with a progressive decrease in the forsterite content of olivine (Fo_{82} to Fo_{74}; Fig. 2.9a). Olivine accumulation exhibits a strong control on the overall geochemical variation within the peridotites (Fig. 2.10a). The peridotites at West Pyrrhotite Lake contain only rare sulphide and therefore have relatively low abundances of chalcophile elements, with Ni concentrations being largely controlled by olivine (Fig. 2.11a). The olivine cumulates have the lowest

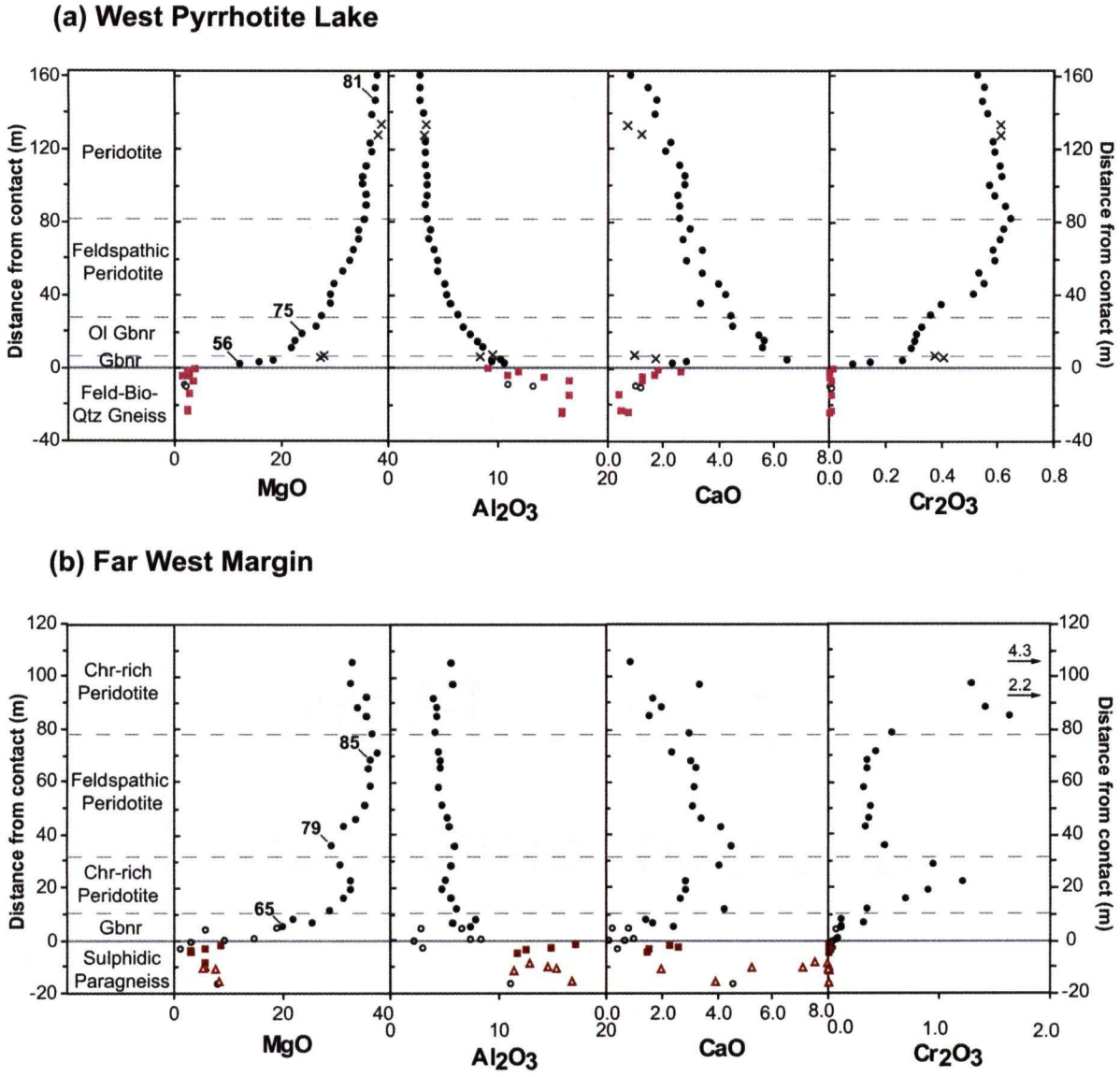

Fig. 2.8: Stratigraphic variations of major elements (all in wt %) at the (a) West Pyrrhotite Lake and (b) Far West Margin sections of the Muskox intrusion. Solid circles are marginal zone rocks, squares are gneissic host rocks, triangles are gabbroic host rocks, open circles are sulphide-rich (>5 wt % sulphur) samples, and crosses are intensely altered samples or gouge material. Ol Gbnr = olivine gabbronorite and Gbnr = gabbronorite. Note the difference of scale in Cr_2O_3 for the two sections. Arrows in the Far West Margin Cr_2O_3 plot point towards very Cr-rich peridotites. The numbers in the MgO plots give the calculated Mg# of the indicated sample (Mg# = $(Mg^{2+}/(Mg^{2+}+Fe^{2+}))$ x 100). The rocks at West Pyrrhotite Lake become progressively more evolved in composition (e.g. decreasing MgO and increasing Al_2O_3) towards the margin, which corresponds to a systematic increase in abundance of postcumulus pyroxene and plagioclase. A similar variation is observed within the feldspathic peridotite horizon at the Far West Margin.

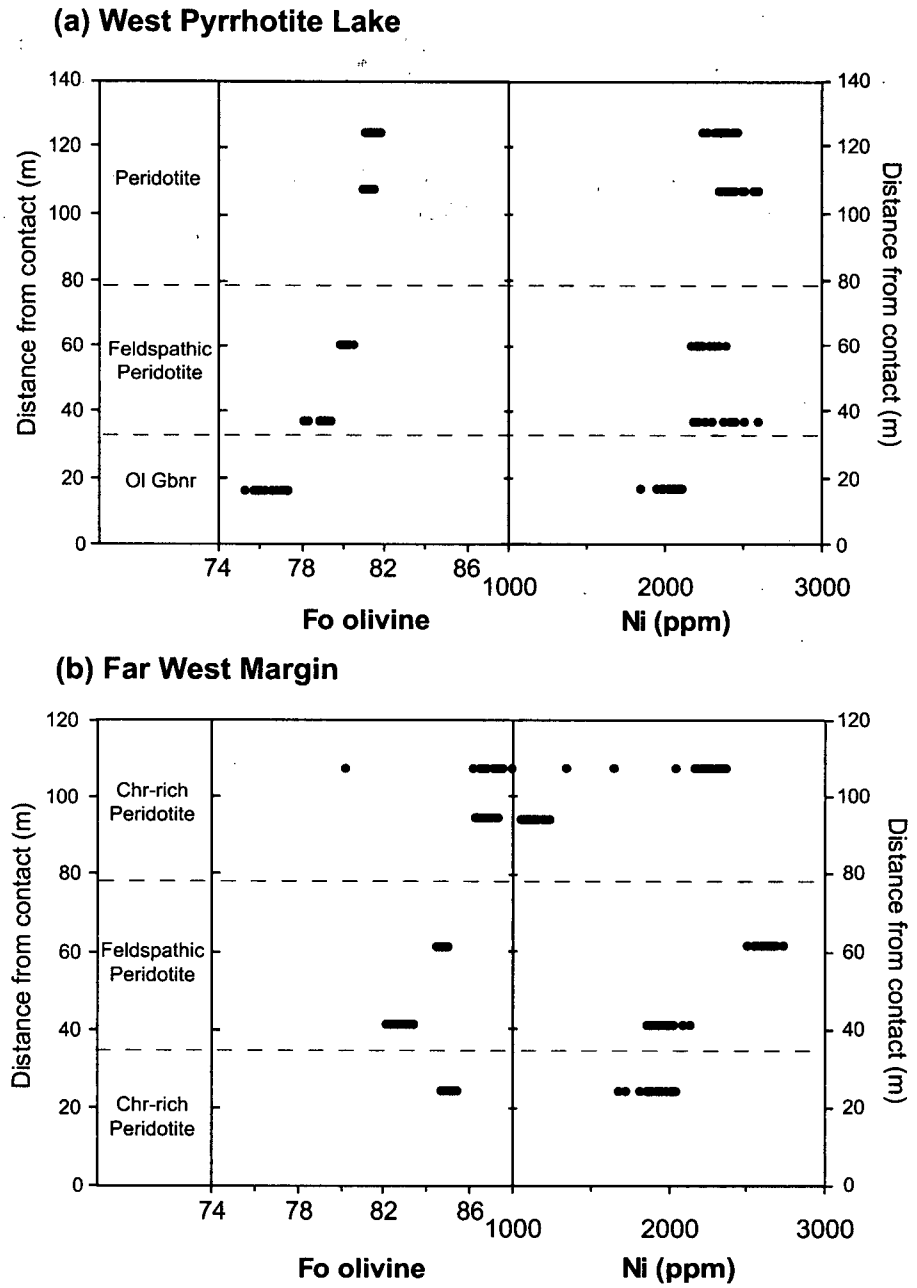

Fig. 2.9: Stratigraphic variations in olivine compositions for (a) West Pyrrhotite Lake and (b) Far West Margin peridotites. Abbreviations as in Fig. 2.8. The olivine grains are typically unzoned, with the exception of the upper chromite-rich horizon at the Far West Margin. At West Pyrrhotite Lake, the forsterite content, and to some extent the Ni content, decreases progressively towards the margin. The correlation between decreasing forsterite content and increasing abundance of postcumulus phases is consistent with the shift expected from re-equilibration with intercumulus liquid during solidification (see text for discussion). At the Far West Margin, a similar variation is observed within the feldspathic peridotite unit. The olivine grains within sulphide-bearing chromite-rich peridotites and the lower feldspathic peridotite sample however have relatively low Ni contents which may record the crystallization of olivine in the presence of a sulphide liquid.

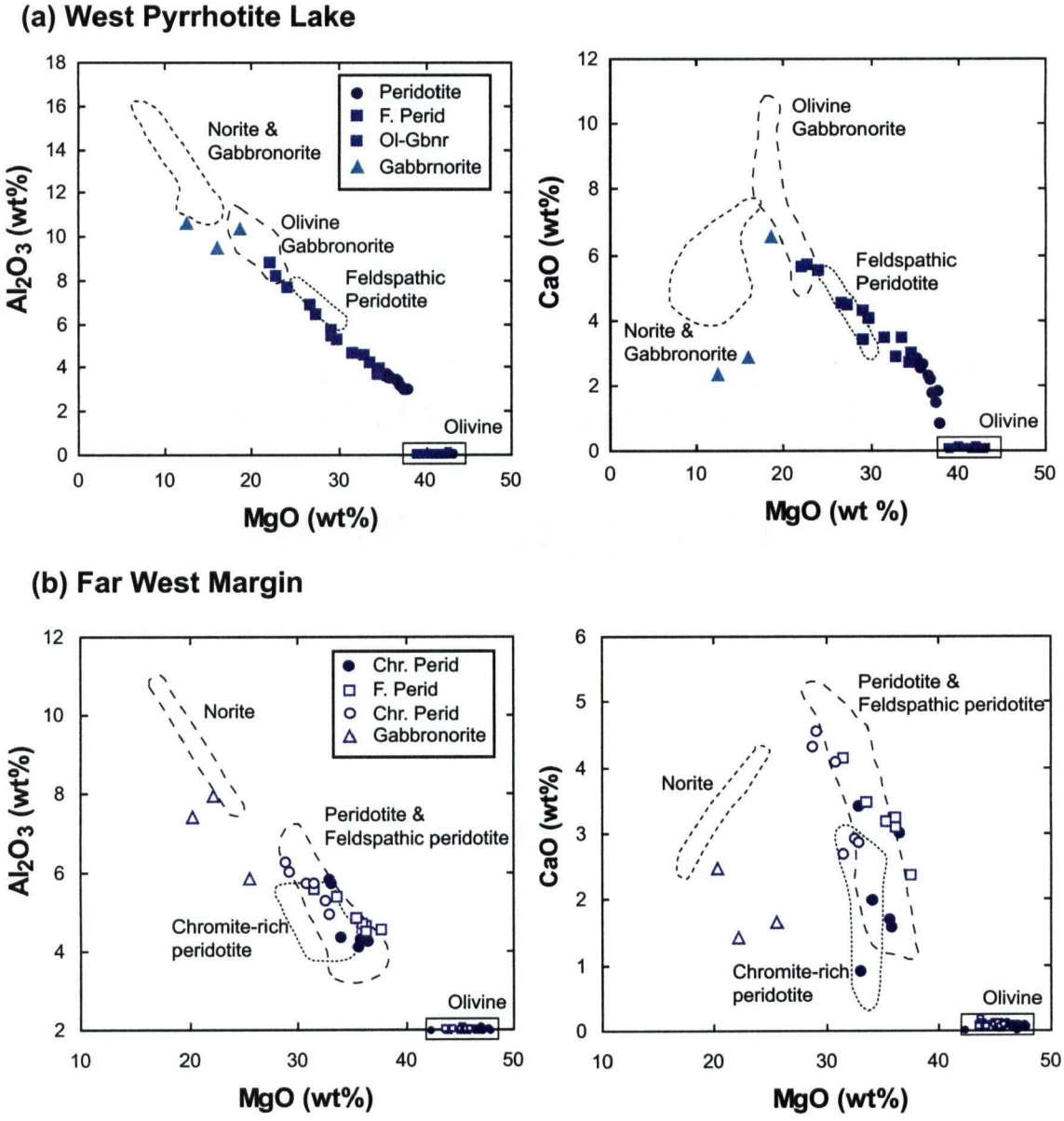

Fig. 2.10: MgO vs. Al2O3 and CaO diagrams for (a) West Pyrrhotite Lake and (b) Far West Margin samples. Note the difference in scale of the Y-axis for the two sections. The range in analyzed olivine compositions is shown for each section. The labeled fields are for equivalent lithologies from a previously studied section along the eastern margin of the intrusion (Pyrrhotite Lake section; Francis, 1994) for the West Pyrrhotite Lake diagrams, and unpublished data from drill core collected ~1 km north of the Far West Margin section (DDH MX04-002) for the Far West Margin diagrams. In general, peridotite samples from all sections plot along an olivine control line, indicating that the rocks represent mixtures of olivine and some proportion of residual liquid that crystallized as postcumulus minerals. Peridotites from the eastern margin (Francis, 1994) are displaced to higher CaO and Al2O3, which could reflect a higher proportion of postcumulus phases at this location. The scatter within the Far West Margin peridotites reflects abundant orthopyroxene and chromite within the chromite-rich peridotites. The contaminated gabbronorite samples in all sections plot off the overall trend and are displaced towards lower CaO.

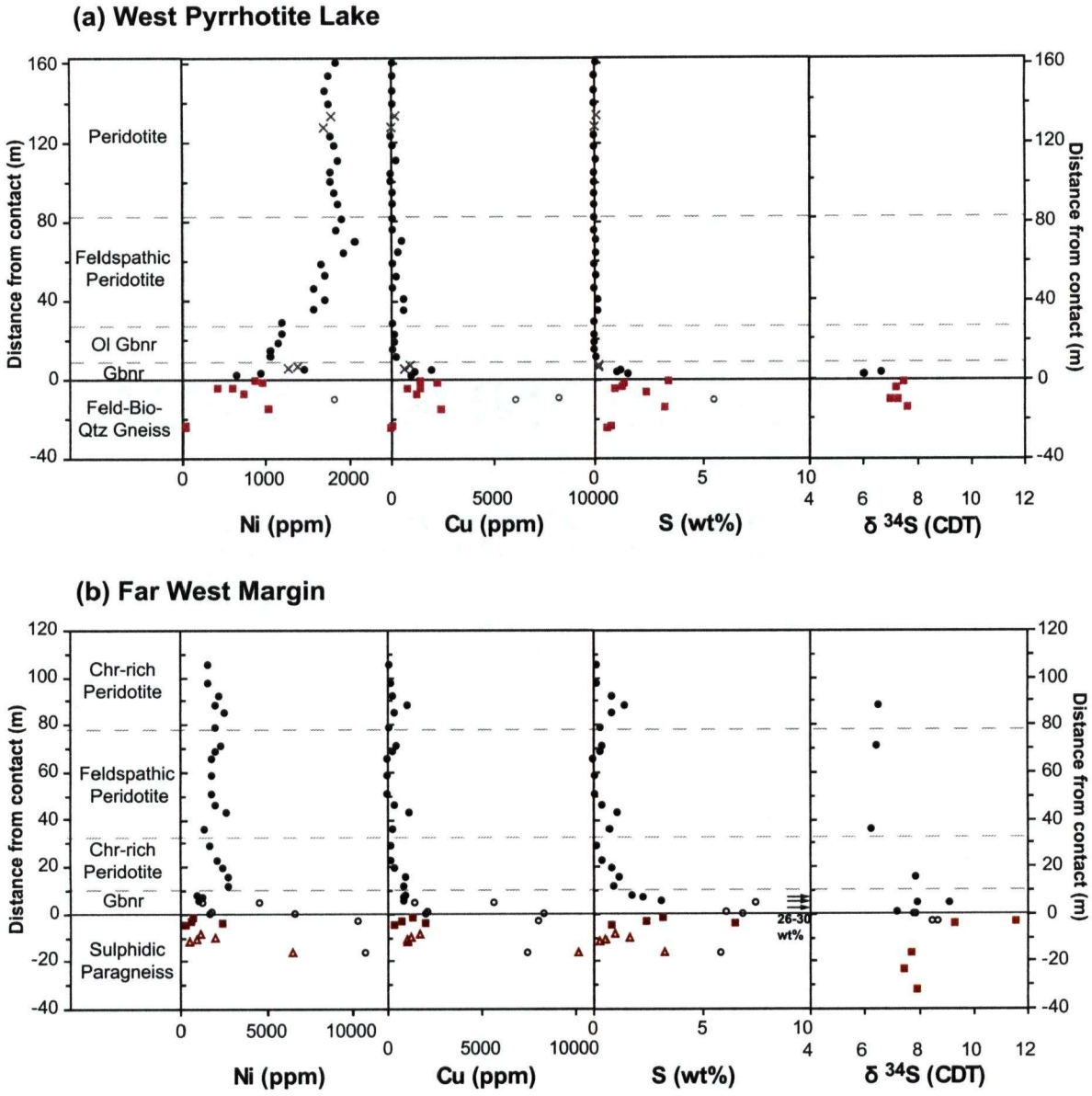

Fig. 2.11: Stratigraphic variations of Ni, Cu, S contents and sulphur isotopic compositions for (a) West Pyrrhotite Lake and (b) Far West Margin sections. Symbols and abbreviations as in Fig. 2.8. CDT = canyon Diablo troilite. As expected from the high partition coefficients between sulphide and silicate liquids, samples that contain sulphide have elevated Ni and Cu contents. Pd and Pt contents (not shown) are also elevated in the mineralized samples. Ni also strongly partitions into olivine and therefore its variation is controlled, in part, by the distribution of olivine. Sulphur isotopic compositions within the gabbronoritic marginal rocks and olivine cumulates are well above the accepted values for mantle-derived sulphur (-2 to +2 per mil; Ripley & Li, 2003) and are comparable to those of the wall rocks, suggesting that the sulphur was derived from the adjacent crust. The δ34S values determined in this study are within the range of previous results from Sasaki (1969) for marginal zone (outer marginal zone δ34S = 4-10 per mil) and crustal rocks (western margin δ34S = 7-9 per mil).

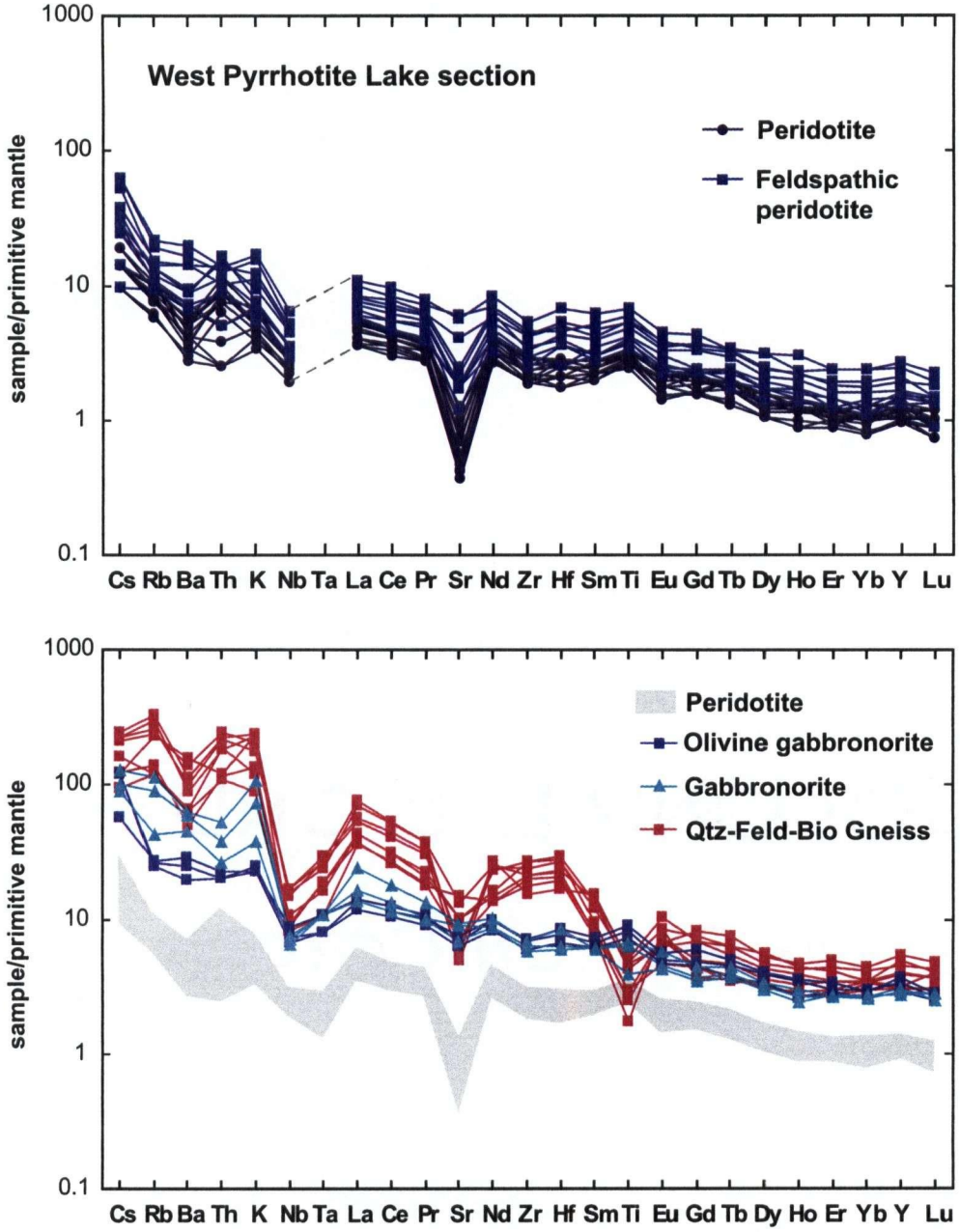

Fig. 2.12a: Primitive mantle-normalized trace element abundance patterns in the West Pyrrhotite Lake section of the Muskox intrusion. Elements are arranged, from right to left, in order of increasing incompatibility and normalizing values are from McDonough & Sun (1995). Tantalum abundances within peridotites are below detection limits and therefore are excluded. There is a progressive increase in the abundance of incompatible trace elements towards the margin. Both marginal zone and crustal rocks are relatively enriched in the most incompatible elements and have prominent Nb-Ta depletions. The gabbronoritic marginal rocks contain distinctly higher abundances of large ion lithophile elements, and La and Ce, than the overlying olivine gabbronorite, while the abundance of heavy rare earth elements remains relatively constant in both groups.

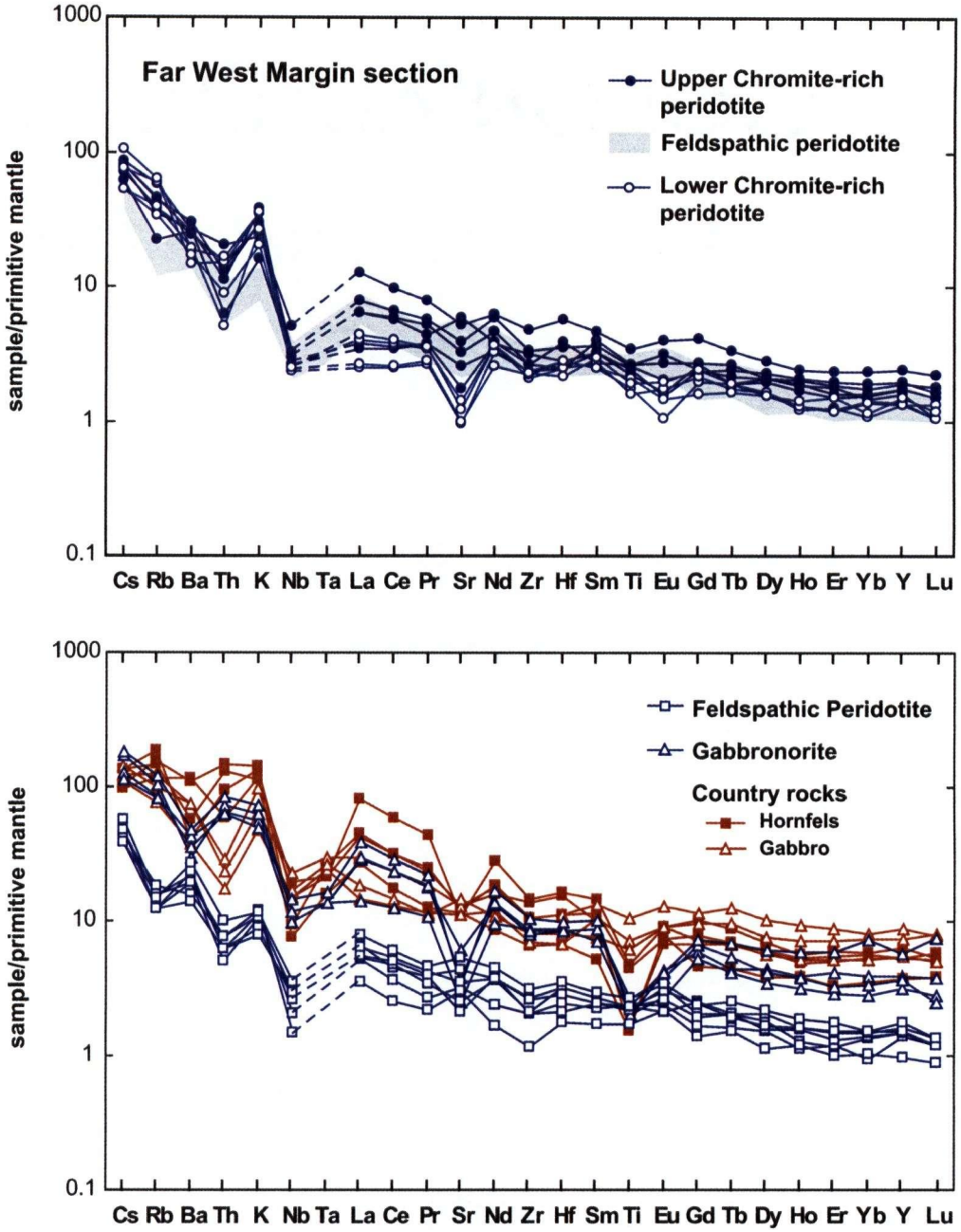

Fig. 2.12b: Primitive mantle-normalized trace element abundance patterns in the Far West Margin section of the Muskox intrusion. Elements are arranged, from right to left, in order of increasing incompatibility and normalizing values are from McDonough & Sun (1995). Tantalum abundances within peridotites are below detection limits and therefore are excluded. All peridotites have similar abundances of trace elements, but the chromite-rich peridotites have positive K anomalies which are likely related to the presence of secondary biotite. The gabbronoritic marginal rocks contain similar abundances of trace elements as the adjacent country rocks. The different country rocks have distinct incompatible trace element patterns, with the hornfelsed paragneiss and granitic pods being more enriched in incompatible elements than the gabbro. Paragneiss samples from other drill holes have similar enriched trace element patterns.

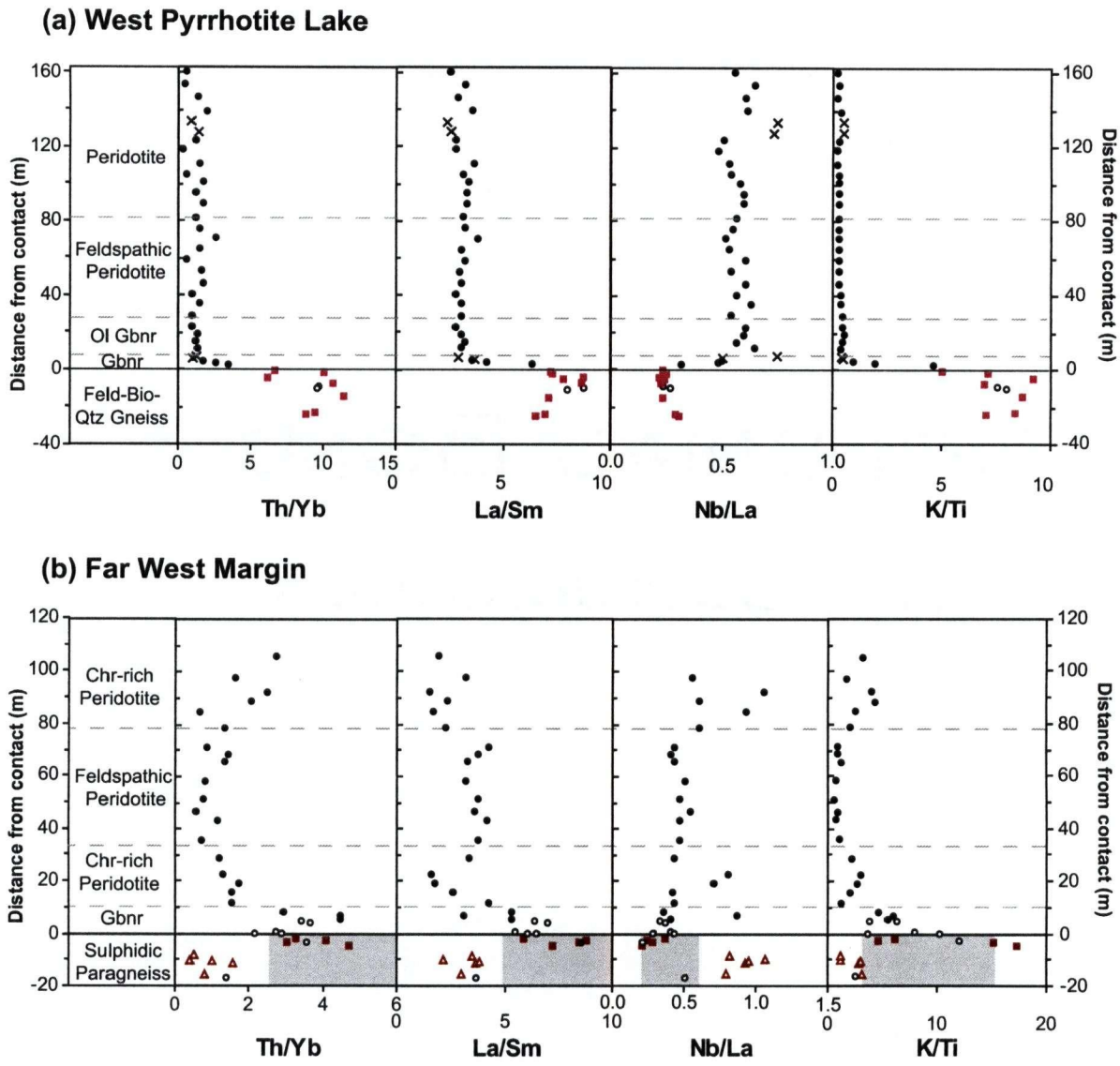

Fig. 2.13: Stratigraphic variations of incompatible trace element ratios for (a) West Pyrrhotite Lake and (b) Far West Margin. Symbols and abbreviations as in Fig. 2.8. The grey shaded region in the Far West Margin section represents the range of values from paragneiss samples collected in other drill holes at this location (unpublished data). Incompatible trace element ratios are not affected by olivine fractionation owing to the extremely small partition coefficients for trace elements in olivine (e.g. D_{REE} = <0.01). These ratios provide an index of crustal contamination, owing to the distinct compositions of crustal rocks compared to mantle-derived magmas. The shift in incompatible element ratios at the transition from peridotite to gabbronorite is consistent with a progressive increase in the amount of contamination within the outer ~10 metres of the intrusion. The chromite-rich peridotite samples have somewhat anomalous compositions (high Th/Yb, Nb/La, K/Ti, and low La/Sm) compared to those of the intervening feldspathic peridotite and the peridotites at West Pyrrhotite Lake, which may be the result of post-magmatic metasomatism. The gabbroic samples within the wall rock at Far West Margin have distinct Nb/La values from of the marginal zone rocks, which may indicate that the gabbroic body is unrelated to the Muskox intrusion.

abundances of trace elements, relatively enriched incompatible element patterns, and pronounced negative Nb-Ta anomalies in primitive mantle-normalized trace element diagrams (Fig. 2.12a). Incompatible element ratios are constant throughout the peridotites, indicating that the amount of enrichment in the most incompatible elements (Th/Yb, La/Sm, and K/Ti) and the magnitude of the Nb depletion (Nb/La) remain the same throughout most of the marginal zone (Fig. 2.13a).

The stratigraphic trends within the underlying gabbronoritic rocks show a continued and somewhat more pronounced decrease in MgO (18-12 wt %), Cr_2O_3 (0.3-0.05 wt %), and Ni (1460 to 550 ppm), and increase in Al_2O_3, LILE, and LREE towards the margin (Fig. 2.8-2.13). The stratigraphic trend of CaO, however, is reversed and progresses to lower values towards the contact (Fig. 2.8a). A similar reversal is observed for TiO_2 and HREE, while the trend of increasing SiO_2, Al_2O_3, K_2O, and Na_2O observed within the olivine cumulates continues through to the contact with the country rocks. Elevated Cu and S abundances occur within the gabbronorite as expected from the appearance of blebby sulphide (Fig. 2.11a). The $\delta^{34}S$ values from the sulphides within the gabbronorite are high compared to mantle-derived sulphur (-2 to + 2 ‰; Ripley, 1999; Ripley & Li, 2003) which indicates that sulphur was largely derived from a crustal source (Fig. 2.11a). The gabbronoritic rocks have enriched incompatible element patterns like those of the overlying peridotite. However the level of enrichment is considerably higher shown by relatively high La/Sm, Th/Yb and K/Ti values. This increased level of enrichment in the most incompatible elements is consistent with the incorporation of crustal material (Fig. 2.12 & 2.13). Similarly, the increased magnitude of the Nb-depletion (low Nb/La values) is likely also the result of crustal contamination.

As expected, the country rock gneisses at the West Pyrrhotite Lake section are highly evolved in composition, and contain higher abundances of Al_2O_3, Cu, S, and most incompatible trace elements, and lower abundances of MgO, Ni, CaO, Cr_2O_3, Ti and Sr than the intrusive rocks (Fig. 2.8a-2.11a). The quartz-rich rocks directly adjacent to the intrusion have typically lower abundances of Al_2O_3 (and K_2O, TiO_2) and incompatible trace elements, and higher abundances of CaO than the banded gneiss further from the contact (the abundance of MgO remains relatively constant). The country rocks have highly enriched trace element patterns and prominent negative Nb-Ta, Sr, and Ti anomalies (Fig. 2.12a & 2.13a).

2.5.2 Far West Margin

Unlike the systematic progression to more evolved composition towards the margin observed at the West Pyrrhotite lake section, the peridotites at Far West Margin are characterized by distinct reversals in major element trends (Fig. 2.8b). The chromite-rich peridotite horizons have high Cr_2O_3 contents (up to 4 wt %) and have relatively low CaO contents compared to the intervening feldspathic peridotite unit, which is consistent with the distribution of cumulus chromite and postcumulus plagioclase. Towards the base of the feldspathic peridotite unit the MgO content decreases progressively and CaO and Al_2O_3 contents increase, consistent with the observed distribution of cumulus olivine and intercumulus plagioclase. These trends have been traced for over 1 km towards the north in other drill holes. The Fo content of olivine within the feldspathic peridotite decrease towards the basal contact, analogous to that observed throughout the West Pyrrhotite Lake section (Fig. 2.9b). Unlike the olivine accumulation trend of the West Pyrrhotite Lake section, the geochemical variation of the peridotites at the Far West Margin is likely controlled by the accumulation/fractionation of olivine, orthopyroxene, and chromite (Fig. 2.10b). Elevated Cu and Ni contents within peridotites occur in three separate horizons and are coincident with elevated S contents (Fig. 2.11b). Sulphur isotopic compositions of sulphide within the peridotites are within the range of those for sulphides within the layered series (+3 to + 7 ‰; Sasaki, 1969). The peridotites have enriched incompatible trace element patterns and variably negative Nb anomalies (Fig. 2.12b). The chromite-rich horizons have positive K anomalies, which are interpreted to be the result of metasomatism as manifested by the appearance of secondary biotite (Fig. 2.13b).

The gabbronoritic rocks at the Far West Margin are variably sulphide-mineralized and therefore the chemical trends across this zone are irregular. The relatively unmineralized (<5 wt % S) samples have relatively low MgO (19-22 wt %), CaO (1-5 wt %), and Cr_2O_3 contents and high incompatible trace element abundances compared to the overlying peridotites, which is analogous to the variation previously described within the contact region at the West Pyrrhotite Lake section (Fig. 2.8). The mineralized samples, as expected, have elevated Ni, Cu, and S contents (Fig. 2.11). Sulphur isotopic compositions of sulphide within the gabbronoritic rocks are shifted from those of the overlying peridotite-hosted sulphide towards the compositions of the adjacent wall rocks. As with the West Pyrrhotite Lake section, the gabbronoritic rocks have elevated La/Sm, Th/Yb, and K/Ti values compared to the overlying peridotites, suggesting that they crystallized from a hybrid magma (Fig. 2.12).

As expected from their lithologic variations, the country rocks at Far West Margin are variable in composition and contain relatively low abundances of MgO and CaO, and high abundances of SiO_2, Al_2O_3, and incompatible trace elements compared to the marginal zone rocks (Fig. 2.8b). The fine-grained hornfelsed sediments, granitic lenses, and paragneiss samples have high Th/Yb, La/Sm, and K/Ti values, and low Nb/La values, similar to the country rocks at West Pyrrhotite Lake (Fig. 2.13b). The gabbroic wall rocks are chemically distinct from the other country rocks and have low Th/Yb, La/Sm, and K/Ti and high Nb/La values.

2.6 DISCUSSION

Although there are some distinct differences in the mineralogical and chemical variations between the two studied sections, the marginal zone of the Muskox intrusion broadly consists of an upper peridotite subzone (including peridotite, feldspathic peridotite, chromite-rich peridotite, and/or olivine gabbronorite), within which there is an overall increase in the abundance of postcumulus minerals towards the base, and a lower gabbronorite subzone that contains variable amounts of granophyre and sulphide. Sulphide is significantly more abundant at the Far West Margin, which is likely related to the presence of the variably sulphidic paragneiss forming the wall rock at this location. The trace element and sulphur isotopic compositions of the gabbronoritic marginal zone rocks clearly indicate that they have incorporated crustal material, whereas the compositional variations within the overlying peridotites appear to be primarily related to variable proportions of cumulus and postcumulus phases. Below, we examine the relationship between crustal contamination and sulphide mineralization within the gabbronoritic marginal rocks at the two studied regions, which provides important constraints on the potential for forming sulphide mineralization throughout the marginal zone of the Muskox intrusion. We then present a conceptual framework for the formation of the peridotite part of the marginal zone involving the accumulation and compaction of a cumulate pile during cooling through the base of the intrusion. To investigate the role of compaction in producing the observed mineralogical and chemical variation observed in the marginal zone, we use the forward modelling capabilities of IRIDIUM (Boudreau, 2003). Finally, we address the implications for the formation of the marginal zone throughout the evolution of the Muskox chamber, and the formation of similar features at the base of other mafic and ultramafic intrusive bodies.

2.6.1 Crustal contamination and sulphide mineralization within the gabbronorite subzone

Crustal contamination is an important process by which a basaltic magma can become saturated with respect to sulphide and is a key factor in the genesis of many Ni-Cu-PGE sulphide deposits (e.g. Keays, 1995; Naldrett, 1997; Mavrogenes & O'Neill, 1999; Lesher et al., 2001; Naldrett, 2004). Sulphide saturation can be initiated through high degrees of fractional crystallization, magma mixing, and/or assimilation of both crustal sulphur and silica (e.g. Li & Naldrett, 1993; Li & Ripley, 2005). The occurrence of sulphide mineralization at the base of the marginal zone of the Muskox intrusion is undoubtedly related to the interaction between basaltic magma within the chamber and the adjacent country rocks. Below, we investigate the genetic link between crustal contamination and the presence of variable amounts of sulphide within the gabbronoritic rocks at the two studied sections. In Chapter 3, the degree of contamination recorded within the marginal rocks and the potential influence of contamination on parental magma composition prior to emplacement within the Muskox chamber (e.g. Nb-Ta depletion in peridotites) will be addressed.

The shift in incompatible trace element ratios (e.g. Th/Yb, La/Sm, Nb/La, K/Ti) at the base of the marginal zone at both sections indicates that the effect of crustal contamination by the adjacent wall rocks is restricted to the thin zone (<10 m) of gabbronoritic rocks directly adjacent to the contact (Fig. 2.13). This change in incompatible element ratios coincides with the physical appearance of granophyre, which records the addition of partial melts derived through melting of the adjacent wall rocks (Fig. 2.6), and euhedral orthopyroxene, which likely formed from relatively silica-rich hybrid magmas along the outer wall of the intrusion. This limited spatial extent of contamination was also observed by Francis (1994) along the eastern margin of the intrusion and indicates that the thickness of the contaminated zone remains relatively constant throughout the intrusion. The sulphur isotopic compositions of sulphide at the Far West Margin also shift towards more crustal values within the outer 10-15 m of the marginal zone (Fig. 2.11b). As shown in Fig. 2.14, the gabbronoritic rocks at the two studied sections have distinct incompatible trace element ratios that trend towards those of the adjacent host rocks, clearly indicating that the contaminant was locally derived. From the overlapping incompatible trace element ratios between the gabbronorite at the Far West Margin and the adjacent wall rocks, it appears that a significant amount of the host paragneiss

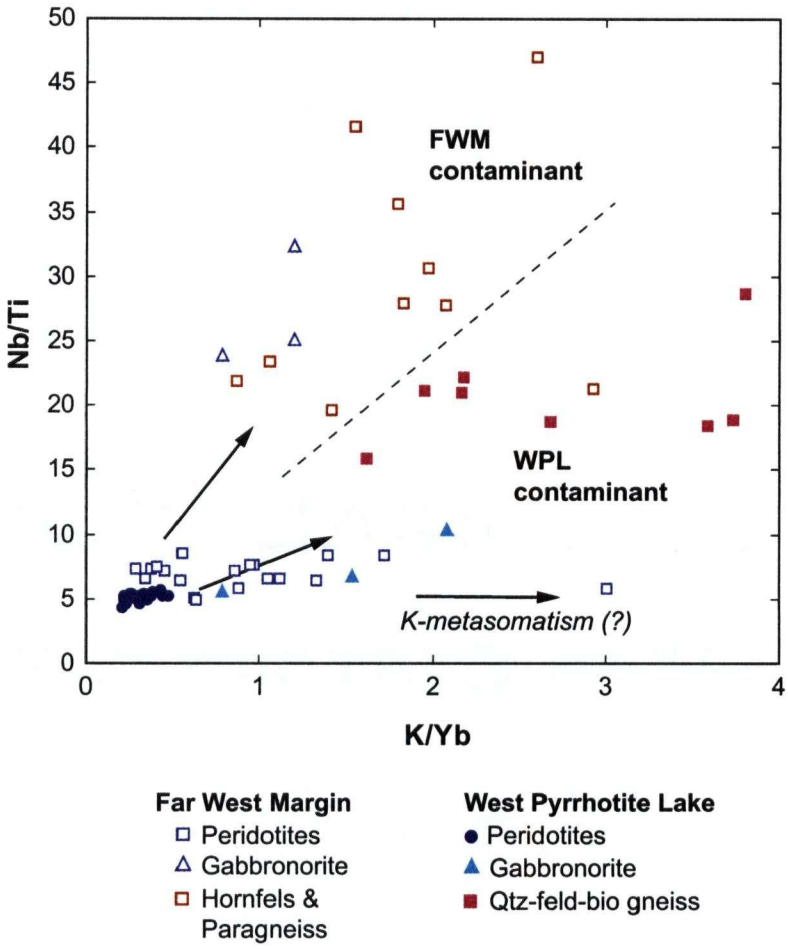

Fig. 2.14: Incompatible trace element ratio diagram (K/Yb vs. Nb/Ti) for marginal zone rocks and adjacent crustal rocks used to discriminate between the chemical effects of contamination and alteration. Nb/Ti is used because they are both high field strength elements and are considered to be relatively immobile during alteration, whereas K/Yb is sensitive to both crustal contamination and alteration effects. Both ratios are not greatly affected by olivine fractionation as demonstrated by the tight cluster formed by the peridotites at West Pyrrhotite Lake despite the 20 wt % change in MgO content. Paragneiss includes samples from both MX03-001and MX03-002 drill holes at the Far West Margin section. The gabbronoritic marginal rocks at each section have distinct compositions that plot towards those of the respective country rocks. This feature is consistent with crustal contamination and suggests that the contaminant was locally derived. Given the scatter of the country rock compositions and the fact that the actual composition of the contaminant is unknown, curvilinear mixing trends have not been included. The chromite-rich peridotites form a horizontal trend towards high K/Yb values which, given the appearance of secondary biotite in these samples, is consistent with the effects of K-metasomatism.

was assimilated at this location. In contrast, the progressive and subtle shift in incompatible trace element ratios at West Pyrrhotite Lake indicates that only minor amounts of the quartz-feldspar-biotite gneiss were incorporated into the magma along the outer wall of the chamber. Sasaki (1969) showed that the sulphur isotopic compositions of sulphides within the outer 50 m of the marginal zone of the Muskox intrusion correlate with those of the adjacent wall rocks, and suggested that the addition of sulphur was also a local phenomenon. The anomalous trace element ratios of the chromite-rich peridotites at the Far West Margin (high K/Ti and Th/Yb; Fig. 2.13) correlate with the appearance of secondary biotite, suggesting that this signature is likely related to alteration/metasomatism as opposed to contamination (Fig. 2.14). We propose that this limited extent and local nature of contamination is likely the result of rapid cooling and solidification of a thin hybrid zone along the outer wall of the intrusion. Rapid solidification of this zone would have effectively prevented overlying magmas from interacting with the surrounding crustal rocks, resulting in the uncontaminated signatures of the overlying peridotites. It is important to note that the contaminated gabbronorite may not be present everywhere within the upper part of the intrusion (Smith, 1962). This indicates that this thin boundary zone may have been locally resorbed, or eroded during active convection within the chamber early in its history, as proposed by Francis (1994), or during subsequent periods of magma replenishment.

The presence of sulphide within the contaminated gabbronorite at both studied sections indicates that the magmas along the outer wall of the chamber became sulphide-saturated. Because of the local nature of the contamination, we might expect that the abundance of sulphide produced was controlled by the availability of sulphur within the adjacent wall rocks. The formation of relatively abundant sulphide at the Far West Margin may reflect the assimilation of a large amount of the host paragneiss, which through the addition of silica and sulphur promoted sulphide saturation in the magma directly adjacent to the contact. The lack of sulphide at West Pyrrhotite Lake appears to reflect the limited ability of the magma to assimilate large quantities of the country rock at this location. This limited interaction resulted in only minor incorporation of crustal sulphur and consequently a relatively small amount of sulphide liquid was produced, represented by the appearance of only minor pyrrhotite blebs within the gabbronorite at this location.

Rapid solidification of the contaminated magmas adjacent to the contact may have prevented segregated sulphide droplets from interacting with large volumes of magma, which

would have a significant affect on the metal content of the sulphides. The metal content of sulphide (i.e. Ni-Cu-PGE tenor) is strongly controlled by the mass ratio between a silicate magma and a coexisting sulphide liquid that it can equilibrate with (R-factor; Campbell and Naldrett, 1979; Lesher & Burnham, 1999). The physical mechanics behind this interaction are still imperfectly understood, however this relationship can be effectively used to compare the composition of sulphide ores found within and between different intrusions (e.g. Barnes & Francis, 1995; Barnes et al. 1997; Theriault et al. 1997; Lesher et al., 2001). For example, the metal contents in 100% sulphide within gabbronoritic rocks at the Far West Margin are relatively low with Ni_{100} = 1.0 wt % and Cu_{100} = 1.0 wt % (calculation procedure described in detail in Chapter 4). As will be shown in Chapter 4, this is typical of marginal zone sulphide in the Muskox intrusion. These low metal contents indicate that the sulphide in the gabbronoritic rocks formed at low R-factors (~100). Such low values are likely the combined result of the addition of relatively large amounts of sulphur from the host paragneiss and the overall small volume of silicate magma the segregated sulphides interacted with, subsequently preserved as a thin contaminated horizon at the base of the marginal zone. This indicates that the typical marginal zone environment (i.e. relatively rapid solidification of the thin contaminated zone) is not optimal for formation of significant quantities of metal-rich sulphide.

Sulphide is also observed within the two chromite-rich peridotite and feldspathic peridotite horizons at the Far West Margin. The sulphur isotopic composition of sulphide within the lower chromite-rich peridotite is equivalent to that of underlying gabbronorite and adjacent wall rocks suggesting that sulphur was externally derived (Fig. 2.11b). The anomalous trace element ratios of this horizon are considered to reflect alteration (Fig. 2.14), and thus the relatively high $\delta^{34}S$ values may indicate that the sulphides migrated upwards (10-15 m) from the underlying gabbronorite zone owing to the high mobility of sulphide liquids (Mungall, 2002). Alternatively, the addition of crustal sulphur may have been decoupled from the addition of silicate material, which would result in only high $\delta^{34}S$ values. The sulphur isotopic compositions of sulphides from the upper chromite-rich horizon and feldspathic peridotite ($\delta^{34}S$ = +6‰) are distinct from those within the underlying rocks and are within the range of values documented throughout the layered series ($\delta^{34}S$ = +3 to +7 ‰; Sasaki, 1969) suggesting that the addition of crustal sulphur from the adjacent wall rocks was minimal. The occurrence of relatively thin disseminated sulphide horizons associated with olivine that has

low Ni contents (Fig. 2.9) suggests that sulphide saturation occurred locally during *in situ* crystallization of olivine (e.g. Li & Naldrett, 1999; Li et al., 2002). The relatively high $\delta^{34}S$ values of the sulphide within these peridotites ($\delta^{34}S$ = +6) compared to those estimated for mantle-derived sulphur ($\delta^{34}S$ = -2 to +2; Ripley, 1999) may indicate that crustal sulphur was added to the parental magmas prior to emplacement within the Muskox chamber. Thus, the sulphides within the peridotite appear to have formed by a distinct mechanism from the sulphides within the underlying gabbronorite and lower chromite-rich peridotite.

2.6.2 Compaction and thermal evolution in the peridotite subzone of the marginal zone

Compaction is an important process in the textural and compositional evolution of mafic-ultramafic flows, sills, and layered intrusions (e.g. Irvine, 1980; Shirley, 1987; Meurer & Boudreau, 1996; Tharp et al., 1998; Meurer & Boudreau, 1998a; 1998b; Boudreau & Philpotts, 2002). Layered mafic-ultramafic intrusions can be considered to form through the effective removal and accumulation of dense crystals (olivine, chromite, pyroxene) at the base of a magma chamber, and may be constructed by repeated injections of crystal-bearing magmas (e.g. Raedeke & McCallum, 1984; Marsh, 2000). The accumulated crystals initially build a cumulate pile composed of cumulus mineral grains and evolved interstitial melt (with 50-60 vol % porosity; Irvine, 1980; Shirley, 1986; Tharp et al., 1998). Given the relatively high density contrast between olivine and pyroxene (3.2-3.5 g/cm^3) and basaltic liquids (~2.7 g/cm^3), compaction within the consolidating cumulate pile will aid in the differentiation process by forcing relatively buoyant interstitial melt upward through the pile. Below, we examine the role of compaction within a temperature gradient along the base of an intrusion in producing the downward differentiation trend within the marginal zone of the Muskox intrusion, a mechanism that has been previously explored for the formation of the overlying layered series by Irvine (1980) and Tharp et al. (1998).

As described earlier, the proportion of postcumulus phases within the marginal zone progressively increases towards the basal margin of the intrusion (~20 vol % to 50 vol %), which corresponds to a systematic decrease in MgO (a proxy for olivine abundance) and increase in Al_2O_3 (a proxy for the abundance of postcumulus plagioclase) and other elements not compatible in olivine (Fig. 2.8). This trend is observed throughout the peridotites of the West Pyrrhotite Lake section and the feldspathic peridotite at the Far West Margin section, and is consistent with the mineralogy of marginal zone rocks throughout most of the intrusion as

originally mapped by Smith (1962). This distribution of postcumulus material can be explained by the crystallization of varying amounts of intercumulus liquid during compaction of the cumulate pile and cooling through the base of the intrusion. In the relatively rapidly cooled region near the margin of the intrusion, significant quantities of intercumulus liquid crystallized, whereas in the more slowly cooled interior of the intrusion, compaction forced intercumulus liquid to percolate upwards through the cumulate pile before it could crystallize (see modeling below).

The majority of the layered series of the Muskox intrusion is composed of olivine cumulates with 7-10 vol % postcumulus phases (Irvine, 1980), whereas the marginal zone peridotites can contain up to 50 vol % postcumulus phases as noted above. Tharp et al. (1998) successfully modeled this distribution of postcumulus material in the Muskox intrusion, including the combined effects of compaction, porous medium flow, thermal conduction, advection of heat, and crystallization. In their model, compaction involved both grain boundary diffusion creep and power law creep, which allowed for compaction to be monitored from initial deposition (50-60% porosity) to nearly zero porosity. The fractions of liquid and crystalline phases were calculated during cooling and fractional crystallization using MELTS (Ghiorso & Sack, 1995). Their results indicated that rapid cooling at the upper and lower boundaries resulted in reduced compaction (i.e. high proportion of crystallized interstitial liquid) due to the conduction of heat to the bounding wall rocks. Based on the available petrographic and geochemical information on the marginal zone (unpublished data for the GSC South drill hole summarized in graphical form in Irvine, 1980), Tharp et al. (1998) proposed that this interplay between compaction and cooling could also potentially explain the progressive increase in the amount of postcumulus material within the marginal zone of the Muskox intrusion.

To address the extent to which a compaction process can explain the range of mineralogical and geochemical variations observed within the marginal zone peridotites in this study, we have used the forward modeling capabilities of IRIDIUM (Boudreau, 2003). The IRIDIUM program combines a mineral-liquid equilibration routine based on the free energy minimization techniques used in the MELTS program (Ghiorso & Sack, 1995), with the 1-dimensional mass and heat transport equations of Mackenzie (1984) as implemented by Shirley (1986) to quantitatively model compaction within crystal-liquid mixtures (Boudreau, 2003). Detailed descriptions of the program operation are given in Boudreau and Philpotts

(2002) and Boudreau (2003) and will only be briefly summarized below. The program assumes that during compaction, the bottom is closed to mass transfer and the overlying assemblage compacts under its own weight. The initial conditions (temperature, pressure, and bulk composition) are specified by the user for each node (i.e. height) in the system and the program calculates the equilibrium mineral-liquid assemblage and various physical parameters (including heat capacity, enthalpy, and liquid viscosity). The program calculates new equilibrium mineral-liquid assemblages at each node after some change in the bulk composition resulting from advection and diffusion of heat and mass during compaction at successive time-steps. IRIDIUM, unlike the model of Tharp et al. (1998), does not explicitly deal with grain boundary or power law creep, but instead the deformation of the solid matrix is approximated using a term for the effective viscosity of the matrix (assumed constant at 5 x 10^{11} Pa s; Shirley, 1986). Given that we are not attempting to produce results below liquid fractions of 10% this difference likely does not affect our results. The boundary conditions are also different in these two models: the Tharp et al. (1998) model assigns specific thermal conductivities and initial temperatures for the bounding wall rocks, whereas IRIDIUM simulates conduction by progressively decreasing the temperature of the bottom and/or top nodes. Our purpose is not to compare in detail the results generated by these different numerical models, but instead is to provide constraints on the role of compaction in producing the observed chemical variations within the marginal zone of the Muskox intrusion.

The compaction parameters used (e.g. solid viscosity and permeability constant) are those from Shirley (1987) with the exception of cumulus mineral grain size, which in the case of the outermost marginal zone rocks of the Muskox intrusion is ~0.05 cm. An olivine gabbronorite from the base of the peridotite subzone at the West Pyrrhotite Lake section (Sample 71133: MgO = 22 wt %) was used as the bulk starting composition. This sample does not represent a liquid composition, but is used to construct a cumulate pile containing olivine and fractionated liquid (justification given below). The pressure was set at 1000 bars which is consistent with estimates for emplacement depth of the intrusion (Irvine, 1980; Tharp et al. 1998). The initial temperature of the system and the porosity of the cumulate pile were defined at 1200°C and 50 vol %, respectively. Based on these parameters, IRIDIUM constructed a cumulate pile composed of olivine and interstitial liquid, and an overlying liquid layer (see below). To simulate heat conducted to the underlying host rocks we incrementally decreased the temperature of the bottom node from 1200°C to 400°C at a specified rate (e.g.

0.01°C/day; ~220 yr cooling interval). The upper boundary was kept at a relatively high temperature (1200°C to 1000°C), which is justified by the fact that the upper boundary would have been separated from the roof rocks by a continually building cumulate pile (Tharp et al., 1998).

The olivine gabbronorite used as the bulk starting composition occurs at the base of the West Pyrrhotite Lake section and is composed of cumulus olivine (40-50 vol %) and postcumulus plagioclase and pyroxene. We consider this to represent a mixture of accumulated olivine and fractionated intercumulus liquid that approximates the initial cumulate pile prior to, or at the early stages of compaction (i.e. contains a high proportion of crystallized intercumulus liquid), as proposed by Irvine (1980). Support for using this starting composition comes from examining the composition of the interstitial liquid within the initial cumulate pile constructed at the beginning of the IRIDIUM run. Under the present conditions, the interstitial liquid contains ~7.5 wt % MgO. Using MELTS (Ghiorso & Sack, 1995), this MgO content is comparable to a residual liquid formed after ~15% fractional crystallization of olivine from an estimated primary magma composition for the Muskox intrusion (Irvine, 1977b), and thus indeed represents a fractionated composition expected within a cumulate pile.

The mineralogical and chemical changes during an IRIDIUM simulation are summarized in Fig. 2.15. The initial state of the system (1200°C throughout) contained a 180 m-thick cumulate pile composed of olivine, spinel, and interstitial liquid (~7.5 wt % MgO), and an overlying 20 m-thick liquid layer (Fig. 2.15). As the temperature was decreased at the base of the column (i.e. simulating the conduction of heat to the underlying wall rocks), plagioclase and clinopyroxene, and then orthopyroxene, began to crystallize, and the lower 5 m of the pile became almost completely solidified within 15 years (Fig. 2.15). Within the hotter interior, the cumulate pile had already begun to compact and the solid components moved downwards relative to the surrounding interstitial liquid, as demonstrated by a decrease in modal olivine abundance within the upper portion of the column. The increase in the amount of olivine near the base is due to both compaction and crystallization. During continued cooling, compaction proceeded to force liquid upwards within the hotter interior, whereas the liquid at the bottom of the column crystallized before it could be expelled due to the thermal gradient that had developed. After 130 years, during which time the temperature of the bottom node decreased from 1200°C to 500°C, the thickness of the solidified zone (<10 % liquid remaining) increased to 90 m (Fig. 2.15b). At this point the model simulation was

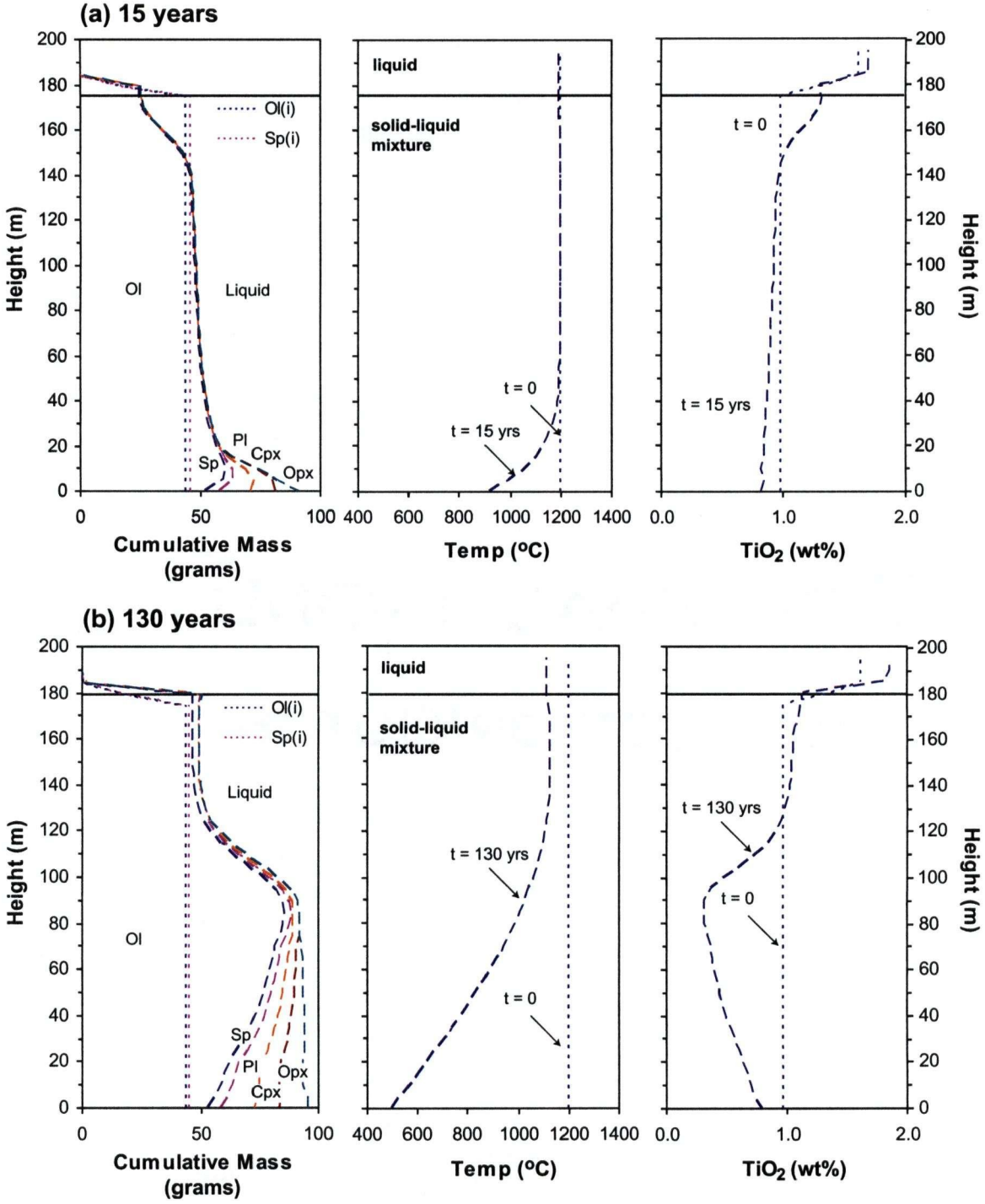

Fig. 2.15: IRIDIUM results comparing the initial state of the system and that after (a) 15 years and (b) 130 years, using an initial porosity of 60% and a bottom cooling rate of 0.05 °C/day. Reported results are the cumulate mass of crystallized phases, the temperature profiles, and bulk TiO2 (wt %). The initial state of the system (dotted line) is at constant temperature and contains a ~20 m-thick liquid layer and an underlying ~180 m-thick cumulate pile with olivine and spinel. An olivine gabbronorite sample (71133) from the West Pyrrhotite Lake section was used as the bulk starting composition. See text for discussion.

halted because under the present setup conditions the temperature within the upper part of the system remained too high for crystallization to proceed. The competition between liquid expulsion during compaction and crystallization of interstitial liquid during cooling resulted in an upward increase in the amount of olivine and a corresponding decrease in the abundance of plagioclase and pyroxene. This variation is analogous to that observed in the marginal zone peridotites of the Muskox intrusion.

The final chemical profiles predicted by a number of different IRIDIUM simulations are compared to the observed profile in the peridotites at West Pyrrhotite Lake in Fig. 2.16 for Al_2O_3, TiO_2, and CaO (measure the of abundance of crystallized interstitial liquid) and MgO (measure of the abundance of olivine). Only the solidified portion (<10 % liquid remaining) at the base of the column for each simulation is shown. The simulations were completed at different initial porosities (50% and 60%) and bottom cooling rates (0.05°C/day and 0.1°C/day) to asses their effect on the final compositional profiles. All simulations reproduced the overall downward differentiation trend observed within the marginal zone (Fig. 2.16). As expected, the compositional profiles change depending on the values for initial porosity and bottom cooling rate, which can be described in terms of the proportion of liquid that crystallized at the base of the column before it can percolate upwards through the cumulate pile. By either decreasing the porosity or increasing the cooling rate, relatively high proportions of liquid crystallize at the base of the column. Increasing only one of these parameters affects the overall curvature of the profile, because this influences the height within the column where significant compaction occurs. This is apparent from the crossover points A and B shown in Fig. 2.16. Increasing only the initial porosity results in an increased amount of crystallization at the base, but due to the high porosity, compaction occurs more rapidly and therefore the site of compaction is relatively close to the bottom. Conversely at low initial porosities, the amount of crystallization at the base is limited and compaction occurs higher up in the column. This trade-off results in the crossover observed between the profiles for simulations with 50% and 60% porosity at approximately 30 m from the base (point A; Fig. 2.16). The effect of changing only the cooling rate results in a similar crossover that occurs higher up in the column at point B.

The IRIDIUM results confirm that cumulate pile compaction during cooling through the base of the intrusion can explain the overall mineralogical and chemical trends observed in the peridotite subzone of marginal zone of the Muskox intrusion, a mechanism originally

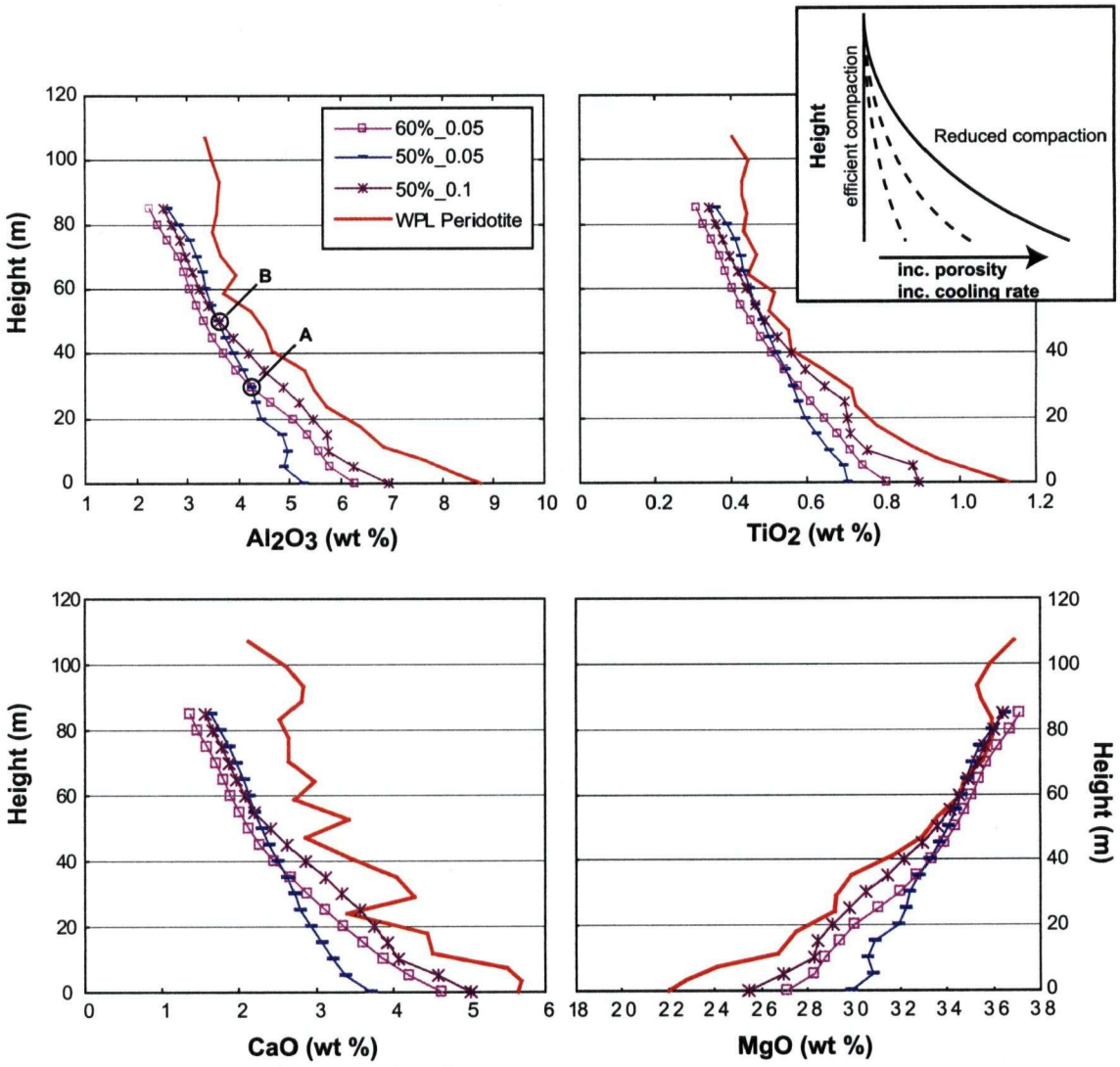

Fig. 2.16: Comparison of bulk chemical profiles for Al_2O_3, TiO_2, CaO, and MgO at the end of different IRIDIUM simulations to those observed at the West Pyrrhotite Lake section. Adjusted parameters are initial porosity (50-60%) and cooling rate (0.05-0.1°C). The 60% porosity simulation is that summarized in Fig. 2.15. The inset shows schematically the effect of changing different parameters. See text for discussion.

proposed by Irvine (1980) and evaluated by Tharp et al. (1998). As expected, the final compositional profile varies as a function of initial porosity of the cumulate pile and bottom cooling rate (Fig. 2.16). We would also expect that if solidification occurred during accumulation, the proportion of crystallized interstitial liquid along the lower contact would be higher than that in the model simulations, and would therefore result in a significantly more exaggerated (curved) chemical profile. In addition, if heat loss occurred both from the top and bottom we would expect more vertical chemical profiles. Increased loading from a thicker cumulate pile would likely enhance compaction and result in a lower proportion of crystallized interstitial liquid at the base than that observed in the model simulations. Thus, it is possible to produce a wide range of compositional profiles.

2.6.3 Implications for the formation of the marginal zone of the Muskox intrusion and the basal margins of other mafic-ultramafic intrusions

A number of additional constraints on the formation of the marginal zone of the Muskox magma chamber can be made based on the results presented in this study. Firstly, the solidification of varying amounts of intercumulus liquid with distance from the base of the marginal zone may also explain the systematic decrease in the forsterite content of olivine observed in peridotites at West Pyrrhotite Lake and the feldspathic peridotite at the Far West Margin section of the Muskox intrusion. Several studies (e.g. Barnes, 1986; Chalokwu & Grant, 1987; Grant & Chalokwu, 1992) have shown that the cumulus minerals in mafic-ultramafic intrusions may re-equilibrate with the surrounding fractionated intercumulus liquid during cooling. This results in a shift towards more evolved mineral compositions (i.e. re-equilibrated olivine is more Fe-rich); the higher the proportion of intercumulus liquid present, the higher the magnitude of this shift. Barnes (1986) demonstrated that the composition of olivine within an olivine cumulate with ~10% intercumulus liquid will show a 2 mol % shift, whereas an olivine cumulate with ~50% intercumulus liquid will show a 5-7 mol % shift. This magnitude of shift in the composition of olivine and variation in amount of interstitial liquid is comparable to that observed for the olivine cumulates at West Pyrrhotite Lake (Fig. 2.9). The Ni content of olivine is relatively unaffected during re-equilibration as a result of the low Ni abundance within the intercumulus liquid, which may explain the relatively constant Ni content of olivine within the peridotites at the West Pyrrhotite Lake section (Fig. 2.9). This re-equilibration process must be a relatively rapid process (e.g. Cawthorn et al., 1992)

considering that it is recorded in mineral grains within a few metres from the basal contact of the Muskox intrusion, which would have undoubtedly solidified soon after emplacement.

The distinct mineralogical and chemical characteristics of the peridotites at the West Pyrrhotite Lake and Far West Margin demonstrate that the character of the marginal zone changes at different positions within the intrusion. Because the compaction model is mainly temperature-controlled, the change in the character of the marginal zone may reflect changes in the minerals that accumulated at different stages during the emplacement of the Muskox intrusion (i.e. the entire marginal zone of the Muskox intrusion was likely not formed from a single, early magma injection). In particular, chromite becomes an important phase within the upper part of the layered series (Fig. 2.4; Smith, 1962; Findlay & Smith, 1965; Irvine & Smith, 1969), which broadly correlates with the appearance of chromite within the marginal zone at the Far West Margin section. In addition, the peridotites at the Far West Margin contain coarse-grained olivine which has only been documented within the upper part of the layered series (Irvine & Smith, 1969). These features suggest that the marginal zone formed at different stages during the evolution (growth) of the Muskox magma chamber and may represent, in part, a lateral extension of the rocks within the layered series.

Changes in the thermal conditions during evolution of the chamber could also have had an impact on the formation of the marginal zone. The initial magmas introduced into the Muskox chamber would have been in contact with relatively cool country rocks, whereas later magmas would have been emplaced into rocks that were progressively heated by previous magma inputs. This would affect the cooling rate along the outer walls of the chamber during the later stages of its evolution, which could produce a more subdued downward trend in differentiation across the marginal zone. It is important to note that the GSC South drill hole intersected two individual downward differentiation cycles in the marginal zone (Fig. 2.3). We speculate that each of these cycles could represent the minerals separated and crystallized from two different magma injections, both of which cooled through the base of the intrusion and contain the predicted downward increase in postcumulus material.

The downward trends in the proportion of postcumulus material and cumulus mineral compositions observed within the marginal zone peridotites in the two studied sections are not unique to the Muskox intrusion. Similar trends are observed along the basal margins of other mafic-ultramafic layered intrusions (e.g. Great Dyke, Zimbabwe, Wilson, 1982; Stillwater complex, Montana, Raedeke & McCallum, 1984), and troctolititc intrusions (e.g. Partridge

River intrusion in the Duluth complex, Minnesota; Grant & Chalokwu, 1992). Thus, compaction may well have played an important role in generating the mineralogical and chemical variations at the base of these other bodies that formed from compositionally distinct parental magmas from that of the Muskox intrusion.

Finally, Latypov (2003) recently proposed that the reversal in differentiation trends at the base of many mafic-ultramafic intrusions and layered intrusions is produced through the diffusion of components within magma along the outer wall of a chamber owing to the presence of a steep thermal gradient across the contact region (Soret diffusion). The main evidence presented by Latypov (2003) against any gravitational mechanism for the formation of marginal zone reversals was that marginal zones are apparently "mirror images" of the overlying layered series with respect to their order of crystallization. According to this proposal, the marginal zone of the Muskox intrusion should record the crystallization sequence preserved within the overlying layered series, which throughout most of the intrusion is olivine-clinopyroxene-plagioclase-orthopyroxene (Fig. 2.3). This progression is not observed within the marginal zone of the Muskox intrusion, and in addition the appearance of cumulus pyroxene (mainly orthopyroxene and minor clinopyroxene) occurs only within the contaminated zone along the outer contact, which has a consolidation history distinct from that of the overlying peridotite subzone of the marginal zone as documented in this study. Strong mineralogical and chemical variations within the marginal zone of the Muskox intrusion mainly occur within a section of olivine cumulates that were isolated physically and geochemically from the underlying crustal rocks by a thin contaminated gabbronorite subzone, and can be appropriately explained by the re-distribution of intercumulus liquid during compaction of a dense cumulate pile during rapid cooling through the base of the intrusion.

2.7 CONCLUSIONS

This detailed petrographic and geochemical study of marginal zone rocks at stratigraphically low (West Pyrrhotite Lake) and high (Far West Margin) positions within the large Muskox layered mafic-ultramafic intrusion reveals that the marginal rocks consist of two distinct parts, a lower gabbronorite subzone and an upper peridotite subzone. The gabbronoritic rocks at the base of the marginal zone crystallized from magmas that were contaminated by partial melts derived from the directly adjacent wall rocks. Rapid solidification of this contaminated zone prevented overlying magmas from interacting with the surrounding crustal rocks, such that the overlying peridotites crystallized from relatively uncontaminated magma. The addition of sulphur and silica to magmas along the outer wall of the chamber promoted local sulphide saturation, however rapid cooling of the thin contaminated zone inhibited segregated sulphide from interacting with large volumes of magma and therefore resulted in metal-poor sulphides. The mineralogical and geochemical variations within the marginal zone peridotites were successfully modeled with the IRIDIUM software and are the result of crystallization of varying amounts of intercumulus liquid during compaction within a thermal gradient at the base of the magma chamber. The distinct mineralogical and geochemical variations observed at the two studied sections correlate with changes in the accumulated minerals within the layered series, indicating that the marginal zone of the Muskox intrusion formed throughout the evolution of the Muskox chamber rather than representing a single initial magma injection. This interplay between the expulsion of interstitial liquid during accumulation and compaction, and solidification of interstitial liquid as a result of cooling through the base of the chamber, likely played an important role in the formation of downward differentiation trends in the basal margins of other mafic-ultramafic bodies.

2.8 ACKNOWLEDGEMENTS

This project would not have been possible without the assistance of Gary De Schutter (Senior Project Geologist, Anglo American Exploration Canada Ltd. (AAEC)) during AAEC summer and winter drill programs on the Muskox intrusion in 2003 and 2004. The author would also like to thank Nathan Rand for his help with sample collection. Mati Raudsep and Elisabetta Pani are thanked for their support in the SEM/Electron microprobe facility at the University of British Columbia. RAM was supported by an NSERC Industrial Postgraduate Scholarship (IPS). Funding for this research was provided by Anglo American Exploration Ltd. (Canada), by a Collaborative Research Development (CRD) grant from NSERC and AAEC, and by an NSERC Discovery Grant to JSS.

2.9 REFERENCES

Baragar, W.R.A. (1969). The Geochemistry of the Coppermine River Basalts. *Geological Survey of Canada Paper* **69-44**, 43 pp.

Baragar, W.R.A., Ernst, R.E., Hulbert, L. & Peterson, T. (1996). Longitudinal petrochemical variation in the Mackenzie dike swarm, Northwestern Canadian Shield. *Journal of Petrology* **37-2**, 317–359.

Barnes, S.J. (1986). The effect of trapped liquid crystallization on cumulus mineral compositions in layered intrusions. *Contributions to Mineralogy and Petrology* **93**, 524-531.

Barnes, S.J. & Francis, D. (1995). The distribution of platinum-group elements, nickel, copper, and gold in the Muskox Layered Intrusion, Northwest Territories, Canada. *Economic Geology* **90**, 135–154.

Barnes, S.J., Zientek, M.L. & Severson, M.J. (1997). Ni, Cu, Au, and platinum-group element contents of sulphides associated with intraplate magmatism: a synthesis. *Canadian Journal of Earth Sciences* **34**, 337–351.

Bédard, J.H. & Taner, M.F. (1992). The upper part of the Muskox intrusion, Northwest Territories. In: *Current Research, Part C; Geological Survey of Canada Paper* **92-1C**, 91–101.

Boudreau, A.E. (2003). IRIDIUM- a program to model reaction of silicate liquid infiltrating a porous solid assemblage. *Computers & Geosciences* **29**, 423–429.

Boudreau, A.E. & Philpotts, A.R. (2002). Quantitative modeling of compaction in the Holyoke flood basalt flow, Hartford Basin, Connecticut. *Contributions to Mineralogy and Petrology* **144**, 176-184.

Campbell, I.H. & Naldrett, A.J. (1979). The influence of silicate:sulfide ratios on the geochemistry of magmatic sulphides. *Economic Geology* **74**, 1503–1506.

Cawthorn, R.G., Sander, B.K. & Jones, I.M. (1992). Evidence for the trapped liquid shift effect in the Mount Ayliff Intrusion, South Africa. *Contributions to Mineralogy and Petrology* **111**, 194–202.

Chalokwu, C.I. & Grant, N.K. (1987). Re-equilibration of olivine with trapped liquid in the Duluth complex, Minnesota. *Geology* **15**, 71–74.

Chamberlain, J.A. (1967). Sulfides in the Muskox intrusion. *Canadian Journal of Earth Sciences* **4**, 105–153.

DesRoches, V. (1992). Petrogenesis of the pyroxenite units in the Muskox intrusion, N.W.T. M.Sc. thesis, McGill University, 61 pp.

Dupuy, C., Michard, A., Dostal, J., Dautel, D. & Baragar, W.R.A. (1992). Proterozoic flood basalts from the Coppermine River area, Northwest Territories: isotope and trace element geochemistry. *Canadian Journal of Earth Sciences* **29**, 1937–1942.

Fahrig, W.F. (1987). The tectonic settings of continental mafic dyke swarms: failed arm and early passive margins. *Geological Association of Canada Special Paper* **34**, 331–348.

Findlay, D.C. & Smith, C.H. (1965). The Muskox Drilling Project. *Geological Survey of Canada Paper* **64-44**, 170 pp.

Fleet, M.E., Stone, W.E. & Crocket, J.H. (1991). Partitioning of palladium, iridium, and platinum between sulfide liquid and basalt melt: effects of melt composition, concentration, and oxygen fugacity. *Geochimica et Cosmochimica Acta* **55**, 2545–2554.

Francis, D. (1994). Chemical interaction between picritic magmas and upper crust along the margins of the Muskox intrusion, Northwest Territories. *Geological Survey of Canada Paper* **92-12**, 94 pp.

Ghiorso, M.S. & Sack, R.O. (1995). Chemical mass transfer in magmatic processes IV: a revised and internally consistent thermodynamic model for the interpretation and extrapolation of liquid–solid equilibria in magmatic systems at elevated temperatures and pressures. *Contributions to Mineralogy and Petrology* **119**, 197–212.

Gibb, F.G.F. & Henderson, C.M.B. (2006). Chemistry of the Shiant Isles main sill, NW Scotland, and wider implications for the petrogenesis of mafic sills. *Journal of Petrology* **47**, 191–230.

Gibson, I.L., Sinah, M.N. & Fahrig, W.F. (1987). The geochemistry of the Mackenzie Dike Swarm, Canada. In: Halls, H.C. & Fahrig, W.F. (eds) *Mafic Dyke Swarms. Geological Association of Canada, Special Paper* **34**, 109–121.

Grant, N.K. & Chalokwu, C.I. (1992). Petrology of the Partridge River intrusion, Duluth Complex, Minnesota: II. Geochemistry and strontium isotope systematics in drill core DDH-221, *Journal of Petrology* **33**, 1007–1038.

Griselin, M., Arndt, N. & Baragar, W.R.A. (1997). Plume-lithosphere interaction and crustal contamination during formation of Coppermine River basalts, Northwest Territories, Canada. *Canadian Journal of Earth Sciences* **34**, 958–975.

Hoffman, P.F. (1980). Wopmay Orogen: a Wilson cycle of early Proterozoic age in the northwest of the Canadian Shield. In: Strangeway, D.W. (ed) *The Continental Crust and its Mineral Deposits. Geological Association of Canada, Special Paper* **20**, 523–549.

Hoffman, P.F. (1984). Geology, Northern Internides of Wopmay Orogen, District of Mackenzie, Northwest Territories. *Geological Survey of Canada, Map* **1576A**.

Hoffman, P.F. & Bowring, S.A. (1984). Short-lived 1.9 Ga continental margin and its destruction, Wopmay Orogen, northwest Canada. *Geology* **12**, 68–72.

Hoffman, P.F. & Hall, L. (1993). Geology, Slave Craton and Environs, District of Mackenzie, Northwest Territories. *Geological Survey of Canada, Open File* **2559**.

Hoover, J.D. (1989). Petrology of the marginal border series of the Skaergaard Intrusion. *Journal of Petrology* **30**, 399–439.

Hornal, R.W. (1968). The gravity anomaly field in the Coppermine area of the Northwest Territories (Canada). *Dominion Observatory Gravity Map Series*, **45**.

Irvine, T.N. (1970). Crystallization sequences in the Muskox intrusion and other layered intrusions – I. Olivine-pyroxene-plagioclase relations. In: Visser, D.J.L. & Von Gruenewaldt, G. (eds) *Symposium on the Bushveld Igneous Complex and Other Layered Intrusions. Geological Society of South Africa, Special Publication* **1**, 441–476.

Irvine, T.N. (1975). Crystallization sequences in the Muskox intrusion and other layered intrusions – II. Origin of chromitite layers and similar deposits of other magmatic ores. *Geochimica et Cosmochimica Acta* **39**, 991–1020.

Irvine, T.N. (1977a). Origin of chromitite layers in the Muskox intrusion and other stratiform intrusions: a new interpretation. *Geology* **5**, 273–277.

Irvine, T.N. (1977b). Definition of primitive liquid compositions for basic magmas. *Carnegie Institute of Washington Year Book* **76**, pp 454–461.

Irvine, T.N. (1980). Magmatic infiltration metasomatism, double-diffusive fractional crystallization, and adcumulus growth in the Muskox intrusion and other layered intrusions. In: Hargraves, R.B. (ed.) *Physics of Magmatic Processes*. Princeton: Princeton University Press, pp. 325–383.

Irvine, T.N. (1988). Muskox intrusion, Northwest Territories. In: *Geological Environments of the Platinum Group Elements. Geological Survey of Canada, Open File* **1440**, 25–39.

Irvine, T.N. & Smith, C.H. (1967). The ultramafic rocks of the Muskox intrusion, Northwest Territories, Canada. In: Wyllie, P.J. (ed.) *Ultramafic and Related Rocks*. New York: John Wiley & Sons, Inc., 38–49.

Irvine, T.N. & Smith, C.H. (1969). Primary oxide minerals in the Layered Series of the Muskox intrusion. In: Wilson, H.D.B. (ed.) *Magmatic Ore Deposits: A Symposium, Economic Geology Monograph* **4**, 76–94.

Keays, R.R. (1995). The role of komatiitic and picritic magmatism and S-saturation in the formation of ore deposits. *Lithos* **34**, 1–18.

Latypov, R.M. (2003). The origin of marginal compositional reversals in basic-ultrabasic sills and layered intrusions by Soret fractionation. *Journal of Petrology* **44**, 1579–1618.

LeCheminant, A.N. & Heaman, L.M. (1989). Mackenzie igneous events, Canada: Middle Proterozoic hotspot magmatism associated with ocean opening. *Earth and Planetary Science Letters* **96**, 38–48.

Lesher, C.M. & Burnham, O.M. (1999). Mass balance and mixing in magmatic systems. In: Keays, R.R., Lesher, C.M., Lightfoot, P.C. & Farrow, C.E.G. (eds.) *Dynamic Processes in Magmatic Ore Deposits and Their Application to Mineral Exploration, Geological Association of Canada, Short Course* **13**, pp 413–449.

Lesher, C.M., Burnham, O.M., Keays, R.R., Barnes, S.J. & Hulburt, L. (2001). Trace-element geochemistry and petrogenesis of barren and ore-associated komatiites. *Canadian Mineralogist* **39**, 673–696.

Li, C. & Naldrett, A.J. (1993). Sulfide capacity of magma: a quantitative model and its application to the formation of sulfide ores at Sudbury Ontario. *Economic Geology* **88**, 1253–1260.

Li, C. & Naldrett, A.J. (1999). Geology and petrology of the Voisey's Bay intrusion: reaction of olivine with sulfide and silicate liquids. *Lithos* **47**, 1–31.

Li, C. & Ripley, E.M. (2005). Empirical equations to predict the sulfur content of mafic magmas at sulfide saturation and applications to magmatic sulfide deposits. *Mineralium Deposita* **40**, 218–230.

Li. C., Ripley, E.M., Maier, W.D. & Gomwe, T.E.S. (2002). Olivine and sulfur isotopic compositions of the Uitkomst Ni-Cu sulfide ore-bearing complex, South Africa: evidence

for sulfur contamination and multiple magma emplacements. *Chemical Geology* **188**, 149–159.

Mackenzie, D. (1984). The generation and compaction of partially molten rock. *Journal of Petrology* **25**, 713–765.

Marsh, B.D. (2000). Magma chambers. In: Sigurdsson, H., Houghton, D., McNutt, S.R., Rymer, H. & Stix, J. (eds.) *Encyclopedia of Volcanoes*. San Diego, Academic Press. pp 191-205.

Mavrogenes, J.A. & O'Neill, H. St.C. (1999). The relative effects of pressure, temperature and oxygen fugacity on the solubility of sulfide in mafic magmas. *Geochimica et Cosmochimica Acta* **63**, 1173–1180.

McDonough, W.F., & Sun, S. (1995). The composition of the Earth. *Chemical Geology* **120**, 223–253.

Meurer, W.P. & Boudreau, A.E. (1996). Compaction of density-stratified cumulates: effect on trapped-liquid distribution. *Journal of Geology* **104**, 115–120.

Meurer, W.P. & Boudreau, A.E. (1998a). Compaction of igneous cumulates part I: geochemical consequences for cumulates and liquid fractionation trends. *Journal of Geology* **106**, 281–292.

Meurer, W.P. & Boudreau, A.E. (1998b). Compaction of igneous cumulates part II: compaction and the development of igneous foliations. *Journal of Geology* **106**, 293–304.

Mungal, J.E. (2002). Late-stage sulfide liquid mobility in the main mass of the Sudbury igneous complex: examples from the Victor Deep, McCreedy East, and Trillabelle Deposits. *Economic Geology* **97**, 1653–1576.

Naldrett, A.J. (1997). Key factors in the genesis of Noril'sk, Sudbury, Jinchuan, Voisey's Bay and other world-class Ni-Cu-PGE deposits: implications for exploration. *Australian Journal of Earth Sciences* **44**, 283–315.

Naldrett, A.J. (2004). Magmatic Sulfide Deposits. Geology, Geochemistry and Exploration. Spinger-Verlag Berlin Heidelberg, 727 pp.

Page, N.J., Zientek, M.L., Lipin, B.R., Raedeke, L.D., Wooden, J.L., Turner, A.R., Loferski, P.J., Foose, M.P., Moring, B.C. & Ryan, M.P.(1985). Geology of the Stillwater Complex exposed in the mountain view area and on the west side of the Stillwater canyon. In: Czamanske, G.K. & Zientek, M.L. (eds.) *The Stillwater Complex, Montana: Geology and Guide. Montana Bureau of Mines and Geology, Special Publication* **92**, pp 147–230.

Peach, C.L., Mathez, E.A., Keays, R.R. & Reeves, S.J. (1994). Experimentally determined sulfide melt-silicate melt partition coefficients for iridium and palladium. *Chemical Geology* **117**, 361–377.

Pouchou, J.L. & Pichoir, F. (1991). Quantitative analysis of homogeneous or stratified microvolumes applying the model "PAP". In: Heinrich, K.F.J. & Newbury, D.E. (eds.) *Electron Microprobe Quantitation*. Plenum Press, New York, pp 31–75.

Raedeke, L.D. & McCallum, I.S. (1984). Investigations in the Stillwater Complex: Part II, Petrology and petrogenesis of the Ultramafic series. *Journal of Petrology* **25**, 395–420

Rajamani, V. & Naldrett, A.J. (1978). Partitioning of Fe, Co, Ni, and Cu between sulfide liquid and basaltic melts and the composition of Ni-Cu sulfide deposits. *Economic Geology* **73**, 82–93.

Ripley, E.M. (1999). Systematics of sulphur and oxygen isotopes in mafic igneous rocks and related Cu-Ni-PGE mineralization. In: Keays, R.R., Lesher, C.M., Lightfoot, P.C. & Farrow, C.E.G. (eds.) *Dynamic Processes in Magmatic Ore Deposits and Their Application to Mineral Exploration, Geological Association of Canada, Short Course* **13**, pp 133–158.

Ripley, E.M. & Li, C. (2003). Sulfur isotope exchange and metal enrichment in the formation of magmatic Cu-Ni-(PGE) deposits. *Economic Geology* **98**, 635–641.

Roach, T.A., Roeder, P.L. & Hulbert, L.J. (1998). Composition of chromite in the Upper Chromitite, Muskox layered intrusion, Northwest Territories. *Canadian Mineralogist* **36**, 117–135.

Rudnick, R.L. & Fountain, D.M. (1995). Nature and composition of the continental crust: a lower crustal perspective. *Reviews of Geophysics* **33**, 267–309.

Sasaki, A. (1969). Sulphur isotope study of the Muskox intrusion, District of Mackenzie (86 J/13, O/3). *Geological Survey of Canada Paper* **68-46**, 68 pp.

Shirley, D.N. (1986). Compaction of igneous cumulates. *Journal of Geology* **94**, 795–809.

Shirley, D.N. (1987). Differentiation and compaction in the Palisades sill, New Jersey. *Journal of Petrology* **28**, 835–865.

Smith, C.H. (1962). Notes on the Muskox Intrusion, Coppermine River area, District of Mackenzie. *Geological Survey of Canada Paper* **61-25**, 16 pp.

Smith, C.H. (1967). Geology of the Muskox Intrusion, District of Mackenzie. *Geological Survey of Canada, A Series Map,* **1213A & 1214A**.

Smith, C.H. & Kapp, H.E. (1963). The Muskox intrusion, a recently discovered layered intrusion in the Coppermine River area, Northwest Territories, Canada. *Mineralogical Society of America, Special Paper* **1,** 30–35.

Stewart, B.W. & DePaolo, D.J. (1992). Diffusive isotopic contamination of mafic magma by coexisting silicic liquid in the Muskox intrusion. *Science* **255**, 708–711.

Stewart, B.W. & DePaolo, D.J. (1996). Isotopic studies of processes in mafic magma chambers: III. The Muskox intrusion, Northwest Territories, Canada. In: Basu, A. & Hart, S. (eds.) *Earth Processes: Reading the Isotopic Code*. Washington, DC: American Geophysical Union, pp 277–292.

Tharp, T.M., Loucks, R.R. & Sack, R.O. (1998). Modeling compaction of olivine cumulates in the Muskox intrusion. *American Journal of Science* **298**, 758–790.

Thériault, R.D., Barnes, S.J. & Severson, M.J. (1997). The influence of country-rock assimilation and silicate sulfide ratios (R factor) on the genesis of the Dunka Road Cu-Ni-platinum group element deposit, Duluth Complex, Minnesota. *Canadian Journal of Earth Sciences* **34**, 375–389.

Wilson, A.H. (1982). The geology of the Great Dyke, Zimbabwe: the ultramafic rocks. *Journal of Petrology* **23**, 240–292.

CHAPTER 3

Age and Hf-Nd isotopic geochemistry of marginal rocks in the Muskox intrusion: implications for crustal contamination and mantle source composition in the 1.27 Ga Mackenzie magmatic event

3.1 INTRODUCTION

The 1.27 Ga Mackenzie magmatic event represents a period of extensive tholeiitic magmatism that resulted in the emplacement of the large Muskox layered mafic-ultramafic intrusion and Mackenzie dike swarm, and the eruption of the Coppermine River flood basalts (LeCheminant & Heaman, 1989; Griselin et al., 1997; Baragar et al., 1996). Previous petrologic, paleomagnetic, and geochronologic studies have indicated that all components of the Mackenzie magmatic event were emplaced within a relatively short time-span of only a few million years, and that they are genetically related and considered to be the products of a mantle plume (Wandless & Loveridge, 1972; Fahrig, 1987; LeCheminant & Heaman, 1989; Baragar et al., 1996; Griselin et al., 1997). An important aspect in the geochemical evolution of these bodies is that the tholeiitic parental magmas ascended through ~40 km of continental crust, which may have imparted distinct trace element and isotopic signatures within both the extrusive and intrusive components (e.g. Siberian flood basalts and associated sills, Noril'sk region, Russia; Wooden et al., 1993; Arndt et al., 2003). Because of the highly enriched incompatible trace element contents of most middle and upper crustal rocks compared to basaltic magmas, the extent to which these magmas interacted with the crust during transit and emplacement can be assessed using radiogenic isotopic compositions and incompatible trace element ratios. Previous investigations of the trace element and isotopic compositional variations within the Coppermine River basalts (Griselin et al., 1997; Dupuy et al., 1992) indicate that the lowermost basalts were contaminated by continental crust during their ascent to the surface, whereas the uppermost basalts emplaced with little or no interaction with crustal material. A previous Nd and Sr isotopic investigation within the Muskox intrusion (Stewart & DePaolo, 1992; 1996) focused on the layered series and roof zone, and suggested that only minimal crustal contamination occurred within the Muskox chamber as a result of the buoyancy and viscosity contrast between mafic magma within the chamber and overlying silicic magma derived through melting of the roof rocks.

In this study, we first present precise U-Pb ages from baddeleyite in marginal zone peridotite and gabbronorite at stratigraphically low and high positions within the Muskox intrusion to constrain the absolute crystallization age of the marginal zone rocks and their temporal relationship with the overlying layered series (1270 ± 4 Ma, U-Pb baddeleyite/zircon; LeCheminant & Heaman, 1989) and the Mackenzie dikes (1268 ± 2 Ma, U-Pb baddeleyite; LeCheminant & Heman, 1989). We then evaluate variations in the Hf-Nd isotopic and trace

element concentrations of the marginal rocks to determine the spatial extent and degree of crustal contamination along the basal margin of the intrusion. Finally, we compare available Nd isotopic compositions from the Muskox intrusion, Coppermine River flood basalts, and Mackenzie dikes to constrain the petrogenetic relationship between these bodies and possible variations in the mantle source composition during the Mackenzie magmatic event. Our results indicate that the Muskox intrusion was emplaced over a geologically restricted time span at 1269 ± 2 Ma (U-Pb baddeleyite) which correlates precisely with the emplacement of the Mackenzie dikes. The effects of local crustal contamination within the marginal zone are restricted to a thin zone (<10 m) of gabbronoritic rocks directly adjacent to the contact with country rocks. The Nd isotopic compositions of overlying marginal zone peridotites are entirely within the range of published values from the layered series cumulates (Stewart & DePaolo, 1996), thus the majority of the marginal zone rocks record the isotopic composition of the magmas that progressively entered the Muskox chamber. An important conclusion from this study is that the Nd isotopic compositions of the marginal zone peridotites and layered series rocks of the Muskox intrusion are comparable to only the lowermost Coppermine River basalts, which indicates that the majority of the basalts bypassed the Muskox magma chamber and were erupted after travelling through a separate conduit system.

3.2 COMPONENTS OF THE MACKENZIE MAGMATIC EVENT

Below we briefly review the essential characteristics and geochemistry of the main components of the 1.27 Ga Mackenzie magmatic event: the Coppermine River flood basalts, the Mackenzie dike swarm, and the Muskox intrusion.

3.2.1 Coppermine River flood basalts

The Copper Creek Formation and overlying Husky Creek Formation comprise the Coppermine River Group and form a northward dipping (5-8°) succession of continental flood basalts and interflow sandstones that are exposed for 250 km south of the Coronation Gulf (Fig. 3.1) (Baragar, 1969; Baragar & Donaldson, 1973; Dostal et al., 1983). The Ekalulia basalts, which are exposed along the northwestern shore of Bathurst Inlet, are thought to be correlative to the Coppermine River basalts indicating that the total east-west extent of the flood basalt succession may have been >500 km (Baragar et al., 1996). The Coppermine River basalts erupted primarily on fluvial to shallow marine sediments of the Dismal Lake and Hornby Bay

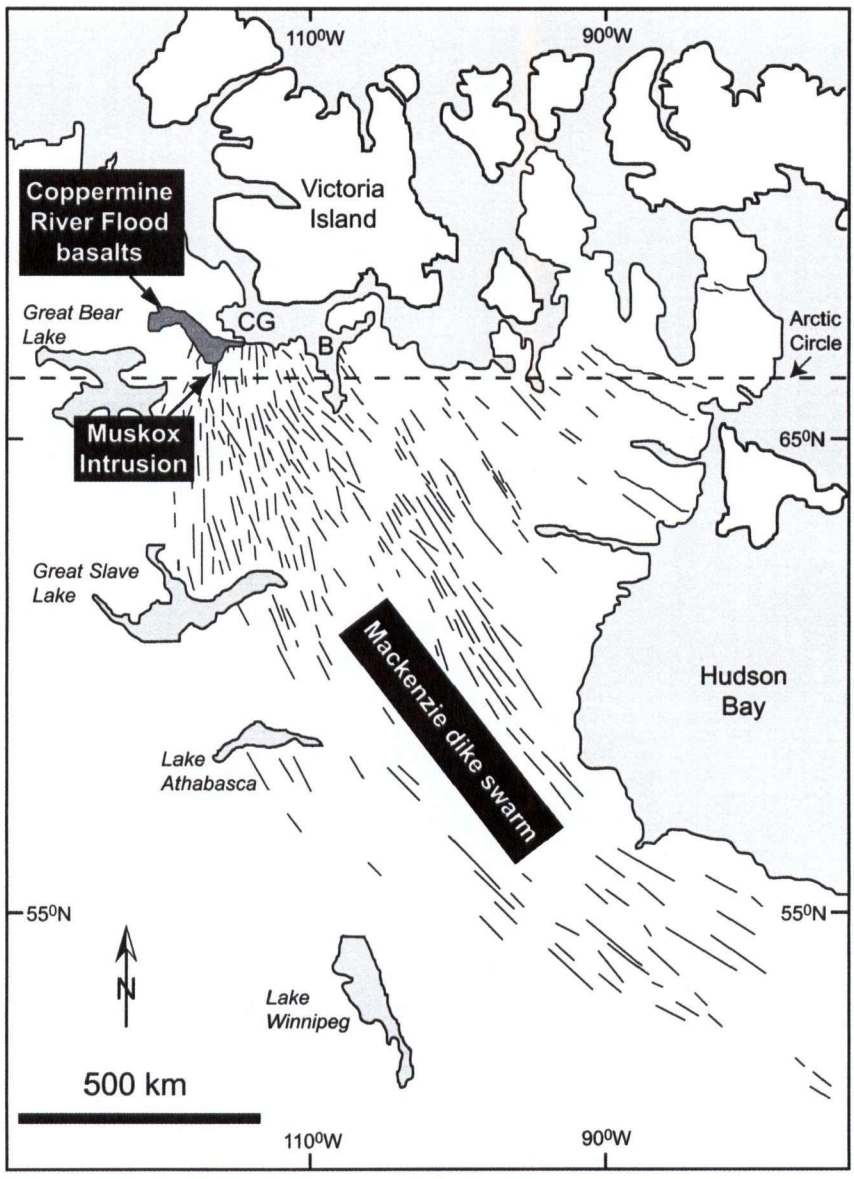

Fig. 3.1: Geographic map showing the distribution of the major components of the 1.27 Ga Mackenzie large igneous province, including the Coppermine River basalts, Mackenzie dike swarm, and Muskox intrusion (modified from LeCheminant & Heaman, 1989; after Gibson et al., 1987). CG = Coronation Gulf; B = Bathurst Inlet.

groups that unconformibly overlie deformed rocks of the 1.8-1.9 Ga Wopmay Orogen (Baragar & Donaldson, 1973; Hoffman, 1984; Hoffman & Bowring, 1984). The flows are typically aphyric and plagioclase microphyric, however olivine or orthopyroxene phenocrysts are present within the lowermost flows (Baragar, 1969). Low Mg/Fe, MgO, and Ni contents and high incompatible element abundances indicate that the lavas fractionated extensively at depth and do not represent primary magma compositions (Dostal et al., 1983). Nd isotopic and trace element compositional variations throughout the flood basalt succession show that the degree of crustal contamination decreased through time with the lower Copper Creek basalts having initial ε_{Nd} values of -5 to +1, and upper Copper Creek and overlying Husky Creek basalts having initial ε_{Nd} values of +1 to +5 (Dupuy et al., 1992; Griselin et al., 1997).

3.2.2 Mackenzie dike swarm

The Mackenzie dikes (1267 ± 2 Ma; LeCheminant & Heaman, 1989) form a series of near-vertically dipping diabase dikes that radiate outwards from the Coronation Gulf towards the south and east for a distance of over 2400 km (Fig. 3.1; Gibson et al., 1987; Baragar et al., 1996). The dikes terminate within the lower Copper Creek basalts, which along with petrological and geochemical considerations, suggests that they represent the feeder system through which the basalts were emplaced (Baragar & Donaldson, 1973; Dostal et al., 1983; Baragar et al., 1996). Two distinct chemical groups, or subswarms, have been identified based on variations in Ce/Yb, which primarily reflects changes in the degree of mantle melting (Baragar et al., 1996; Gibson et al., 1987). Crustal contamination within the dikes is more pronounced closer to the focus of the swarm based on incompatible element ratios (e.g. K/Ti; Baragar et al., 1996). Magma flow direction in the dikes is considered to be near-vertical within 500 km of the focal point of the dike swarm and near-horizontal at greater distances (Ernst & Baragar, 1992). An unpublished Nd isotopic study (Dundas & Peterson, 1992) indicates that in all the dikes sampled, including those from each subswarm, the initial ε_{Nd} values range from -2.8 to +4.9, which is consistent with the range observed in the Coppermine River basalts. Dikes of a similar age and composition (Bear River dikes, Yukon) have recently been identified and may represent part of the Mackenzie dike swarm, broadening the extent of the swarm by approximately 50° towards the west (Schwab et al., 2004).

3.2.3 Muskox intrusion

The Muskox intrusion is a layered mafic-ultramafic intrusion that was emplaced within rocks of the 1.8-1.9 Ga Wopmay Orogen along the western margin of the Slave Craton (Fig. 3.2) (Smith, 1962; Hoffman, 1984; Hoffman & Bowring, 1984; Gandhi et al., 2001). The intrusion and underlying feeder dike are exposed for over >100 km south of the Coronation Gulf near the focal point of the Mackenzie dike swarm. The main body of the intrusion is funnel-shaped in cross-section and forms an elongate body that plunges shallowly (4-8°) northward beneath the overlying Hornby Bay sandstones, Dismal Lake carbonates, and Coppermine River basalts (Smith, 1962; Findlay & Smith, 1967; Baragar & Donaldson, 1973). The northward-plunging attitude of the intrusion provides an oblique section through its entire stratigraphy from the basal feeder and margin in the south to the upper roof zone in the north. The surrounding crustal rocks consist of metasedimentary rocks of the Recluse and Epworth groups to the east and metavolcanic, metasedimetary, and metaplutonic rocks of the Akaitcho Group and Hepburn Intrusive Suite to the west.

The Muskox intrusion is divided into a feeder dike, marginal zone, layered series, and granophyric roof zone (Fig. 3.2) (Smith, 1962; Smith & Kapp, 1963). The feeder dike is exposed south of the main body of the intrusion and consists of mainly gabbronorite (bronzite gabbro) and norite with minor olivine-bearing units near the base of the intrusion. The dike is considered to represent a feeder through which the initial magmas entered the Muskox magma chamber; subsequent magma pulses may have been injected from an unexposed feeder to the north (Irvine, 1980). The marginal zone forms a sheath along the inward-dipping walls of the intrusion, separating the layered series rocks from the surrounding crustal rocks (Smith, 1962; Findlay & Smith, 1967; Francis, 1994). The layered series is composed of numerous northward-dipping layers of mainly olivine-chromite cumulates, and olivine-pyroxene cumulates in the lower part of the intrusion, and pyroxene and plagioclase cumulates within the upper part of the intrusion (Smith, 1962; Bédard & Taner, 1992; DesRoches, 1992; Francis, 1994). The upper part also hosts two chromite-rich layers that are similar to those of the lower part of the Bushveld Complex, South Africa, but contain an order of magnitude less PGE (Irvine & Smith, 1969; Irvine, 1988; Barnes & Francis, 1995; Roach et al., 1998). The granophyric roof zone is a heterogeneous zone composed of granophyric gabbro and granophyre with varying abundances of host rock xenoliths and is considered to represent both

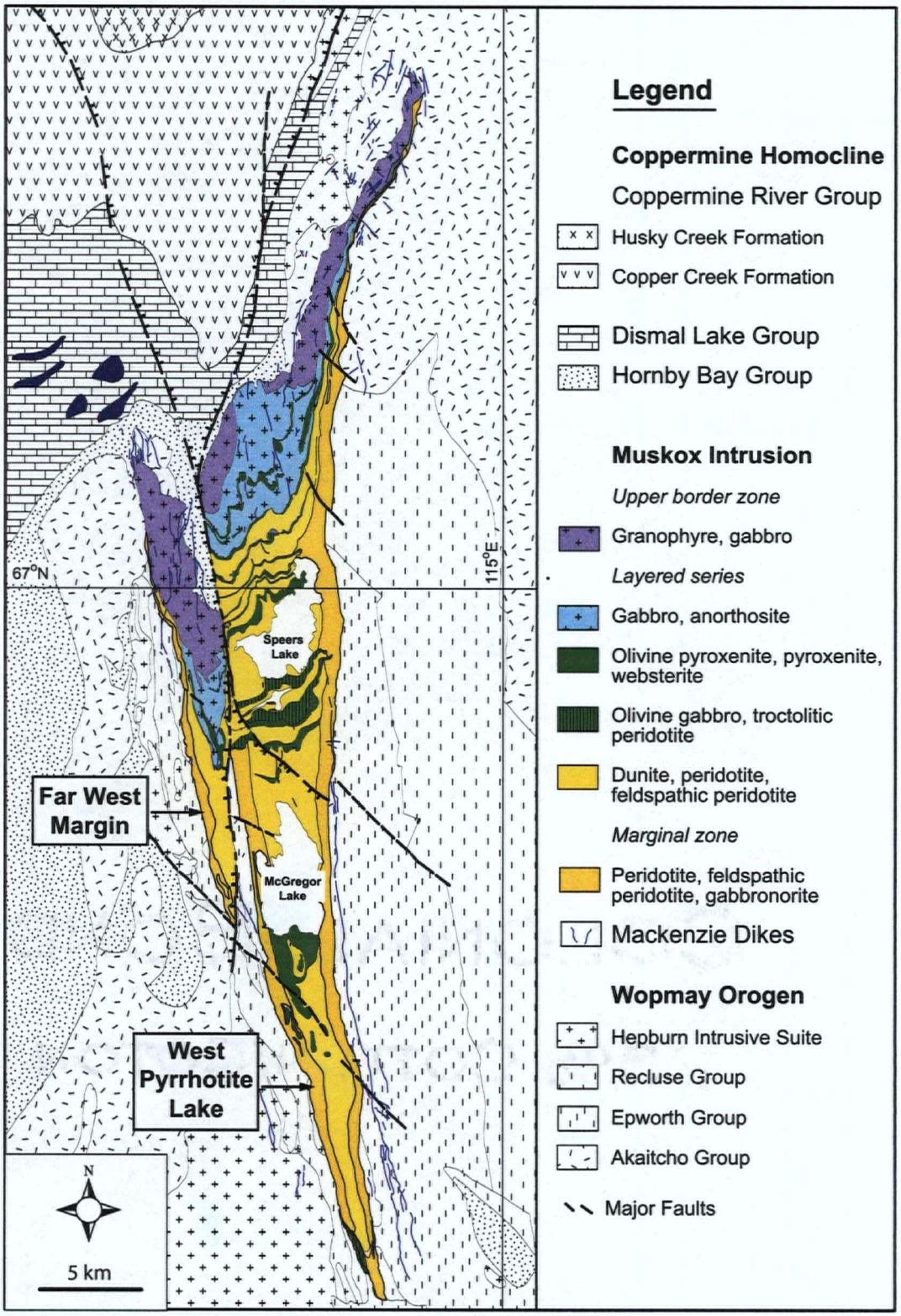
Legend
Coppermine Homocline
Coppermine River Group
Husky Creek Formation
Copper Creek Formation
Dismal Lake Group
Hornby Bay Group
Muskox Intrusion
Upper border zone
Granophyre, gabbro
Layered series
Gabbro, anorthosite
Olivine pyroxenite, pyroxenite, websterite
Olivine gabbro, troctolitic peridotite
Dunite, peridotite, feldspathic peridotite
Marginal zone
Peridotite, feldspathic peridotite, gabbronorite
Mackenzie Dikes
Wopmay Orogen
Hepburn Intrusive Suite
Recluse Group
Epworth Group
Akaitcho Group
Major Faults
67°N
115°E
Speers Lake
McGregor Lake
Far West Margin
West Pyrrhotite Lake
N
5 km

Figure 3.2

Fig. 3.2: Geologic map of the Muskox intrusion showing the location of the West Pyrrhotite Lake and Far West Margin sections (after Hulbert, 2005; mapping by Smith, 1962). The intrusion plunges shallowly to the north (4-8°) exposing a large section of the stratigraphy from a basal feeder zone in the south to the granophyric roof zone in the north. The West Pyrrhotite Lake section is near the base of the intrusion, while the Far West Margin section is at a stratigraphically higher position near the roof of the intrusion. The Muskox feeder dike, extends to the south (off the map) for ~60 km. Rivers and lakes have been omitted for clarity, with the exception of McGregor and Speers lakes.

extremely fractionated liquid within the chamber and siliceous melt derived by melting of the overlying roof rocks (Irvine & Smith, 1967; Stewart & DePaolo, 1996).

The cumulate rocks within the intrusion are considered to have formed through the fractionation and accumulation of mineral grains from multiple magma injections and subsequent compaction within a cumulate pile (Irvine & Smith, 1967; Irvine, 1970; Irvine, 1980; Tharp et al., 1998). Irvine and Smith (1967) divided the layered series into 25 cyclic units, each of which represents an influx of relatively undifferentiated magma and removal (eruption) of fractionated residual liquid. The appearance of pyroxenite layers within the upper part of the intrusion marks a change in the order of crystallization, which reflects a change to a more evolved magma composition during the later stages of the evolution of the Muskox chamber. Irvine (1970) postulated that this advanced crystallization of orthopyroxene was the result of contamination of the magma within the chamber by silicic material derived from melting of the roof rocks. Irvine (1975) initially suggested that the chromite-rich horizons formed by the same mechanism, however he later proposed (Irvine, 1977) that mixing between primitive and evolved magmas within the chamber was a more viable process to explain the formation of the chromite-rich horizons. Nd isotopic compositions of the Muskox intrusion (Stewart & DePaolo, 1996) show relatively limited variation throughout the layered series (initial ε_{Nd} = -2.5 to 0.5), which supports the magma mixing model for the formation of the chromite-rich horizons and suggests that the early crystallization of orthopyroxene may have also resulted from magma mixing as opposed to crustal contamination.

3.3 MARGINAL ROCKS OF THE MUSKOX INTRUSION

The marginal zone is a structurally distinct unit within the Muskox intrusion that separates the rocks of the overlying layered series from the adjacent crustal rocks, trends parallel to the inward dipping walls, and extends throughout the entire stratigraphic height of the intrusion (Fig. 3.2 & 3.3) (Smith, 1962; Francis, 1994). In this study, we evaluate the trace element and isotopic compositions of drill core collected in 2003 from stratigraphically low (West Pyrrhotite Lake) and high (Far West Margin) positions along the western margin of the intrusion (Fig. 3.2 & 3.3). As described in Chapter 2, the marginal zone at both sections is composed of a thick upper subzone (~100-150 m) of olivine and olivine-chromite cumulates and a relatively thin (<10 m) lower subzone containing granophyre-bearing gabbronoritic

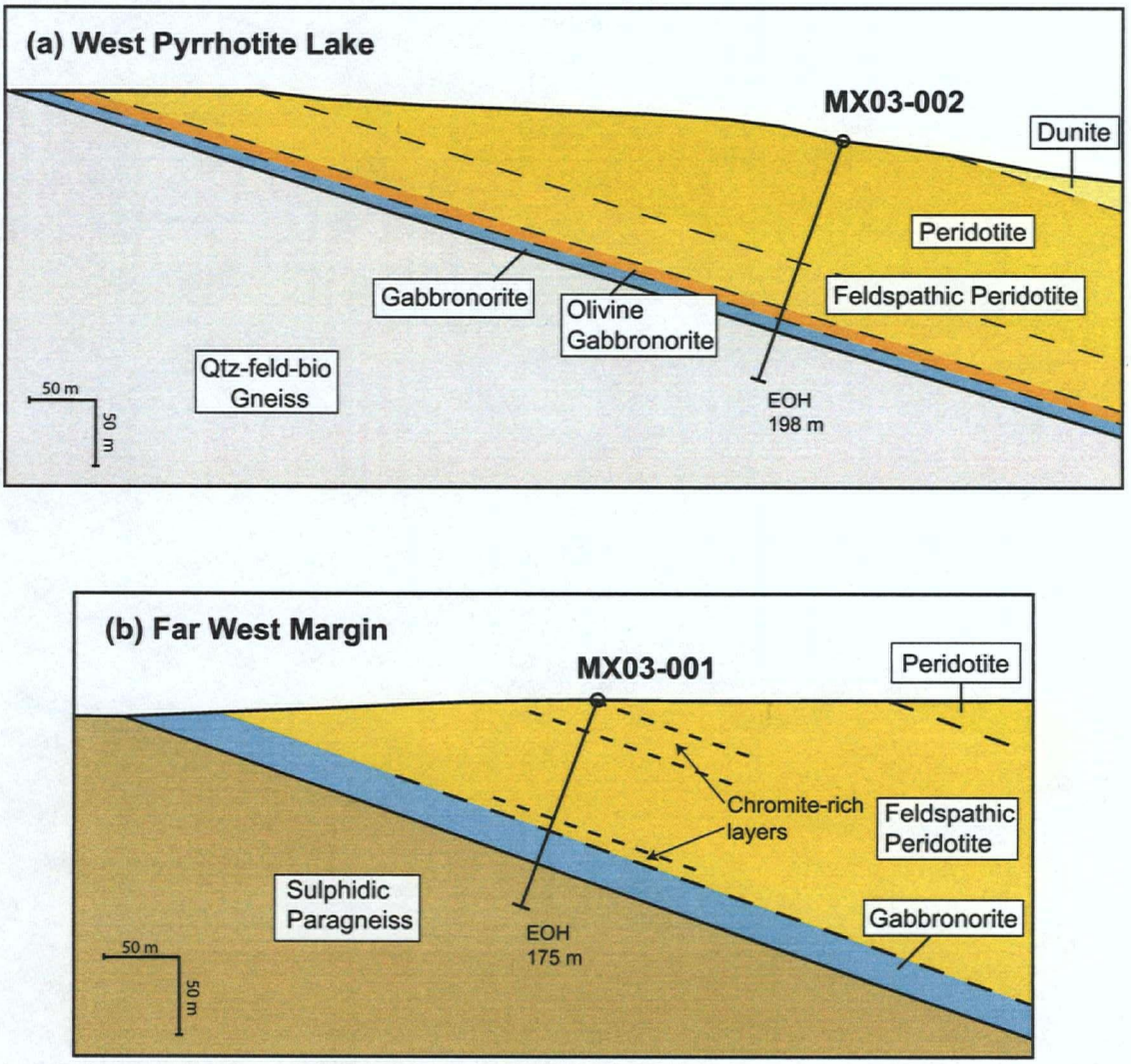

Fig. 3.3: Interpreted cross-sections (facing north) of the (a) West Pyrrhotite Lake and (b) Far West Margin sections showing locations and depths of drill holes. Surface geologic contacts and topography are from Smith (1962) and down-hole contacts are based on drill core and petrographic observations and stratigraphic shifts in major element chemistry (see Chapter 2). EOH = end of hole. Qtz-feld-bio = quartz-feldspar-biotite.

rocks at the contact with the adjacent gneisses (Fig. 3.3). The peridotite part of the marginal zone becomes progressively more evolved in composition towards the margin owing to a systematic increase in the proportion of postcumulus pyroxene, plagioclase, and phlogopite relative to cumulus olivine. This downward trend to more evolved compositions is the result of rapid cooling and solidification of intercumulus liquid near the margin of the intrusion and expulsion of intercumulus liquid during compaction within the relatively slowly cooled interior (see Chapter 2). The gabbronoritic rocks at the base of the marginal zone contain granophyre and have distinct incompatible trace element ratios (Th/Yb, La/Sm, Nb/La, and K/Ti) indicating that they were contaminated by the adjacent wall rocks during emplacement. The Hf and Nd isotopic compositions determined in this study, not only allow us to confirm the extent of contamination predicted by trace element ratios, but provide a link between the marginal zone and layered series rocks (Stewart & DePaolo, 1996; Purves, 2005 (unpublished)), as well as the other components of the Mackenzie magmatic event (Griselin et al., 1997; Dundas & Peterson, 1992 (unpublished)) for which there is available isotopic data.

3.4 ANALYTICAL TECHNIQUES

3.4.1 U-Pb concentrations and isotopic compositions

Mafic and ultramafic cumulate rocks typically contain low concentrations of incompatible elements (e.g. 20-40 ppm Zr in marginal zone peridotites of the Muskox intrusion) and therefore contain only trace amounts of U-rich minerals suitable for U-Pb geochronology. Baddeleyite (ZrO_2), however, which can crystallize from fractionated interstitial liquid, contains high concentrations of U (~500 ppm) and can be used to precisely date mafic rocks (Heaman & LeCheminant, 1993). In the Muskox intrusion, baddeleyite occurs not only in marginal gabbronorite, but also in peridotite with MgO contents up to 38 wt %. A total of 15 fractions of baddeleyite were separated from peridotite (71112) from the West Pyrrhotite Lake section, and from chromite-rich peridotite (71064) and gabbronorite (71084) from the Far West Margin section (Fig. 3.3). All separation and analytical procedures were completed at the Pacific Centre for Isotopic and Geochemical Research (PCIGR) at the University of British Columbia, Vancouver. Samples 71064 and 71084 represent a one metre interval of halved drill core, whereas sample 71112 represents a composite sample of four one metre intervals taken over a 20 m-wide zone of homogeneous peridotite.

Two different baddeleyite separation procedures were used for the three samples. For samples 71112 and 71084, a heavy mineral concentrate was obtained from 5-10 kg of crushed sample following standard density and magnetic separation procedures. For sample 71064, baddeleyite was hand-picked following only magnetic separation procedures. The density separation procedure involved both Wilfley table and heavy liquid techniques. Magnetic separation was completed on a model L1 Frantz Isodynamic Separator by progressively decreasing the side tilt (20°, 5°, and 2°) and increasing the amperage (0.6 and 1.8 amps). The highest yield of baddeleyite was typically under the 5° side tilt and 1.8 amps settings. Baddeleyite grains within the Muskox samples are light brown to tan and form euhedral, blade- and needle-shaped crystals with striated crystal faces. They are typically <20 x 50 μm, but smaller fragments can also be observed. Approximately 60-80 individual grains (70-90% of total yield) were hand-picked from each sample using a binocular microscope and ~2-30 grains were selected for each fraction to ensure only the clearest and inclusion-free grains were analyzed.

Ion exchange column techniques were used to separate U and Pb for 13 fractions, and the remaining two fractions were analyzed without column chemistry to assess whether or not the column chemistry procedure would produce more precise results (Table 3.1). Each fraction was dissolved in concentrated HF and HNO_3 with a mixed $^{233\text{-}235}U$-^{205}Pb tracer. Ion exchange column techniques are those of Parrish et al. (1987). U and Pb were eluted separately and loaded together on a single Re filament using a phosphoric acid-silica gel emitter. U and Pb isotopic compositions were measured on a modified single collector VG-54R thermal ionization mass spectrometer fitted with a Daly photomultiplier. U and Pb concentrations, isotopic ratios, and apparent ages are shown in Table 3.1. During the analyses, procedural blanks for U and Pb were in the range of <1 pg and 2-5 pg, respectively. The amount of U fractionation was determined directly on individual runs using a double ^{233}U-^{235}U tracer. The Pb isotopic ratios were corrected for a fractionation of 0.0027-0.0037%/amu based on replicate analyses of the NBS-982 Pb standard. All analytical errors were propagated through the age calculations using the method described by Roddick (1987). Concordia intercept ages and associated errors were calculated using Isoplot/Ex 3.00 (Ludwig, 1980; 2003; York, 1969) by both free-fit and forced-zero regression methods and are reported with and without uncertainties in the decay constant in Table 3.2.

Table 3.1: U-Pb ID-TIMS analytical data for baddeleyite from the marginal rocks of the Muskox intrusion

Fraction[1]	Mass	U[2]	Pb*[3]	$^{206}Pb/^{204}Pb$[4]	Pb[5]	Th/U[6]	Isotopic ratios (±1s,%)[7]			Apparent ages (±2s,Ma)[7]			Discordance
	(mg)	(ppm)	(ppm)		(pg)		$^{206}Pb/^{238}U$	$^{207}Pb/^{235}U$	$^{207}Pb/^{206}Pb$	$^{206}Pb/^{238}U$	$^{207}Pb/^{235}U$	$^{207}Pb/^{206}Pb$	(%)
71064 (Far West Margin Chromite-rich peridotite)													
B1, 13	13	606	121	15528	6.6	0.02	0.21400 (0.16)	2.4467 (0.19)	0.08292 (0.09)	1250.1 (3.7)	1256.5 (2.8)	1267.3 (3.3)	1.5
B2, 13	13	347	70	11032	5.4	0.02	0.21548 (0.08)	2.4679 (0.14)	0.08306 (0.08)	1258.0 (1.9)	1262.7 (2.0)	1270.7 (2.9)	1.1
B3, ~30	10	773	158	1048	100	0.03	0.21771 (0.19)	2.4945 (0.28)	0.08310 (0.18)	1269.8 (4.3)	1270.5 (4.0)	1271.6 (7.1)	0.2
B5 NC, 4	2	843	171	4104	5.4	0.03	0.21538 (0.09)	2.4618 (0.16)	0.08290 (0.09)	1257.4 (2.0)	1260.9 (2.3)	1266.9 (3.7)	0.8
B6 NC, 5	2	324	66	1269	6.9	0.03	0.21712 (0.17)	2.4850 (0.29)	0.08301 (0.21)	1266.6 (3.9)	1267.7 (4.2)	1269.5 (8.0/8.1)	0.2
71084 (Far West Margin Gabbronorite)													
B1, 1	4	444	90	5514	4.2	0.04	0.21516 (0.11)	2.4615 (0.18)	0.08298 (0.11)	1256.2 (2.6)	1260.8 (2.6)	1268.6 (4.5)	1.1
B3, 1	4	440	90	4225	5.6	0.07	0.21670 (0.11)	2.4795 (0.20)	0.08298 (0.16)	1264.4 (2.6)	1266.1 (3.0)	1268.8 (6.2)	0.4
B5, 1	2	257	52	2646	2.6	0.03	0.21499 (0.18)	2.4591 (0.33)	0.08296 (0.26)	1255.4 (4.1)	1260.1 (4.7)	1268.2 (10.2)	1.1
B6, 1	3	272	55	2505	4.4	0.01	0.21562 (0.14)	2.4663 (0.29)	0.08296 (0.23)	1258.7 (3.2)	1262.2 (4.2)	1268.2 (9.0/9.1)	0.8
B7, 2	2	378	77	2978	3.4	0.04	0.21540 (0.18)	2.4651 (0.25)	0.08300 (0.19)	1257.5 (4.2)	1261.9 (3.6)	1269.3 (7.4)	1.0
71112 (West Pyrrhotite Lake Peridotite)													
B1, 2	3	172	35	2304	3.0	0.02	0.21764 (0.24)	2.4896 (0.40)	0.08296 (0.31)	1269.4 (5.6)	1269.0 (5.9)	1268.3 (12.2/12.3)	-0.1
B2-2, 3	2	627	127	4612	3.6	0.02	0.21611 (0.14)	2.4771 (0.25)	0.08313 (0.19)	1261.3 (3.3)	1265.4 (3.6)	1272.2 (7.5)	0.9
B3, 5	2	270	55	2692	2.7	0.02	0.21735 (0.21)	2.4888 (0.36)	0.08305 (0.28)	1267.9 (4.8)	1268.8 (5.2)	1272.2 (7.5)	0.2
B4-1, 6	4	317	64	6020	2.8	0.02	0.21423 (0.13)	2.4548 (0.20)	0.08311 (0.15)	1251.3 (3.0)	1258.9 (2.9)	1271.7 (5.9)	1.8
B5-1, 12	2	444	90	3137	3.8	0.02	0.21608 (0.13)	2.4750 (0.27)	0.08307 (0.21)	1261.1 (3.1)	1264.8 (3.9)	1270.9 (8.3)	0.8

[1] Baddeleyite fraction followed by the number of grains or fragments analysed. NC signifies "no chemistry" fraction.

[2] U blank correction of 1 pg ± 20%; U fractionation corrections were measured for each run with a double ^{233}U-^{235}U spike.

[3]Radiogenic Pb

[4]Measured ratio corrected for spike and Pb fractionation of 0.0028-0.0032/amu ± 20% (Daly collector) determined by repeated analysis of the NBS Pb 982 standard throughout the course of this study.

[5]Total common Pb in analysis based on blank isotopic composition.

[6]Model Th/U; Th derived from radiogenic ^{208}Pb and $^{207}Pb/^{206}Pb$ age of fraction.

[7]Blank and common Pb corrected; Pb procedural blanks were 2-5 pg and U <1 pg. Common Pb isotopic compositions are based on Stacey and Kramers (1975) model Pb at the interpreted age of the rock or the $^{207}Pb/^{206}Pb$ age of the fraction.

Table 3.2: Summary of U-Pb age calculation methods

Sample	Method[1]	Upper intercept (Ma)	2σ[2]	Lower intercept (Ma)	2σ	MSWD[3]	Probability[4]
71064	free-fit linear regression	1271	6.1 (8.8)	299	500	1.05	0.37
	fixed-zero linear regression	1269	1.7 (5.5)			1.06	0.37
	weighted-mean (2 fractions)	1269	2.7 (2.9)			0.53	0.66
71084	free-fit linear regression	1269	9.7 (11)	63	1500	0.01	0.99
	fixed-zero linear regression	1269	2.9 (5.9)			0.01	1.00
71112	free-fit linear regression	1270	6.4 (7.9)	-204	1100	0.07	0.97
	fixed-zero linear regression	1271	3.6 (6.3)			0.09	0.99
	weighted-mean (2 fractions)	1269	3.4 (3.5)			0.09	0.97
All Samples	free-fit linear regression	1271	4.1 (7.2)	194	430	0.43	0.96
	fixed-zero linear regression	1269	1.4 (5.4)			0.45	0.96
	weighted-mean (4 fractions)	1269	2.1 (2.4)			0.26	0.97

All calculations methods are described by Ludwig (2003) and calculated using the Isoplot/Ex 3.00 software.

[1] Linear regression methods were completed using the algorithm of York (1969); Weighted mean ("concordia age") method is based on Ludwig (1998).

[2] The calculated 2σ errors are shown with (in brackets) or without the uncertainty in U-decay constants.

[3] MSWD = mean square weighted deviates. For weighted mean method MSWD is for both concordance and X-Y equivalence of multiple data points.

[4] Probablity of fit for regression methods; and probability of concordance and X-Y equivalence for weighted mean method.

3.4.2 Trace element and Hf-Nd isotopic compositions

Trace element concentrations and Hf-Nd isotopic compositions of 17 samples and 3 duplicates were measured at the PCIGR, University of British Columbia. All samples were previously analyzed for major and trace element compositions at ACME Analytical Laboratories Ltd. and are a subset of the 81 drill core samples discussed in Chapter 2. Samples were selected for trace element and isotopic ratio determination based on the detailed chemical profiles provided in Chapter 2 and thin section observations to include those least affected by post-magmatic alteration or serpentinization. The original sample powders, which were ground at ACME Laboratories, Vancouver, were re-ground by hand with an agate mortar and pestle to ensure a uniform particle size less than 60 microns. Procedural duplicates were made for three Muskox peridotite samples (71072, 71078, and 71128) to monitor data reproducibility. In addition, two USGS reference materials (G-2 granite; DTS-2 dunite) were analyzed to monitor the accuracy of the concentration results. Both trace element and isotopic compositions for each sample were determined from a single digestion procedure. All samples, duplicates, and reference materials were digested within Teflon bombs enclosed in metallic bombs (modified Krogh design) and placed in an oven at 190°C for 120 hrs in HF-HNO_3-$HClO_4$ (7:1:1) and 24 hrs in HCl. Sample weights were 100 mg for rocks with >1 ppm Hf and 150 mg for rocks with <1 ppm Hf. Following this initial multi-acid digestion, the sample solutions were transferred to Savillex™ and dried on a hotplate. Each sample was then re-dissolved in HCl (4 g) on a hotplate and an aliquot (0.8 g) was removed and placed in a separate Savillex™ for trace element analysis. The remaining sample solution (3.2 g) was kept for isotope ratio determination (see column chemistry procedures below). In preparation for the dilution procedure, the trace element fraction was re-dissolved in HNO_3 and then dried. Taking into account the exact weight of the trace element aliquot removed, each sample was diluted by 800 to 2000 times in 1% HNO_3 with 1 ppb In depending on the expected elemental concentrations.

Trace element concentrations were analyzed on a Thermo Finnigan Element2 high-resolution inductively coupled plasma mass spectrometer (HR-ICP-MS). Rare earth elements were measured in high resolution for gabbronorite and country rock samples and low resolution for peridotite samples. U, Pb and Ta were measured in low resolution and all remaining elements in medium resolution for all samples. All trace element concentrations are shown in Table 3.3. External calibration and concentration calculations were achieved using a series of six standards obtained from sequential dilution of 1000 ppm High Purity® stock

Table 3.3: Trace element concentrations by HR-ICP-MS for marginal rocks of the Muskox intrusion.

Sample Site	Far West Margin (MX03-001)								
Rock type	Chromite-rich Peridotite	Feld-spathic Peridotite	Feld-spathic Peridotite	Feld-spathic Peridotite	Chromite-rich Peridotite	Chromite-rich Peridotite	Gabbro-norite	Gabbro-norite	Hornfelsed paragneiss
Sampe No.[1]	71064	71072a	71072b	71076	71078a	71078b	71082	71084	71094
Depth (m)	28.7	58.9	58.9	81.4	94.7	94.7	109.1	111.8	120.1
Weight (mg)[2]	150	150	150	100	150	150	100	100	100
Cs (ppm)	1.76	0.55	0.56	1.25	1.67	1.57	2.70	3.59	2.88
Rb	30	7	7	13	30	30	45	64	82
Ba	na	na	na	165	148	na	na	na	na
Th	1.1	0.5	0.5	0.6	0.2	0.7	4.6	5.9	8.3
U	0.30	0.15	0.15	0.18	0.23	0.21	0.95	1.16	1.29
Ta	0.095	0.093	0.095	0.091	0.072	0.117	0.425	0.516	0.818
Nb	1.2	1.4	1.4	1.4	1.1	1.8	5.9	7.2	12.0
La	2.1	2.7	2.7	3.8	1.8	1.9	17.2	15.7	42.6
Ce	5.5	6.0	6.1	8.7	5.9	5.7	30.7	31.4	76.1
Pr	0.8	0.8	0.8	1.1	0.9	0.8	3.8	3.8	8.6
Nd	3.62	3.45	3.44	4.78	4.29	4.07	14.25	14.58	31.08
Pb	17	4	4	19	44	41	70	22	38
Sr	25	42	41	107	46	43	103	65	174
Zr	20	21	21	30	19	23	74	88	156
Hf	0.54	0.60	0.59	0.91	0.65	0.68	2.04	2.35	3.98
Sm	0.94	0.89	0.89	1.20	1.13	1.10	2.88	2.95	5.20
Eu	0.22	0.41	0.41	0.49	0.21	0.25	0.60	0.56	1.20
Gd	1.0	1.0	1.0	1.3	1.2	1.2	2.6	2.8	4.8
Tb	0.17	0.18	0.18	0.22	0.22	0.21	0.41	0.43	0.74
Dy	0.91	1.00	1.00	1.40	1.23	1.18	2.54	2.58	4.44
Ho	0.19	0.22	0.22	0.28	0.26	0.26	0.51	0.47	0.79
Er	0.50	0.58	0.58	0.84	0.74	0.68	1.50	1.28	2.30
Yb	0.44	0.53	0.53	0.74	0.61	0.61	1.61	1.32	2.40
Y	4.1	4.5	4.6	6.9	5.1	5.5	13.1	12.7	22.8
Lu	0.07	0.09	0.09	0.11	0.08	0.10	0.23	0.18	0.33
Sc	9.51	12.2	10.8	17.8	4.30	9.02	7.53	7.77	14.0
V	85	81	85	139	131	121	64	65	101
Co	145	80	79	133	125	100	56	76	40
Cu	702	15	16	270	149	128	373	328	312
Zn	104	57	55	107	131	105	74	63	57
Ga	4.5	4.4	4.3	6.9	6.1	5.4	4.9	4.2	8.3

na = not analysed

<lod = below limit of detection.

[1] Sample numbers with "a" and "b" denote complete procedural duplicates.

[2] Approximate sample powder weight in milligrams.

Table 3.3 (continued):Trace element concentrations by HR-ICP-MS for marginal rocks of the Muskox intrusion.

Sample Site		West Pyrrhotite Lake (MX03-002)								
Rock type	Granitic pod	Peridotite	Peridotite	Feld-spathic Peridotite	Feld-spathic Peridotite	Feld-spathic Peridotite	Olivine Gabbro-norite	Gabbro-norite	Gneiss	Gneiss
Sampe No.[1]	71097	71106	71115	71122	71128a	71128b	71133	71138	71141	71147
Depth (m)	121.8	31.8	72.5	113.0	149.3	149.3	162.8	173.6	179.3	200.9
Weight (mg)[2]	100	150	150	150	100	100	100	100	100	100
Cs (ppm)	2.03	0.21	0.28	0.36	1.30	1.28	2.35	1.83	1.71	4.94
Rb	91	5	4	5	11	11	15	48	69	174
Ba	na	25	na	na	104	99	na	na	na	na
Th	10.0	0.3	0.5	0.6	1.0	1.0	1.6	3.0	11.2	12.2
U	3.76	0.12	0.14	0.15	0.26	0.26	0.37	0.71	3.28	3.56
Ta	0.963	0.093	0.069	0.120	0.180	0.176	0.208	0.289	0.564	0.870
Nb	6.2	1.4	1.1	1.9	2.9	2.9	3.6	3.9	6.6	9.5
La	24.9	2.2	2.7	3.4	5.5	5.5	8.3	9.3	26.3	31.3
Ce	46.1	6.1	6.8	8.1	13.8	13.7	17.8	18.7	48.2	60.4
Pr	5.1	0.8	0.9	1.0	1.8	1.8	2.4	2.4	5.2	7.3
Nd	18.19	3.58	3.88	4.38	7.88	7.98	10.38	9.52	19.62	25.84
Pb	19	3	2	5	3	3	3	62	173	207
Sr	245	10	11	33	109	108	120	141	166	97
Zr	147	21	21	25	53	50	57	61	250	248
Hf	3.68	0.63	0.59	0.70	1.49	1.46	1.49	1.66	6.95	6.61
Sm	3.43	0.83	0.95	1.08	1.94	1.87	2.52	1.96	3.38	4.41
Eu	0.90	0.27	0.35	0.41	0.63	0.62	0.79	0.60	1.03	0.94
Gd	3.2	0.8	1.0	1.2	1.8	1.9	2.7	1.9	2.8	3.4
Tb	0.56	0.14	0.18	0.20	0.32	0.32	0.40	0.29	0.41	0.48
Dy	3.86	0.88	0.97	1.08	1.93	1.98	2.61	1.92	2.53	2.87
Ho	0.73	0.17	0.20	0.23	0.38	0.38	0.48	0.39	0.47	0.51
Er	2.17	0.46	0.53	0.60	1.07	1.05	1.34	1.06	1.44	1.45
Yb	2.47	0.42	0.47	0.53	0.97	0.93	1.20	1.09	1.58	1.62
Y	20.4	3.8	4.2	4.8	8.6	8.5	11.6	9.4	13.5	14.9
Lu	0.34	0.06	0.08	0.08	0.13	0.14	0.18	0.17	0.23	0.24
Sc	7.46	7.74	10.3	11.5	17.2	16.5	9.88	13.7	2.66	5.17
V	41	108	92	118	168	164	77	167	19	47
Co	17	132	102	103	110	109	46	48	25	6
Cu	174	64	37	238	96	94	54	427	981	21
Zn	29	90	62	85	82	79	43	124	248	180
Ga	6.4	4.2	4.2	4.8	8.4	7.8	4.6	4.9	5.8	8.8

na = not analysed

<lod = below limit of detection.

[1] Sample numbers with "a" and "b" denote complete procedural duplicates.

[2] Approximate sample powder weight in milligrams.

standard solutions of 1% HNO_3 with 1 ppb In. Data reproducibility was determined from the three procedural duplicates and is shown in Appendix V. Results for USGS reference materials (G-2 and DTS-2) are within error (2σ) of the range of previously published values (see Appendix VI) (Robinson et al., 1986; Totland et al., 1992; Govindaraju, 1994; Liang et al., 2000; Raczek et al., 2000; Meisel et al., 2001; Pretorius et al., in press). For comparison of trace element results determined at PCIGR and ACME Analytical Laboratories Ltd. see Appendix VII. Relative standard deviations for each pair of analyses are typically less than 5% for most elements, however deviations are between 5-15% for Pb, Y, Zr, Nb, and Ta, and up to 20% for Sc. These relatively high uncertainties are the result of a poor analysis of one duplicate (71078a) where the standard deviation determined during the analysis was considerably larger than all other analyses, which may reflect sample inhomogeneity. As a result, this sample has been removed from all plots.

The REE (including Nd) were separated from Hf using a Teflon column with Biorad AG 50W-X8 100-200 mesh resin and a progressively increasing concentration of HCl from 1.5 N to 4.0 N. The Hf separate was then passed through a polypropylene column and a Savillex™ column, using a 0.1 N HF / 0.5 N HCl solution and Biorad AG 1-X8 100-200 mesh resin, and a 0.3 N HF / 2.5 N HCl solution and Biorad AG 50W-X8 200-400 mesh resin, respectively. Nd was separated from the REE in a separate quartz column using 0.16 N HCl.

The Nd isotopic measurements were made on a Thermo Finnigan Triton-TI thermal ionization mass spectrometer (TIMS) in static mode with relay matrix rotation. The results are shown in Table 3.4. The measured compositions of each sample are the mean of 125-130 analyses. Samples were measured in two separate batches. During the analysis of each batch the La Jolla Nd standard was measured six times giving a mean value of $^{143}Nd/^{144}Nd$ = 0.511857 ± 0.000008 (2σ) and 0.511858 ± 0.000006 (2σ) for the first and second batch, respectively. The three procedural duplicates are all within analytical error (2σ). All measurements were corrected for internal mass fractionation using $^{146}Nd/^{144}Nd = 0.7219$. The Nd isotopic compositions of the USGS G-2 reference material are within analytical error (2σ) of previously reported results (Weis et al., submitted). Due to very low Nd concentrations (0.01 ppm), the Nd isotopic composition of the DTS-2 reference material was not determined.

The Hf isotopic compositions were analyzed in static mode on the PCIGR Nu Plasma multi-collector inductively coupled plasma mass spectrometer (MC-ICP-MS) in the "dry" plasma mode using a desolvating nebulizer (DSN). Measured ratios and age-corrected values

Table 3.4: Hf and Nd isotopic compositions of marginal rocks from the Muskox intrusion.

Drillhole	MX03-001 (Far West Margin)									
Rock type	Chromite-rich Peridotite	Feldspathic Peridotite	Feldspathic Peridotite	Feldspathic Peridotite	Chromite-rich Peridotite	Chromite-rich Peridotite	Gabbronorite	Gabbronorite	Hornfelsed paragneiss	Granitic pod
Sample no.[1]	71064	71072a	71072b	71076	71078a	71078b	71082	71084	71094	71097
Drilled depth (m)	28.7	58.9	58.9	81.4	94.7	94.7	109.1	111.8	120.1	121.8
Distance (m)[2]	88.3	58.1	58.1	35.6	22.3	22.3	7.9	5.2	-3.1	-4.8
Lu (ppm)	0.07	0.09	0.09	0.11	0.08	0.10	0.23	0.18	0.33	0.34
Hf (ppm)	0.54	0.60	0.59	0.91	0.65	0.68	2.04	2.35	3.98	3.68
Lu/Hf	0.130	0.145	0.147	0.116	0.129	0.145	0.115	0.075	0.082	0.091
$^{176}Lu/^{177}Hf$	0.0184	0.0206	0.0209	0.0164	0.0184	0.0206	0.0163	0.0106	0.0116	0.0130
$^{176}Hf/^{177}Hf$ (m)	0.282088	0.282364	0.282375	0.282363	0.282373	0.282369	0.281911	0.281816	0.281646	0.281504
2σ	0.000004	0.000016	0.000014	0.000019	0.000008	0.000005	0.000008	0.000006	0.000007	0.000008
$^{176}Hf/^{177}Hf$ (i)	0.28163	0.28185	0.28186	0.28196	0.28192	0.28186	0.28151	0.28155	0.28136	0.28118
ε_{Hf}(i)	-11.2	-3.4	-3.3	0.3	-1.1	-3.2	-15.6	-14.0	-20.9	-27.2
t_{CHUR} (Ga)	2.34	1.65	1.65	1.25	1.37	1.63	2.57	2.15	2.63	3.15
t_{DM} (Ga)	2.93	2.52	2.53	2.05	2.22	2.50	3.04	2.61	3.01	3.44
Sm (ppm)	0.94	0.89	0.89	1.20	1.13	1.10	2.88	2.95	5.20	3.43
Nd (ppm)	3.62	3.44	3.44	4.78	4.29	4.07	14.25	14.58	31.07	18.19
Sm/Nd	0.259	0.258	0.258	0.251	0.264	0.270	0.202	0.202	0.167	0.188
$^{147}Sm/^{144}Nd$	0.1564	0.1559	0.1559	0.1517	0.1597	0.1634	0.1221	0.1223	0.1011	0.1138
$^{143}Nd/^{144}Nd$ (m)	0.511948	0.512196	0.512188	0.512118	0.512171	0.512177	0.511319	0.511378	0.511088	0.511086
2σ	0.000006	0.000011	0.000007	0.000008	0.000012	0.000010	0.000007	0.000006	0.000006	0.000006
$^{143}Nd/^{144}Nd$ (i)	0.51064	0.51090	0.51089	0.51085	0.51084	0.51081	0.51030	0.51036	0.51024	0.51014
ε_{Nd} (i)	-6.9	-2.0	-2.1	-2.8	-3.1	-3.6	-13.6	-12.5	-14.7	-16.8
t_{CHUR} (Ga)	2.59	1.65	1.68	1.76	1.92	2.10	2.68	2.57	2.46	2.84
t_{DM} (Ga)	3.17	2.50	2.52	2.53	2.75	2.93	3.03	2.93	2.78	3.13

All Hf ratios determined by MC-ICP-MS, Nd ratios determined by TIMS, and concentration data by HR-ICP-MS at the PCIGR, UBC. Initial ratios calculated a 1270 Ma using λ144Nd = 6.54x10-12 (Lugmair & Marti, 1978) and λ176Lu = 1.93x10-11 y-1 (Sguigua et al., 1982). Epsilon values and model ages calculatec using $177Hf/176Hf_{CHUR}$ = 0.282772 and $176Lu/177Hf_{CHUR}$= 0.0332 (Blichert-Toft & Albarède, 1997), $177Hf/176Hf_{DM}$ = 0.28325 and $176Lu/177Hf_{DM}$ = 0.0384; and $143Nd/144Nd_{CHUR}$ = 0.512638 and $147Sm/144Nd_{CHUR}$ = 0.1967 (DePaolo & Wasserburg, 1976), $143Nd/144Nd_{DM}$ = 0.51314 and $147Sm/144Nd_{DM}$ = 0.2137.

[1]Procedural duplicates are denoted 'a' and 'b'.

[2]Drilled distance in metres from the outer intrusive contact.

Table 3.4 (continued): Hf and Nd isotopic compositions of marginal rocks from the Muskox intrusion.

Drillhole	MX03-002 (West Pyrrhotite Lake)								
Rock type	Peridotite	Peridotite	Feldspathic Peridotite	Feldspathic Peridotite	Feldspathic Peridotite	Olivine gabbronorite	Gabbronorite	Gneiss	Gneiss
Sample no.[a]	71106	71115	71122	71128a	71128b	71133	71138	71141	71147
Drilled depth (m)	31.8	72.5	113.0	149.3	149.3	162.8	173.6	179.3	200.9
Distance (m)[b]	145.2	104.5	64.0	27.7	27.7	14.2	3.4	-2.3	-23.9
Lu (ppm)	0.06	0.08	0.08	0.13	0.14	0.18	0.17	0.23	0.24
Hf (ppm)	0.63	0.59	0.70	1.49	1.46	1.49	1.66	6.95	6.61
Lu/Hf	0.097	0.132	0.121	0.088	0.094	0.119	0.102	0.033	0.036
$^{176}Lu/^{177}Hf$	0.0137	0.0187	0.0171	0.0125	0.0134	0.0168	0.0145	0.0047	0.0051
$^{176}Hf/^{177}Hf$ (m)	0.282340	0.282313	0.282350	0.282317	0.282318	0.282292	0.282157	0.281246	0.281394
2σ	0.000005	0.000008	0.000004	0.000008	0.000009	0.000009	0.000018	0.000004	0.000004
$^{176}Hf/^{177}Hf$ (i)	0.28200	0.28185	0.28192	0.28201	0.28199	0.28187	0.28180	0.28113	0.28127
ε_{Hf} (i)	1.8	-3.5	-0.8	2.1	1.4	-2.6	-5.3	-29.0	-24.1
t_{chur} (Ga)	1.14	1.61	1.34	1.13	1.17	1.50	1.67	2.70	2.48
t_{DM} (Ga)	1.88	2.41	2.15	1.83	1.89	2.25	2.31	2.99	2.81
Sm (ppm)	0.83	0.95	1.08	1.87	1.87	2.52	1.96	3.38	4.41
Nd (ppm)	3.58	3.88	4.38	7.98	7.98	10.38	9.52	19.62	25.84
Sm/Nd	0.232	0.244	0.246	0.234	0.234	0.243	0.206	0.172	0.171
$^{147}Sm/^{144}Nd$	0.1402	0.1476	0.1490	0.1413	0.1413	0.1469	0.1243	0.1041	0.1031
$^{143}Nd/^{144}Nd$ (m)	0.512195	0.512190	0.512190	0.512168	0.512185	0.512167	0.511754	0.511086	0.511121
2σ	0.000008	0.000006	0.000006	0.000006	0.000006	0.000006	0.000006	0.000007	0.000006
$^{143}Nd/^{144}Nd$ (i)	0.51103	0.51096	0.51095	0.51099	0.51101	0.51094	0.51072	0.51022	0.51026
ε_{Nd} (i)	0.5	-0.8	-1.0	-0.2	0.2	-1.1	-5.5	-15.3	-14.4
t_{chur} (Ga)	1.20	1.39	1.43	1.29	1.25	1.44	1.86	2.54	2.46
t_{DM} (Ga)	1.98	2.20	2.25	2.06	2.03	2.23	2.37	2.85	2.78

All Hf ratios determined by MC-ICP-MS, Nd ratios determined by TIMS, and concentration data by HR-ICP-MS at the PCIGR, UBC. Initial ratios calculated a 1270 Ma using λ144Nd = 6.54x10-12 (Lugmair & Marti, 1978) and λ176Lu = 1.93x10-11 y-1 (Sguigua et al., 1982). Epsilon values and model ages calculate using $177Hf/176Hf_{CHUR}$ = 0.282772 and $176Lu/177Hf_{CHUR}$= 0.0332 (Blichert-Toft & Albarède, 1997), $177Hf/176Hf_{DM}$ = 0.28325 and $176Lu/177Hf_{DM}$ = 0.0384; and $143Nd/144Nd_{CHUR}$ = 0.512638 and $147Sm/144Nd_{CHUR}$ = 0.1967 (DePaolo & Wasserburg, 1976), $143Nd/144Nd_{DM}$ = 0.51314 and $147Sm/144Nd_{DM}$ = 0.2137.

[1]Procedural duplicates are denoted 'a' and 'b'.

[2]Drilled distance in metres from the outer intrusive contact.

are shown in Table 3.4. The measured compositions of each sample are the mean of 25-30 cycles. The measured Hf isotopic ratios were corrected for interferences by monitoring Lu and Yb beams throughout each analysis. Samples were measured in three separate batches. Replicate measurements of the Hf JMC 475 in-house standard gave a mean value of $^{176}Hf/^{177}Hf = 0.282148 \pm 0.000006$ (2σ on 10 measurements) for the first batch and 0.292151 ± 0.000007 (2σ on 11 measurements) for both the second and third batches; the values are within the range of previously published values (Blichert-Toft et al., 1997; Chauvel & Blichert-Toft, 2001; Goolaerts et al., 2004). The three procedural duplicates are within analytical error (2σ). All reported values were normalized to $^{176}Hf/^{177}Hf = 0.282160$ as suggested by Vervoort & Blichert-Toft (1999). The Hf isotopic compositions of the USGS G-2 reference material are within analytical error (2σ) of previously reported results (Weis et al., submitted). As a result of the very low Hf concentrations (<0.004 ppm) of the DTS-2 reference material, its Hf isotopic compositions have not been previously published and therefore the accuracy of the results for this material cannot be verified.

3.5 RESULTS

3.5.1 U-Pb geochronology

The U-Pb concentrations and isotopic compositions of baddeleyite from two peridotites and one gabbronorite sample from the marginal rocks of the Muskox intrusion are shown in Table 3.1 and displayed on concordia diagrams in Fig. 3.4. The concentrations of U and Pb for each fraction range from 170-840 ppm to 55-160 ppm, respectively. The high $^{206}Pb/^{204}Pb$ values (1000 to 15,000) indicate a negligible contribution of initial common Pb. The U-Pb data for all fractions from all three samples plot near concordia (<2% discordance), which is consistent with closed-system behavior with respect to U-loss or Pb-gain since the time of crystallization (Fig. 3.4). Table 3.2 summarizes the different U-Pb age calculation methods applied to each sample as discussed below.

Sample 71064 was collected from a chromite-rich peridotite layer within the layered series at the Far West Margin section (Fig. 3.2 & 3.3). The chromite-rich peridotite consists of cumulus olivine and chromite enclosed within orthopyroxene oikocrysts (up to 2 cm across) and minor interstitial plagioclase and phlogopite. The U-Pb data for five fractions of baddeleyite are nearly concordant (<1.5% discordance) with apparent $^{207}Pb/^{206}Pb$ ages ranging from 1267 to 1271 Ma (Table 3.1). Linear regression through the data points results in an

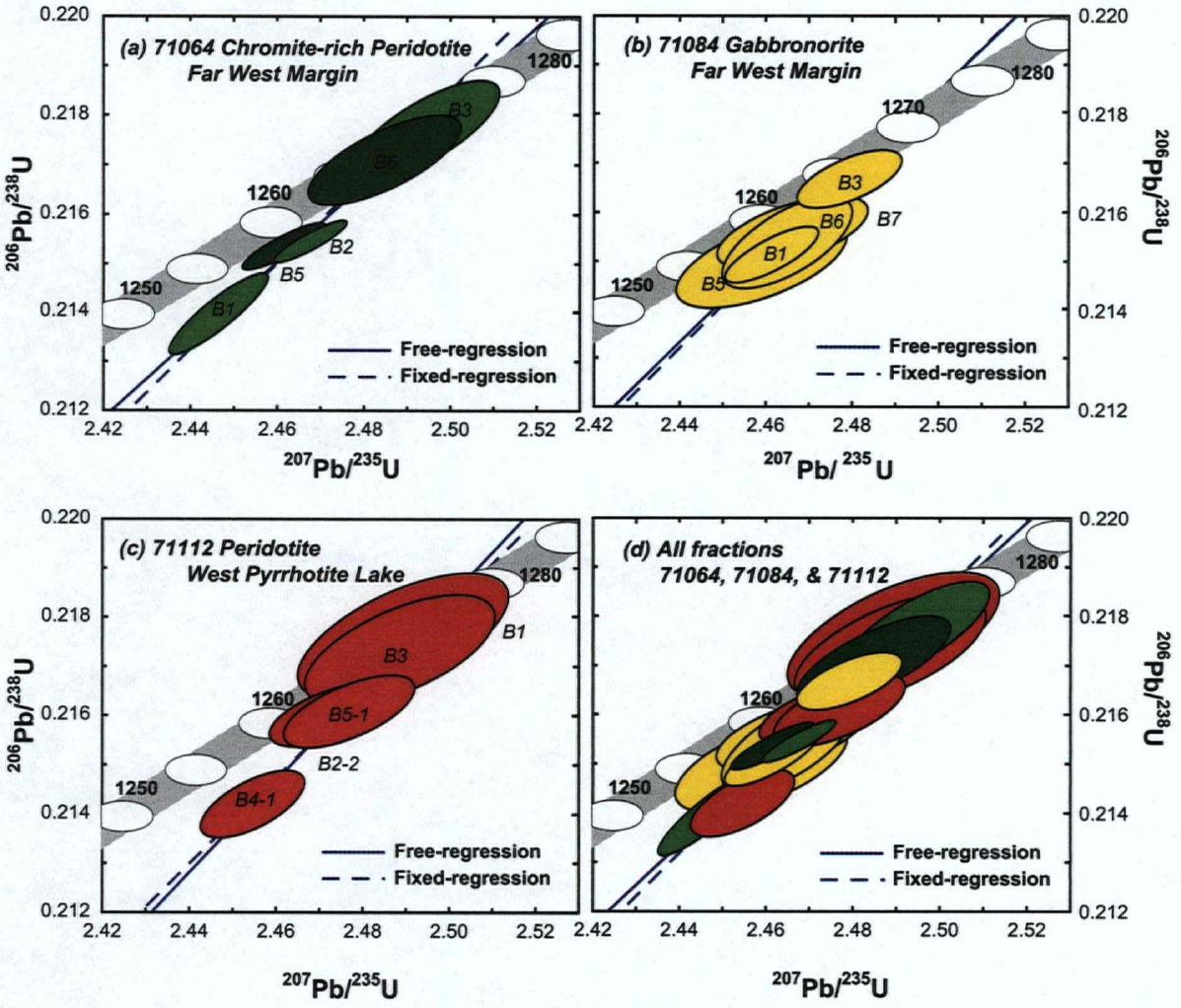

Fig. 3.4: Concordia diagrams showing U-Pb geochronologic results for baddeleyite fractions separated from three samples at two different locations within the Muskox intrusion. (a) Chromite-rich peridotite (71064), Far West Margin; (b) Gabbronorite (71084), Far West Margin; (c) Peridotite (71112), West Pyrrhotite Lake; (d) All samples (71064, 71084 & 71112). Individual fractions are represented by a 2σ error ellipse and are labelled B1, B2, etc. Diagrams were made with Isoplot/Ex 3.0 including the error on concordia and using both free-fit and fixed-zero regression methods, as indicated. See text for interpretation of results.

upper intercept with concordia at 1271 ± 6 Ma (2σ) using a free-fit regression method and 1269 ± 2 (2σ) Ma using a forced-zero regression method (Table 3.2; Fig. 3.4a). The weighted-mean of two concordant fractions gives an apparent age of 1268 ± 3 Ma (2σ), which is considered the best estimate for the crystallization age of this chromite-rich layer in the Muskox intrusion.

Sample 71084 was collected from a gabbronorite unit within the marginal zone of the intrusion at the Far West Margin (Fig. 3.2 & 3.3). The gabbronorite consists of cumulus orthopyroxene (and minor clinopyroxene) that partially enclose subhedral calcic-plagioclase laths and interstitial phlogopite, sodic-plagioclase, and minor granophyre. The U-Pb data for five baddeleyite fractions are nearly concordant (<1.0% discordance) and all give apparent $^{207}Pb/^{206}Pb$ ages of 1268 Ma. Linear regression through the data points intercepts concordia at 1269 ± 9 Ma (2σ) using a free-fit regression and 1269 ± 3 (2σ) Ma using a forced-zero regression (Table 3.2; Fig. 3.4b). Because all data points are nearly equivalent and plot close to concordia, the free-fit regression results in large uncertainties. Therefore, the intercept with concordia using the forced-zero regression method is interpreted as the crystallization age of the sample, which is within error of the interpreted crystallization age of the chromite-rich peridotite layer (sample 71064).

Sample 71112 was collected near the base of the intrusion from the innermost part of the marginal zone at West Pyrrhotite Lake (Fig. 3.2 & 3.3). The peridotite consists of closely-packed cumulus olivine enclosed within orthopyroxene and clinopyroxene oikocrysts. Plagioclase and phlogopite are minor interstitial phases. The U-Pb data for five fractions of baddeleyite are nearly concordant (<2.0% discordance) with apparent $^{207}Pb/^{206}Pb$ ages ranging from 1268 to 1272 Ma (Table 3.1). Linear regression through the data points gives an upper intercept with concordia at 1270 ± 6 Ma (2σ) using a free-fit regression and 1271 ± 4 Ma (2σ) using a forced-zero regression (Table 3.2; Fig. 3.4c). The weighted-mean of two concordant fractions gives an apparent age of 1269 ± 3 Ma (2σ), which is considered the best estimate for the crystallization age of the peridotite and is within error of the interpreted crystallization ages of both the gabbronorite and chromite-rich peridotite samples discussed above.

The interpreted crystallization ages of each sample are within analytical uncertainty and therefore all data can be treated together. Linear regression through all 15 baddeleyite fractions gives an upper intercept with concordia at 1271± 4 Ma (2σ) using a free-fit regression and 1269 ± 5 Ma (2σ) using a forced-zero regression (Table 3.2; Fig. 3.4d). If it is

assumed that each of the samples crystallized contemporaneously and disregard fractions where the grains have experienced minor Pb loss, then the best estimate for the crystallization age of the Muskox intrusion is 1269 ± 2 Ma based on four concordant analyses, which is within error of a previously reported U-Pb age of 1270 ± 4 Ma (baddeleyite and zircon) by LeCheminant & Heaman (1989) for a pyroxenite layer within the upper part of the layered series of the Muskox intrusion.

3.5.2 Trace element variations

The stratigraphic variations in parent-daughter elemental concentrations and ratios for the Sm-Nd and Lu-Hf systems from both the West Pyrrhotite Lake and Far West Margin sections are shown in Fig. 3.5. At West Pyrrhotite Lake the abundances of incompatible trace elements (Sm, Nd, Lu, Hf) are constant within peridotite and then progressively increase through the feldspathic peridotite and olivine gabbronorite units (Fig. 3.5). This trend is expected from the progressive increase in the amount of postcumulus phases (pyroxene and plagioclase) at the expense of olivine, because the partition coefficients for incompatible trace elements in pyroxene and plagioclase are much larger than those for olivine (e.g. McKenzie & O'Nions, 1991). At the Far West Margin, trace element abundances are relatively constant within both chromite-rich horizons and feldspathic peridotite, with the exception of a slight relative increase within the lowermost feldspathic peridotite sample (Fig. 3.5). The Sm/Nd values are relatively high and constant within the peridotites at both sections and then decrease within gabbronorite towards the values typical of the adjacent country rocks. This shift is consistent with the effects of crustal contamination. The Lu/Hf values are variable within peridotites at both locations. The reason for this is uncertain however. It may reflect the heterogeneous distribution of accessory phases (baddeleyite?) that crystallized from local pockets of extremely fractionated interstitial liquids. Alternatively, fluctuations in this ratio may be the result of slight mobility of Lu and Hf during post-crystallization alteration/metasomatism (i.e. high Lu/Hf in the stratigraphically lower serpentinized peridotite sample from West Pyrrhotite Lake section).

Primitive mantle-normalized trace element patterns and chondrite-normalized rare earth element (REE) patterns for marginal rocks from West Pyrrhotite Lake and Far West Margin are shown in Fig. 3.6. All intrusive rocks at both sections are enriched in light rare earth elements (LREE) and large ion lithophile elements (LILE) relative to heavy rare earth

(a) West Pyrrhotite Lake

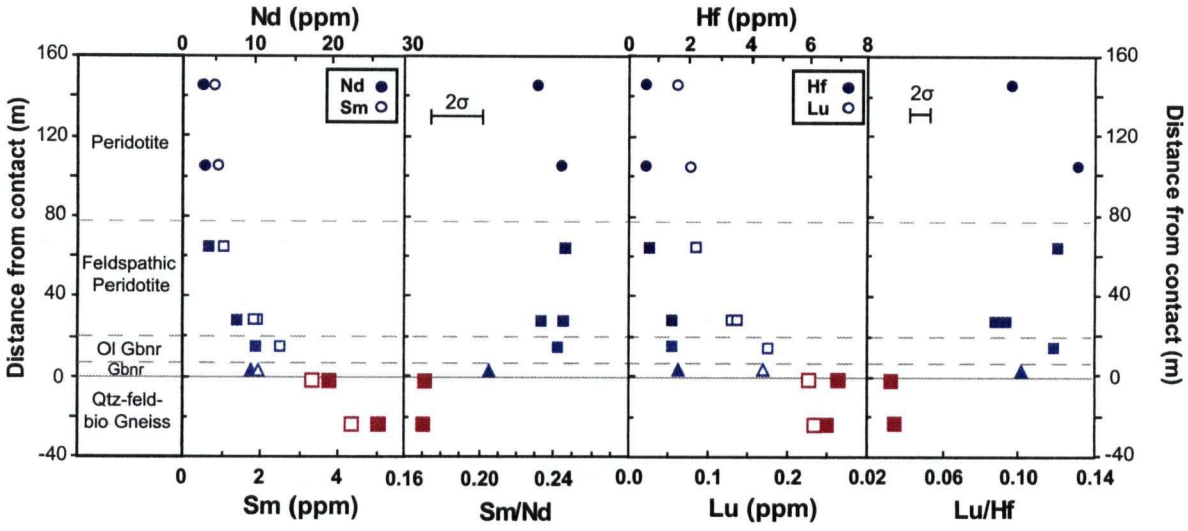

(b) Far West Margin

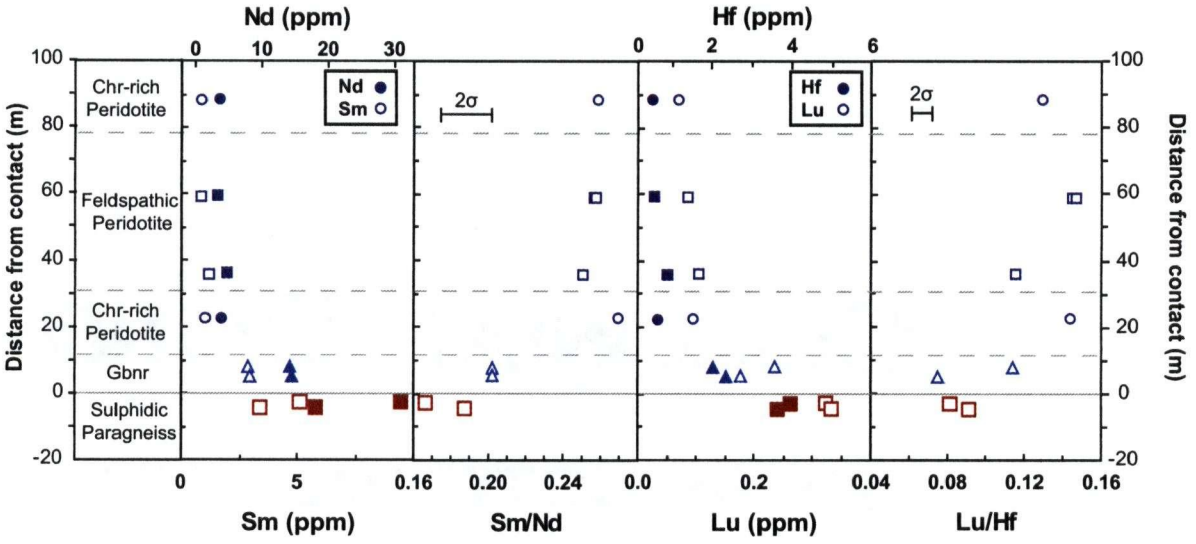

Fig. 3.5: Parent-daughter (Sm-Nd, Lu-Hf) elemental concentrations and ratios for the (a) West Pyrrhotite Lake and (b) Far West Margin sections of the Muskox intrusion. Elemental concentrations for Sm (open symbols) and Nd (closed symbols), and for Lu (open symbols) and Hf (closed symbols), are plotted within the same graph. Abbreviations: Chr-rich = chromite-rich; Ol Gbnr = olivine gabbronorite, Gbnr = gabbronorite, and Qtz-feld-bio = quartz-feldspar-biotite. Distance from contact = distance from contact in metres along the drill hole. Average analytical error (2σ) is equal to, or less than, symbol size unless otherwise shown.

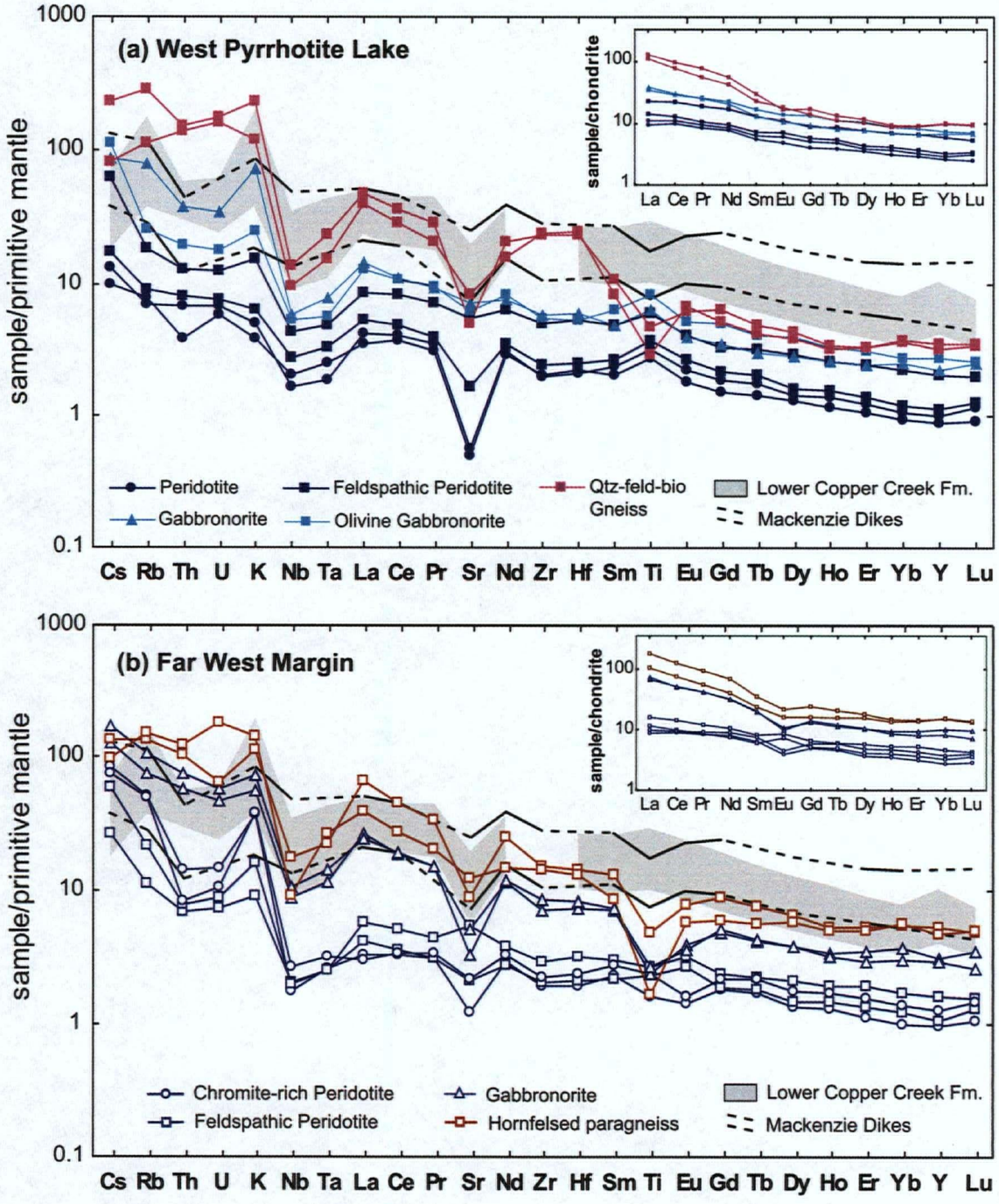

Fig. 3.6: Primitive mantle-normalized trace element patterns of all samples from the (a) West Pyrrhotite Lake and (b) Far West Margin sections of the Muskox intrusion. Chondrite-normalized rare earth element patterns are shown in the insets. Element incompatibility increases to the left in each diagram and normalizing values are from McDonough & Sun (1995). The shaded region represents the range observed in basalts from the Copper Creek Formation (Griselin et al., 1997) and the region between solid and dashed lines represents that of the Mackenzie dikes (Baragar et al., 1996). All samples from both sections, including the peridotites, are relatively enriched in LREE and LILE and have prominent Nb-Ta depletions. The Lower Copper Creek Formation and Mackenzie dikes have comparable enriched patterns and Nb-Ta depletions.

elements (HREE). The degree of enrichment within the Muskox intrusion rocks is lowest in peridotite, feldspathic peridotite, olivine gabbronorite, and chromite-rich peridotite (La/Yb(pm)= 2.5 to 4.5). The gabbronorites have more enriched patterns (La/Yb(pm) = 5.0 to 7.7) approaching those of the crustal rocks (La/Yb(pm) = 4.5 to 7.7). The increased degree of trace element enrichment within the gabbronoritic rocks at the margin is consistent with the addition of crustal material. The shapes of the trace element patterns observed for the intrusive rocks are broadly similar to those of the Mackenzie dikes (Baragar et al., 1996) and Coppermine River flood basalts (Griselin et al., 1997), especially when compared to the gabbronorites. All intrusive rocks and crustal rocks at both sections, with the exception of the chromite-rich horizons, are relatively depleted in Nb-Ta (Fig. 3.6). This signature is typical of crustal rocks and can be used as a proxy for crustal contamination within mantle-derived basaltic rocks (e.g. Rudnick & Fountain, 1995). The fact that Nb-Ta depletion is observed even within the peridotites may reflect contamination of the Muskox magmas prior to emplacement (see discussion). The chromite-rich peridotite horizons have relatively flat LREE patterns compared to the other peridotite samples, which likely is a consequence of the relatively high modal abundance of orthopyroxene in these samples (e.g. McKenzie & O'Nions, 1991).

3.5.3 Hf-Nd Isotopic Variations

Age-corrected (1270 Ma) epsilon Hf-Nd values for samples from both the West Pyrrhotite Lake and Far West Margin section are plotted against the distance from the margin in Fig. 3.7. The peridotite and olivine gabbronorite samples from the West Pyrrhotite Lake section have a relatively restricted range in initial ε_{Hf} (+2 to -4) and ε_{Nd} (-1.0 to 0.5). These results overlap with previously published results for the overlying layered series for ε_{Nd} (Stewart & DePaolo, 1996) and unpublished ε_{Hf} results from Purves (2005). The gabbronorite samples within 10 m of the margin however have more negative initial ε_{Hf} (-2.5 to -5.0) and initial ε_{Nd} (-1.0 to -5.5) values. The crustal rocks are characterized by very negative ε_{Hf} (-24 to -29) and ε_{Nd} values (-14 to -15) that are consistent with their relatively low Lu/Hf and Sm/Nd, and time-integrated enrichment of Hf relative to Lu and Nd relative to Sm since formation of these rocks (Fig. 3.5). The shift to more negative values within the gabbronorites coincides with the appearance of both granophyre and euhedral orthopyroxene. The feldspathic peridotite and the lower chromite-rich peridotite samples at the Far West Margin section have initial ε_{Hf} (0 to -3.0) and

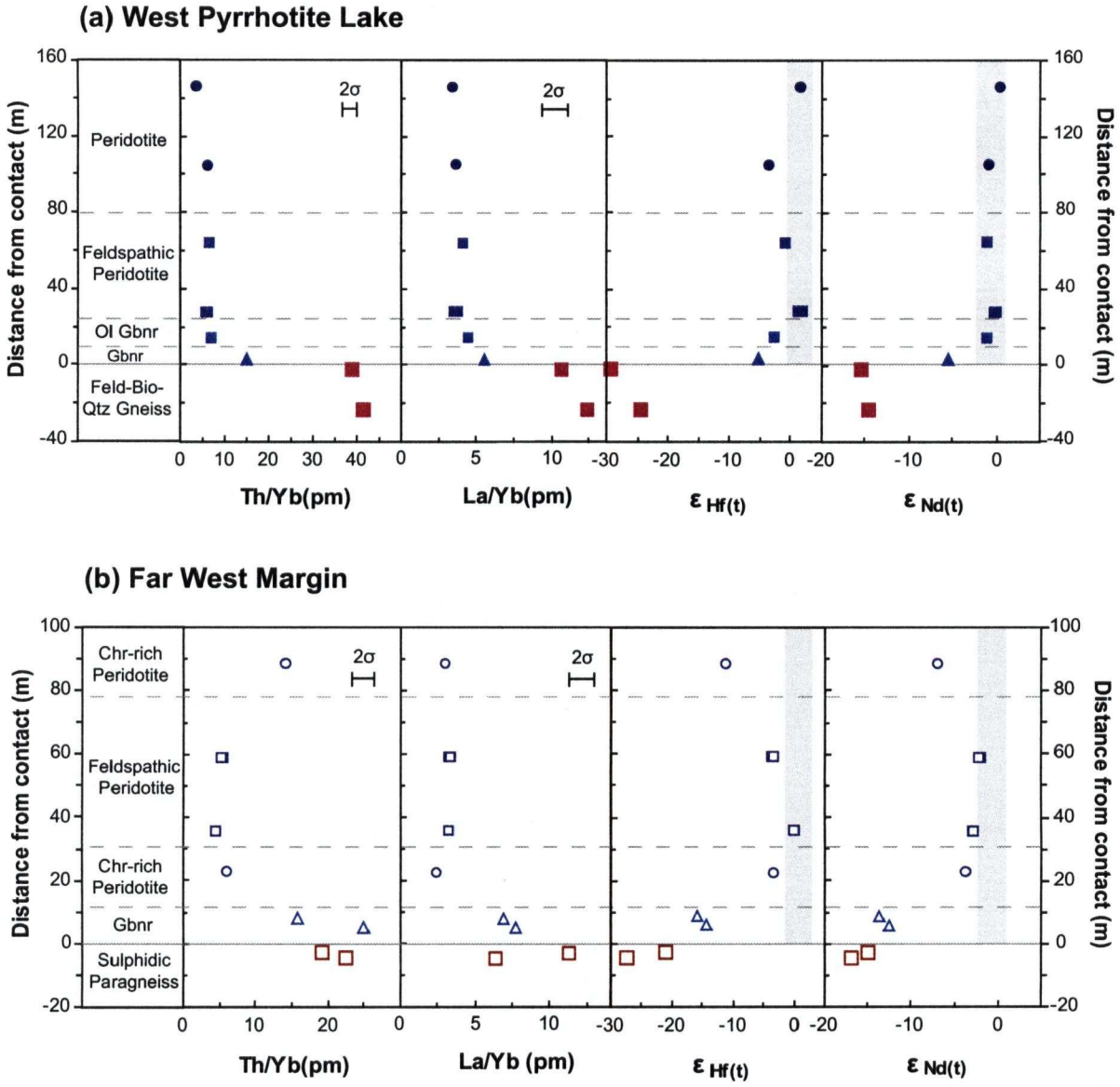

Fig. 3.7: Stratigraphic variations in Th/Yb(pm), La/Yb(pm), $\varepsilon_{Hf(t)}$, and $\varepsilon_{Nd(t)}$ values for the (a) West Pyrrhotite Lake and (b) Far West Margin sections of the Muskox intrusion, where (pm) refers to the primitive-mantle normalized ratio and (t) equals 1.27 Ga. Symbols and abbreviations are the same as for Fig. 3.6. Uncertainty in trace element ratios is estimated from the average analytical uncertainty of all samples. The shaded region indicates the range in published initial ε_{Nd} (Stewart & DePaolo, 1996) and reported initial ε_{Hf} (Purves et al., 2005) for rocks of the overlying layered series for comparison. The shift towards lower Th/Yb(pm) and La/Yb(pm), and higher $\varepsilon_{Hf(t)}$ and $\varepsilon_{Nd(t)}$, at the transition from peridotite to gabbronorite within ~10 m from the contact is consistent with the affects of local crustal contamination. The $\varepsilon_{Hf(t)}$ and $\varepsilon_{Nd(t)}$ values within the peridotites are relatively constant and are comparable to those of the layered series, with the exception of the upper chromite-rich peridotite at the Far West Margin section. The relatively low Th/Yb(pm) and La/Yb(pm), and high $\varepsilon_{Hf(t)}$ and $\varepsilon_{Nd(t)}$ values within the peridotites indicate that they formed from magmas that were not exposed to local crustal contamination.

initial ε_{Nd} (-2.0 to 2.8) values that are within error of the initial epsilon values reported for the layered series (references noted above). The chromite-rich peridotite sample at the top of the section, however, has considerably more negative initial ε_{Hf} and ε_{Nd} values (-11 and -7, respectively) than the other peridotites. As with the West Pyrrhotite Lake section, the gabbronorite samples within the Far West Margin section have low initial ε_{Hf} (-14 to -15) and initial ε_{Nd} (-12 to -13) values and likely represent strongly contaminated marginal rocks.

3.5.4 Alteration/metasomatic effects?

Although the HFSE and HREE (including Sm-Nd and Lu-Hf) are typically considered to be immobile during hydrothermal alteration, several studies of altered komatiitic and basaltic rocks (e.g. Lahaye et al., 1995; Polat et al., 2003) have demonstrated that this is not always the case and, importantly, perturbations in the values of Rb/Sr, Sm/Nd, and Lu/Hf correlate with anomalous isotopic compositions. Given the presence of secondary mica in the chromite-rich peridotite horizons, the anomalous isotopic and trace element compositions of sample 71064 need to be evaluated. Sample 71064 was collected from a chromite-rich peridotite horizon within the upper part of the Far West Margin section (Fig. 3.3). The sample has anomalously low initial ε_{Nd} (-6.9), initial ε_{Hf} (-11.2), and La/Yb(pm) (3.0), and high Th/Yb(pm) (2.6) values and positive K anomalies compared to those of all other peridotite samples (Fig. 3.6 & 3.7). The elevated Th/Yb and K values are a typical feature of both chromite-rich horizons, which suggests that K, and possibly other LILE, may have been added during or after serpentinization. However, given that the Sm/Nd and Lu/Hf ratios of the chromite-rich peridotite are comparable to those of the adjacent peridotites (Fig. 3.5), it is suggested that the relatively low initial epsilon values of the chromite-rich peridotite are reflective of the magma from which they crystallized and have not been affected by secondary alteration processes.

3.6 DISCUSSION

Using the new U-Pb geochronologic, trace element, and Hf-Nd isotopic results obtained during this study, below we provide constraints on (1) the magnitude and spatial extent of crustal contamination along the basal margin of the Muskox intrusion, (2) the timing of emplacement of the Muskox intrusion and the genetic relationship between the Muskox intrusion and the other elements of the Mackenzie magmatic event, especially the overlying Coppermine River basalts, and (3) the composition of the mantle source for the Muskox magmas and potential influence of crustal contamination prior to emplacement within the Muskox chamber. Finally, we provide a brief synthesis of the evolution of the Mackenzie event based on the results of this study combined with previous investigations of the different Mackenzie components.

3.6.1 Spatial extent and degree of crustal contamination within marginal rocks of the Muskox intrusion

Variations in initial ε_{Hf} and ε_{Nd} values and incompatible trace element ratios from the marginal zone of the Muskox intrusion provide important constraints on the extent and degree of crustal contamination that occurred along the basal contact of the intrusion, which has important implications for the emplacement history of the Muskox intrusion and the potential for magmatic sulphide mineralization. At both West Pyrrhotite Lake and Far West Margin, the gabbronoritic marginal rocks have more negative initial ε_{Hf} and ε_{Nd} values and higher Th/Yb(pm) and La/Yb(pm) values than the directly overlying peridotites (Fig. 3.7). Thus, the chemical effects of crustal contamination are restricted to the orthopyroxene- and granophyre-bearing rocks within 10 m from the outer contact. A similar thickness of contaminated gabbronorite was noted by Francis (1994) in his study of marginal zone rocks along the eastern margin of the intrusion. This limited extent of contamination recorded within the gabbronoritic marginal rocks is the result of local contamination of the magmas (potentially partially solidified) along the outer walls of the Muskox magma chamber. The addition of siliceous material led to a local increase in silica activity, which stabilized orthopyroxene over olivine (e.g. Irvine, 1970). Because of the heat loss to the surrounding rocks the contaminated magmas would have solidified rapidly (see Chapter 2) and would have prevented subsequent magma influxes from interacting with the surrounding crustal rocks. This explains the uncontaminated signatures within the peridotites at both sections and throughout the layered

series. An apparent exception to this is the anomalously low initial ε_{Hf} and ε_{Nd} values within the upper chromite-rich peridotite at the Far West Margin. This peridotite may represent a cumulate layer that accumulated from an influx of contaminated magma during construction of this part of the marginal zone, or potentially assimilation of overlying roof rocks.

The approximate amount of crustal contamination within the gabbronoritic marginal rocks can be estimated using binary mixing relationships (Fig. 3.8). As a parental magma composition the isotopic composition of a relatively uncontaminated peridotite from the West Pyrrhotite Lake (initial ε_{Hf}= 1.3; initial ε_{Nd} = 0.2) and Far West Margin sections (initial ε_{Hf}= -3; initial ε_{Nd} = -2) and the trace element concentrations of a lower Copper Creek Formation basalt from the overlying Coppermine River basalts are used (Table 3.5). The contaminant, in terms of isotopic and trace element composition, is given by the average country rock composition at each section. The binary mixing calculations assume simple end-member mixing with no associated fractional crystallization and provide a first-order estimate of the different amounts of crustal material added to the Muskox magmas at the two studied locations. In Fig 3.8, the initial ε_{Hf} and ε_{Nd} isotopic compositions of the marginal rocks from the Muskox intrusion and country rocks are plotted against two different incompatible element ratios (Th/Yb(pm), Sm/Ti(pm)) that have different sensitivities to contamination and that show the effects of assimilating host rocks of different compositions. In general, rocks from the thin gabbronoritic subzone plot along the mixing arrays, which is consistent with contamination by local assimilation of the adjacent crustal rocks. The calculated degree of contamination within the gabbronorite at West Pyrrhotite Lake is ~20% with respect to the Sm-Nd isotopic system and ~40% with respect to Lu-Hf. For the gabbronorite at Far West Margin, the degree of contamination is considerably higher at >80% for both the Sm-Nd and Lu-Hf systems. As documented in Chapter 2, the difference in amount of contamination at the two studied regions likely reflects the greater ability of the Muskox magmas to assimilate the paragneiss at the Far West Margin than the quartz-feldspar-biotite gneiss at West Pyrrhotite Lake. The actual composition of the contaminant could have been derived through bulk assimilation, partial melting, and/or diffusive exchange with the wall rocks during the formation of the Muskox magma chamber. Stewart & DePaolo (1992) showed that diffusive exchange between a lens of melted roof rock and underlying basaltic magma could explain the decoupling of Nd and Sr isotopic systematics; a consequence of the high relative diffusivity of Sr relative to Nd in silicate melts. Assuming that Hf diffusivity is comparable to that of Nd, diffusive exchange is

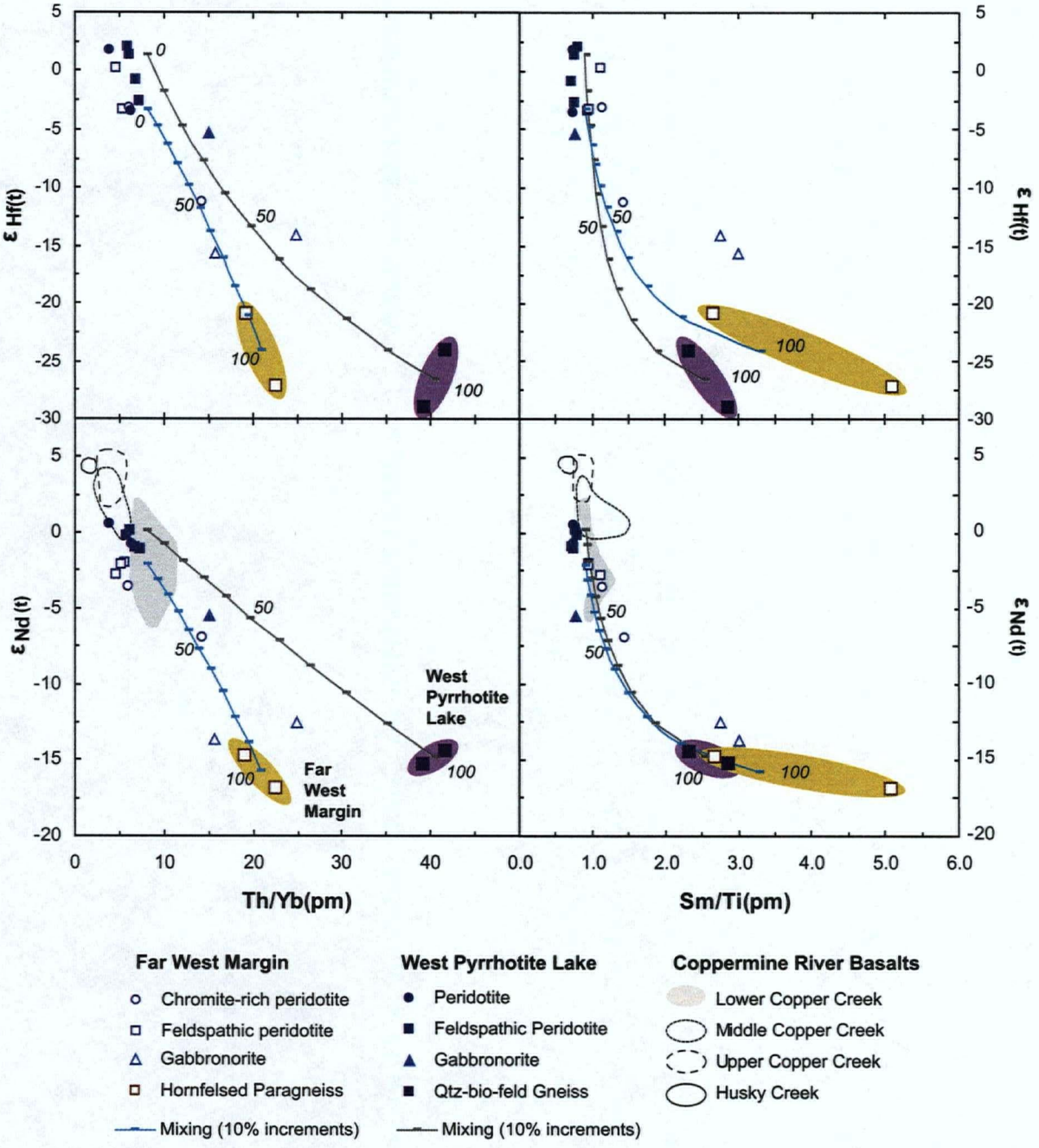

Fig. 3.8: Initial εHf(t) and εNd(t) isotopic compositions vs. selected incompatible trace element ratios for marginal rocks from the Muskox intrusion showing the results of binary mixing calculations. Mixing lines are calculated for the parental magma to the marginal zone using the isotopic composition of a relatively uncontaminated peridotite from each respective locality and the trace element composition of a lower Copper Creek Formation basalt for the parental magma composition, and the isotopic composition and trace element abundances of the average wall rock composition at each locality. Tick marks along curves indicate the addition of crustal material at increments of 10%. Gabbronorite samples plot along the mixing lines between the assumed parental magma composition and the average wall rock sample at both the West Pyrrhotite Lake and Far West Margin sections.

Table 3.5: Composition of Muskox magmas and potential contaminants used in mixing calculations.

Section	West Pyrrhotite Lake		Far West Margin	
Endmember[1]	Magma	Contaminant	Magma	Contaminant
Th (ppm)	4.2	11.6	4.2	9.2
Yb	2.8	1.6	2.8	2.4
Sm	8.5	3.9	8.5	4.3
Ti	28100	4550	28100	3880
$\varepsilon_{Hf(t)}$	1.3	-27	-2.1	-16
$\varepsilon_{Nd(t)}$	0.2	-15	-3.2	-24

[1]Composition of Muskox magma estimated from the trace element abundances of a lower Copper Creek basalt (Griselin et al., 1997) and the isotopic composition of Muskox marginal zone rocks (this study); Composition of the contaminant is taken as the average country rock composition at each studied section.

unlikely to produce variations in the Nd and Hf isotopic compositions of the marginal rocks. Francis (1994) proposed that the contamination process within the marginal rocks of the Muskox intrusion may have been selective, because the estimated level of enrichment within the contaminated rocks depended on which trace element ratio was used. For example, when using LILE/HFSE the level of enrichment was considerably greater (30-50%) than using LREE/HFSE (10-30%). We observe a similar relationship and estimate variable degrees of contamination within the gabbronoritic marginal rocks with respect to Nd and Hf isotopic compositions and different trace element ratios. In plots of K/Yb vs. K/Ti the estimated degree of contamination is 50%, and using Sm/Ti vs. K/Ti it is approximately 30% (not shown). This feature is likely the combined result of the relative compatibilities between LILE vs. HREE during partial melting of the crustal rocks, and also the preferred diffusive exchange for the most incompatible elements as documented by Stewart & DePaolo (1992). The presence of granophyre globules within the gabbronorites at both sections indicates that the contaminated signature was in part derived directly through the addition of partial melts from the adjacent rocks that did not fully mix with the magmas along the outer wall of the Muskox chamber. The appearance of early-forming cumulus orthopyroxene indicates that contamination also involved some amount of complete mixing of crustal material with the Muskox magmas along the contact region.

3.6.2 Temporal relationships and isotopic compositions of the Muskox intrusion, Coppermine River basalts, and Mackenzie dikes

The U-Pb geochronologic and Nd isotopic compositions from the marginal rocks of the Muskox intrusion determined in this study can be used to better constrain the genetic relationships between the different members of the Mackenzie magmatic event. U-Pb ages obtained in this study indicate that rocks within the marginal zone (including contaminated gabbronorite) crystallized within error of each other at ~1269 Ma. They are also within error of a previous U-Pb age (baddeleyite and zircon) of 1270 ± 4 Ma reported by LeCheminant & Heaman (1989) for a feldspathic pyroxenite layer within the layered series, confirming that the entire Muskox intrusion crystallized within a few million years (Fig. 3.9). This is consistent with the estimated duration of emplacement for the Muskox intrusion of 50,000-100,000 years, as predicted by Stewart & DePaolo (1992) on the basis of the timescale for diffusive isotopic exchange between basaltic magma within the chamber and an overlying silicic magma derived

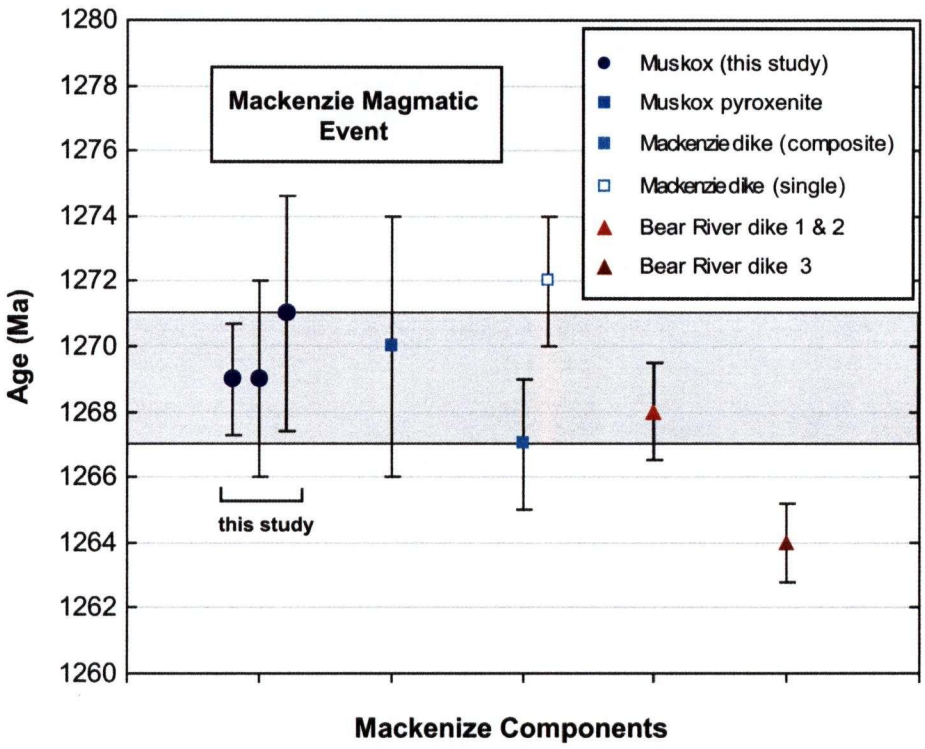

Fig. 3.9: Compilation of precise U-Pb ages for Mackenzie magmatic event samples. The ages are concordia-intercept ages for the Muskox intrusion (this study; and LeCheminant & Heaman, 1989), Mackenzie dikes (LeCheminant & Heaman, 1989; 1991), and Bear River dikes (Schwab et al., 2004). Error bars are the reported 2σ analytical uncertainties. The shaded region represents the weighted mean of 4 concordant fractions from the two studied sections and the associated 2σ uncertainty as described in the text.

through melting of the overlying roof rocks. Precise U-Pb concordia-intercept ages for the emplacement of the Mackenzie dikes (1267 ± 2 Ma; LeCheminant & Heaman, 1989) and two dikes from the Bear River region of the Yukon Territory (1268 ± 2 Ma; Schwab et al., 2004) overlap with the crystallization age of the Muskox intrusion (1269 ± 2 Ma; this study) (Fig. 3.8). Field relations demonstrate that the Mackenzie dikes cross-cut and are cut by the Muskox intrusion, supporting their synchronous emplacement (Fig. 3.2) (Smith, 1962). The age of the Coppermine River basalts is not well constrained (1257 ± 45 Ma, Rb-Sr isochron; Wandless & Loveridge, 1972) however, their temporal relationship with Muskox intrusion comes from the observation that most of the Mackenzie dikes (emplaced synchronously with the Muskox intrusion) terminate within the lower Copper Creek Formation basalts (Baragar, 1969).

A compilation of all available Nd isotopic compositions from the Muskox intrusion (this study & Stewart & DePaolo, 1996), Mackenzie dikes (unpublished; Dundas & Peterson, 1992), and Coppermine River flood basalts (Griselin et al., 1997) is shown with respect to relative stratigraphic position in Fig. 3.10. The initial ε_{Nd} values of the layered series and the peridotite portion of the marginal zone of the Muskox intrusion overlap with those of basalts in the lowermost 1000 m of the Copper Creek Formation and some of the Mackenzie dikes, and they are distinctly more negative than those of the basalts at higher stratigraphic levels (Fig. 3.10). This observation indicates that only the lowermost flows of the Coppermine River basalts could be directly related to magmas that produced the Muskox intrusion. These basalts may represent residual magmas after the removal of olivine within the Muskox chamber given their relatively low MgO contents (5-10 wt %; Baragar, 1969) compared to the proposed picritic parental magmas to the Muskox intrusion (14 wt % MgO; Irvine, 1977). The overlying Husky Creek Formation basalts formed from magmas that apparently bypassed the Muskox chamber and erupted through a separate conduit system. Assuming that the lower Coppermine River basalts are directly related to the Muskox intrusion, this also suggests that the Muskox intrusion remained active for only the early stages of the Mackenzie event. The Mackenzie dikes have Nd isotopic compositions that span the range of compositions within the entire Coppermine River basalts, which supports the idea that the dikes represent the conduits for the basalts. Importantly, Ernst & Baragar (1992) have shown from the anisotropy of magnetic susceptibility measurements that the magma flow direction within the dikes records the vertical ascent of magmas within 500 km of the focus of the dike swarm and outward flow

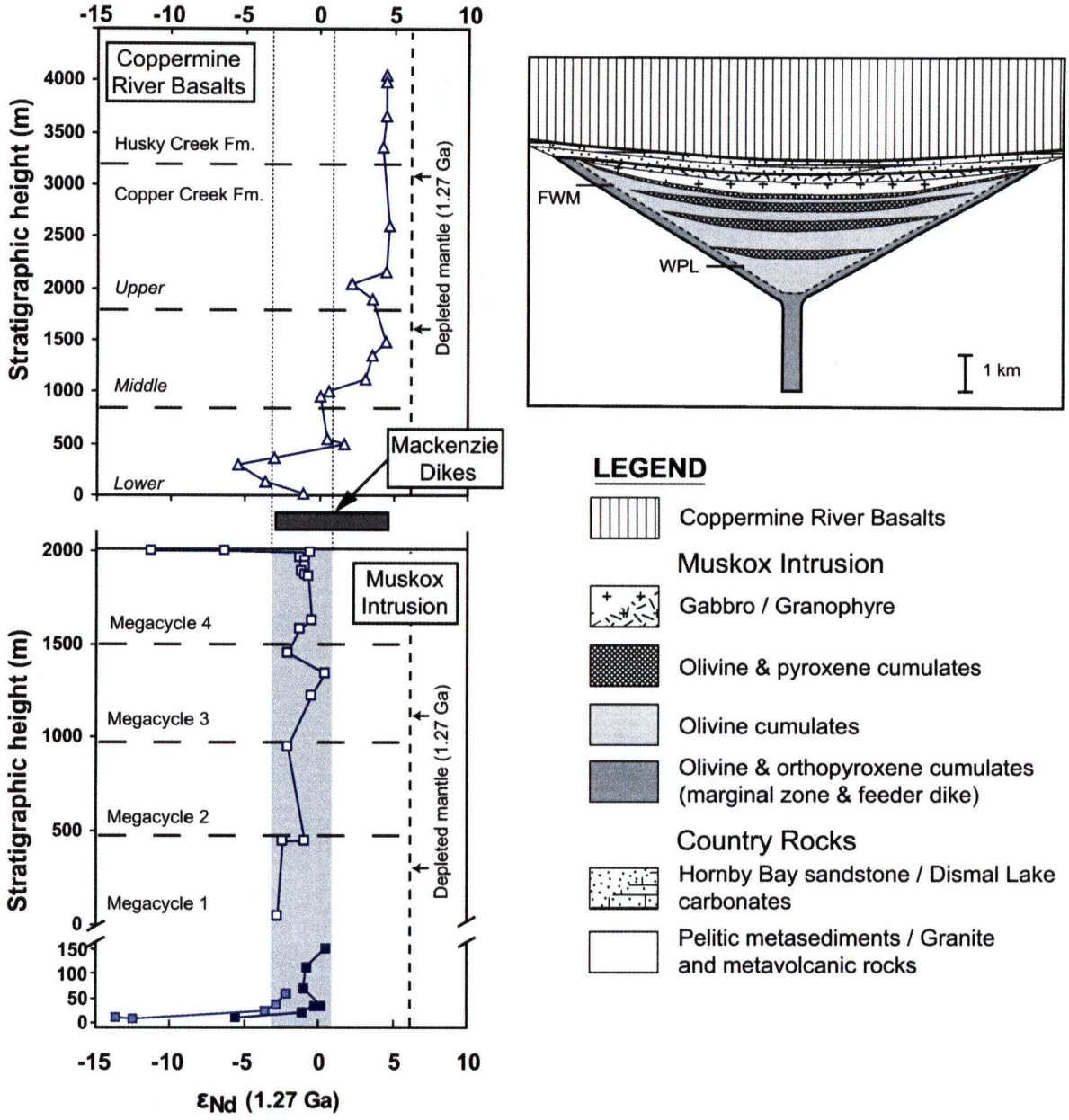

Fig. 3.10: Compilation diagram showing the stratigraphic variations in initial ε_{Nd} isotopic composition for the marginal zone (this study; solid squares; light blue = Far West Margin; dark blue = West Pyrrhotite Lake) and layered series (Stewart & DePaolo, 1996; open squares) of the Muskox intrusion, the Coppermine River flood basalts (Griselin et al., 1997; open triangles) and Mackenzie dikes (unpublished; Dudas & Peterson, 1992). The horizontal dashed lines separate the major divisions of the Muskox intrusion (Francis, 1994) and the Coppermine River basalts (Baragar, 1969). The grey field covers the range of values from the Muskox intrusion that were not affected by local crustal contamination. This range in ε_{Nd} is projected onto the Coppermine River basalt stratigraphy as two vertical dotted lines. For comparison the initial ε_{Nd} range for the depleted mantle at 1.27 Ga is shown by the vertical dashed line (determined from the ε_{Nd} range of mid-ocean ridge basalts (Vervoort & Blichert-Toft, 1999; Hofmann, 2005)).

at greater distances. This implies that the dikes exposed throughout most of the dike swarm likely represent the lateral extension of the conduit system through which the basalts were erupted. The similar Nd isotopic compositions of the Mackenzie dikes and Coppermine River basalts also suggest that distinct sets of the dikes could be related to compositionally (and stratigraphically) distinct members of the flood basalts.

3.6.3 Mantle source composition of the Muskox intrusion and other Mackenzie components

The Hf and Nd isotopic composition and incompatible trace element concentrations and patterns of peridotites from this study, combined with available Nd isotopic compositions of layered series rocks of the Muskox intrusion (Stewart & DePaolo, 1996) and Coppermine River basalts, allow the composition of the mantle source region from which the Muskox magmas were derived to be constrained (Fig. 3.6 & 3.10). The peridotites have low initial ε_{Nd} (-2 to +1) and ε_{Hf} (-5 to +3) values and are clearly enriched in LILE and LREE. These geochemical characteristics are consistent with the derivation of their parental magmas from a mantle source more enriched than depleted asthenospheric mantle. There is however evidence that indicates the Muskox magmas were contaminated by continental crust prior to emplacement within the Muskox chamber, which (as discussed below) may indicate that the Nd and Hf isotopic compositions of the primary Muskox magmas had more positive ε-values (i.e. were more depleted).

All rocks within the marginal zone of the Muskox intrusion, including the peridotites furthest from the margin, have prominent negative Nb-Ta anomalies in primitive mantle-normalized trace element patterns (Fig. 3.6). Similar anomalies were also noted by Francis (1994) in his study of marginal zone and layered series rocks within the Muskox intrusion. As noted previously, negative Nb-Ta anomalies are typical of continental crust (e.g. Rudnick & Fountain, 1995) and are not considered to represent variations in the degree or depth of melting in the mantle (e.g. Wooden et al., 1993; Arndt et al., 2003). Thus the appearance of these anomalies within intrusive and extrusive rocks must record some amount of interaction with continental material during magma ascent through the crust (Arndt et al., 1993). However, t_{CHUR} Nd model ages of many marginal zone and layered series rocks are comparable to the U-Pb crystallization age of 1269 Ma of the intrusion (Fig. 3.11), which suggests that the amount of contamination prior to emplacement within the Muskox chamber

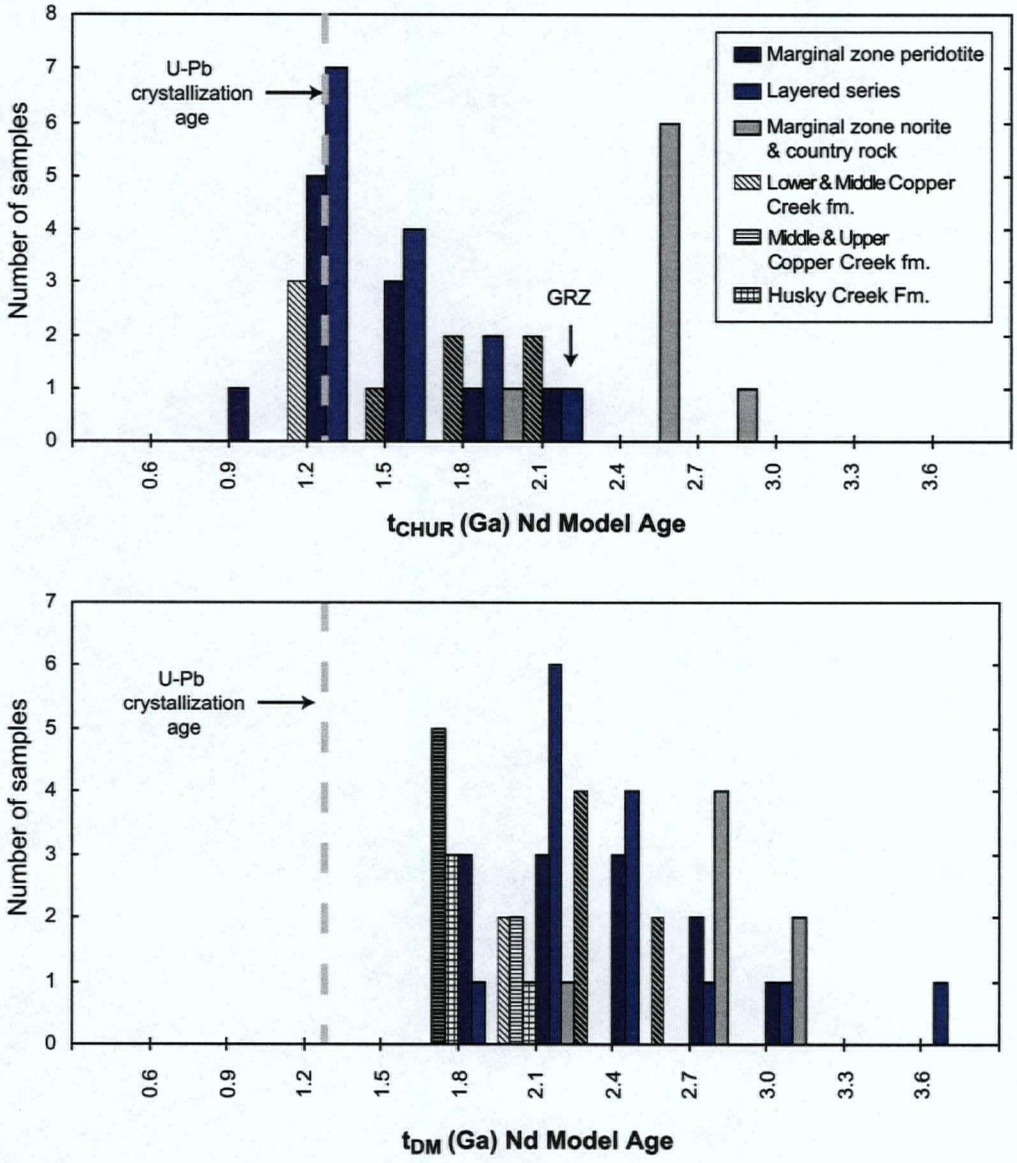

Fig. 3.11: Histograms of Nd model ages (t_{CHUR} and t_{DM}) for marginal zone peridotites (this study) and layered series rocks (Stewart & DePaolo, 1996) of the Muskox intrusion, basalts from the Coppermine River and Husky Creek groups (Griselin et al., 1997), and contaminated gabbronorites and crustal rocks from the margin of the Muskox intrusion (this study). t_{CHUR} model ages cannot be calculated for the Husky Creek Formation basalts because their present-day $^{143}Nd/^{144}Nd$ values are more radiogenic than CHUR, and therefore these samples are only included in the t_{DM} histogram. Many of the marginal zone and layered series rocks have t_{CHUR} model ages that are comparable to the U-Pb crystallization age of the intrusion, which suggests that these rocks crystallized from a relatively uncontaminated magmas that were derived from a near-chondritic mantle source. The contaminated gabbronoritic marginal rocks and granophyric roof zone rocks (GRZ) are displaced towards the older model ages of the crustal rocks.

was minimal, although sufficient enough to produce the negative Nb-Ta anomalies. The Husky Creek Formation basalts have positive initial ε_{Nd} values (+4.5) and lack Nb-Ta depletion indicating that they represent an uncontaminated end-member composition of the mantle source during the Mackenzie event; this places a limit on the isotopic composition of the primary Muskox magmas. The range in Nd isotopic compositions of the Mackenzie components (ε_{Nd} = -2 to + 4.5) is consistent with those of many modern-day oceanic island and plateau basalts (e.g. Hoffman, 2005), suggesting that they formed from a similar enriched mantle source region that is distinct from that estimated for the depleted asthenospheric mantle at 1.27 Ga (ε_{Nd} = +6 to +12 & ε_{Hf} = +10 to +14; Vervoort & Blichert-Toft, 1999). Some of the variation in isotopic compositions within the Coppermine River basalts and Muskox intrusion may reflect heterogeneities within the mantle source region, rather than exclusively crustal contamination.

3.6.4 Evolution of the Mackenzie magmatic event

The magmatic episode that led to the emplacement of the Muskox intrusion, Mackenzie dikes, and the eruption of the Coppermine River basalts is considered to reflect the impingement of a mantle plume at the base of the lithosphere (LeCheminant & Heaman, 1989; Baragar et al., 1996; Griselin et al., 1997). Domal uplift associated with plume emplacement is recorded by pre-flood basalt karst topography, which extends for >400 km from 100 km to the west of the Muskox intrusion to Bathurst Inlet towards the east, and the radial fracture system into which the Mackenzie dikes were emplaced (LeCheminant & Heaman, 1989; Baragar et al., 1996). As indicated above, the enriched trace element and isotopic compositions and Nb-depletions of the lowermost Coppermine River basalts are consistent with their being directly related to the Muskox intrusion. A large volume of fractionated magma would have been expelled from the Muskox chamber to account for the abundance of olivine (Irvine & Smith, 1967) and given that there is little evidence of a substantial erosional event within the overlying sediments (Kerans, 1983), it is likely that the lowermost Coppermine basalts resided within the Muskox chamber. Trace element characteristics of the Lower Copper Creek Formation basalts (e.g. high Gd/Yb and low Lu/Hf) indicate that they were derived by partial melting of the mantle within the garnet stability field (>100 km; Griselin et al., 1997). During ascent these magmas were contaminated by continental crust (possibly the lower crust), which resulted in a decrease in Nb/La and a shift towards more negative initial ε_{Nd}. Griselin et al. (1997) demonstrated

that the subcontinental lithospheric mantle was unlikely the source of the chemical signatures observed in the Lower Copper Creek basalts, based on the distinct trace element characteristics of mantle peridotite xenoliths, and lithospheric mantle-derived volcanic rocks (e.g. lamprophyres). The magmas from which the Lower Copper Creek basalts were derived then resided within the Muskox chamber, prior to eruption on the surface. The Muskox intrusion itself formed through repeated picritic magma injections and likely represents a shallow-level staging chamber where magmas stagnated and fractionated during their ascent to the surface. Local crustal contamination within the Muskox intrusion along the walls and roof (Stewart & DePaolo, 1996) of the intrusion only affected a small amount of magma, which would explain the lack of significantly more enriched isotopic compositions within the Lower Copper Creek Formation basalts. At some point, the Muskox chamber became inactive and ascending magmas utilized alternate conduits systems. Several discrete gravity anomalies occur near the focus of the dike swarm to the north of the Muskox intrusion, which, as suggested by Baragar et al. (1996), could represent unexposed intrusions related to the Mackenzie event. The Husky Creek Formation basalts lack the chemical signature of residual garnet, which indicates that at later stages within the Mackenzie event mantle melting took place at shallower levels, perhaps as result of lithospheric thinning, or at higher degrees of melting (Griselin et al. 1997). The parental magmas to the Husky Creek basalts were not contaminated by continental crust during transit due to the combined effects of lithospheric thinning, plating of conduit walls by crystallization products of earlier magma pulses, and/or ascent through conduits where wall rocks had been previously melted and dehydrated.

3.7 CONCLUSIONS

This detailed geochronologic and geochemical study of the marginal rocks of the Muskox intrusion, Nunavut, provides important constraints on the timing of emplacement of the Muskox intrusion, the spatial extent and degree of contamination along the basal margin of the intrusion, the relationship between the marginal zone and layered series of the Muskox intrusion, and the genetic relationship between the different components of the 1.27 Ga Mackenzie magmatic event. Precise U-Pb baddeleyite ages from uncontaminated peridotites and contaminated gabbronorites obtained in this study indicate that the marginal zone of the Muskox intrusion crystallized synchronously with the layered series and the Mackenzie dikes. Hf and Nd isotopic compositions and incompatible trace element ratios of marginal zone rocks indicate that crustal contamination by the adjacent crustal rocks is restricted to a thin (<10 m) zone of gabbronoritic rocks at the base of the Muskox intrusion. The degree of contamination varies at different locations along the margin of the intrusion, which likely relates to the different wall rock lithologies to the intrusion. The Nd isotopic compositions of the marginal zone peridotites and layered series rocks of the Muskox intrusion and the overlying Coppermine River basalts indicate that only the lower Copper Creek basalts can be directly related to the Muskox intrusion, perhaps as residual melts formed during fractionation within the Muskox chamber. Nb-Ta depletions within Muskox peridotites suggest that magmas which entered the chamber were previously contaminated, likely during ascent through the lower and middle crust, although the correlation between t_{CHUR} model ages for the peridotites and their U-Pb crystallization ages indicates that the degree of lower crustal contamination must have been minimal. The Nd isotopic compositions of the uncontaminated Husky Creek Formation basalts represent the least enriched component within the Mackenzie event and are comparable to those of modern-day oceanic island and plateau basalts. Thus, the voluminous magmas that fed the Muskox intrusion, the Mackenzie dikes, and the Coppermine River basalts at 1.27 Ga were ultimately derived from an enriched mantle source. The radial nature of the Mackenzie dikes and pre-flood basalt erosional features near the focus of the dike swarm, combined with the isotopic compositions strongly support a mantle plume origin for the Mackenzie magmatic event.

3.8 ACKNOWLEDGEMENTS

The author is grateful for assistance from Gwen Williams and Diane Hanano with sample digestion and dilution procedures; Jane Barling, Bert Mueller, Wilma Pretorius, Rich Freidman, and Elisa Dietrich-Sainsaulieu for their help with HR-ICP-MS, TIMS, and MC-ICP-MS analyses at the Pacific Centre for Isotopic and Geochemical Research, University of British Columbia, Vancouver; and Claude Maerschalk for assistance with column chemistry. RAM thanks Gary DeScuhtter (Senior Project Geologist, Anglo American Exploration Ltd. Canada), Nathan Rand, and Tansy O'Connor for their wonderful support in logistics and sample collection. RAM was supported by an NSERC Industrial Postgraduate Scholarship (IPS). Funding for this research was provided by Anglo American Exploration Ltd. (Canada), (AAEC) by a Collaborative Research Development (CRD) grant from NSERC and AAEC, and by an NSERC Discovery Grant to JSS.

3.9 REFERENCES

Arndt, N.T., Czamanske, G.K., Wooden, J.L. & Fedorenko, V.A. (1993). Mantle and crustal contributions to continental flood volcanism. *Tectonophysics* **223**, 39–52.

Arndt, N.T., Czamanske, G.K., Walker, R.J., Chauvel, C. & Fedorenko, V.A. (2003). Geochemistry and origin of the intrusive hosts of the Noril'sk-Talnakh Cu-Ni-PGE sulfide deposits. *Economic Geology* **98**, 495–515.

Baragar, W.R.A. (1969). The Geochemistry of the Coppermine River basalts. *Geological Survey of Canada Paper* **69-44**, 43 pp.

Baragar, W.R.A. & Donaldson, J.A. (1973). Coppermine and Dismal Lakes map areas. *Geological Survey of Canada Paper* **71-39**, 20 pp.

Baragar, W.R.A., Ernst, R.E., Hulbert, L. & Peterson, T. (1996). Longitudinal petrochemical variation in the Mackenzie dike swarm, Northwestern Canadian Shield. *Journal of Petrology* **37-2**, 317–359.

Barnes, S.J. & Francis, D. (1995). The distribution of platinum-group elements, nickel, copper, and gold in the Muskox layered intrusion, Northwest Territories, Canada. *Economic Geology* **90**, 135–154.

Bédard, J.H. & Taner, M.F. (1992). The upper part of the Muskox intrusion, Northwest Territories. In: *Current Research, Part C; Geological Survey of Canada Paper* **92-1C**, 91–101.

Blichert-Toft, J. & Albarède, F. (1997). The Lu-Hf isotope geochemistry of chondrites and the evolution of the mantle-crust system. *Earth and Planetary Science Letters* **148**, 243–258.

Blichert-Toft, J., Chauvel, C. & Albarède, F. (1997). Separation of Hf and Lu for high-precision isotope analysis of rock samples by magnetic sector-multiple collector ICP-MS. *Contributions to Mineralogy and Petrology* **127**, 248–260.

Chauvel, C. & Blichert-Toft, J. (2001). A hafnium isotope and trace element perspective on melting of the depleted mantle. *Earth and Planetary Science Letters* **190**, 137–151.

DePaolo, D.J. & Wasserburg, G.J. (1976). Nd isotopic variations and petrogenetic models. *Geophysical Research Letters* **3**, 249–252.

DesRoches, V. (1992). Petrogenesis of the pyroxenite units in the Muskox intrusion, N.W.T. M.Sc. thesis, McGill University, 61 pp.

Dostal, J., Baragar, W.R.A. & Dupuy, C. (1983). Geochemistry and petrogenesis of basaltic rocks from the Coppermine River area, Northwest Territories. *Canadian Journal of Earth Science* **20**, 684–698.

Dudas, F.O. & Peterson, T.D. (1992). Nd isotopic composition of Mackenzie dikes, Northwest Territories, Canada (Abstract). *EOS, Transactions of the American Geophysical Union, Spring Meeting Supplement* 339.

Dupuy, C., Michard, A., Dostal, J., Dautel, D., & Baragar, W.R.A. (1992). Proterozoic flood basalts from the Coppermine River area, Northwest Territories: isotope and trace element geochemistry. *Canadian Journal of Earth Sciences* **29**, 1937–1942.

Ernst, R.E., & Baragar, W.R.A. (1992). Evidence from magnetic fabric for the flow pattern of the magma in the Mackenzie giant radiating dike swarm. *Nature* **356**, 511–531.

Fahrig, W.F. (1987). The tectonic settings of continental mafic dyke swarms: failed arm and early passive margins. *Geological Association of Canada Special Paper* **34**, 331–348.

Findlay, D.C. & Smith, C.H. (1965). The Muskox Drilling Project. *Geological Survey of Canada Paper* **64-44**, 170 pp.

Francis, D. (1994). Chemical interaction between picritic magmas and upper crust along the margins of the Muskox intrusion, Northwest Territories. *Geological Survey of Canada Paper* **92-12**, 94 pp.

Gandhi, S.S., Mortensen, J.K., Prasad, N. & van Breemen, O. (2001). Magmatic evolution of the southern Great Bear continental arc, northwestern Canadian Shield: geochronological constraints. *Canadian Journal of Earth Sciences* **38**, 767–785.

Gibson, I.L., Sinah, M.N., & Fahrig, W.F. (1987). The geochemistry of the Mackenzie Dike Swarm, Canada. In: Halls, H.C. & Fahrig, W.F. (eds) *Mafic Dyke Swarms. Geological Association of Canada, Special Paper* **34**, 109–121.

Goolaerts, A., Mattielli, N., de Jong, J., Weis, D. & Scoates, J.S. (2004). Hf and Lu isotopic reference values for the zircon standard 91500 by MC-ICP-MS. *Chemical Geology* **206**, 1–9.

Govindaraju, K. (1994). 1994 compilation of working values and sample description for 383 geostandards. *Geostandards Newsletter Special Issue* **18**, 158 pp.

Griselin, M., Arndt, N. & Baragar, W.R.A. (1997). Plume-lithosphere interaction and crustal contamination during formation of Coppermine River basalts, Northwest Territories, Canada. *Canadian Journal of Earth Sciences* **34**, 958–975.

Heaman, L.M. & LeCheminant, A.N. (1993). Paragenesis and U-Pb systematics of baddeleyite (ZrO_2). *Chemical Geology* **110**, 95–126.

Hoffman, P.F. (1984). Geology, Northern Internides of Wopmay Orogen, District of Mackenzie, Northwest Territories. *Geological Survey of Canada, Map* **1576A**.

Hoffman, P.F. & Bowring, S.A. (1984). Short-lived 1.9 Ga continental margin and its destruction, Wopmay Orogen, northwest Canada. *Geology* **12**, 68–72.

Hofmann, A.W. (2005). Sampling mantle heterogeneity through oceanic basalts: isotopes and trace elements. In: Carlson, R.W. (ed) *The Mantle and Core. Treatise on Geochemistry* **2**, Elsevier, 61–97.

Hulbert, L. (2005). Geology of the Muskox intrusion and associated Ni and Cu occurrences. *Geological Survey of Canada, Open File 4881, CD-ROM.*

Irvine, T.N. (1970). Crystallization sequences in the Muskox intrusion and other layered intrusions – I. Olivine-pyroxene-plagioclase relations. In: Visser, D.J.L. & Von Gruenewaldt, G. (eds) *Symposium on the Bushveld Igneous Complex and Other Layered Intrusions. Geological Society of South Africa, Special Publication* **1**, 441–476.

Irvine, T.N. (1975). Crystallization sequences in the Muskox intrusion and other layered intrusions – II. Origin of chromitite layers and similar deposits of other magmatic ores. *Geochimica et Cosmochimica Acta* **39**, 991–1020.

Irvine, T.N. (1977). Origin of chromitite layers in the Muskox intrusion and other stratiform intrusions: a new interpretation. *Geology* **5**, 273–277.

Irvine, T.N. (1980). Magmatic infiltration metasomatism, double-diffusive fractional crystallization, and adcumulus growth in the Muskox intrusion and other layered intrusions. In: Hargraves, R.B. (ed.) *Physics of Magmatic Processes*. Princeton: Princeton University Press, pp. 325–383.

Irvine, T.N. (1988). Muskox intrusion, Northwest Territories. In: Hulbert, L.J. et al. (eds) *Geological Environments of the Platinum Group Elements. Geological Survey of Canada, Open File* **1440**, 25–39.

Irvine, T.N. & Smith, C.H. (1967). The ultramafic rocks of the Muskox intrusion, Northwest Territories, Canada. In: Wyllie, P.J. (ed.) *Ultramafic and Related Rocks*. New York: John Wiley & Sons, Inc., 38–49.

Irvine, T.N. & Smith, C.H. (1969). Primary oxide minerals in the Layered Series of the Muskox intrusion. In: Wilson, H.D.B. (ed.) *Magmatic Ore Deposits: A Symposium, Economic Geology Monograph* **4**, 76–94.

Lahaye, Y., Arndt, N., Byerly, G., Chauvel, C., Fourcade, S. & Gruau, G. (1995). The influence of alteration on the trace element and Nd isotopic compositions of komatiites. *Chemical Geology* **126**, 43–64.

LeCheminant, A.N. & Heaman, L.M. (1989). Mackenzie igneous events, Canada: Middle Proterozoic hotspot magmatism associated with ocean opening. *Earth and Planetary Science Letters* **96**, 38–48.

LeCheminant, A.N. & Heaman, L.M. (1991). U-Pb ages for the 1.27 Ga Mackenzie igneous events, Canada: support for a plume initial model. *Geological Association of Canada/Mineralogical Association of Canada Meeting, Program with Abstracts* **16**, A73.

Liang, Q., Jing, H. & Grégoire, D.C. (2000). Determination of trace elements in granites by inductively coupled plasma-mass spectrometry, *Talanta* **51**, 507–513.

Ludwig, K.R. (1980). Calculation of uncertainties of U-Pb isotopic data. *Earth and Planetary Science Letters* **46**, 212–220.

Ludwig, K.R. (1998). On the treatment of concordant uranium-lead ages. *Geochimica et Cosmochimica Acta* **62**, 665–676.

Ludwig, K.R. (2003). Users manual for Isoplot/Ex 3.00, a geochronological toolkit for Microsoft Excel. *Berkeley Geochronology Center, Special Publication* **4**, 71 pp.

Lugmair, G.W. & Marti, K. (1978). Lunar initial $^{143}Nd/^{144}Nd$: Differential evolution of the lunar crust and mantle. *Earth and Planetary Science Letters* **39**, 349–357.

McDonough, W.F., & Sun, S. (1995). The composition of the Earth. *Chemical Geology* **120**, 223–253.

McKenzie, D. & O'Nions, R.K. (1991). Partial melt distributions from inversion of rare earth element concentrations. *Journal of Petrology* **32**, 1021–1091.

Meisel, T., Schoner, N., Paliulionyte, V., & Kahr, E. (2001) Determination of rare earth elements, Y, Th, Zr, Hf, Nb and Ta in geological reference materials G-2, G-3, SCo-1 and WGB-1 by sodium peroxide sintering and inductively coupled plasma-mass spectrometry. *Geostandards Newsletter: The Journal of Geostandards and Geoanalysis* **26**, 1–9.

Parrish, R., Roddick, J.C., Loveridge, W.D., & Sullivan, R.W. (1987). Uranium-lead analytical techniques at the geochronology laboratory, Geological Survey of Canada. In: *Radiogenic Age and Isotopic Studies, Report 1, Geological Survey of Canada, Paper* **87-2**, 3–7.

Polat, A. Hofmann, A.W., Munker, C., Regelous, M. & Appel, P.W.U. (2003). Contrasting geochemical patterns in the 3.7–3.8 Ga pillow basalt cores and rims, Isua greenstone belt, Southwest Greenland: Implications for postmagmatic alteration processes. *Geochimica et Cosmochimica Acta* **67**, 441–457.

Pretorius, W., Weis, D., Williams, G., Hanano, D., Kieffer, B., and Scoates, J.S. (in press). Complete trace elemental characterization of granitoid (USGS G-2, USGS GSP-2)

reference materials by high resolution inductively coupled plasma-mass spectrometry. *Geostandards Newsletters: The Journal of Geostandards and Geoanalysis.*

Purves, M.C., Heaman, L.M., Creaser, R.A., Schmidberger, S.S., Simonetti, A. & Francis, D. (2005). Origin and isotopic evolution of the Muskox intrusion, Nunavut. *Geological Association of Canada- Mineralogical Association of Canada- Canadian Society of Petroleum Geology- Canadian Society of Soil Science Joint Meeting, Halifax, Nova Scotia, Abstracts Volume* **30**, pp 164.

Raczek, I., Stoll, B., Hofmann, A.W., & Jochum, K.P. (2000) High-precision trace element data for the USGS reference materials BCR-1, BCR-2, BHVO-1, BHVO-2, AGV-1, AGV-2, DTS-1, DTS-2, GSP-1 and GSP-2 by ID-TIMS and MIC-SSMS. *Geostandards Newsletter: The Journal of Geostandards and Geoanalysis* **25,** 77–86.

Roach, T.A., Roeder, P.L. & Hulbert, L.J. (1998). Composition of chromite in the Upper Chromitite, Muskox layered intrusion, Northwest Territories. *Canadian Mineralogist* **36**, 117–135.

Robinson, P., Higgins, N.C. & Jenner G.A. (1986). Determination of rare-earth elements, yttrium and scandium in rocks by an ion exchange-X-ray fluorescence technique. *Chemical Geology* **55**, 121–137.

Roddick, J.C. (1987). Generalized numerical error analysis with application to geochronology and thermodynamics. *Geochimica et Cosmochimica Acta* **51**, 2129–2135.

Rudnick, R.L. & Fountain, D.M. (1995). Nature and composition of the continental crust: a lower crustal perspective. *Reviews of Geophysics* **33,** 267–309.

Schwab, D.L., Thorkelson, D.J., Mortensen, J.K., Creaser, R.A. & Abbott, J.G. (2004). The Bear River dykes (1265-1269 Ma): westward continuation of the Mackenzie dyke swarm into Yukon, Canada. *Precambrian Research* **133**, 175–186.

Sguigna, A.P., Larabee, A.J. & Waddington, J.C. (1982). The half-life of ^{176}Hf by γ- γ coincidence measurement. *Canadian Journal of Physics* **60**, 361–364.

Smith, C.H. (1962). Notes on the Muskox Intrusion, Coppermine River area, District of Mackenzie. *Geological Survey of Canada Paper* **61-25**, 16 pp.

Stacey, J.S. & Kramers, J.D. (1975). Approximation of terrestrial lead isotope evolution by two-stage model. *Earth and Planetary Science Letters* **26**, 207–221.

Stewart, B.W. & DePaolo, D.J. (1992). Diffusive isotopic contamination of mafic magma by coexisting silicic liquid in the Muskox intrusion. *Science* **255**, 708–711.

Stewart, B.W. & DePaolo, D.J. (1996). Isotopic studies of processes in mafic magma chambers: III. The Muskox intrusion, Northwest Territories, Canada. In: Basu, A. & Hart, S. (eds) *Earth Processes: Reading the Isotopic Code*. Washington, DC: American Geophysical Union, pp 277–292.

Tharp, T.M., Loucks, R.R. & Sack, R.O. (1998). Modeling compaction of olivine cumulates in the Muskox intrusion. *American Journal of Science* **298**, 758–790.

Totland, M., Jarvis, I. & Jarvis, K.E. (1992). An assessment of dissolution techniques for the analysis of geological samples by plasma spectrometry. *Chemical Geology* **95**, 140–143.

Vervoort, J.D. & Blichert-Toft, J. (1999). Evolution of the depleted mantle: Hf isotope evidence from juvenile rocks through time. *Geochimica et Cosmochimica Acta* **63**, 533–556.

Wanless, R.K. & Loveridge, W.D. (1972). Rubidium-strontium isochron age studies, *Geological Survey of Canada Paper* **72-23**.

Weis, D., Kieffer, B., Maerschalk, C., Barling, J., de Jong, J., Williams, G.A., Hanano, D., Pretorius, W., Mattielli, N., Scoates, J.S., Goolaerts, A., Freidman, R. & Mahoney, J.B. (submitted). High precision isotopic characterization of USGS reference materials by TIMS and MC-ICP-MS. *Geochemistry, Geophysics, and Geosystems*.

Wooden, J.L., Czamanske, G.K., Fedorenko, V.A., Arndt, N.T., Chauvel, C., Bouse, R.M., King, B.W., Knight, R.J. & Siems, D.F. (1993). Isotopic and trace element constraints on mantle and crustal contributions to Siberian continental flood basalts, Noril'sk area, Siberia. *Geochimica et Cosmochimica Acta* **57**, 3677–3704.

York, D. (1969). Least-squares fitting of a straight line with correlated errors. *Earth and Planetary Science Letters* **5**, 320–324.

CHAPTER 4

Controls on the chalcophile element concentrations of sulphide within the marginal rocks of the Muskox intrusion, Nunavut

4.1 INTRODUCTION

The 1.27 Ga Muskox intrusion, one of the world's largest layered intrusions, has been the site of numerous exploration programs for Ni-Cu-platinum group element mineralization since its discovery in 1956 by members of the Canadian Nickel Company (Smith & Kapp, 1963). The intrusion is considered to have formed through multiple injections of basaltic magma during the Mackenzie magmatic event, which is also recorded by the emplacement of the Mackenzie dike swarm and eruption of the Coppermine River flood basalts (Irvine & Smith, 1967; Irvine, 1970; 1980; Fahrig, 1987; LeCheminant & Heaman, 1989; Baragar et al., 1996; Griselin et al., 1997). Sulphide mineralization is sporadically distributed along the basal margins of the intrusion and typically occurs as disseminated to massive sulphide within noritic rocks at the base of the marginal zone and as thin sulphide veins within the matrix of brecciated and partially melted wall rocks (Fig. 4.1) (Smith, 1962; Chamberlain, 1967; Irvine, 1988; Francis, 1994). Marginal zone sulphides typically have low metal contents and rarely form zones greater than a few metres in thickess. However, the occurrence of metal-rich sulphides (>10 wt % Ni and 20 wt % Cu in 100% sulphide) indicates that significant metal enrichment occurred locally during emplacement and crystallization of the Muskox magmas. Sulphur isotopic compositions of marginal zone sulphides have a strong crustal component indicating the availability of crustal sulphur was likely a controlling factor in the formation of marginal zone sulphide (Sasaki, 1969; Barnes & Francis, 1995; Chapter 2).

In this study we evaluate variations in the Ni, Cu, and Pd contents of sulphide from the marginal rocks of the Muskox intrusion to constrain the processes affecting the formation of metal-rich and metal-poor sulphides at different regions along the margins of the intrusion. This study utilizes compositional data from all known mineralized regions along the basal margin of the intrusion and provides unique insights into sulphide mineralization in the Muskox intrusion. It will be shown that the majority of sulphides are metal-poor (<2 wt% Ni; 4 wt% Cu in 100% sulphide), however both Ni- and Cu-rich sulphides are locally developed within the marginal zone. Numerical modeling of the potential compositional variations produced in the initial sulphide liquid in response to changes in R-factor (silicate magma/sulphide liquid mass ratio) indicate that most of the metal-poor sulphide can be explained by relatively low R-factors of ~100, while the compositions of most of the Cu- and Ni-rich sulphides require R-factors ranging from 500-1000. This indicates that local conditions along the margin of the intrusion provided environments where significant metal

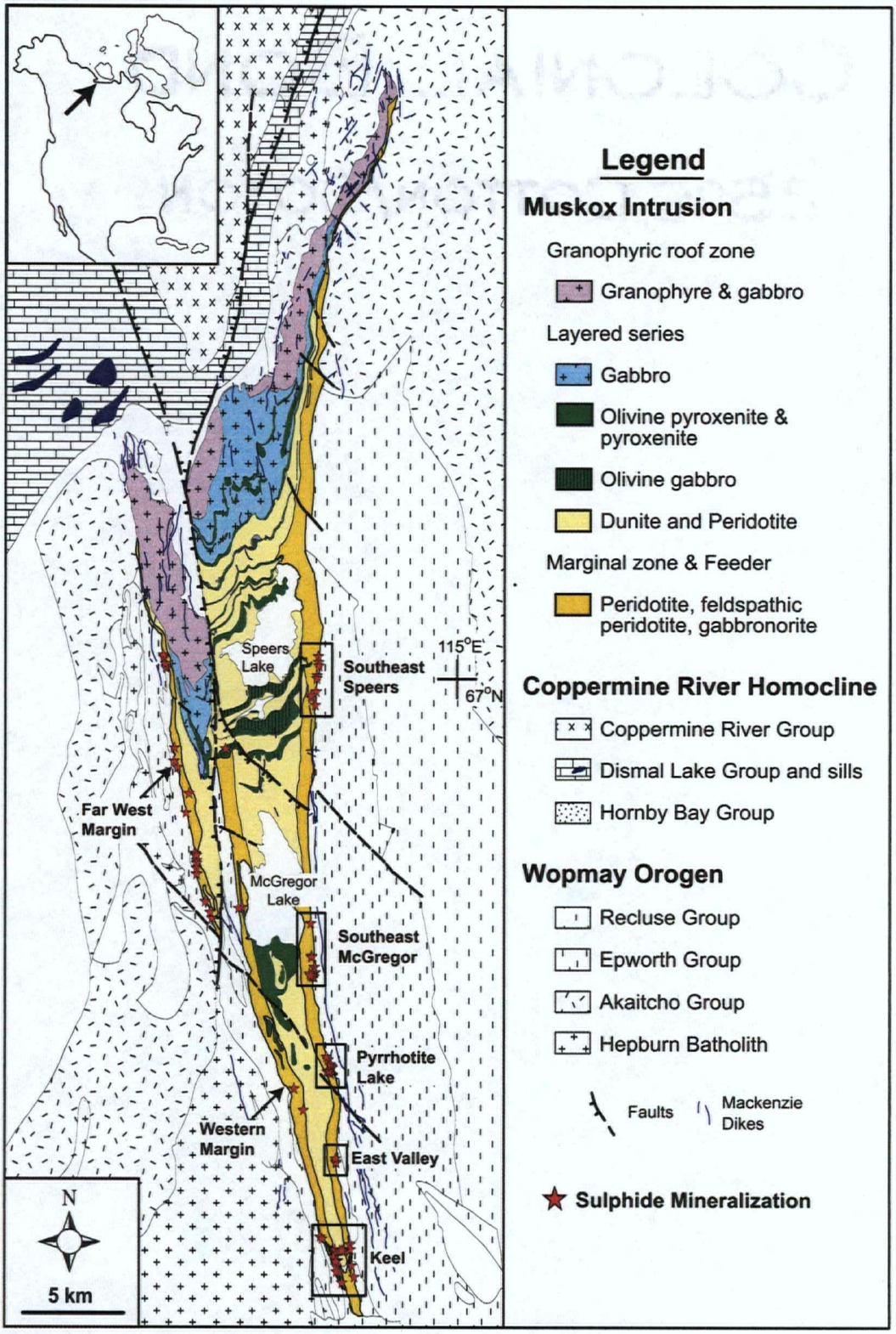
Legend
Muskox Intrusion
Granophyric roof zone
Granophyre & gabbro
Layered series
Gabbro
Olivine pyroxenite & pyroxenite
Olivine gabbro
Dunite and Peridotite
Marginal zone & Feeder
Peridotite, feldspathic peridotite, gabbronorite
Coppermine River Homocline
Coppermine River Group
Dismal Lake Group and sills
Hornby Bay Group
Wopmay Orogen
Recluse Group
Epworth Group
Akaitcho Group
Hepburn Batholith
Faults
Mackenzie Dikes
Sulphide Mineralization
Speers Lake
Southeast Speers
115°E
67°N
Far West Margin
McGregor Lake
Southeast McGregor
Pyrrhotite Lake
Western Margin
East Valley
Keel
N
5 km

Figure 4.1

Fig. 4.1: Geological map of the Muskox intrusion and surrounding crustal rocks showing the location of the sample regions (after Hulbert, 2005; mapping by Smith (1962); supplied by Anglo American Exploration (Canada) Ltd.). The Muskox intrusion and its underlying feeder dike (extends off the map to the south) are exposed for over 120 km within metasedimentary rocks of the Recluse and Epworth groups, metaplutonic rocks of the Hepburn Intrusive Suite, and metasedimentary and metavolcanic rocks of the Akaitcho Group in the Wopmay Orogen. The intrusion forms an elongate funnel-shaped body that plunges shallowly towards the north beneath the overlying Dismal Lake carbonates and Hornby Bay sandstones. Sporadically distributed sulphide mineralization occurs at the base of the marginal zone and within the adjacent host rocks (indicated with red stars). Locations referred to in the text along the marginal zone are indicated.

enrichment could occur. We argue that extremely Cu-rich sulphides likely formed by fractional crystallization of sulphide liquid, analogous to the mechanism described for Cu-rich ores in the Noril'sk region of Russia (Naldrett et al., 1997) and the footwall ore in the Sudbury Igneous Complex (Mungal, 2002; Naldrett et al., 1992; Li & Naldrett, 1994). Finally, we will show that many sulphides contain relatively low Pd contents and argue that this is the result of sulphide segregation from contaminated magmas with elevated Cu/Pd values, as proposed for the formation of sulphide mineralization within the Partridge River intrusion, Duluth Complex, Minnesota (Thériault et al., 1997; 2002).

4.2 DATASET AND RECALCULATION PROCEDURE

The compositional data used in this study was obtained from a previously compiled proprietary dataset of over 4000 samples (property of Muskox Minerals Corporation (now Prize Mining Corporation)). The samples were collected through both diamond drilling and surface prospecting and the dataset was filtered to include only samples with >2 wt % S and that had also been analyzed for Ni, Cu, Pd, and S concentrations. The resultant dataset consisted of ~300 samples, including mainly geochemical results from drill core collected by Prize Mining Corporation (2000-2003) and Equinox Resources Ltd. (late 1980s). The whole rock data was recalculated to 100% sulphide to remove the variations due to variable abundances of sulphide within different samples. The recalculation method is that described in Barnes & Francis (1995), in which the whole rock Ni contents were assigned to pentlandite, the Cu contents were assigned to chalcopyrite, and any remaining sulphur was assigned to pyrrhotite. The Pd contents in 100% sulphide were estimated by dividing the whole rock data by the weight fraction of sulphide. A correction was applied to remove any contribution of metals from non-sulphide phases (e.g. Ni in olivine; Cu in pyroxene) for samples that contained <10% sulphur and that are hosted within gabbronorite and olivine gabbronorite. The estimated metal content of the silicate fraction (500 ppm Ni and 200 ppm Cu) is considered to be a slight overestimate for sulphides within the noritic rocks, and an underestimate for any sulphides within olivine-bearing rocks. Only samples with >2 wt % S have been used because the non-sulphide metal content correction becomes very significant at low S contents (Kerr, 2001). The recalculated data used in this study is taken as an estimate of the bulk sulphide composition, and the combined analytical uncertainties for S and base metal analyses are likely on the order of 15-20% relative (Kerr, 2001).

4.3 SULPHIDE COMPOSITIONAL VARIATIONS

The majority of the sulphides have metal contents below 2 wt % Ni_{100} (51% of samples) and 4 wt % Cu_{100} (70% of samples) (Fig. 4.2). These relatively metal-poor sulphides typically occur along the northern and southern sections of the Far West Margin, and at the East Valley and Speers Lake regions (Fig. 4.1). The remaining sulphides have a wide range in metal contents (2 to 26 wt % Ni_{100}; 4 to 30 wt % Cu_{100}) and typically occur in the middle section of the Far West Margin, and at the Keel, Pyrrhotite Lake, and Southeast McGregor regions (Fig. 4.1). The Pd contents in 100% sulphide show a large variation within an individual region (<0.2 ppm to >10 ppm). For comparison, komatiite-related ores in the Cape Smith Belt, Nuvilik (Katinniq & Donaldson deposits) range from 10-17 wt % Ni_{100} and 2-9 wt % Cu_{100}, and tholeiitic basalt-related massive ores in the Noril'sk region of Russia (Oktyabrsky & Talnakh deposits) typically range from 2-5 wt % Ni and 3-5 wt % Cu, with Cu-rich massive ore containing up to 22 wt % Cu (compilation in Naldrett, 2004). Similar Cu-rich ores are also found in the footwall deposits of the Sudbury Igneous Complex, and these extremely Cu-rich compositions are considered to form through fractional crystallization of a sulphide liquid (Naldrett et al., 1992; 1997).

The compositional variability in sulphides from the different contact regions of the Muskox intrusion can be observed in atomic ratio diagrams (Fig. 4.3; as in Beswick, 2002). All samples plot within a triangle defined by any three of the major sulphide minerals pyrrhotite, pentlandite, cubanite, chalcopyrite, and rarely bornite. This is consistent with the sulphide mineralogy described by Chamberlain (1967) and noted in drill logs throughout the intrusion and adjacent wall rocks. The metal-poor sulphides, as expected, plot near the pyrrhotite apex, while the metal-rich sulphides form two separate arrays that trend towards pentlandite, and cubanite and chalcopyrite. The Pyrrhotite Lake region contains both Ni-rich and Cu-rich sulphides, whereas the Southeast McGregor and Keel regions contain mainly Cu-rich sulphides. These compositional variations, in particular the trend towards relatively Cu-rich sulphides, are broadly consistent with the effects of sulphide liquid fractionation and will be quantitatively evaluated below.

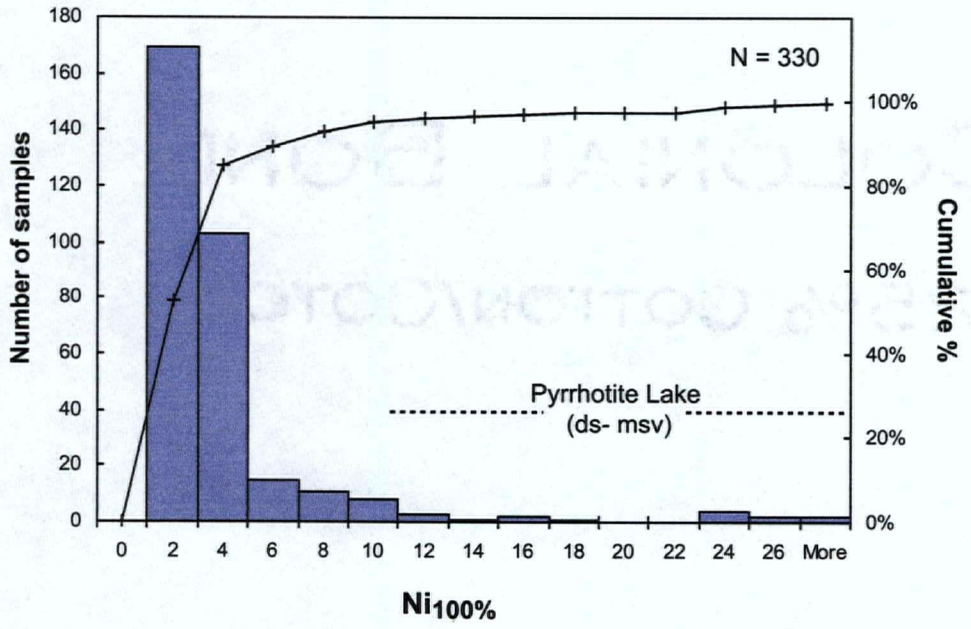

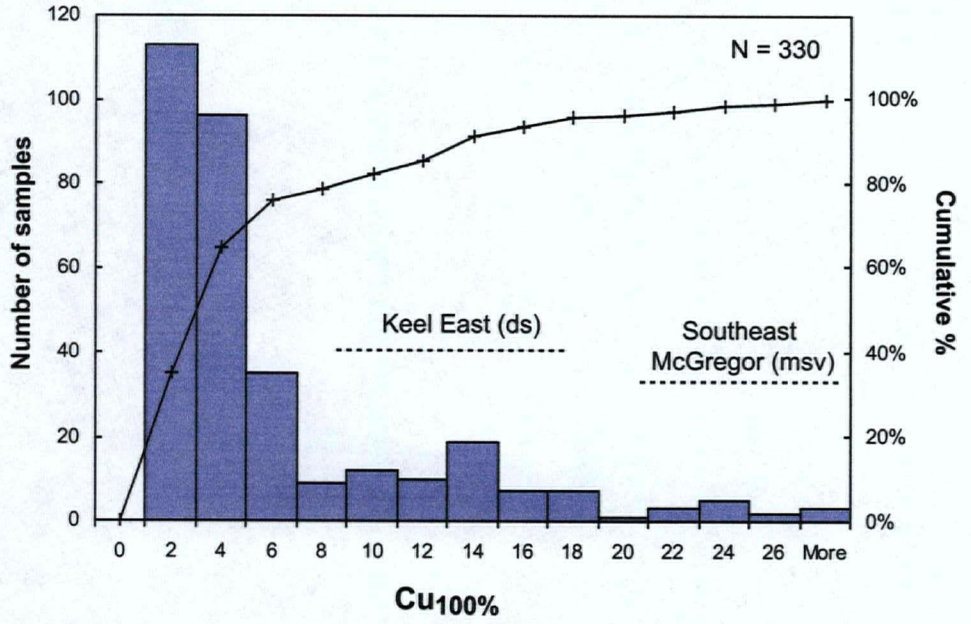

Fig. 4.2: Histograms and cumulative percentages of Ni and Cu contents of sulphides (i.e. recalculated to 100% sulphide) from the marginal zone of the Muskox intrusion. Short dashed lines indicate the range in compositions that are characteristic of a given geographic region (ds = disseminated; msv = massive sulphide). The majority of the marginal zone sulphides contain relatively low metal contents (<2 wt % Ni_{100}; <4 wt % Cu_{100}). Metal-rich sulphides occur at three locations: Pyrrhotite Lake (>15 wt % Ni_{100}), Southeast McGregor (>20 wt % Cu_{100}), and Keel Region (10-14 wt % Cu_{100}).

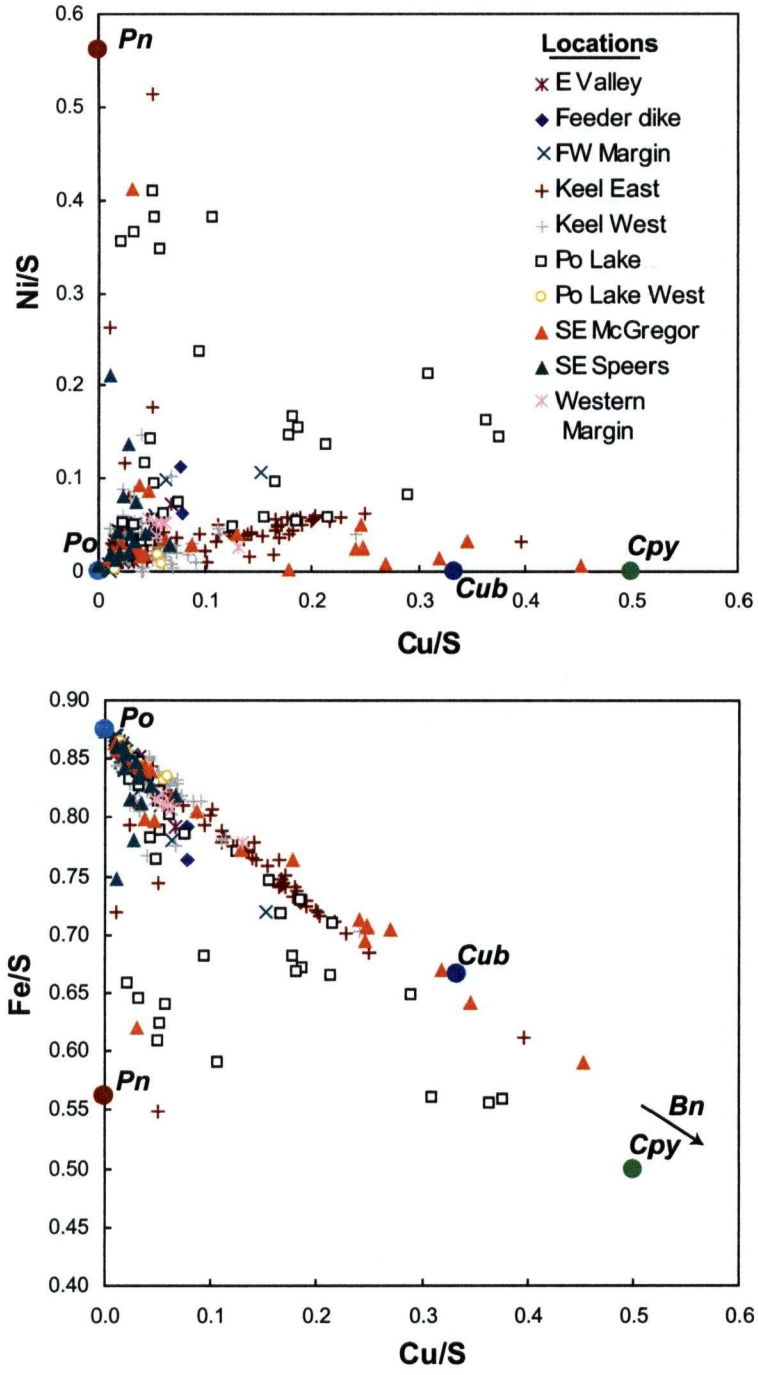

Fig. 4.3: Atomic ratio diagrams showing the compositional variations in marginal zone sulphides at different locations in the Muskox intrusion. The compositions of end member sulphide minerals are shown for reference (Po = pyrrhotite, Cpy = Chalcopyrite, Cub = Cubanite; Pn = Pentlandite; Brn = bornite). Linear arrays towards relatively high Cu/S values are consistent with the effects of sulphide liquid fractionation. Note the distinct Ni-rich and Cu-rich sulphides that are characteristic of the Pyrrhotite Lake (Po Lake) region. See text for discussion.

4.4 DISCUSSION

Sulphide saturation of a basaltic magma will result in the formation of an immscible sulphide liquid into which chalcophile elements (Ni, Cu, and PGE) partition (e.g. Ebel & Naldrett, 1997). In the case of the marginal rocks of the Muskox intrusion, the magmas along the outer contact with the country rocks undoubtedly became sulphide-saturated in response to the addition of both crustal sulphur and silica as discussed in Chapters 2 and 3. As described by Campbell and Naldrett (1979), the composition of the sulphide liquid that initially segregates from the basaltic magma depends on the composition of the magma, the effective silicate/sulfide mass ratio (R-factor), and the sulfide liquid/silicate liquid partition coefficients, as expressed below.

$$C_{sul} = \frac{C^0_{sil} D_{sul/sil} (R+1)}{D_{sul/sil} + R},$$

where C_{sul} is the final concentration a element in the sulphide melt, $D_{sul/sil}$ is the partition coefficient expressing the partitioning of the element in the sulphide liquid relative to silicate magma at equilibrium, R is the ratio of the mass of silicate magma to the mass of sulphide liquid, and C^0_{sil} refers to the original concentration of the metal in the silicate magma. The R-factor is a measure of the amount of silicate liquid that a sulphide liquid equilibrates with, and is considered to reflect the physical environment in which the sulphides formed. Many major magmatic Ni-Cu sulphide deposits occur within channels or conduit systems through which a significant volume of magma has flowed (high R-factors) (Naldrett, 1997).

An additional control on the composition of sulphide liquids is the initial crystallization of an Fe-rich monosulphide solid solution (mss), such that, the composition of the residual sulphide liquid during crystallization reflects the partitioning of chalcophile elements between mss and the sulphide liquid (Barnes et al., 1997a; Ebel & Naldrett, 1997). The crystallization of mss is, in some cases, followed by the crystallization of an intermediate solid solution (iss) from highly evolved sulphide liquids. Experimental and empirical studies have shown that Ir, Rh, and Ru partition into mss, while Cu, Pd, Pt, and Au partition into the sulphide liquid (e.g. Fleet et al., 1991; Li et al., 1996; Naldrett et al., 1997; Barnes et al., 1997a; Ballhaus et al., 2001; Mungall et al., 2005). The behaviour of Ni is more complicated, as described by Ballhaus et al. (2001), and appears to be incompatible in mss at high temperatures and high metal/sulphur ratios, while at low temperatures and metal/sulphur ratios Ni is compatible in mss. Barnes et al. (1997b) documented empirically that Ni partitions into the Fe-rich portion

of ores in tholeiitic systems, whereas in komatiitic systems Ni partitions, along with Pd and Pt, into the Cu-rich portion.

The occurrence of Ni- and Cu-rich sulphides within the marginal zone is consistent with the effects of fractional crystallization of sulphide liquid. In the atomic ratio diagrams (Fig. 4.3), as discussed by Beswick (2002), the fractionation of any particular phase or combination of phases from a parental liquid will result in a linear trend of derivative liquid compositions projecting away from that of the fractionated solid. Considering that mss (approximated by pyrrhotite) was likely the first phase to crystallize, the trend extending from pyrrhotite to cubanite and chalcopyrite observed for the Southeast McGregor and Keel sulphides undoubtedly reflects one of these linear arrays. Several samples from each of these regions plot off this trend and are relatively Ni-rich. Assuming that the sulphides from each region originated from a common parental sulphide liquid, this can be explained by (1) fractionation of pyrrhotite ($Fe_{1-x}S$), which results in progressive enrichment of the residual liquid in Cu and Ni, and (2) fractionation of Ni-bearing pyrrhotite (i.e. a composition along the pyrrhotite-pentlandite join), which results in further enrichment in Cu. The latter process may reflect a change in compatibility of Ni in mss from incompatible to compatible. Depending on the initial sulphide liquid composition, the point at which Ni becomes compatible in mss, and the effectiveness of physically separating solids from liquids, numerous paths could be followed. The metal-poor sulphides that are common throughout the intrusion likely do not represent fractionated mss cumulates, but instead reflect metal-poor parental sulphide liquids. The sulphides at Pyrrhotite Lake are anomalously enriched in both Cu and Ni, which suggests that they may represent a fractionated component of a metal-rich sulphide liquid where both Ni and Cu remained incompatible in mss.

As described above, the variation in the metal content of sulphides is controlled by the exchange of metals between silicate and sulphide melts, and may also record subsequent fractional crystallization of mss from residual sulphide liquid. The compositional variation in the initial segregated sulphide liquid produced by changes in R-factors has been calculated based on the method outlined by Li and Naldrett (1994) and Mungall (2002), using a parental magma composition of an uncontaminated norite from Muskox feeder dike (Francis, 1994) and appropriate partition coefficients between silicate/sulphide melt (Fig. 4.4 & 4.5). The composition of the parental magma and calculated sulphide liquid composition and partition coefficients used in the calculation are shown in Table 4.1. The compositional effects during

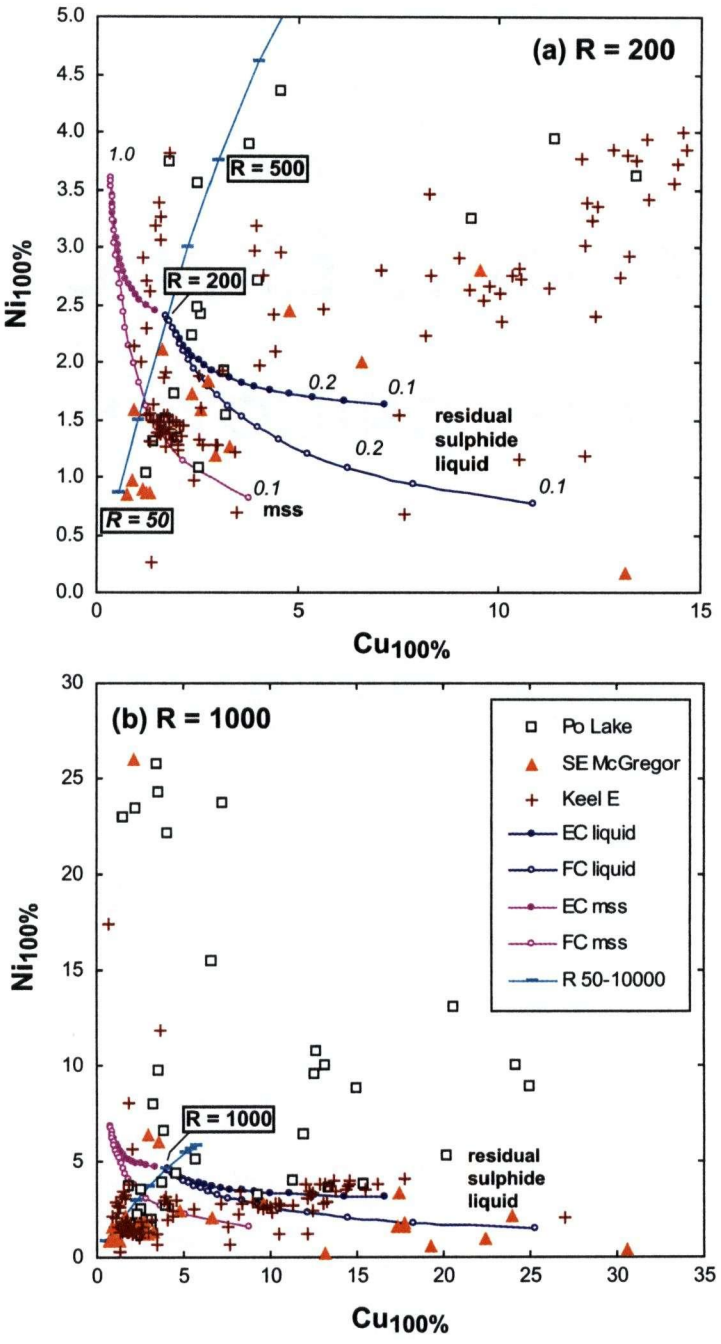

Fig. 4.4: Ni and Cu contents of sulphides (recalculated to 100% sulphide) for the Southeast McGregor, Keel East, and Pyrrhotite Lake regions (shown at two scales) showing the modeling results with constant $D_{Ni(mss/sul)}$. Model curves represent the compositional variation in equilibrium sulphide liquid with changing R-factor (light grey line with horizontal ticks; R=50-10000), and compositional variations produced during equilibrium crystallization (EC; solid curves with solid circles) and fractional crystallization (FC; solid curves with open circles) of monosulphide solid solution (mss) at R = 200 (a) and R = 1000 (b). The mss/sulphide liquid partition coefficient for Ni is assumed to be constant at 1.5. The fraction of liquid remaining is indicated for each curve at increments of 0.05 (circles). Mixtures of mss and liquid span the region between the two sets of curves. The parental magma composition and partition coefficients are shown in Table 1. See text for discussion.

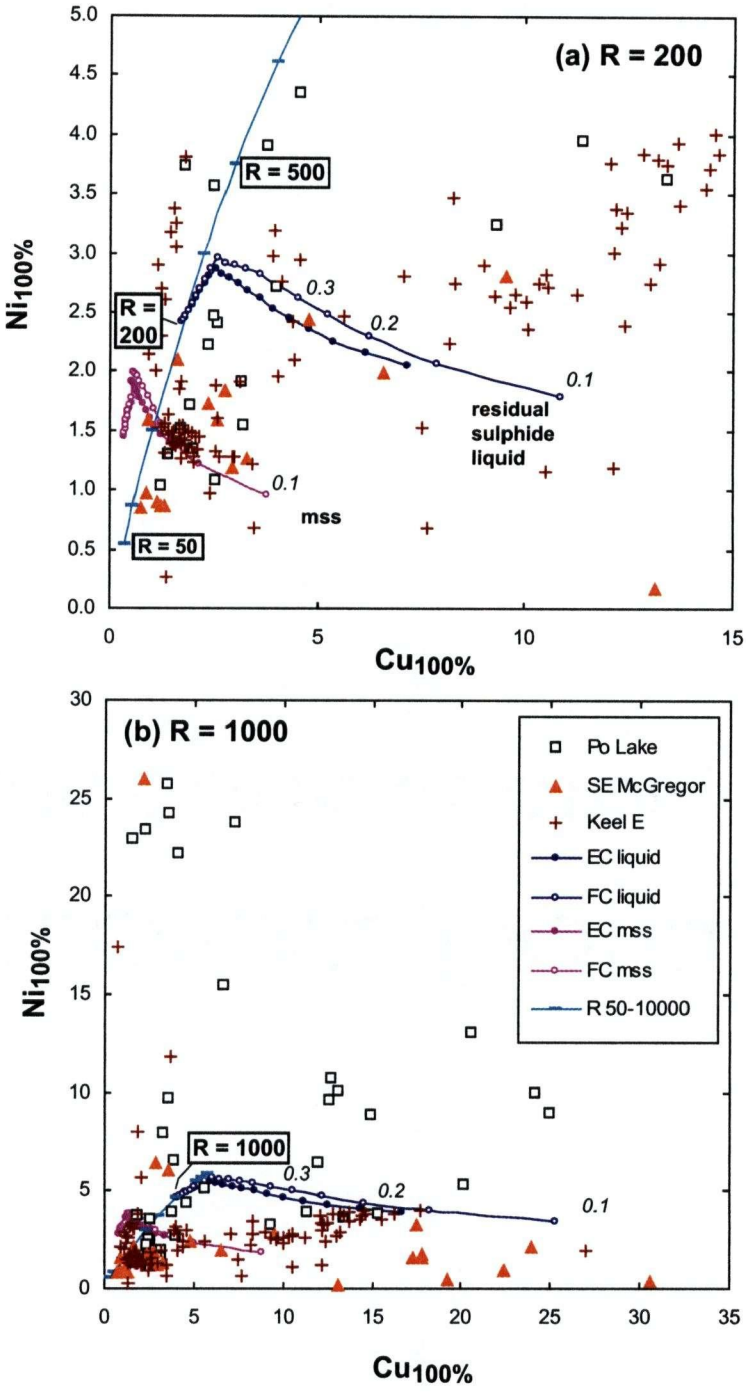

Fig. 4.5: Ni and Cu contents of sulphides (recalculated to 100% sulphide) for the Southeast McGregor, Keel East, and Pyrrhotite Lake regions (shown at two scales) showing the modeling results with variable $D_{Ni(mss/sul)}$. Model parameters as indicated in Figure 4.4. Calculated model curves assume R-factors of 200 (a) and 1000 (b). $D_{Ni(mss/sul)}$ varies from 0.6 to 1.2 during crystallization. The fraction of liquid remaining is indicated for each curve at increments of 0.05 (circles). See text for discussion.

Table 4.1: R-factor and sulphide liquid fractionation model parameters

R = 1000

Element	Parental Magma	Sulphide liquid	Depleted magma	$D_{sul/sil}$	$D_{mss/sul}$
Cu (ppm)	120	40040	80	500	0.18
Ni (ppm)	200	46200	154	300	0.6-1.5
Pd (ppb)	4	3875	0.13	30000	0.1

R = 200

Element	Parental Magma	Sulphide liquid	Depleted magma	$D_{sul/sil}$	$D_{mss/sul}$
Cu (ppm)	120	17229	34	500	0.18
Ni (ppm)	200	24120	80	300	0.6-1.5
Pd (ppb)	4	799	0.03	30000	0.1

"Parental magma" is the estimated composition of the inital Muskox magma prior to sulphide segregation, from the uncontaminated chilled margin of the Muskox feeder dike (from Francis, 1994); "Sulphide liquid" is the calculated composition of the sulphide that equilibrated with the parental magma at the stated R-factor; "Depleted magma" is the calculated composition of the Muskox magma after sulphide segregation. D(sul/sil) and D (mss/sul) are partition coefficients for sulphide liquid/silicate liquid and mss/sulphide liquid, respectively. Partition coefficients are estimated from experimental results of Peach et al. (1990), Bezmen et al. (1994), Peach et al. (1994), Li et al. (1996), Crocket et al. (1997), Ballhaus et al. (2001), Mungal et al. (2005), Barnes et al. (1997a), and Gaetani & Grove (1997).

subsequent sulphide liquid fractionation can be modeled at a given R-factor using experimentally determined partition coefficients between mss and sulphide liquid under both equilibrium and fractional crystallization conditions (Table 1). The partitioning of Cu and Pd between mss and sulphide liquid has been determined experimentally and is treated as constant at D equals 0.2 and 0.1, respectively (Li et al., 1996; Barnes et al. 1997a). As discussed above, the partitioning of nickel is not as well constrained and therefore model curves have been calculated for both the compatible and incompatible behaviour of Ni in mss. In Figure 4.4, a partition coefficient of 1.5 is used throughout crystallization to simulate the compositional variation produced during equilibrium and fractional crystallization assuming Ni is compatible in mss. In Figure 4.5, the partition coefficient is adjusted from 0.6 to 1.2 progressively from 50-100% crystallized to simulate the change in the compatibility of Ni during cooling. The corresponding equilibrium and fractional crystallization curves show an inflection at the point where the assigned partition coefficient equals one.

The modeling results indicate that samples with <1.5% Ni_{100} and <5 % Cu_{100}, which represent the majority of sulphides within the marginal zone, can be explained by R-factors of ~100, regardless of the behaviour of Ni during fractionation (Fig. 4.4 & 4.5). As suggested in Chapter 2, this likely reflects local sulphide saturation of magmas along the outer wall of the magma chamber. Rapid cooling and solidification of this magma likely prevented segregated sulphide droplets from interacting with large volumes of basaltic magma. Using the variable D_{Ni} model, sulphides with 20 wt % Cu_{100} (Southeast McGregor and Keel regions) require R-factors of at least 500, and sulphides with 5 wt % Ni_{100} (Pyrrhotite Lake region) require R-factors of 1000. The constant D_{Ni} model shows more consistent results for samples with relatively high Ni_{100} (6-7 wt %) and Cu_{100} (15-25 wt %) contents at R-factors of 800-1000. These high R-factors may reflect an increased circulation of sulphide droplets due to flow of magma over irregularities in the chamber wall (Irvine, 1988). Neither set of calculations however adequately explains the extremely Ni-rich sulphides (~25 wt % Ni_{100}) at Pyrrhotite Lake. To generate sulphides with these Ni contents, the parental magma would have to contain 700 ppm Ni, which is inconsistent with the proposed picritic parental magma to the Muskox intrusion (<300 ppm Ni). For similar Ni- and Cu-rich sulphides in the footwall of the McCreedy West region of the Sudbury Igneous Complex, Naldrett et al. (1997) suggested that they may represent the product of fractionation of pentlandite from Cu-rich residual sulphide

liquid. Ballhaus et al. (2001) also noted that in a metal-rich sulphide liquid, Ni may remain incompatible in mss and become progressively enriched in the residual liquid.

Finally, given the large difference in the partition coefficients of Cu and Pd during sulphide segregation from a basaltic magma ($D_{Pd(sul/sil)}$ = 30000; $D_{Cu(sul/sil)}$ = 500), the Cu/Pd value is sensitive to changes in R-factor, and can also be used to examine the potential effects of previous sulphide segregation events and addition of crustal material (e.g. Thériault et al., 1997; Barnes & Maier, 1999; Thériault et al., 2000). As described by Thériault et al. (2000), the extraction of a small amount of sulphide results in high Cu/Pd ratios in the later-forming sulphides. Similarly, the mixing of a basaltic magma with crustal material results in an increase in Cu/Pd within the hybrid magma as well as the equilibrium sulphide liquid. Many of the mineralized Muskox samples have extremely high Cu/Pd, which, given that the sulphides occur within mainly noritic marginal rocks and adjacent country rocks, this likely reflects the formation of sulphide liquid from hybrid magmas as proposed in Chapter 2 (Fig. 4.6).

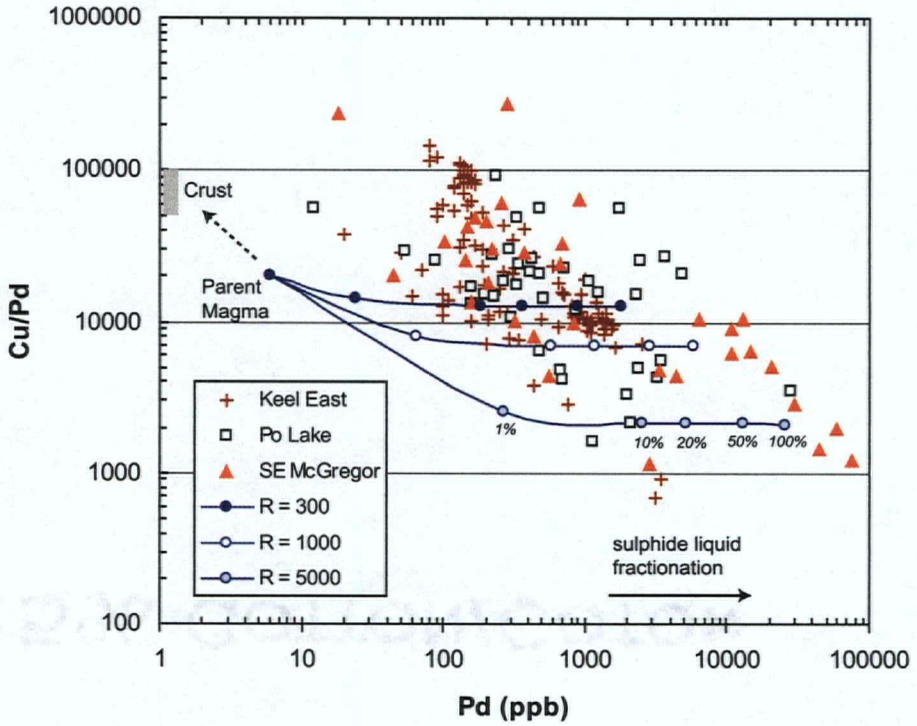

Fig. 4.6: Plot of Cu/Pd vs. Pd (not recalculated) for mineralized samples from the Southeast McGregor, Keel East, and Pyrrhotite Lake regions of the Muskox intrusion. Model curves represent mixing lines between the assumed parental magma composition (Table 1) and its equilibrium sulphide liquid at a given R-factor. Points along the mixing line indicate the composition of rocks that would contain 1, 10, 20, 50, and 100% sulphide. Many of the samples can be modeled at various R-factors (<300 to 5000); however samples with high Cu/Pd values (>20000) require a parental magma with significantly higher Cu/Pd than that of the assumed parent. This may reflect the formation of a hybrid magma derived through assimilation of crust and would shift the model curves towards higher Cu/Pd values. Residual sulphide liquids formed during fractional crystallization would trend towards high Pd contents ($D_{Pd} = 0.1$; $D_{Cu} = 0.2$), which would explain why massive sulphide samples from Pyrrhotite Lake and Southeast McGregor plot at higher Pd contents than the modeled trends at 100% sulphide.

4.5 CONCLUSIONS

This study of the metal contents of sulphides within the marginal zone of the Muskox intrusion allows the processes affecting the formation sulphide mineralization at different locations along the basal contact of the intrusion to be constrained. The majority of the marginal zone sulphide in the Muskox intrusion formed at low R-factors. As described in Chapter 2, this is considered to reflect rapid cooling of sulphide-saturated magma along the outer wall of the chamber, which likely prevented the segregated sulphide droplets from interacting with large amounts of silicate magma. The extreme compositional variability of sulphides within, and between, geographic regions along the basal margin of the Muskox intrusion likely reflects the formation of isolated pockets of sulphide liquid, each of which evolved under local conditions. The occurrence of sporadically distributed metal-rich sulphides may record regions of enhanced circulation of sulphide droplets in a larger volume of basaltic magma in response to irregularities in the wall of the chamber, however it is uncertain if this mechanism could generate significant quantities of sulphide. Cu-rich sulphides at the Southeast McGregor and Keel regions appear to have formed from a fractionated sulphide liquid. The mss component of these liquids would contain 2-4 wt % Ni, however it is not clear based on the present sample suite that this component has been found. This is an important observation as the liquid component would be volumetrically small compared to the mss portion, indicating that these regions should be targeted in future exploration programs. The Keel region, and its northward extension, is of particular interest given that this position in the intrusion represents the site where multiple magmas entered the chamber, as evidenced by the occurrence of magmatic breccia horizons (Francis, 1994). Ni- and Cu-rich sulphides at Pyrrhotite Lake require a unique mechanism of formation, perhaps involving crystallization of sulphide liquid at relatively high temperatures and/or the fractionation of pentlandite from a fractionated Cu-rich sulphide liquid. The few Pyrrhotite Lake samples with >20 wt % Cu may represent a mixture of pentlandite and Cu-rich sulphide at this location. The Pd-depleted signature of many of the sulphides is consistent with other geochemical and isotopic evidence (Chapter 2 & 3) and suggests that they formed from a sulphide liquid that segregated from a hybrid silicate magma along the outer wall of the magma chamber.

4.6 ACKNOWLEDGEMENTS

Prize Mining Corporation (formerly Muskox Minerals Corp.), in cooperation with Larry Hulbert (National Resources Canada; Geological Survey of Canada) and Anglo American Exploration (Canada) Ltd. (AAEC), supplied the geochemical and corresponding spatial data from all historic drilling on the Muskox intrusion, and for that the author is grateful. Dave Peck (AAEC) is thanked for his helpful reviews of this work and for ongoing discussions on the processes involved in the formation of magmatic sulphide deposits. The author would also like to acknowledge the contribution of all previous exploration and research projects on the Muskox intrusion over the past 50 years.

4.7 REFERENCES

Ballhaus, C., Tredoux, M. & Spath, A. (2001). Phase relations in the Fe-Ni-Cu-PGE-S system at magmatic temperature and application to massive sulphide ores of the Sudbury Igneous Complex. *Journal of Petrology* **42**, 1911–1926.

Baragar, W.R.A., Ernst, R.E., Hulbert, L. & Peterson, T. (1996). Longitudinal petrochemical variation in the Mackenzie dike swarm, Northwestern Canadian Shield. *Journal of Petrology* **37-2**, 317–359.

Barnes, S.J. & Francis, D. (1995). The distribution of platinum-group elements, nickel, copper, and gold in the Muskox Layered Intrusion, Northwest Territories, Canada. *Economic Geology* **90**, 135–154.

Barnes, S.J., Makovicky, E., Makovicky, M., Rose-Hansen, J. & Karup-Moller, S. (1997a). Partitioning coefficients for Ni, Cu, Pd, Pt, Rh, and Ir between monosulfide solid solution and sulfide liquid and the formation of compositionally zoned Ni-Cu sulfide bodies by fractional crystallization. *Canadian Journal of Earth Sciences* **34**, 366–374.

Barnes, S.J., Zientek, M.L. & Severson, M.J. (1997b). Ni, Cu, Au, and platinum-group element contents of sulphides associated with intraplate magmatism: a synthesis. *Canadian Journal of Earth Sciences* **34**, 337–351.

Barnes, S.J. & Maier, W.D. (1999). The fractionation of Ni, Cu, and the noble metals in silicate and sulphide liquids. In: Keays, R.R., Lesher, C.M., Lightfoot, P.C. & Farrow, C.E.G. (eds.) *Dynamic Processes in Magmatic Ore Deposits and Their Application to Mineral Exploration, Geological Association of Canada, Short Course* **13**, pp 69–106.

Beswick, A.E. (2002). An analysis of compositional variations and spatial relationships within Fe-Ni-Cu sulfide deposits on the North Range of the Sudbury Igneous Complex. *Economic Geology* **97**, 1487–1508.

Bezmen, N.I., Asif, M., Brügmann, G.E., Romanenko, I.M. & Naldrett, A.J. (1994). Distribution of Pd, Rh, Ru, Ir, Os, and Au between sulfide and silicate metals. *Geochimica et Cosmochimica Acta* **58**, 1251–1260.

Campbell, I.H. & Naldrett, A.J. (1979). The influence of silicate:sulfide ratios on the geochemistry of magmatic sulphides. *Economic Geology* **74**, 1503–1506.

Chamberlain, J.A. (1967). Sulfides in the Muskox intrusion. *Canadian Journal of Earth Sciences* **4**, 105–153.

Crocket, J.H., Fleet, M.E. & Stone, W.E. (1997). Implications of composition for experimental partitioning of platinum-group elements and gold between sulfide liquid and basalt melt: the significance of nickel content. *Geochimica et Cosmochimica Acta* **61**, 4139–4149.

Ebel, D.S. & Naldrett, A.J. (1997). Crystallization of sulfide liquids and the interpretation of ore composition. *Canadian Journal of Earth Sciences* **34**, 352–365.

Fahrig, W.F. (1987). The tectonic settings of continental mafic dyke swarms: Failed arm and early passive margins. *Geological Association of Canada Special Paper* **34**, 331–348.

Fleet, M.E., Stone, W.E. & Crocket, J.H. (1991). Partitioning of palladium, iridium, and platinum between sulfide liquid and basalt melt: Effects of melt composition, concentration, and oxygen fugacity. *Geochimica et Cosmochimica Acta* **55**, 2545–2554.

Francis, D. (1994). Chemical interaction between picritic magmas and upper crust along the margins of the Muskox intrusion, Northwest Territories. *Geological Survey of Canada Paper* **92-12**, 94 pp.

Gaetani, G.A. & Grove, T.L. (1997) Partitioning of moderately siderophile elements among olivine, silicate melt, and sulfide melt: Constraints on core formation in the Earth and Mars. *Geochimica et Cosmochimica Acta* **61**, 1829–1846.

Griselin, M., Arndt, N. & Baragar, W.R.A. (1997). Plume-lithosphere interaction and crustal contamination during formation of Coppermine River basalts, Northwest Territories, Canada. *Canadian Journal of Earth Sciences* **34**, 958–975.

Hulbert, L. (2005). Geology of the Muskox intrusion and associated Ni and Cu occurrences. *Geological Survey of Canada, Open File 4881, CD-ROM.*

Kerr, A. (2001). The calculation and use of sulfide metal contents in the study of magmatic ore deposits: a methodological analysis. *Exploration and Mining Geology* **10**, 289–301.

Li, C. & Naldrett, A.J. (1994). A numerical model for the compositional variations of Sudbury sulfide ores and its application to exploration. *Economic Geology* **89**, 1599–1607.

Li, C., Barnes, S.J., Makovicky, E., Rose-Hansen, J. & Makovicky, M. (1996). Partitioning of nickel, copper, iridium, rhenium, platinum, and palladium between monosulfide solid solution and sulfide liquid: effects of composition and temperature. *Geochimica et Cosmochimica Acta* **60**, 1231–1238.

Irvine, T.N. (1970). Crystallization sequences in the Muskox intrusion and other layered intrusions – I. Olivine-pyroxene-plagioclase relations. In: Visser, D.J.L. & Von

Gruenewaldt, G. (eds) *Symposium on the Bushveld Igneous Complex and Other Layered Intrusions. Geological Society of South Africa, Special Publication* **1**, 441–476.

Irvine, T.N. (1980). Magmatic infiltration metasomatism, double-diffusive fractional crystallization, and adcumulus growth in the Muskox intrusion and other layered intrusions. In: Hargraves, R.B. (ed.) *Physics of Magmatic Processes*. Princeton: Princeton University Press, pp. 325–383.

Irvine, T.N. (1988). Muskox intrusion, Northwest Territories. In: Hulbert, L.J. et al. (eds.) Geological Environments of the Platinum Group Elements. *Geological Survey of Canada, Open File* **1440**, 25–39.

Irvine, T.N. & Smith, C.H. (1967). The ultramafic rocks of the Muskox intrusion, Northwest Territories, Canada. In: Wyllie, P.J. (ed.) *Ultramafic and Related Rocks*. New York: John Wiley & Sons, Inc., pp. 38–49.

LeCheminant, A.N. & Heaman, L.M. (1989). Mackenzie igneous events, Canada: Middle Proterozoic hotspot magmatism associated with ocean opening. *Earth and Planetary Science Letters* **96**, 38–48.

Mungall, J.E. (2002). Late-stage sulfide liquid mobility in the main mass of the Sudbury Igneous Complex: examples from the Victor Deep, McCreedy East, and Trillabelle Deposits. *Economic Geology* **97**, 1563–1576.

Mungall, J.E., Andrews, D.R.A., Cabri, L.J., Sylvester, P.J. & Tubrett, M. (2005). Partitioning of Cu, Ni, Au, and platinum-group elements between monosulfide solid solution and sulfide melt under controlled oxygen and sulfur fugacities. *Geochimica et Cosmochimica Acta* **69**, 4349–4360.

Naldrett, A.J. (1997). Key factors in the genesis of Noril'sk, Sudbury, Jinchuan, Voisey's Bay and other world-class Ni-Cu-PGE deposits: implications for exploration. *Australian Journal of Earth Sciences* **44**, 283–315.

Naldrett, A.J. (2004). Magmatic Sulfide Deposits. Geology, Geochemistry and Exploration. Spinger-Verlag Berlin Heidelberg, 727 pp.

Naldrett, A.J., Coats, C.J.A. & Johannessen, P. (1992). Platinum, palladium, gold, and copper-rich stringers at the Strathcona Mine, Sudbury: their enrichment by fractionation of a sulphide liquid. *Economic Geology* **87**, 1584–1598.

Naldrett, A.J., Ebel, D.S., Asif, M., Morrison, G. & Moore, C.M. (1997). Fractional crystallization of sulfide melts as illustrated at Noril'sk and Sudbury. *European Journal of Mineralogy* **9**, 629–635.

Peach, C.L., Mathez, E.A. & Keays, R.R. (1990). Sulfide melt-silicate melt distribution coefficients for noble metals and other chalcophile elements as deduced from MORB: implications for partial melting. *Geochimica et Cosmochimica Acta* **54**, 3379–3389.

Peach, C.L., Mathez, E.A., Keays, R.R. & Reeves, S.J. (1994). Experimentally determined sulfide melt-silicate melt partition coefficients for iridium and palladium. *Chemical Geology* **117**, 361–377.

Sasaki, A. (1969). Sulphur isotope study of the Muskox intrusion, District of Mackenzie (86 J/13, O/3). *Geological Survey of Canada Paper* **68-46**, 68 pp.

Smith, C.H. (1962). Notes on the Muskox Intrusion, Coppermine River area, District of Mackenzie. *Geological Survey of Canada Paper* **61-25**, 16 pp.

Smith, C.H. & Kapp, H.E. (1963). The Muskox intrusion, a recently discovered layered intrusion in the Coppermine River area, Northwest Territories, Canada. *Mineralogical Society of America, Special Paper* **1**, 30–35.

Thériault, R.D., Barnes, S.J. & Severson, M.J. (1997). The influence of country-rock assimilation and silicate-sulfide ratios (R factor) on the genesis of the Dunka Road Cu-Ni-platinum group element deposit, Duluth Complex, Minnesota. *Canadian Journal of Earth Sciences* **34**, 375–389.

Thériault, R.D., Barnes, S.J. & Severson, M.J. (2000). Origin of Cu-Ni-PGE sulphide mineralization in the Partridge River Intrusion, Duluth Complex, Minnesota. *Economic Geology* **95**, 929–943.

CHAPTER 5

Summary and Conclusions

5.1 SUMMARY AND CONCLUSIONS

This detailed study of the marginal rocks at two locations (West Pyrrhotite Lake and Far West Margin) along base of the Muskox intrusion includes petrography, major and trace element geochemistry, olivine chemistry, and Hf-Nd-S isotope geochemistry, combined with the metal contents of sulphides throughout the intrusion to evaluate the processes by which the marginal zone and associated sulphide mineralization formed. In addition, new U-Pb geochronology of marginal zone rocks of the Muskox intrusion and available Nd isotopic compositions of the Muskox intrusion, Mackenzie dikes, and Coppermine River basalts provide important constraints on the petrogenetic relationship between each of the main components of the 1.27 Ga Mackenzie magmatic event in northern Canada.

The marginal zone of the Muskox intrusion, based on the observations made in this study, consists of a lower gabbronorite subzone and an upper peridotite subzone. The gabbronoritic rocks within the outer 10 m of the marginal zone are characterized by the early crystallization of orthopyroxene and by the appearance of granophyre globules. These petrographic observations correlate with shifts in whole rock Hf and Nd isotopic compositions and incompatible trace element ratios towards those of the surrounding country rocks, indicating that the gabbronoritic marginal rocks represent a hybrid zone. Incompatible trace element ratios of the gabbronorites (this study) and sulphur isotopic compositions of sulphides (this study and Sasaki, 1969) indicate that the addition of silicate material and sulphur occurred *in situ* and that the contaminant was derived directly from the adjacent wall rocks. The gabbronorite at the Far West Margin is significantly more contaminated than that at West Pyrrhotite Lake, which may reflect an enhanced ability of the magma to incorporate the biotite- and sulphide-rich paragneiss at this location. Early solidification of this contaminated zone appears to have prevented overlying magmas from interacting with the adjacent crustal rocks, and resulted in uncontaminated incompatible trace element and Nd and Hf isotopic signatures within the overlying peridotites.

The peridotite subzone of the marginal zone of the Muskox intrusion is characterized by an overall progression to more evolved compositions towards the base (decreasing whole rock MgO and increasing Al_2O_3 and other elements incompatible in olivine) and a corresponding increase in the proportion of postcumulus material. This variation is consistent with the effects produced by the crystallization of varying amounts of intercumulus liquid relative to cumulus olivine grains during compaction of the cumulate pile and cooling through

the base or outer walls of the magma chamber. The overall mineralogical and chemical variations observed can be successfully modeled using IRIDIUM and the results indicate that this simple temperature-driven compaction model is a viable mechanism to explain the inverted character of the marginal zone in the Muskox intrusion. The compositional variation of cumulus olivine within the marginal zone is consistent with the re-equilibration of olivine with varying amounts of intercumulus liquid during solidification (i.e. lower forsterite contents of olivine correlate with increased abundances of postcumulus material). The distinct mineralogical and geochemical variations observed within the Far West Margin peridotites (e.g. abundant chromite and coarse-grained olivine) appear to correspond to changes within the layered series at a comparable stratigraphic height. This indicates that the marginal zone of the Muskox intrusion may have formed throughout the evolution (growth) of the Muskox chamber, rather than representing a single initial magma injection. Thus, it can be expected that the compositional and mineralogical variations within the marginal zone of the Muskox intrusion reflect both the minerals initially accumulated at different stages in the evolution of the chamber (Irvine & Smith, 1967) and superimposed effects of compaction and cooling through the base of the chamber.

Sulphide mineralization within the Muskox intrusion typically occurs within the gabbronorite at the base of the marginal zone and as veins within brecciated wall rocks (Chamberlain, 1967). Based on the associations observed at the West Pyrrhotite Lake and Far West Margin sections, these basal sulphide accumulations reflect sulphide saturation of magma(s) along the outer wall of the chamber in response to the local addition of both sulphur and silica. The large variation in the metal contents of the sulphides within, and between, geographic regions likely reflects the formation of isolated pockets of sulphide liquid, each of which evolved under local conditions. The majority of the marginal zone sulphide in the Muskox intrusion appears to have formed in a relatively non-dynamic environment (low R-factors), which is considered to reflect the early solidification of the contaminated zone along the margin of the intrusion. The occurrence of metal-rich sulphide at specific regions along the outer contact of the intrusion (Southeast McGregor and Pyrrhotite Lake regions) may be the result of increased circulation of sulphide droplets owing to irregularities in the outer contact of the intrusion (Irvine, 1988), however it is uncertain whether this environment could produce significant quantities of sulphide. The Cu-rich character of the sulphides at the Southeast McGregor and Keel regions is consistent with their formation from a fractionated

sulphide liquid. The evidence for multiple magma injections at the Keel region (magmatic breccia horizons; Francis, 1994) indicates that this position holds the highest potential for the formation of significant quantities of metal-rich sulphide mineralization.

U-Pb baddeleyite ages from uncontaminated peridotites and contaminated gabbronorites obtained in this study indicate that the marginal zone (1269 ±2 Ma; weighted mean of 4 concordant analyses) of the Muskox intrusion crystallized synchronously with the layered series and the Mackenzie dikes (1269 Ma; LeCheminant & Heaman, 1989), confirming the relatively short duration of the Mackenzie magmatic event (<4 million years). The Nd isotopic compositions of the marginal zone peridotites (this study) and layered series rocks (Stewart & DePaolo, 1996) of the Muskox intrusion and the overlying Coppermine River basalts (Griselin et al., 1997) indicate that only the lower Copper Creek basalts can be directly related to the Muskox intrusion. Given the relatively low MgO content of these basalts (<10 wt %), they likely represent the fractionated residual liquids that were expelled from the Muskox chamber. The presence of negative Nb-Ta anomalies in marginal zone peridotites that were unaffected by *in situ* contamination indicates that magmas which entered the chamber had experienced some amount of contamination prior to emplacement within the Muskox magma chamber. The Nd isotopic compositions of the uncontaminated Husky Creek Formation basalts (initial ε_{Nd} = +4.5; Griselin et al., 1997) represent the least enriched component within the Mackenzie event, however they are distinct from that estimated for the depleted mantle at 1.27 Ga (ε_{Nd} = +6 to +12 & ε_{Hf} = +10 to +14; Vervoort & Blichert-Toft, 1999). This indicates that the voluminous magmas generated during the Mackenize magmatic event were derived from an enriched mantle source. These geochemical constraints, combined with the evidence for domal uplift prior to the eruption of the Coppermine River basalts (Baragar et al., 1996), are consistent with a mantle plume origin for the Mackenzie magmas.

REFERENCES

Baragar, W.R.A., Ernst, R.E., Hulbert, L. & Peterson, T. (1996). Longitudinal petrochemical variation in the Mackenzie dike swarm, Northwestern Canadian Shield. *Journal of Petrology* **37-2**, 317–359.

Chamberlain, J.A. (1967). Sulfides in the Muskox intrusion. *Canadian Journal of Earth Sciences* **4**, 105–153.

Francis, D. (1994). Chemical interaction between picritic magmas and upper crust along the margins of the Muskox intrusion, Northwest Territories. *Geological Survey of Canada Paper* **92-12**, 94 pp.

Griselin, M., Arndt, N. & Baragar, W.R.A. (1997). Plume-lithosphere interaction and crustal contamination during formation of Coppermine River basalts, Northwest Territories, Canada. *Canadian Journal of Earth Sciences* **34**, 958–975.

Irvine, T.N. (1988). Muskox intrusion, Northwest Territories. In: Hulbert, L.J. et al. (eds) *Geological Environments of the Platinum Group Elements. Geological Survey of Canada, Open File* **1440**, 25–39.

Irvine, T.N. & Smith, C.H. (1967). The ultramafic rocks of the Muskox intrusion, Northwest Territories, Canada. In: Wyllie, P.J. (ed.) *Ultramafic and Related Rocks*. New York: John Wiley & Sons, Inc., 38–49.

LeCheminant, A.N. & Heaman, L.M. (1989). Mackenzie igneous events, Canada: Middle Proterozoic hotspot magmatism associated with ocean opening. *Earth and Planetary Science Letters* **96**, 38–48.

Sasaki, A. (1969). Sulphur isotope study of the Muskox intrusion, District of Mackenzie (86 J/13, O/3). *Geological Survey of Canada Paper* **68-46**, 68 pp.

Stewart, B.W. & DePaolo, D.J. (1996). Isotopic studies of processes in mafic magma chambers: III. The Muskox intrusion, Northwest Territories, Canada. In: Basu, A. & Hart, S. (eds) *Earth Processes: Reading the Isotopic Code*. Washington, DC: American Geophysical Union, pp 277–292.

Vervoort, J.D. & Blichert-Toft, J. (1999). Evolution of the depleted mantle: Hf isotope evidence from juvenile rocks through time. *Geochimica et Cosmochimica Acta* **63**, 533–556.

APPENDICES

Appendix I: ACME Analytical Laboratory whole-rock analyses

Package	4AWR	4BWR	1FMS	7TDA	4ALO[1]	4ALC[2]
Sample wt (g)	0.2	0.2	30	0.5		10
Digestion	LiBO2 fusion	LiBO2 fusion	Aqua Regia HNO3-HCL-H2O	H2O-Hf-HCLO4-HNO3	-	-
Acid	5% HNO3	5% HNO3	2:2:2	18:10:3:6	-	-
Instrument	ICP-ES	ICP-MS	ICP-MS	ICP-ES		
Oxide/Element	SiO_2	Cs	Mo	Ni	LOI	TOT/C
	Al_2O_3	Ga	Cu			TOT/S
	Fe_2O_3	Hf	Pb			
	MgO	Nb	Zn			
	CaO	Rb	Ag			
	Na_2O	Sn	Ni *			
	K_2O	Sr	Co			
	TiO_2	Ta	Mn			
	P_2O_5	Th	As			
	MnO	U	Au			
	Cr_2O_3	V	Cd			
	Ba	W	Sb			
		Zr	Bi			
		Y	Cr			
		La	B *			
		Ce	Tl			
		Pr	Hg			
		Nd	Se			
		Sm	Te			
		Eu	Ge			
		Gd	Sc *			
		Tb	In			
		Dy	Re			
		Ho	Be			
		Er	Li *			
		Tm	Pd			
		Yb	Pt			
		Lu				

[1] Loss on ignition (LOI) determined by weight difference after ignition at 1000°C.

[2] Total carbon and sulphur determined by Leco analyses.

Appendix II: Duplicate analyses of major and trace elements from ACME Analytical Laboratories[1].

Sample No.	71068	71069	avg	σ	%RSD	71008	71009	avg	σ	%RSD	71128	71129	avg	σ	%RSD
Batch No.	A303993	A303993				A303994	A303994				A304116	A304116			
Major elements (wt %)															
SiO_2	38.13	38.33	38.23	0.14	0.37	50.21	50.31	50.26	0.07	0.1	40.78	41.02	40.90	0.17	0.4
TiO_2	0.42	0.41	0.42	0.01	1.7	0.61	0.61	0.61	0.00	0.0	0.72	0.74	0.73	0.01	1.9
Al_2O_3	4.13	4.15	4.14	0.01	0.34	7.38	7.42	7.40	0.03	0.4	5.85	5.83	5.84	0.01	0.2
Fe_2O_3[2]	11.15	11.06	11.11	0.06	0.57	12.93	12.93	12.93	0.00	0.0	14.78	14.86	14.82	0.06	0.4
MnO	0.13	0.13	0.13	0.00	0.00	0.15	0.15	0.15	0.00	0.0	0.17	0.17	0.17	0.00	0.0
MgO	32.2	32.3	32.3	0.08	0.26	18.5	18.6	18.5	0.06	0.3	25.2	25.4	25.30	0.08	0.3
CaO	2.73	2.79	2.76	0.04	1.54	6.23	6.32	6.28	0.06	1.0	4.08	3.96	4.02	0.08	2.1
Na_2O	0.13	0.09	0.11	0.03	25.71	0.88	0.87	0.88	0.01	0.8	0.52	0.48	0.50	0.03	5.7
K_2O	0.28	0.30	0.29	0.01	4.88	0.52	0.51	0.52	0.01	1.4	0.37	0.37	0.37	0.00	0.0
P_2O_5	0.08	0.08	0.08	0.00	0.00	0.04	0.04	0.04	0.00	0.0	0.09	0.10	0.10	0.01	7.4
Cr_2O_3	0.316	0.300	0.308	0.011	3.673	0.261	0.265	0.263	0.003	1.1	0.335	0.338	0.337	0.002	0.6
LOI	10.2	10.0	10.1	0.1	1.4	2.0	1.7	1.9	0.2	11	6.7	6.8	6.8	0.1	1.0
TOT/C	0.03	0.04	0.04	0.01	20.2	0.02	0.05	0.04	0.02	61	0.04	0.02	0.03	0.01	47
TOT/S	0.37	0.35	0.36	0.01	3.93	1.37	1.32	1.35	0.04	2.6	0.02	0.01	0.02	0.01	47
SUM	100.19	100.25	100.22	0.04	0.04	99.90	99.90	99.90	0.00	0.0	99.80	100.20	100.00	0.28	0.3
Chalcophile elements (ppm)															
Co	115	113	114	1	1.3	80	82	81	1	1.7	90	87	89	2	2.5
Ni	2086	2098	2092	8	0.4	1613	1603	1608	7	0.4	1200	1231	1216	22	1.8
Ni *	1726	1728	1727	2	0.1	1150	1199	1175	35	2.9	960	957	959	3	0.3
Cu	265	262	264	2	0.6	1252	1262	1257	7	0.6	95	91	93	2	2.5
Pd (ppb)	14	27	21	9	45	118	120	119	1	1.2	20	22	21	1	6.7
Pt (ppb)	2	3	3	1	28	30	32	31	1	4.6	9	8	9	1	8.3
Au (ppb)	2.3	1.7	2	0.4	21	10.1	9.1	9.6	0.7	7.4	1.2	1.0	1.1	0.1	13
Trace elements (ppm)															
Li *	35.4	34.6	35.0	0.6	1.6	7.7	7.7	7.7	0.0	0.0	15.7	15.7	15.7	0.0	0.0
Be	0.4	0.2	0.3	0.1	47.1	0.2	<.1	0.2			0.2	0.2	0.2	0.0	0.0
B *	191	187	189	3	1	8	10	9	1	16	24	25	25	1	3
Sc *	6	6	6	0	2	2	2	2	0	0	4	4	4	0	3
V	107	108	108	1	1	187	193	190	4	2	165	154	160	8	5
Cr	400	399	400	0	0	216	223	220	5	2	239	245	242	4	2
Mn	1141	1132	1137	6	1	104	103	104	1	1	1127	1113	1120	10	1
Zn	88	88	88	0	0	15	20	17	3	20	56	54	55	1	3
Ga	5	6	6	1	13	10	10	10	0	4	8	10	9	1	10
Ge	0.3	0.2	0.3	0.1	28	<.1	0.1	0.1			0.2	0.2	0.2	0.0	0.0
As	0.5	0.6	0.6	0.1	13	1.5	1.6	1.6	0.1	4.6	1.6	1.5	1.6	0.1	4.6
Se	0.6	0.7	0.7	0.1	10.9	2	2	2	0.0	0.0	0.2	0.2	0.2	0.00	0.0
Rb	9.4	9.5	9.5	0.1	0.7	13.1	13.9	13.5	0.6	4.2	11.4	10.6	11	0.6	5.1
Sr	64	66	65	1	2	108	112	110	3	3	117	111	114	4	4

Appendix II (continued)

Sample No.	71068	71069	avg	σ	%RSD	71008	71009	avg	σ	%RSD	71128	71129	avg	σ	%RSD
Batch No.	A303993	A303993				A303994	A303994				A304116	A304116			
Y	5.9	5.3	5.6	0.4	7.6	10.8	10.4	10.6	0.3	2.7	10.5	10.3	10.4	0.1	1.4
Zr	21.4	20.7	21.1	0.5	2.4	37.3	39.2	38.3	1.3	3.5	47.8	47.4	47.6	0.3	0.6
Nb	1.4	1.9	1.65	0.35	21	2.5	2	2.25	0.35	16	3.5	3.7	3.6	0.14	3.9
Mo	0.23	0.25	0.24	0.01	5.9	0.34	0.31	0.33	0.02	6.5	0.28	0.23	0.26	0.04	13.9
Cd	0.28	0.30	0.29	0.01	4.9	0.33	0.36	0.35	0.02	6.1	0.02	0.02	0.02	0.00	0.0
In	0.03	0.02	0.03	0.01	28	<.02	0.02	0.02			0.02	0.02	0.02	0.00	0.0
Sn	1	1	1			<1	1	1			<1	<1			
Sb	<.02	0.02	0.02			0.02	0.02	0.02	0.00	0.0	<.02	<.02			
Cs	0.8	0.9	0.9	0.1	8.3	0.4	0.4	0.4	0.0	0.0	1.3	1.4	1.4	0.1	5.2
Ba	126	127	127	1	1	209	209	209	0	0.0	107	109	108	1	1.3
La	3.4	3.4	3.4	0.0	0.0	4.9	5.0	5.0	0.1	1.4	6.4	6.1	6.3	0.2	3.4
Ce	6.1	6.7	6.4	0.4	6.6	11.3	11.1	11.2	0.1	1.3	13.9	13.9	13.9	0.0	0.0
Pr	0.7	0.8	0.7	0.1	8.8	1.4	1.5	1.4	0.0	2.4	1.8	1.7	1.8	0.1	4.0
Nd	3	3.5	3.25	0.35	11	6.8	6.1	6.45	0.49	7.7	8.5	7.4	7.95	0.78	9.8
Sm	0.9	1	0.95	0.07	7.4	1.6	1.6	1.6	0.00	0.0	2.1	2	2.05	0.07	3.4
Eu	0.37	0.41	0.39	0.03	7.3	0.55	0.55	0.55	0.00	0.0	0.56	0.54	0.55	0.01	2.6
Gd	0.90	0.76	0.83	0.10	11.9	1.62	2.08	1.85	0.33	18	1.92	1.96	1.94	0.03	1.5
Tb	0.16	0.18	0.17	0.01	8.3	0.28	0.32	0.30	0.03	9.4	0.33	0.31	0.32	0.01	4.4
Dy	1.01	1.08	1.05	0.05	4.7	1.61	1.51	1.56	0.07	4.5	2.10	1.85	1.98	0.18	9.0
Ho	0.17	0.19	0.18	0.01	7.9	0.36	0.37	0.37	0.01	1.9	0.34	0.34	0.34	0.00	0.0
Er	0.52	0.55	0.54	0.02	4.0	1.10	1.03	1.07	0.05	4.6	1.03	0.97	1.00	0.04	4.2
Tm	0.09	0.08	0.09	0.01	8.3	0.13	0.13	0.13	0.00	0.0	0.13	0.12	0.13	0.01	5.7
Yb	0.42	0.58	0.50	0.11	23	0.91	0.94	0.93	0.02	2.3	1.03	0.94	0.99	0.06	6.5
Lu	0.08	0.08	0.08	0.0	0.0	0.14	0.15	0.15	0.01	4.9	0.13	0.12	0.13	0.01	5.7
Hf	0.7	0.7	0.7	0.0	0.0	1.2	1.1	1.2	0.1	6.1	1.3	1.3	1.3	0.0	0.0
Ta	0.1	0.1	0.1	0.0		<.1	<.1				0.3	0.2	0.3	0.1	28
W	0.2	0.2	0.2	0.0	0.0	0.1	0.1	0.1	0.0	0.0	0.2	0.1	0.2	0.1	47
Ag (ppb)	287	283	285	3	1	641	697	669	40	5.9	54	53	54	1	1.3
Tl	0.26	0.25	0.255	0.01	2.8	0.18	0.18	0.18	0.00	0.0	0.04	0.03	0.035	0.01	20
Pb	46	41	43	3	7	17	21	19	3	15	3	3	3	0	0.5
Th	0.6	0.6	0.6	0.00	0.00	0.5	1.5	1	0.71	71	1	1.3	1.15	0.21	18
U	0.2	0.2	0.2	0.00	0.00	0.2	0.2	0.2	0.00	0.0	0.3	0.3	0.3	0.00	0.0

[1] Duplicate analyses are multiple digestions of a single crushed sample.

[2] All Fe as Fe_2O_3.

* Partial digestion only.

LOI = loss on ignition

TOT/C = total carbon; TOT/S = total sulphur by leuco

Appendix II (continued): Duplicate analyses of major and trace elements from ACME Analytical Laboratories [1].

Sample No.	71188	71189	avg	σ	%RSD	71228	71229	avg	σ	%RSD	Average
Batch No.	A304221	A304221				A304331	A304331				%RSD
Major elements (wt %)											
SiO2	37.7	37.27	37.485	0.30	0.81	34.49	34.99	34.74	0.35	1.02	0.55
TiO2	0.37	0.38	0.375	0.01	1.89	0.19	0.19	0.19	0.00	0.00	1.11
Al2O3	2.72	2.64	2.68	0.06	2.11	2.01	2.03	2.02	0.01	0.70	0.76
Fe2O3	13.05	12.96	13.005	0.06	0.49	15.59	15.86	15.725	0.19	1.21	0.53
MnO	0.12	0.12	0.12	0.00	0.00	0.17	0.17	0.17	0.00	0.00	0.00
MgO	32.69	32.76	32.725	0.05	0.15	33.62	33.17	33.395	0.32	0.95	0.41
CaO	0.42	0.42	0.42	0.00	0.00	0.42	0.36	0.39	0.04	10.88	3.11
Na2O	0.05	0.06	0.055	0.01	12.86	<.01	<.01				11.26
K2O	0.14	0.12	0.13	0.01	10.88	0.07	0.07	0.07	0.00	0.00	3.43
P2O5	0.01	0.01	0.01	0.00	0.00	<.01	<.01				1.86
Cr2O3	0.550	0.560	0.555	0.007	1.274	0.527	0.540	0.534	0.009	1.723	1.68
LOI	12.0	12.5	12.3	0.4	2.9	12.4	12.2	12.3	0.1	1.1	3.59
TOT/C	0.03	0.05	0.04	0.01	35.36	0.05	0.07	0.06	0.01	23.57	37.38
TOT/S	0.08	0.09	0.085	0.01	8.32	0.01	0.02	0.015	0.01	47.14	21.83
SUM	100.06	100.03	100.045	0.02	0.02	99.7	99.8	99.75	0.07	0.07	0.08
Chalcophile elements (ppm)											
Co	87	86	87	1	0.8	109	100	104	6	5.8	2.41
Ni	1800	1810	1805	7	0.4	1671	1713	1692	30	1.8	0.96
Ni *	1487	1544	1515	40	2.7	1428	1374	1401	39	2.8	1.75
Cu	1.19	1.21	1.2	0	1.2	5	4	5	1	17	4.4
Pd (ppb)	13	<10	13			19	10	15	6	44	24
Pt (ppb)	6	7	6.5	1	11	5	3	4	1	35	17
Au (ppb)	0.8	0.3	0.6	0.4	64	1.2	0.7	0.95	0.4	37	29
Trace elements (ppm)											
Li *	19.6	19.5	19.55	0.07	0.36	18.6	14.8	16.7	2.69	16.09	3.61
Be	0.3	0.2	0.25	0.07	28.28	<.1	<.1				
B *	202	207	204.5	3.54	1.73	25	24	24.5	0.71	2.89	4.94
Sc *	10.8	10.6	10.7	0.14	1.32	9.2	8.9	9.05	0.21	2.34	1.86
V	119	115	117	2.83	2.42	106	114	110	5.66	5.14	3.07
Cr	591.7	614.9	603.3	16.40	2.72	549.3	535.9	542.6	9.48	1.75	1.66
Mn	1052	1062	1057	7.07	0.67	1502	1435	1468.5	47.38	3.23	1.20
Zn	13.1	14.8	13.95	1.20	8.62	27	24.3	25.65	1.91	7.44	7.70
Ga	5.8	4.4	5.1	0.99	19.41	3.1	3.7	3.4	0.42	12.48	11.57
Ge	0.1	0.1	0.1	0.00	0.00	0.2	0.2	0.2	0.00	0.00	7.07
As	0.3	0.4	0.35	0.07	20.20	<.1	0.1	0.1			
Se	0.3	0.2	0.25	0.07	28.28	0.4	0.4	0.4	0.00	0.00	7.83
Rb	6.8	6.1	6.45	0.49	7.67	2.6	4.1	3.35	1.06	31.66	9.88
Sr	13	16	15	2	14	5	5	5	0	5	6

Appendix II (continued)

Sample No.	71188	71189	avg	σ	%RSD	71228	71229	avg	σ	%RSD	%RSD
Batch No.	A304221	A304221				A304331	A304331				avg
Y	6.5	6.4	6.5	0.1	1.1	3.0	2.9	3.0	0.1	2.4	3.0
Zr	25.9	24.7	25.3	0.8	3.4	9.3	10.0	9.7	0.5	5.1	3.0
Nb	1.9	2.2	2.05	0.21	10	0.7	0.6	0.65	0.07	11	12
Mo	0.12	0.12	0.12	0.00	0.0	0.09	0.07	0.08	0.01	18	8.8
Cd	0.01	0.01	0.01	0.00	0.0	<.01	0.01	0.01			
In	0.02	0.02	0.02	0.00	0.0	0.02	<.02	0.02			
Sn	<1	<1				<1	<1				
Sb	<.02	<.02				<.02	<.02				
Cs	0.5	0.2	0.35	0.21	61	0.2	0.3	0.25	0.07	28	20
Ba	28	31	30	2	7.2	17	24	21	5	24	6.6
La	4.5	4.8	4.7	0.2	4.6	1.5	1.5	1.5	0.0	0.0	1.9
Ce	9.4	9.3	9.4	0.1	0.8	3.7	3.5	3.6	0.1	3.9	2.5
Pr	1.3	1.2	1.2	0.0	3.4	0.5	0.4	0.4	0.0	4.9	4.7
Nd	4.8	5.3	5.05	0.35	7.0	2.5	2.3	2.4	0.14	5.9	8.2
Sm	1.2	1.4	1.3	0.14	11	0.5	0.7	0.6	0.14	24	9.1
Eu	0.61	0.72	0.67	0.08	12	0.19	0.19	0.19	0.00	0.0	4.3
Gd	1.44	1.32	1.38	0.08	6.1	0.63	0.76	0.70	0.09	13	10
Tb	0.20	0.21	0.21	0.01	3.4	0.11	0.08	0.10	0.02	22	9.6
Dy	1.09	1.07	1.08	0.01	1.3	0.47	0.54	0.51	0.05	9.8	5.9
Ho	0.23	0.20	0.22	0.02	9.9	0.12	0.10	0.11	0.01	13	6.5
Er	0.64	0.52	0.58	0.08	15	0.23	0.28	0.26	0.04	14	8.3
Tm	0.07	0.06	0.07	0.01	11	0.05	<.05	0.05			
Yb	0.48	0.45	0.47	0.02	4.6	0.34	0.32	0.33	0.01	4.3	8.0
Lu	0.06	0.06	0.06	0.00	0.0	0.04	0.04	0.04	0.00	0.0	2.1
Hf	0.6	0.8	0.7	0.1	20	<.5	<.5				6.6
Ta	0.1	<.1	0.1		0.0	<.1	<.1				14
W	<.1	0.1	0.1			0.1	<.1	0.1			
Ag (ppb)	61	52	57	6	11.3	24	26	25	1	5.7	5.0
Tl	0.11	0.11	0.11	0.00	0.0	<.02	<.02				
Pb	2	2	2	0	2.1	2	1	2	0	5.0	6.0
Th	0.2	0.2	0.2	0.00	0.0	0.6	<.1	0.6		0.0	18
U	0.2	0.2	0.2	0.00	0.0	<.1	0.1	0.1		0.0	0.0

[1] Duplicate analyses are multiple digestions of a single crushed sample.

[2] All Fe as Fe_2O_3.

* Partial digestion only.

LOI = loss on ignition

TOT/C = total carbon; TOT/S = total sulphur by leuco

Appendix III: All olivine core, middle, and rim compositions by EPMA

Region / Drillhole	West Pyrrhotite Lake / MX03-002										
Rock	Peridotite	Peridotite	Peridotite	Peridotite	Peridotite	Peridotite	Peridotite	Peridotite	Peridotite	Peridotite	Peridotite
Thin Section	RMX02-3A	RMX02-3A	RMX02-3A	RMX02-3A	RMX02-3A	RMX02-3A	RMX02-3A	RMX02-3A	RMX02-3A	RMX02-3A	RMX02-3A
Geochem ID	71112	71112	71112	71112	71112	71112	71112	71112	71112	71112	71112
Probe point	2_3a_10	2_3a_11	2_3a_12	2_3a_13	2_3a_14	2_3a_15	2_3a_16	2_3a_17	2_3a_18	2_3a_1	2_3a_2
Drilled depth (m)	53	53	53	53	53	53	53	53	53	53	53
Area	O1	O1	O1	O1	O1	O1	O1	O1	O1	O2	O2
Grain	1	1	1	2	2	2	3	3	3	1	1
Site	core	mid	rim	core	mid	rim	core	mid	rim	core	mid
Oxide wt %											
SiO2	39.35	39.17	39.47	39.27	39.00	39.28	39.01	39.15	39.13	39.23	39.43
TiO2	0.03	0.04	0.00	0.02	0.05	0.06	0.03	0.01	0.02	0.02	0.05
FeO	17.45	17.48	17.63	17.65	17.78	17.75	17.37	17.69	17.31	17.65	17.21
MnO	0.23	0.26	0.23	0.20	0.25	0.24	0.23	0.20	0.27	0.30	0.19
MgO	42.97	42.83	42.84	43.00	42.97	42.87	42.86	42.96	43.15	42.80	42.74
CaO	0.06	0.05	0.05	0.05	0.04	0.06	0.07	0.04	0.04	0.07	0.07
Cr2O3	0.04	0.06	0.06	0.03	0.00	0.07	0.10	0.00	0.00	0.00	0.00
NiO[1]	0.31	0.31	0.30	0.29	0.31	0.30	0.30	0.29	0.30	0.30	0.31
NiO[2]	0.34	0.33	0.33	0.33	0.27	0.25	0.26	0.36	0.26	0.30	0.30
total	100.4	100.2	100.6	100.5	100.4	100.6	99.98	100.3	100.2	100.4	100.0
Cation (p.f.u.)											
Si	0.996	0.994	0.998	0.994	0.991	0.994	0.992	0.994	0.993	0.996	1.001
Ti	0.001	0.001	0.000	0.000	0.001	0.001	0.001	0.000	0.000	0.000	0.001
Fe^{2+}	0.369	0.371	0.373	0.374	0.378	0.375	0.369	0.375	0.367	0.375	0.365
Mn	0.005	0.006	0.005	0.004	0.005	0.005	0.005	0.004	0.006	0.006	0.004
Mg	1.622	1.621	1.615	1.623	1.627	1.617	1.625	1.626	1.633	1.619	1.618
Ca	0.002	0.001	0.001	0.001	0.001	0.002	0.002	0.001	0.001	0.002	0.002
Cr	0.002	0.003	0.003	0.001	0.000	0.003	0.005	0.000	0.000	0.000	0.000
Ni	0.006	0.006	0.006	0.006	0.006	0.006	0.006	0.006	0.006	0.006	0.006
Sum	3.002	3.003	3.001	3.004	3.008	3.003	3.005	3.006	3.006	3.004	2.998
Endmembers %											
Fo	81.4	81.4	81.2	81.3	81.2	81.2	81.5	81.2	81.6	81.2	81.6
Fa	18.6	18.6	18.8	18.7	18.8	18.8	18.5	18.8	18.4	18.8	18.4

[1] Data collected using 100 nA beam current, 100 second counting time, and a fixed matrix composition.

[2] Data collected using the standard 20 nA beam current and 20 second counting time.

Appendix III (continued): All olivine core, middle, and rim compositions by EPMA

Region / Drillhole											
Rock	Peridotite	Peridotite	Peridotite	Peridotite	Peridotite	Peridotite	Peridotite	Peridotite	Peridotite	Peridotite	Peridotite
Thin Section	RMX02-3A	RMX02-3A	RMX02-3A	RMX02-3A	RMX02-3A	RMX02-3A	RMX02-3A	RMX02-4	RMX02-4	RMX02-4	RMX02-4
Geochem ID	71112	71112	71112	71112	71112	71112	71112	71115	71115	71115	71115
Probe point	2_3a_3	2_3a_4	2_3a_5	2_3a_6	2_3a_7	2_3a_8	2_3a_9	2_4_1	2_4_2	2_4_3	2_4_4
Depth (m)	53	53	53	53	53	53	53	71	71	71	71
Area	O2	O2	O2	O2	O2	O2	O2	O1	O1	O1	O1
Grain	1	2	2	3	3	4	4	1	1	1	2
Site	rim	mid	rim	mid	rim	mid	rim	core	mid	rim	core
Oxide wt %											
SiO2	39.22	39.25	39.36	39.11	39.37	39.10	39.37	39.35	38.91	39.33	39.20
TiO2	0.07	0.02	0.03	0.01	0.00	0.03	0.04	0.04	0.02	0.01	0.02
FeO	17.75	17.29	17.57	16.95	17.26	17.00	17.44	17.89	17.58	17.78	17.60
MnO	0.19	0.22	0.25	0.27	0.26	0.26	0.28	0.22	0.18	0.25	0.22
MgO	42.76	42.80	42.94	43.10	43.17	42.90	43.07	42.96	42.93	42.96	42.92
CaO	0.02	0.06	0.04	0.08	0.04	0.06	0.03	0.07	0.06	0.07	0.04
Cr2O3	0.02	0.08	0.02	0.11	0.02	0.00	0.01	0.01	0.13	0.02	0.05
NiO[1]	0.30	0.30	0.30	0.31	0.30	0.31	0.29	0.31	0.31	0.32	0.30
NiO[2]	0.31	0.32	0.30	0.37	0.29	0.25	0.31	0.27	0.28	0.35	0.29
total	100.3	100.0	100.5	99.93	100.4	99.66	100.5	100.9	100.1	100.7	100.4
Cation (p.f.u.)											
Si	0.995	0.997	0.996	0.993	0.996	0.997	0.996	0.994	0.989	0.995	0.994
Ti	0.001	0.000	0.001	0.000	0.000	0.001	0.001	0.001	0.000	0.000	0.000
Fe^{2+}	0.377	0.367	0.372	0.360	0.365	0.362	0.369	0.378	0.374	0.376	0.373
Mn	0.004	0.005	0.005	0.006	0.006	0.006	0.006	0.005	0.004	0.005	0.005
Mg	1.618	1.620	1.620	1.631	1.628	1.630	1.624	1.618	1.627	1.619	1.622
Ca	0.001	0.002	0.001	0.002	0.001	0.002	0.001	0.002	0.002	0.002	0.001
Cr	0.001	0.004	0.001	0.005	0.001	0.000	0.000	0.000	0.006	0.001	0.002
Ni	0.006	0.006	0.006	0.006	0.006	0.006	0.006	0.006	0.006	0.006	0.006
Sum	3.003	3.001	3.003	3.004	3.003	3.003	3.003	3.005	3.008	3.005	3.004
Endmembers %											
Fo	81.1	81.5	81.3	81.9	81.7	81.8	81.5	81.1	81.3	81.2	81.3
Fa	18.9	18.5	18.7	18.1	18.3	18.2	18.5	18.9	18.7	18.8	18.7

[1] Data collected using 100 nA beam current, 100 second counting time, and a fixed matrix composition.

[2] Data collected using the standard 20 nA beam current and 20 second counting time.

Appendix III (continued): All olivine core, middle, and rim compositions by EPMA

Region / Drillhole											
Rock	Peridotite	Peridotite	Peridotite	Peridotite	Peridotite	Peridotite	Peridotite	Peridotite	Peridotite	Peridotite	Peridotite
Thin Section	RMX02-4	RMX02-4	RMX02-4	RMX02-4	RMX02-4	RMX02-4	RMX02-4	RMX02-4	RMX02-4	RMX02-4	RMX02-4
Geochem ID	71115	71115	71115	71115	71115	71115	71115	71115	71115	71115	71115
Probe point	2_4_5	2_4_6	2_4_7	2_4_8	2_4_9	2_4_10	2_4_11	2_4_12	2_4_13	2_4_14	2_4_15
Depth (m)	71	71	71	71	71	71	71	71	71	71	71
Area	O1	O1	O1	O1	O2	O2	O2	O2	O2	O2	O2
Grain	2	2	3	3	1	1	1	2	2	2	3
Site	mid	rim	mid	rim	core	mid	rim	core	mid	rim	core
Oxide wt %											
SiO2	39.08	39.12	39.36	39.18	39.25	39.38	39.36	39.57	39.28	39.33	39.29
TiO2	0.03	0.04	0.04	0.00	0.06	0.02	0.04	0.03	0.04	0.02	0.03
FeO	18.01	17.39	17.97	17.69	17.56	17.61	17.42	17.70	17.55	17.41	17.85
MnO	0.27	0.23	0.21	0.22	0.21	0.21	0.26	0.20	0.27	0.18	0.23
MgO	43.15	43.01	43.12	43.21	43.17	43.19	43.27	43.14	43.24	43.13	43.32
CaO	0.05	0.04	0.05	0.04	0.05	0.05	0.04	0.05	0.06	0.03	0.05
Cr2O3	0.00	0.10	0.02	0.00	0.02	0.00	0.00	0.00	0.01	0.02	0.00
NiO[1]	0.31	0.30	0.31	0.32	0.31	0.33	0.33	0.32	0.33	0.33	0.32
NiO[2]	0.31	0.31	0.32	0.34	0.30	0.35	0.34	0.32	0.36	0.28	0.26
total	100.9	100.2	101.1	100.7	100.6	100.8	100.7	101.0	100.8	100.4	101.1
Cation (p.f.u.)											
Si	0.989	0.992	0.993	0.992	0.993	0.994	0.994	0.997	0.992	0.995	0.991
Ti	0.001	0.001	0.001	0.000	0.001	0.000	0.001	0.001	0.001	0.000	0.001
Fe^{2+}	0.381	0.369	0.379	0.374	0.371	0.372	0.368	0.373	0.371	0.368	0.376
Mn	0.006	0.005	0.004	0.005	0.004	0.004	0.006	0.004	0.006	0.004	0.005
Mg	1.627	1.626	1.621	1.630	1.628	1.626	1.629	1.620	1.628	1.627	1.628
Ca	0.001	0.001	0.001	0.001	0.001	0.001	0.001	0.001	0.002	0.001	0.001
Cr	0.000	0.005	0.001	0.000	0.001	0.000	0.000	0.000	0.000	0.001	0.000
Ni	0.006	0.006	0.006	0.006	0.006	0.007	0.007	0.006	0.007	0.007	0.006
Sum	3.011	3.005	3.006	3.008	3.006	3.005	3.005	3.003	3.007	3.004	3.009
Endmembers %											
Fo	81.0	81.5	81.1	81.3	81.4	81.4	81.6	81.3	81.5	81.5	81.2
Fa	19.0	18.5	18.9	18.7	18.6	18.6	18.4	18.7	18.5	18.5	18.8

[1] Data collected using 100 nA beam current, 100 second counting time, and a fixed matrix composition.

[2] Data collected using the standard 20 nA beam current and 20 second counting time.

Appendix III (continued): All olivine core, middle, and rim compositions by EPMA

Region / Drillhole											
Rock	Peridotite	Peridotite	F. Peridotite	F. Peridotite	F. Peridotite	F. Peridotite	F. Peridotite	F. Peridotite	F. Peridotite	F. Peridotite	F. Peridotite
Thin Section	RMX02-4	RMX02-4	RMX02-5	RMX02-5	RMX02-5	RMX02-5	RMX02-5	RMX02-5	RMX02-5	RMX02-5	RMX02-5
Geochem ID	71115	71115	71123	71123	71123	71123	71123	71123	71123	71123	71123
Probe point	2_4_16	2_4_17	2_5_1	2_5_2	2_5_3	2_5_4	2_5_5	2_5_6	2_5_7	2_5_8	2_5_9
Depth (m)	71	71	118	118	118	118	118	118	118	118	118
Area	O2	O2	O1	O1	O1	O1	O1	O1	O1	O1	O1
Grain	3	3	1	1	1	2	2	2	3	3	3
Site	mid	rim	core	mid	rim	core	mid	rim	core	mid	rim
Oxide wt %											
SiO2	39.42	39.29	39.27	38.82	39.16	39.13	38.97	39.00	39.04	39.02	39.00
TiO2	0.03	0.00	0.04	0.05	0.03	0.04	0.03	0.08	0.04	0.03	0.06
FeO	17.57	17.57	18.97	18.44	18.64	18.63	18.29	18.33	18.87	18.61	18.24
MnO	0.22	0.21	0.27	0.29	0.24	0.24	0.30	0.25	0.27	0.24	0.32
MgO	43.37	43.34	42.20	42.17	42.17	42.31	42.49	42.62	42.57	42.32	42.43
CaO	0.04	0.04	0.05	0.05	0.03	0.04	0.04	0.06	0.05	0.04	0.05
Cr2O3	0.03	0.00	0.12	0.00	0.12	0.03	0.00	0.03	0.00	0.07	0.00
NiO[1]	0.32	0.31	0.30	0.28	0.30	0.29	0.29	0.29	0.30	0.30	0.29
NiO[2]	0.36	0.36	0.31	0.34	0.29	0.28	0.39	0.27	0.34	0.34	0.27
total	101.0	100.8	101.2	100.1	100.7	100.7	100.4	100.7	101.2	100.6	100.4
Cation (p.f.u.)											
Si	0.993	0.993	0.993	0.992	0.994	0.994	0.992	0.990	0.989	0.991	0.993
Ti	0.001	0.000	0.001	0.001	0.001	0.001	0.001	0.002	0.001	0.001	0.001
Fe^{2+}	0.370	0.371	0.401	0.394	0.395	0.396	0.389	0.389	0.400	0.395	0.388
Mn	0.005	0.004	0.006	0.006	0.005	0.005	0.006	0.005	0.006	0.005	0.007
Mg	1.629	1.632	1.590	1.607	1.595	1.602	1.612	1.613	1.608	1.603	1.610
Ca	0.001	0.001	0.001	0.001	0.001	0.001	0.001	0.002	0.001	0.001	0.001
Cr	0.001	0.000	0.006	0.000	0.006	0.001	0.000	0.001	0.000	0.003	0.000
Ni	0.006	0.006	0.006	0.006	0.006	0.006	0.006	0.006	0.006	0.006	0.006
Sum	3.006	3.007	3.004	3.007	3.003	3.005	3.007	3.008	3.010	3.006	3.006
Endmembers %											
Fo	81.5	81.5	79.9	80.3	80.1	80.2	80.6	80.6	80.1	80.2	80.6
Fa	18.5	18.5	20.1	19.7	19.9	19.8	19.4	19.4	19.9	19.8	19.4

[1] Data collected using 100 nA beam current, 100 second counting time, and a fixed matrix composition.

[2] Data collected using the standard 20 nA beam current and 20 second counting time.

Appendix III (continued): All olivine core, middle, and rim compositions by EPMA

Region / Drillhole											
Rock	F. Peridotite	F. Peridotite	F. Peridotite	F. Peridotite	F. Peridotite	F. Peridotite	F. Peridotite	F. Peridotite	F. Peridotite	F. Peridotite	F. Peridotite
Thin Section	RMX02-5	RMX02-5	RMX02-5	RMX02-5	RMX02-5	RMX02-5	RMX02-5	RMX02-5	RMX02-6	RMX02-6	RMX02-6
Geochem ID	71123	71123	71123	71123	71123	71123	71123	71123	71127	71127	71127
Probe point	2_5_10	2_5_11	2_5_12	2_5_13	2_5_14	2_5_15	2_5_16	2_5_17	2_6_1	2_6_2	2_6_3
Depth (m)	118	118	118	118	118	118	118	118	141	141	141
Area	O2	O2	O2	O2	O2	O2	O2	O2	O2	O2	O2
Grain	1	1	1	2	2	2	3	3	1	1	2
Site	core	mid	rim	core	mid	rim	core	mid	core	mid	core
Oxide wt %											
SiO2	38.70	38.82	38.62	38.73	38.74	38.99	38.59	38.94	38.21	38.61	38.48
TiO2	0.02	0.01	0.05	0.04	0.03	0.01	0.05	0.05	0.04	0.04	0.04
FeO	18.39	18.66	18.74	18.70	18.58	18.78	18.77	18.87	20.09	20.31	19.43
MnO	0.29	0.28	0.30	0.29	0.25	0.29	0.29	0.29	0.25	0.26	0.28
MgO	42.20	41.94	42.18	42.46	42.47	42.07	42.01	41.96	40.88	40.75	41.39
CaO	0.09	0.11	0.05	0.05	0.07	0.04	0.05	0.07	0.05	0.07	0.08
Cr2O3	0.02	0.02	0.02	0.00	0.13	0.03	0.03	0.00	0.09	0.08	0.08
NiO[1]	0.28	0.28	0.28	0.28	0.28	0.28	0.29	0.28	0.28	0.29	0.29
NiO[2]	0.30	0.21	0.27	0.30	0.29	0.31	0.29	0.32	0.32	0.31	0.24
total	99.99	100.1	100.2	100.5	100.5	100.5	100.1	100.5	99.88	100.4	100.1
Cation (p.f.u.)											
Si	0.990	0.993	0.987	0.987	0.985	0.993	0.988	0.993	0.986	0.991	0.988
Ti	0.000	0.000	0.001	0.001	0.001	0.000	0.001	0.001	0.001	0.001	0.001
Fe^{2+}	0.393	0.399	0.401	0.398	0.395	0.400	0.402	0.402	0.434	0.436	0.417
Mn	0.006	0.006	0.006	0.006	0.005	0.006	0.006	0.006	0.005	0.006	0.006
Mg	1.610	1.599	1.608	1.613	1.610	1.598	1.604	1.595	1.573	1.560	1.585
Ca	0.002	0.003	0.001	0.001	0.002	0.001	0.001	0.002	0.001	0.002	0.002
Cr	0.001	0.001	0.001	0.000	0.006	0.001	0.001	0.000	0.005	0.004	0.004
Ni	0.006	0.006	0.006	0.006	0.006	0.006	0.006	0.006	0.006	0.006	0.006
Sum	3.009	3.007	3.011	3.012	3.011	3.006	3.010	3.006	3.011	3.006	3.009
Endmembers %											
Fo	80.4	80.0	80.1	80.2	80.3	80.0	80.0	79.9	78.4	78.2	79.2
Fa	19.6	20.0	19.9	19.8	19.7	20.0	20.0	20.1	21.6	21.8	20.8

[1] Data collected using 100 nA beam current, 100 second counting time, and a fixed matrix composition.

[2] Data collected using the standard 20 nA beam current and 20 second counting time.

Appendix III (continued): All olivine core, middle, and rim compositions by EPMA

Region / Drillhole											
Rock	F. Peridotite	F. Peridotite	F. Peridotite	F. Peridotite	F. Peridotite	F. Peridotite	F. Peridotite	F. Peridotite	F. Peridotite	Ol-Gbnr	Ol-Gbnr
Thin Section	RMX02-6	RMX02-6	RMX02-6	RMX02-6	RMX02-6	RMX02-6	RMX02-6	RMX02-6	RMX02-6	RMX02-8	RMX02-8
Geochem ID	71127	71127	71127	71127	71127	71127	71127	71127	71127	71133	71133
Probe point	2_6_4	2_6_5	2_6_6	2_6_7	2_6_8	2_6_9	2_6_10	2_6_11	2_6_12	2_8_1	2_8_2
Depth (m)	141	141	141	141	141	141	141	141	141	162	162
Area	O2	O2	O2	O3	O3	O3	O3	O3	O3	O1	O1
Grain	2	3	3	1	1	2	2	3	3	1	1
Site	rim	core	rim	core	rim	core	mid	core	mid	core	mid
Oxide wt %											
SiO2	38.67	38.85	38.73	38.81	38.74	38.42	38.48	38.51	38.82	38.13	38.32
TiO2	0.02	0.06	0.00	0.02	0.03	0.04	0.04	0.02	0.05	0.01	0.04
FeO	19.52	19.62	19.43	19.27	19.37	19.19	19.12	19.28	19.06	21.99	22.01
MnO	0.27	0.27	0.24	0.28	0.27	0.28	0.27	0.25	0.22	0.28	0.27
MgO	41.48	41.15	40.96	41.41	41.30	41.33	41.52	41.49	41.23	39.14	39.06
CaO	0.05	0.07	0.08	0.06	0.08	0.06	0.02	0.06	0.07	0.02	0.06
Cr2O3	0.12	0.00	0.02	0.00	0.03	0.04	0.04	0.02	0.03	0.00	0.00
NiO[1]	0.28	0.28	0.28	0.30	0.31	0.33	0.32	0.31	0.31	0.25	0.25
NiO[2]	0.28	0.36	0.33	0.34	0.32	0.35	0.25	0.32	0.31	0.26	0.27
total	100.4	100.3	99.75	100.2	100.1	99.70	99.82	99.95	99.78	99.82	100.0
Cation (p.f.u.)											
Si	0.989	0.996	0.997	0.995	0.994	0.990	0.990	0.990	0.997	0.994	0.996
Ti	0.000	0.001	0.000	0.000	0.001	0.001	0.001	0.000	0.001	0.000	0.001
Fe^{2+}	0.417	0.420	0.418	0.413	0.415	0.413	0.411	0.414	0.409	0.479	0.479
Mn	0.006	0.006	0.005	0.006	0.006	0.006	0.006	0.005	0.005	0.006	0.006
Mg	1.582	1.572	1.572	1.583	1.579	1.588	1.592	1.590	1.579	1.521	1.514
Ca	0.001	0.002	0.002	0.002	0.002	0.002	0.001	0.002	0.002	0.001	0.002
Cr	0.006	0.000	0.001	0.000	0.001	0.002	0.002	0.001	0.001	0.000	0.000
Ni	0.006	0.006	0.006	0.006	0.006	0.007	0.007	0.006	0.006	0.005	0.005
Sum	3.008	3.003	3.002	3.005	3.005	3.008	3.009	3.009	3.001	3.006	3.003
Endmembers %											
Fo	79.1	78.9	79.0	79.3	79.2	79.3	79.5	79.3	79.4	76.0	76.0
Fa	20.9	21.1	21.0	20.7	20.8	20.7	20.5	20.7	20.6	24.0	24.0

[1] Data collected using 100 nA beam current, 100 second counting time, and a fixed matrix composition.

[2] Data collected using the standard 20 nA beam current and 20 second counting time.

Appendix III (continued): All olivine core, middle, and rim compositions by EPMA

Region / Drillhole											
Rock	Ol-Gbnr	Ol-Gbnr	Ol-Gbnr	Ol-Gbnr	Ol-Gbnr	Ol-Gbnr	Ol-Gbnr	Ol-Gbnr	Ol-Gbnr	Ol-Gbnr	Ol-Gbnr
Thin Section	RMX02-8	RMX02-8	RMX02-8	RMX02-8	RMX02-8	RMX02-8	RMX02-8	RMX02-8	RMX02-8	RMX02-8	RMX02-8
Geochem ID	71133	71133	71133	71133	71133	71133	71133	71133	71133	71133	71133
Probe point	2_8_3	2_8_4	2_8_5	2_8_6	2_8_7	2_8_8	2_8_9	2_8_10	2_8_11	2_8_12	2_8_13
Depth (m)	162	162	162	162	162	162	162	162	162	162	162
Area	O1	O1	O1	O1	O1	O1	O1	O2	O2	O2	O2
Grain	1	2	2	2	3	3	3	1	1	1	2
Site	rim	core	mid	rim	core	mid	rim	core	mid	rim	core
Oxide wt %											
SiO2	38.14	38.11	38.32	38.24	38.51	38.36	38.41	38.38	38.29	38.18	38.57
TiO2	0.03	0.01	0.02	0.04	0.02	0.02	0.04	0.03	0.02	0.00	0.04
FeO	22.54	22.03	22.78	22.04	21.03	20.89	21.46	21.48	21.97	21.64	21.30
MnO	0.28	0.34	0.32	0.27	0.28	0.28	0.26	0.29	0.33	0.30	0.29
MgO	39.37	38.94	39.07	38.87	40.09	39.79	39.95	39.53	39.64	39.66	40.07
CaO	0.05	0.05	0.07	0.06	0.07	0.06	0.07	0.03	0.06	0.04	0.09
Cr2O3	0.00	0.02	0.00	0.01	0.03	0.03	0.00	0.05	0.00	0.02	0.01
NiO[1]	0.25	0.24	0.26	0.25	0.25	0.25	0.25	0.26	0.26	0.27	0.26
NiO[2]	0.26	0.23	0.25	0.18	0.25	0.28	0.28	0.30	0.27	0.29	0.25
total	100.7	99.73	100.8	99.78	100.3	99.69	100.4	100.1	100.6	100.1	100.6
Cation (p.f.u.)											
Si	0.988	0.994	0.992	0.997	0.994	0.996	0.992	0.995	0.991	0.991	0.993
Ti	0.001	0.000	0.000	0.001	0.000	0.000	0.001	0.001	0.000	0.000	0.001
Fe^{2+}	0.488	0.481	0.493	0.480	0.454	0.453	0.463	0.465	0.475	0.470	0.459
Mn	0.006	0.008	0.007	0.006	0.006	0.006	0.006	0.006	0.007	0.007	0.006
Mg	1.521	1.515	1.508	1.511	1.542	1.539	1.538	1.527	1.529	1.534	1.538
Ca	0.001	0.001	0.002	0.002	0.002	0.002	0.002	0.001	0.002	0.001	0.002
Cr	0.000	0.001	0.000	0.001	0.002	0.002	0.000	0.003	0.000	0.001	0.000
Ni	0.005	0.005	0.005	0.005	0.005	0.005	0.005	0.006	0.005	0.006	0.005
Sum	3.011	3.005	3.008	3.002	3.005	3.003	3.007	3.003	3.009	3.009	3.006
Endmembers %											
Fo	75.7	75.9	75.4	75.9	77.3	77.3	76.8	76.6	76.3	76.6	77.0
Fa	24.3	24.1	24.6	24.1	22.7	22.7	23.2	23.4	23.7	23.4	23.0

[1] Data collected using 100 nA beam current, 100 second counting time, and a fixed matrix composition.

[2] Data collected using the standard 20 nA beam current and 20 second counting time.

Appendix III (continued): All olivine core, middle, and rim compositions by EPMA

Region / Drillhole	Far West Margin / MX03-001										
Rock	Ol-Gbnr	Ol-Gbnr	Ol-Gbnr	Ol-Gbnr	Ol-Gbnr	Ol-Gbnr	Cr. Peridotite	Cr. Peridotite	Cr. Peridotite	Cr. Peridotite	Cr. Peridotite
Thin Section	RMX02-8	RMX02-8	RMX02-8	RMX02-8	RMX02-8	RMX02-8	RMX01-1	RMX01-1	RMX01-1	RMX01-1	RMX01-1
Geochem ID	71133	71133	71133	71133	71133	71133	71061	71061	71061	71061	71061
Probe point	2_8_14	2_8_15	2_8_16	2_8_17	2_8_18	2_8_19	1_1_1	1_1_2	1_1_3	1_1_4	1_1_5
Depth (m)	162	162	162	162	162	162	10	10	10	10	10
Area	O2	O2	O2	O2	O2	O2	O1	O1	O1	O1	O1
Grain	2	3	3	4	4	4	1	1	1	2	2
Site	rim	core	rim	core	mid	rim	core	mid	rim	core	mid
Oxide wt %											
SiO2	38.51	38.58	38.22	38.61	38.61	38.50	39.97	40.02	39.28	40.40	40.26
TiO2	0.03	0.00	0.02	0.00	0.02	0.04	0.02	0.01	0.01	0.00	0.04
FeO	21.16	21.50	21.20	21.08	21.01	21.00	12.95	12.78	18.54	12.36	12.86
MnO	0.31	0.26	0.27	0.26	0.31	0.28	0.23	0.18	0.14	0.19	0.13
MgO	40.11	40.04	40.18	40.29	40.21	40.22	46.80	46.87	42.33	47.11	47.19
CaO	0.08	0.05	0.09	0.08	0.03	0.06	0.07	0.05	0.01	0.07	0.09
Cr2O3	0.02	0.00	0.00	0.02	0.04	0.00	0.16	0.09	0.13	0.15	0.04
NiO[1]	0.27	0.26	0.27	0.26	0.27	0.27	0.28	0.29	0.17	0.28	0.29
NiO[2]	0.26	0.31	0.21	0.25	0.27	0.29	0.29	0.24	0.14	0.28	0.31
total	100.5	100.7	100.2	100.6	100.5	100.4	100.5	100.3	100.6	100.6	100.9
Cation (p.f.u.)											
Si	0.993	0.994	0.989	0.993	0.994	0.993	0.990	0.992	0.996	0.996	0.993
Ti	0.001	0.000	0.000	0.000	0.000	0.001	0.000	0.000	0.000	0.000	0.001
Fe^{2+}	0.456	0.463	0.459	0.453	0.452	0.453	0.268	0.265	0.393	0.255	0.265
Mn	0.007	0.006	0.006	0.006	0.007	0.006	0.005	0.004	0.003	0.004	0.003
Mg	1.541	1.537	1.549	1.545	1.543	1.546	1.728	1.733	1.599	1.731	1.734
Ca	0.002	0.001	0.002	0.002	0.001	0.002	0.002	0.001	0.000	0.002	0.002
Cr	0.001	0.000	0.000	0.001	0.002	0.000	0.008	0.004	0.006	0.007	0.002
Ni	0.005	0.005	0.006	0.005	0.006	0.006	0.006	0.006	0.003	0.006	0.006
Sum	3.006	3.006	3.011	3.006	3.005	3.006	3.006	3.005	3.001	3.000	3.006
Endmembers %											
Fo	77.2	76.9	77.2	77.3	77.3	77.3	86.6	86.7	80.3	87.2	86.7
Fa	22.8	23.1	22.8	22.7	22.7	22.7	13.4	13.3	19.7	12.8	13.3

[1] Data collected using 100 nA beam current, 100 second counting time, and a fixed matrix composition.

[2] Data collected using the standard 20 nA beam current and 20 second counting time.

Appendix III (continued): All olivine core, middle, and rim compositions by EPMA

Region / Drillhole											
Rock	Cr. Peridotite	Cr. Peridotite	Cr. Peridotite	Cr. Peridotite	Cr. Peridotite	Cr. Peridotite	Cr. Peridotite	Cr. Peridotite	Cr. Peridotite	Cr. Peridotite	Cr. Peridotite
Thin Section	RMX01-1	RMX01-1	RMX01-1	RMX01-1	RMX01-1	RMX01-1	RMX01-1	RMX01-1	RMX01-1	RMX01-1	RMX01-1
Geochem ID	71061	71061	71061	71061	71061	71061	71061	71061	71061	71061	71061
Probe point	1_1_6	1_1_7	1_1_8	1_1_9	1_1_10	1_1_11	1_1_12	1_1_13	1_1_14	1_1_15	1_1_16
Depth (m)	10	10	10	10	10	10	10	10	10	10	10
Area	O1	O1	O1	O1	O2	O2	O2	O2	O2	O2	O2
Grain	2	3	3	3	1	1	1	2	2	3	3
Site	rim	core	mid	rim	core	mid	rim	core	rim	core	mid
Oxide wt %											
SiO2	40.08	40.18	40.07	40.73	40.34	40.33	40.18	40.54	40.38	40.76	40.59
TiO2	0.04	0.02	0.01	0.03	0.01	0.01	0.03	0.03	0.02	0.01	0.01
FeO	12.77	12.89	12.72	13.00	11.99	12.13	12.26	12.11	12.10	12.05	11.69
MnO	0.25	0.20	0.21	0.22	0.13	0.13	0.15	0.18	0.16	0.17	0.18
MgO	47.04	47.04	47.10	47.03	47.13	47.13	47.14	47.71	47.83	47.86	47.85
CaO	0.04	0.07	0.08	0.07	0.07	0.06	0.06	0.08	0.05	0.06	0.05
Cr2O3	0.11	0.06	0.16	0.06	0.02	0.01	0.07	0.00	0.10	0.07	0.04
NiO[1]	0.29	0.29	0.30	0.28	0.30	0.30	0.29	0.26	0.28	0.28	0.30
NiO[2]	0.27	0.33	0.31	0.35	0.34	0.29	0.29	0.29	0.21	0.25	0.28
total	100.6	100.7	100.6	101.4	99.97	100.1	100.2	100.9	100.9	101.3	100.7
Cation (p.f.u.)											
Si	0.991	0.992	0.990	0.999	0.999	0.999	0.995	0.996	0.991	0.997	0.997
Ti	0.001	0.000	0.000	0.001	0.000	0.000	0.001	0.001	0.000	0.000	0.000
Fe^{2+}	0.264	0.266	0.263	0.266	0.248	0.251	0.254	0.249	0.248	0.246	0.240
Mn	0.005	0.004	0.004	0.005	0.003	0.003	0.003	0.004	0.003	0.004	0.004
Mg	1.733	1.732	1.734	1.719	1.741	1.740	1.740	1.747	1.751	1.744	1.752
Ca	0.001	0.002	0.002	0.002	0.002	0.002	0.002	0.002	0.001	0.002	0.001
Cr	0.005	0.003	0.008	0.003	0.001	0.000	0.003	0.000	0.005	0.003	0.002
Ni	0.006	0.006	0.006	0.006	0.006	0.006	0.006	0.005	0.005	0.006	0.006
Sum	3.006	3.006	3.006	2.999	3.000	3.001	3.003	3.004	3.006	3.002	3.002
Endmembers %											
Fo	86.8	86.7	86.8	86.6	87.5	87.4	87.3	87.5	87.6	87.6	87.9
Fa	13.2	13.3	13.2	13.4	12.5	12.6	12.7	12.5	12.4	12.4	12.1

[1] Data collected using 100 nA beam current, 100 second counting time, and a fixed matrix composition.

[2] Data collected using the standard 20 nA beam current and 20 second counting time.

Appendix III (continued): All olivine core, middle, and rim compositions by EPMA

Region / Drillhole											
Rock	Cr. Peridotite	Cr. Peridotite	Cr. Peridotite	Cr. Peridotite	Cr. Peridotite	Cr. Peridotite	Cr. Peridotite	Cr. Peridotite	Cr. Peridotite	Cr. Peridotite	Cr. Peridotite
Thin Section	RMX01-1	RMX01-3	RMX01-3	RMX01-3	RMX01-3	RMX01-3	RMX01-3	RMX01-3	RMX01-3	RMX01-3	RMX01-3
Geochem ID	71061	71063	71063	71063	71063	71063	71063	71063	71063	71063	71063
Probe point	1_1_17	1_3_1	1_3_2	1_3_3	1_3_4	1_3_5	1_3_6	1_3_7	1_3_8	1_3_9	1_3_10
Depth (m)	10	23	23	23	23	23	23	23	23	23	23
Area	O2	O2	O2	O2	O2	O2	O2	O1	O1	O1	O1
Grain	3	1	1	1	2	2	2	1	1	2	2
Site	rim	core	mid	rim	core	mid	rim	core	mid	core	mid
Oxide wt %											
SiO2	40.22	40.35	40.10	40.45	40.01	40.14	39.89	40.18	40.37	40.18	40.34
TiO2	0.00	0.05	0.02	0.01	0.03	0.03	0.08	0.05	0.02	0.00	0.02
FeO	13.46	12.95	13.07	12.70	13.04	12.88	13.06	12.59	12.79	12.27	12.73
MnO	0.17	0.18	0.19	0.19	0.17	0.26	0.22	0.19	0.17	0.18	0.20
MgO	47.04	46.66	46.75	46.51	46.20	46.59	46.92	46.57	46.71	47.01	47.04
CaO	0.01	0.08	0.08	0.07	0.11	0.10	0.09	0.09	0.06	0.03	0.08
Cr2O3	0.00	0.05	0.05	0.08	0.05	0.00	0.00	0.00	0.10	0.03	0.03
NiO[1]	0.21	0.15	0.15	0.14	0.16	0.16	0.14	0.14	0.15	0.14	0.15
NiO[2]	0.21	0.13	0.14	0.09	0.15	0.12	0.19	0.12	0.14	0.16	0.16
total	101.1	100.5	100.4	100.2	99.76	100.2	100.4	99.80	100.4	99.84	100.6
Cation (p.f.u.)											
Si	0.992	0.998	0.994	1.002	0.998	0.997	0.990	1.000	0.999	0.998	0.996
Ti	0.000	0.001	0.000	0.000	0.001	0.001	0.001	0.001	0.000	0.000	0.000
Fe^{2+}	0.278	0.268	0.271	0.263	0.272	0.268	0.271	0.262	0.265	0.255	0.263
Mn	0.004	0.004	0.004	0.004	0.004	0.005	0.005	0.004	0.004	0.004	0.004
Mg	1.730	1.721	1.728	1.718	1.718	1.726	1.736	1.727	1.722	1.740	1.732
Ca	0.000	0.002	0.002	0.002	0.003	0.003	0.002	0.002	0.002	0.001	0.002
Cr	0.000	0.002	0.002	0.004	0.002	0.000	0.000	0.000	0.005	0.001	0.001
Ni	0.004	0.003	0.003	0.003	0.003	0.003	0.003	0.003	0.003	0.003	0.003
Sum	3.008	3.000	3.004	2.996	3.000	3.002	3.008	2.999	2.999	3.002	3.002
Endmembers %											
Fo	86.2	86.5	86.4	86.7	86.3	86.6	86.5	86.8	86.7	87.2	86.8
Fa	13.8	13.5	13.6	13.3	13.7	13.4	13.5	13.2	13.3	12.8	13.2

[1] Data collected using 100 nA beam current, 100 second counting time, and a fixed matrix composition.

[2] Data collected using the standard 20 nA beam current and 20 second counting time.

Appendix III (continued): All olivine core, middle, and rim compositions by EPMA

Region / Drillhole											
Rock	Cr. Peridotite	Cr. Peridotite	Cr. Peridotite	Cr. Peridotite	Cr. Peridotite	Cr. Peridotite	Cr. Peridotite	Peridotite	Peridotite	Peridotite	Peridotite
Thin Section	RMX01-3	RMX01-3	RMX01-3	RMX01-3	RMX01-3	RMX01-3	RMX01-3	RMX01-4	RMX01-4	RMX01-4	RMX01-4
Geochem ID	71063	71063	71063	71063	71063	71063	71063	71072	71072	71072	71072
Probe point	1_3_11	1_3_12	1_3_13	1_3_14	1_3_15	1_3_16	1_3_17	1_4_1	1_4_2	1_4_3	1_4_4
Depth (m)	23	23	23	23	23	23	23	56	56	56	56
Area	O1	O1	O1	O1	O1	O1	O1	O1	O1	O1	O1
Grain	2	3	3	3	4	4	4	1	1	1	2
Site	rim	core	mid	rim	core	mid	rim	core	mid	rim	core
Oxide wt %											
SiO2	40.24	40.21	40.22	40.22	40.18	40.24	40.08	39.85	39.86	39.95	39.69
TiO2	0.00	0.03	0.04	0.01	0.00	0.03	0.03	0.06	0.02	0.05	0.02
FeO	12.17	12.87	12.97	13.11	12.56	12.90	12.47	14.32	14.88	14.27	14.35
MnO	0.17	0.21	0.23	0.18	0.16	0.17	0.19	0.21	0.16	0.17	0.20
MgO	47.22	46.55	46.31	46.86	46.78	46.82	46.98	45.35	45.37	45.18	45.42
CaO	0.04	0.10	0.08	0.05	0.09	0.05	0.05	0.07	0.10	0.06	0.11
Cr2O3	0.05	0.03	0.00	0.03	0.07	0.02	0.13	0.02	0.09	0.04	0.00
NiO[1]	0.15	0.15	0.13	0.14	0.15	0.14	0.14	0.33	0.33	0.34	0.34
NiO[2]	0.19	0.12	0.09	0.17	0.16	0.13	0.11	0.35	0.27	0.35	0.29
total	100.0	100.2	99.99	100.6	100.0	100.4	100.1	100.2	100.8	100.1	100.1
Cation (p.f.u.)											
Si	0.997	0.998	1.001	0.995	0.997	0.997	0.994	0.997	0.993	1.000	0.994
Ti	0.000	0.001	0.001	0.000	0.000	0.001	0.001	0.001	0.000	0.001	0.000
Fe^{2+}	0.252	0.267	0.270	0.271	0.261	0.267	0.258	0.299	0.310	0.299	0.301
Mn	0.004	0.004	0.005	0.004	0.003	0.004	0.004	0.004	0.003	0.004	0.004
Mg	1.744	1.723	1.718	1.728	1.731	1.729	1.736	1.691	1.685	1.685	1.696
Ca	0.001	0.003	0.002	0.001	0.002	0.001	0.001	0.002	0.003	0.002	0.003
Cr	0.002	0.001	0.000	0.001	0.003	0.001	0.006	0.001	0.004	0.002	0.000
Ni	0.003	0.003	0.003	0.003	0.003	0.003	0.003	0.007	0.007	0.007	0.007
Sum	3.002	3.000	2.999	3.004	3.001	3.002	3.003	3.002	3.005	2.998	3.005
Endmembers %											
Fo	87.4	86.6	86.4	86.4	86.9	86.6	87.0	85.0	84.5	85.0	84.9
Fa	12.6	13.4	13.6	13.6	13.1	13.4	13.0	15.0	15.5	15.0	15.1

[1] Data collected using 100 nA beam current, 100 second counting time, and a fixed matrix composition.

[2] Data collected using the standard 20 nA beam current and 20 second counting time.

Appendix III (continued): All olivine core, middle, and rim compositions by EPMA

Region / Drillhole											
Rock	Peridotite	Peridotite	Peridotite	Peridotite	Peridotite	Peridotite	Peridotite	Peridotite	Peridotite	Peridotite	Peridotite
Thin Section	RMX01-4	RMX01-4	RMX01-4	RMX01-4	RMX01-4	RMX01-4	RMX01-4	RMX01-4	RMX01-4	RMX01-4	RMX01-4
Geochem ID	71072	71072	71072	71072	71072	71072	71072	71072	71072	71072	71072
Probe point	1_4_5	1_4_6	1_4_7	1_4_8	1_4_9	1_4_10	1_4_11	1_4_12	1_4_13	1_4_14	1_4_15
Depth (m)	56	56	56	56	56	56	56	56	56	56	56
Area	O1	O1	O1	O1	O1	O2	O2	O2	O2	O2	O2
Grain	2	2	3	3	3	1	1	1	2	2	3
Site	mid	rim	core	mid	rim	core	mid	rim	core	rim	core
Oxide wt %											
SiO2	39.69	39.97	39.83	39.64	39.85	39.87	39.66	39.85	39.50	39.74	39.62
TiO2	0.04	0.02	0.06	0.04	0.05	0.05	0.01	0.05	0.04	0.01	0.01
FeO	14.45	14.68	14.45	14.28	14.54	14.76	14.53	14.85	14.26	14.39	14.62
MnO	0.29	0.25	0.21	0.20	0.19	0.17	0.24	0.21	0.22	0.15	0.20
MgO	45.71	45.68	45.24	45.34	45.47	45.30	45.14	45.44	45.19	45.26	44.98
CaO	0.04	0.05	0.06	0.06	0.07	0.10	0.11	0.05	0.07	0.05	0.13
Cr2O3	0.00	0.01	0.07	0.00	0.00	0.02	0.10	0.04	0.00	0.00	0.07
NiO[1]	0.33	0.33	0.33	0.33	0.33	0.34	0.34	0.33	0.35	0.34	0.34
NiO[2]	0.34	0.28	0.36	0.32	0.36	0.34	0.35	0.34	0.37	0.42	0.31
total	100.5	101.0	100.2	99.88	100.5	100.6	100.1	100.8	99.63	99.94	99.97
Cation (p.f.u.)											
Si	0.991	0.994	0.996	0.995	0.995	0.995	0.994	0.993	0.994	0.997	0.995
Ti	0.001	0.000	0.001	0.001	0.001	0.001	0.000	0.001	0.001	0.000	0.000
Fe^{2+}	0.302	0.305	0.302	0.300	0.304	0.308	0.304	0.309	0.300	0.302	0.307
Mn	0.006	0.005	0.004	0.004	0.004	0.004	0.005	0.004	0.005	0.003	0.004
Mg	1.701	1.693	1.686	1.697	1.692	1.685	1.686	1.688	1.696	1.693	1.684
Ca	0.001	0.001	0.002	0.002	0.002	0.003	0.003	0.001	0.002	0.001	0.003
Cr	0.000	0.000	0.003	0.000	0.000	0.001	0.005	0.002	0.000	0.000	0.003
Ni	0.007	0.007	0.007	0.007	0.007	0.007	0.007	0.007	0.007	0.007	0.007
Sum	3.008	3.006	3.001	3.004	3.004	3.003	3.004	3.005	3.005	3.003	3.003
Endmembers %											
Fo	84.9	84.7	84.8	85.0	84.8	84.5	84.7	84.5	85.0	84.9	84.6
Fa	15.1	15.3	15.2	15.0	15.2	15.5	15.3	15.5	15.0	15.1	15.4

[1] Data collected using 100 nA beam current, 100 second counting time, and a fixed matrix composition.

[2] Data collected using the standard 20 nA beam current and 20 second counting time.

Appendix III (continued): All olivine core, middle, and rim compositions by EPMA

Region / Drillhole											
Rock	Peridotite	Peridotite	Peridotite	Peridotite	F. Peridotite	F. Peridotite	F. Peridotite	F. Peridotite	F. Peridotite	F. Peridotite	F. Peridotite
Thin Section	RMX01-4	RMX01-4	RMX01-4	RMX01-4	RMX01-5	RMX01-5	RMX01-5	RMX01-5	RMX01-5	RMX01-5	RMX01-5
Geochem ID	71072	71072	71072	71072	71075	71075	71075	71075	71075	71075	71075
Probe point	1_4_16	1_4_17	1_4_18	1_4_19	1_5_1	1_5_2	1_5_3	1_5_4	1_5_5	1_5_6	1_5_7
Depth (m)	56	56	56	56	76	76	76	76	76	76	76
Area	O2	O2	O2	O2	O1	O1	O1	O1	O1	O1	O1
Grain	3	3	4	4	1	1	1	2	2	2	3
Site	mid	rim	mid	rim	core	mid	rim	core	mid	rim	core
Oxide wt %											
SiO2	39.76	39.84	40.00	40.01	39.63	39.65	39.27	39.75	39.48	39.62	39.59
TiO2	0.04	0.09	0.06	0.02	0.02	0.00	0.01	0.04	0.01	0.05	0.03
FeO	14.69	14.55	14.67	14.80	16.08	16.76	16.32	16.21	15.92	15.81	15.66
MnO	0.20	0.17	0.24	0.21	0.20	0.25	0.24	0.27	0.22	0.22	0.23
MgO	45.24	45.21	45.30	45.41	43.71	43.85	43.67	43.88	43.90	43.99	44.03
CaO	0.11	0.07	0.07	0.08	0.17	0.11	0.07	0.10	0.09	0.04	0.11
Cr2O3	0.00	0.10	0.00	0.04	0.11	0.00	0.00	0.04	0.08	0.14	0.00
NiO[1]	0.32	0.33	0.35	0.33	0.25	0.24	0.27		0.25	0.26	0.25
NiO[2]	0.30	0.33	0.34	0.32	0.24	0.22	0.17	0.24	0.28	0.21	0.22
total	100.4	100.4	100.7	100.9	100.2	100.9	99.85	100.3	99.95	100.1	99.92
Cation (p.f.u.)											
Si	0.995	0.995	0.997	0.996	0.998	0.996	0.995	0.999	0.997	0.997	0.999
Ti	0.001	0.002	0.001	0.000	0.000	0.000	0.000	0.001	0.000	0.001	0.001
Fe^{2+}	0.307	0.304	0.306	0.308	0.339	0.352	0.346	0.341	0.336	0.333	0.331
Mn	0.004	0.004	0.005	0.004	0.004	0.005	0.005	0.006	0.005	0.005	0.005
Mg	1.688	1.683	1.684	1.684	1.642	1.642	1.650	1.644	1.652	1.650	1.657
Ca	0.003	0.002	0.002	0.002	0.005	0.003	0.002	0.003	0.002	0.001	0.003
Cr	0.000	0.005	0.000	0.002	0.005	0.000	0.000	0.002	0.004	0.007	0.000
Ni	0.006	0.007	0.007	0.007	0.005	0.005	0.006	0.005	0.005	0.005	0.005
Sum	3.004	3.001	3.002	3.003	2.998	3.004	3.004	2.999	3.001	2.999	3.000
Endmembers %											
Fo	84.6	84.7	84.6	84.5	82.9	82.3	82.7	82.8	83.1	83.2	83.4
Fa	15.4	15.3	15.4	15.5	17.1	17.7	17.3	17.2	16.9	16.8	16.6

[1] Data collected using 100 nA beam current, 100 second counting time, and a fixed matrix composition.

[2] Data collected using the standard 20 nA beam current and 20 second counting time.

Appendix III (continued): All olivine core, middle, and rim compositions by EPMA

Region / Drillhole											
Rock	F. Peridotite	F. Peridotite	F. Peridotite	F. Peridotite	F. Peridotite	F. Peridotite	F. Peridotite	F. Peridotite	F. Peridotite	F. Peridotite	F. Peridotite
Thin Section	RMX01-5	RMX01-5	RMX01-5	RMX01-5	RMX01-5	RMX01-5	RMX01-5	RMX01-5	RMX01-5	RMX01-5	RMX01-5
Geochem ID	71075	71075	71075	71075	71075	71075	71075	71075	71075	71075	71075
Probe point	1_5_8	1_5_9	1_5_10	1_5_11	1_5_12	1_5_13	1_5_14	1_5_15	1_5_16	1_5_17	1_5_18
Depth (m)	76	76	76	76	76	76	76	76	76	76	76
Area	O1	O1	O2	O2	O2	O2	O2	O2	O2	O2	O2
Grain	3	3	1	1	1	2	2	2	3	3	3
Site	mid	rim	core	mid	rim	core	mid	rim	core	mid	rim
Oxide wt %											
SiO2	39.72	39.74	39.63	39.60	39.51	39.75	39.42	39.50	39.56	39.50	39.81
TiO2	0.01	0.04	0.00	0.03	0.02	0.04	0.03	0.04	0.00	0.04	0.03
FeO	15.54	15.79	16.85	16.35	17.01	16.34	16.44	16.19	16.72	16.40	16.83
MnO	0.26	0.17	0.25	0.27	0.24	0.21	0.22	0.26	0.19	0.20	0.23
MgO	43.96	44.23	43.85	43.61	43.81	44.14	44.22	44.24	43.72	43.56	43.57
CaO	0.13	0.07	0.12	0.08	0.08	0.08	0.07	0.06	0.06	0.06	0.07
Cr2O3	0.07	0.06	0.13	0.06	0.03	0.00	0.00	0.03	0.09	0.00	0.00
NiO[1]	0.26	0.24	0.25	0.27	0.25	0.25	0.24	0.24	0.26	0.26	0.25
NiO[2]	0.19	0.21	0.29	0.25	0.24	0.24	0.23	0.29	0.23	0.28	0.24
total	99.94	100.3	101.1	100.3	100.9	100.8	100.6	100.6	100.6	100.0	100.8
Cation (p.f.u.)											
Si	1.001	0.998	0.993	0.999	0.993	0.997	0.992	0.993	0.995	0.999	1.001
Ti	0.000	0.001	0.000	0.001	0.000	0.001	0.001	0.001	0.000	0.001	0.001
Fe^{2+}	0.327	0.332	0.353	0.345	0.357	0.343	0.346	0.340	0.352	0.347	0.354
Mn	0.006	0.004	0.005	0.006	0.005	0.004	0.005	0.006	0.004	0.004	0.005
Mg	1.651	1.656	1.638	1.639	1.641	1.650	1.658	1.658	1.640	1.642	1.632
Ca	0.004	0.002	0.003	0.002	0.002	0.002	0.002	0.002	0.002	0.002	0.002
Cr	0.003	0.003	0.006	0.003	0.001	0.000	0.000	0.001	0.004	0.000	0.000
Ni	0.005	0.005	0.005	0.005	0.005	0.005	0.005	0.005	0.005	0.005	0.005
Sum	2.997	3.000	3.004	2.999	3.006	3.002	3.008	3.006	3.002	3.000	2.999
Endmembers %											
Fo	83.5	83.3	82.3	82.6	82.1	82.8	82.7	83.0	82.3	82.6	82.2
Fa	16.5	16.7	17.7	17.4	17.9	17.2	17.3	17.0	17.7	17.4	17.8

[1] Data collected using 100 nA beam current, 100 second counting time, and a fixed matrix composition.

[2] Data collected using the standard 20 nA beam current and 20 second counting time.

Appendix III (continued): All olivine core, middle, and rim compositions by EPMA

Region / Drillhole											
Rock	Cr. Peridotite	Cr. Peridotite	Cr. Peridotite	Cr. Peridotite	Cr. Peridotite	Cr. Peridotite	Cr. Peridotite	Cr. Peridotite	Cr. Peridotite	Cr. Peridotite	Cr. Peridotite
Thin Section	RMX01-6	RMX01-6	RMX01-6	RMX01-6	RMX01-6	RMX01-6	RMX01-6	RMX01-6	RMX01-6	RMX01-6	RMX01-6
Geochem ID	71078	71078	71078	71078	71078	71078	71078	71078	71078	71078	71078
Probe point	1_6_1	1_6_2	1_6_3	1_6_4	1_6_5	1_6_6	1_6_7	1_6_8	1_6_9	1_6_10	1_6_11
Depth (m)	93	93	93	93	93	93	93	93	93	93	93
Area	O1	O1	O1	O1	O1	O1	O1	O1	O1	O2	O2
Grain	1	1	1	2	2	2	3	3	3	1	1
Site	core	mid	rim	core	mid	rim	core	mid	rim	core	mid
Oxide wt %											
SiO2	39.92	40.07	40.10	39.86	39.54	39.67	39.70	39.95	39.67	40.01	39.67
TiO2	0.02	0.03	0.06	0.06	0.05	0.02	0.02	0.02	0.01	0.03	0.03
FeO	14.40	14.19	14.14	14.79	14.40	14.45	14.10	14.48	13.89	14.41	14.53
MnO	0.24	0.17	0.23	0.14	0.18	0.22	0.21	0.18	0.25	0.21	0.21
MgO	45.56	45.54	45.64	45.89	45.56	45.90	45.66	45.43	45.80	45.62	45.25
CaO	0.07	0.07	0.05	0.07	0.08	0.07	0.08	0.11	0.06	0.12	0.13
Cr2O3	0.00	0.00	0.17	0.03	0.06	0.01	0.14	0.00	0.05	0.07	0.00
NiO[1]	0.25	0.26	0.24	0.26	0.26	0.26	0.25	0.25	0.24	0.24	0.23
NiO[2]	0.19	0.21	0.28	0.29	0.23	0.23	0.16	0.22	0.22	0.23	0.29
total	100.5	100.3	100.6	101.1	100.1	100.6	100.2	100.4	99.97	100.7	100.1
Cation (p.f.u.)											
Si	0.996	0.999	0.996	0.990	0.990	0.989	0.992	0.997	0.993	0.995	0.995
Ti	0.000	0.001	0.001	0.001	0.001	0.000	0.000	0.000	0.000	0.001	0.001
Fe^{2+}	0.300	0.296	0.294	0.307	0.302	0.301	0.294	0.302	0.291	0.300	0.305
Mn	0.005	0.004	0.005	0.003	0.004	0.005	0.004	0.004	0.005	0.004	0.004
Mg	1.695	1.693	1.690	1.699	1.701	1.707	1.700	1.691	1.708	1.692	1.692
Ca	0.002	0.002	0.001	0.002	0.002	0.002	0.002	0.003	0.002	0.003	0.003
Cr	0.000	0.000	0.008	0.001	0.003	0.000	0.007	0.000	0.002	0.003	0.000
Ni	0.005	0.005	0.005	0.005	0.005	0.005	0.005	0.005	0.005	0.005	0.005
Sum	3.004	3.000	2.999	3.008	3.007	3.010	3.005	3.002	3.006	3.003	3.004
Endmembers %											
Fo	84.9	85.1	85.2	84.7	84.9	85.0	85.2	84.8	85.5	85.0	84.7
Fa	15.1	14.9	14.8	15.3	15.1	15.0	14.8	15.2	14.5	15.0	15.3

[1] Data collected using 100 nA beam current, 100 second counting time, and a fixed matrix composition.

[2] Data collected using the standard 20 nA beam current and 20 second counting time.

Appendix III (continued): All olivine core, middle, and rim compositions by EPMA

Region / Drillhole										
Rock	Cr. Peridotite	Cr. Peridotite	Cr. Peridotite	Cr. Peridotite	Cr. Peridotite	Cr. Peridotite	Cr. Peridotite	Cr. Peridotite	Cr. Peridotite	Cr. Peridotite
Thin Section	RMX01-6	RMX01-6	RMX01-6	RMX01-6	RMX01-6	RMX01-6	RMX01-6	RMX01-6	RMX01-6	RMX01-6
Geochem ID	71078	71078	71078	71078	71078	71078	71078	71078	71078	71078
Probe point	1_6_12	1_6_13	1_6_14	1_6_15	1_6_16	1_6_17	1_6_18	1_6_19	1_6_20	1_6_21
Depth (m)	93	93	93	93	93	93	93	93	93	93
Area	O2	O2	O2	O2	O2	O2	O2	O2	O2	O2
Grain	1	2	2	2	3	3	3	4	4	4
Site	rim	core	mid	rim	core	mid	rim	core	mid	rim
Oxide wt %										
SiO2	39.98	40.27	39.75	39.74	39.73	39.67	39.86	39.59	39.91	39.87
TiO2	0.02	0.04	0.04	0.05	0.04	0.01	0.04	0.04	0.03	0.04
FeO	14.66	13.74	14.70	14.17	14.47	14.26	14.39	13.77	14.30	14.45
MnO	0.24	0.14	0.22	0.23	0.20	0.19	0.21	0.22	0.23	0.18
MgO	45.60	44.96	45.50	45.37	45.50	45.56	45.46	45.39	45.58	45.93
CaO	0.06	0.09	0.06	0.07	0.07	0.03	0.04	0.13	0.07	0.08
Cr2O3	0.00	0.09	0.00	0.07	0.00	0.09	0.07	0.00	0.00	0.03
NiO[1]	0.24	0.26	0.25	0.25	0.24	0.25	0.25	0.22	0.22	0.22
NiO[2]	0.21	0.22	0.16	0.25	0.28	0.26	0.25	0.24	0.26	0.24
total	100.8	99.59	100.5	99.95	100.27	100.1	100.3	99.35	100.3	100.8
Cation (p.f.u.)										
Si	0.995	1.008	0.993	0.995	0.994	0.993	0.995	0.996	0.996	0.992
Ti	0.000	0.001	0.001	0.001	0.001	0.000	0.001	0.001	0.001	0.001
Fe^{2+}	0.305	0.288	0.307	0.297	0.303	0.298	0.300	0.290	0.299	0.300
Mn	0.005	0.003	0.005	0.005	0.004	0.004	0.004	0.005	0.005	0.004
Mg	1.692	1.678	1.694	1.694	1.697	1.700	1.692	1.703	1.696	1.703
Ca	0.002	0.002	0.002	0.002	0.002	0.001	0.001	0.004	0.002	0.002
Cr	0.000	0.004	0.000	0.003	0.000	0.004	0.003	0.000	0.000	0.001
Ni	0.005	0.005	0.005	0.005	0.005	0.005	0.005	0.004	0.004	0.004
Sum	3.004	2.989	3.006	3.002	3.005	3.005	3.002	3.003	3.003	3.007
Endmembers %										
Fo	84.7	85.4	84.7	85.1	84.9	85.1	84.9	85.5	85.0	85.0
Fa	15.3	14.6	15.3	14.9	15.1	14.9	15.1	14.5	15.0	15.0

[1] Data collected using 100 nA beam current, 100 second counting time, and a fixed matrix composition.

[2] Data collected using the standard 20 nA beam current and 20 second counting time.

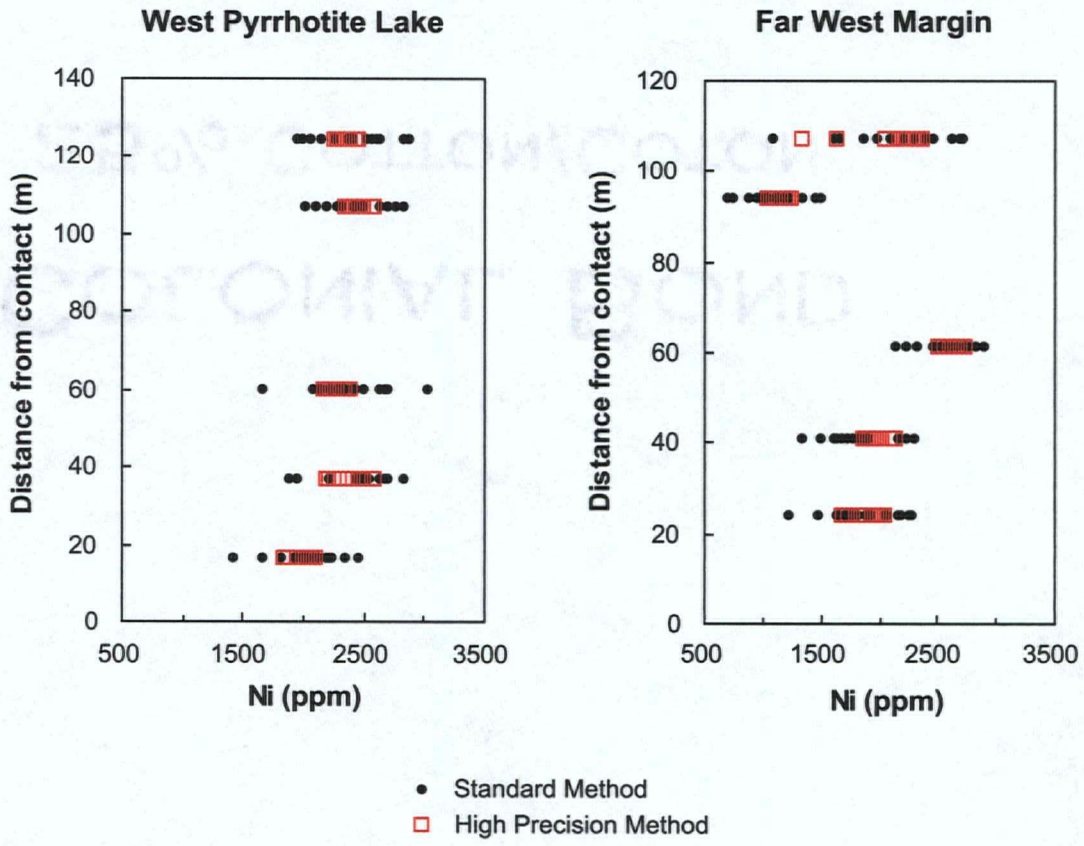

Appendix IV: Comparison of the Ni abundance (ppm) of olivine by different EPMA methods. The standard method used a 20 nA beam current and 20 second counting time, and resulted in analytical uncertainties of 10-20% relative. The high precision method used a 100 nA beam current and 100 second counting time. This resulted in signficantly lower uncertainties (%RSD 2-5) and greatly reduced the range of measured Ni concentrations.

Appendix V: Duplicate analyses of trace element abundances by HR-ICP-MS[1]

Sample No.	71072 (Feldspathic Peridotite; 36 wt% MgO)					71078 (Feldspathic Peridotite; 32 wt% MgO)					71128 (Feldspathic Peridotite; 27.5 wt% MgO)				
Analysis	a	b	avg	σ	% RSD	a	b	avg	σ	% RSD	a	b	avg	σ	% RSD
La	2.69	2.73	2.71	0.03	1.3	1.76	1.95	1.86	0.13	6.9	5.45	5.49	5.47	0.03	0.5
Ce	6.05	6.10	6.07	0.04	0.6	5.94	5.71	5.83	0.17	2.8	13.79	13.71	13.75	0.06	0.4
Pr	0.79	0.79	0.79	0.00	0.1	0.90	0.84	0.87	0.04	4.2	1.79	1.81	1.80	0.02	1.0
Nd	3.45	3.44	3.45	0.01	0.2	4.29	4.07	4.18	0.16	3.7	7.88	7.98	7.93	0.07	0.8
Sr	41.5	41.2	41.4	0.2	0.6	45.9	42.7	44.3	2.3	5.2	109.1	108.2	108.6	0.6	0.6
Sm	0.89	0.89	0.89	0.00	0.2	1.13	1.10	1.12	0.02	2.1	1.94	1.87	1.90	0.05	2.7
Eu	0.41	0.41	0.41	0.00	0.1	0.21	0.25	0.23	0.03	11	0.63	0.62	0.62	0.01	1.2
Gd	1.01	1.00	1.01	0.01	0.7	1.15	1.17	1.16	0.02	1.4	1.80	1.94	1.87	0.10	5.5
Tb	0.18	0.18	0.18	0.00	0.3	0.22	0.21	0.21	0.00	1.8	0.32	0.32	0.32	0.00	0.4
Dy	1.00	1.00	1.00	0.00	0.1	1.23	1.18	1.21	0.04	2.9	1.93	1.98	1.96	0.03	1.5
Ho	0.22	0.22	0.22	0.00	0.2	0.26	0.26	0.26	0.00	0.2	0.38	0.38	0.38	0.00	0.9
Er	0.58	0.58	0.58	0.00	0.6	0.74	0.68	0.71	0.04	5.6	1.07	1.05	1.06	0.02	1.8
Yb	0.53	0.53	0.53	0.00	0.7	0.61	0.61	0.61	0.00	0.1	0.97	0.93	0.95	0.03	3.0
Lu	0.09	0.09	0.09	0.00	0.3	0.08	0.10	0.09	0.01	10	0.13	0.14	0.13	0.00	3.1
U	0.15	0.15	0.15	0.00	0.6	0.23	0.21	0.22	0.01	5.4	0.26	0.26	0.26	0.01	2.1
Pb	3.5	4.1	3.8	0.4	11	43.9	40.8	42.4	2.2	5.2	2.6	2.6	2.6	0.00	0.0
Li	27.1	25.1	26.1	1.4	5.5	50.9	39.8	45.3	7.8	17	22.0	21.3	21.7	0.5	2.3
Sc	12.17	10.79	11.48	0.97	8.5	4.30	9.02	6.66	3.34	50	17.17	16.45	16.81	0.51	3.0
V	80.8	85.1	83.0	3.1	3.7	130.5	120.7	125.6	6.9	5.5	167.8	164.0	165.9	2.7	1.6
Co	79.6	79.1	79.3	0.3	0.4	125.4	99.8	112.6	18.1	16	109.7	109.0	109.3	0.5	0.4
Cu	15.5	15.6	15.6	0.1	0.7	149.4	127.9	138.6	15.2	11	96.0	94.3	95.1	1.2	1.3
Zn	57	55	56	1.4	2.4	130.6	105.2	117.9	17.9	15	82.2	79.0	80.6	2.3	2.8
Ga	4.41	4.28	4.34	0.09	2.0	6.10	5.37	5.73	0.52	9.0	8.39	7.79	8.09	0.42	5.2
Rb	6.7	6.7	6.7	0.0	0.1	30.1	29.7	29.9	0.3	0.9	10.9	10.7	10.8	0.2	1.4
Sr	41.5	41.2	41.4	0.2	0.6	45.9	42.7	44.3	2.3	5.2	109.1	108.2	108.6	0.6	0.6
Y	4.49	4.57	4.53	0.05	1.2	5.15	5.46	5.30	0.22	4.1	8.64	8.49	8.57	0.11	1.2
Zr	21.0	20.5	20.8	0.36	1.7	19.4	23.2	21.3	2.63	12	52.67	50.28	51.47	1.69	3.3
Nb	1.39	1.40	1.39	0.01	0.7	1.13	1.79	1.46	0.47	32	2.94	2.86	2.90	0.05	1.9
Cd	0.07	0.07	0.07	0.00	0.2	0.14	0.21	0.17	0.05	28	<lod	<lod			
Sn	0.91	0.14	0.53	0.54	103	0.12	0.08	0.10	0.03	29	0.10	0.04	0.07	0.04	60
Sb	0.05	0.07	0.06	0.01	19	0.01	0.10	0.05	0.06	107	<lod	<lod			
Cs	0.55	0.56	0.55	0.00	0.7	1.67	1.57	1.62	0.07	4.4	1.30	1.28	1.29	0.02	1.2
Hf	0.60	0.59	0.60	0.01	1.2	0.65	0.68	0.66	0.02	2.4	1.49	1.46	1.47	0.03	1.9
Ta	0.09	0.09	0.09	0.00	1.6	0.07	0.12	0.09	0.03	33	0.18	0.18	0.18	0.00	1.5
W	0.15	0.11	0.13	0.03	21	0.07	0.10	0.09	0.02	20	0.24	0.27	0.26	0.02	8.3
Bi	0.03	0.03	0.03	0.00	1.0	0.16	0.41	0.29	0.18	64	<lod	<lod			
Th	0.5	0.5	0.5	0.0	5.4	0.2	0.7	0.4	0.3	71	1.0	1.0	1.0	0.0	0.8
Ba						148					104	99	102	3	3.4

[1] Duplicate analyses are multiple digestions of a single powdered sample.

[2] Average %RSD of samples 71072, 71078, & 71128.

[3] Analysis a from 100 mg and b from 150 mg.

<lod = Below detection limit

Appendix V (continued): Duplicate analyses of trace element abundances by HR-ICP-MS[1]

Sample No.	G-2 Granite (USGS referenc material; 0.75 wt% MgO)					DTS-2 Dunite (USGS reference material; 49.4 wt% MgO)[3]					%RSD
Analysis	a	b	avg	σ	% RSD	a	b	avg	σ	% RSD	average[2]
La	82.07	77.96	80.02	2.91	3.6	0.009	0.012	0.011	0.002	21	2.9
Ce	149.80	136.66	143.23	9.29	6.5	0.028	0.024	0.026	0.003	10	1.3
Pr	15.69	14.79	15.24	0.64	4.2	<lod	0.003	0.003			1.8
Nd	50.77	47.81	49.29	2.10	4.3	0.01	0.01	0.01	0.002	17	1.6
Sr	439.5	455.9	447.7	11.6	2.6	0.7	0.4	0.6	0.2	37	2.1
Sm	6.70	6.06	6.38	0.45	7.1	0.005	0.003	0.004	0.001	28	1.7
Eu	1.21	1.19	1.20	0.01	1.0	<lod	0.002	0.002			4.1
Gd	3.62	3.45	3.54	0.12	3.3	0.005	0.021	0.013	0.012	91	2.5
Tb	0.41	0.40	0.41	0.00	0.8	<lod	0.001	0.001			0.8
Dy	2.01	2.02	2.02	0.01	0.3	0.005	0.004	0.004	0.001	14	1.5
Ho	0.33	0.32	0.33	0.00	1.5	<lod	0.002	0.002			0.5
Er	0.82	0.78	0.80	0.03	3.8	0.005	0.004	0.004	0.000	11	2.7
Yb	0.70	0.71	0.70	0.00	0.5	0.009	0.009	0.009	0.000	3.9	1.2
Lu	0.10	0.10	0.10	0.00	2.2	<lod	0.002	0.002			4.6
U	1.57	2.06	1.81	0.35	19	<lod	0.002	0.002			2.7
Pb	23.5	23.8	23.6	0.2	0.7	3.0	2.7	2.8	0.193	6.8	5.3
Li	12.6	14.3	13.4	1.2	8.9	1.63	1.31	1.47	0.23	16	8.3
Sc	1.69	1.77	1.73	0.05	3.2	3.11	2.82	2.96	0.20	6.8	21
V	15.9	16.3	16.1	0.2	1.4	21.1	22.1	21.6	0.7	3.3	3.6
Co	2.0	2.2	2.1	0.1	4.4	134.2	101.7	117.9	22.9	19	5.6
Cu	3.6	6.9	5.3	2.4	45	2.6	1.9	2.2	0.5	23	4.3
Zn	37.5	40.6	39.1	2.2	5.6	49.1	38.1	43.6	7.7	18	6.8
Ga	10.01	10.05	10.03	0.03	0.3	0.71	0.84	0.78	0.09	11	5.4
Rb	77.1	76.7	76.9	0.3	0.4	0.91	<lod	0.91			0.8
Sr	217.9	227.8	222.9	7.0	3.1	0.71	0.42	0.56	0.21	37	2.1
Y	4.03	4.23	4.13	0.14	3.4	0.01	0.03	0.02	0.01	51	2.2
Zr	129.0	129.9	129.5	0.7	0.5	0.11	0.12	0.12	0.01	8.0	5.8
Nb	4.38	5.02	4.70	0.45	9.6	0.08	0.04	0.06	0.03	57	11
Cd	0.13	0.14	0.14	0.01	6.3	<lod	0.019	0.019			14
Sn	0.07	0.09	0.08	0.01	14	0.15	0.37	0.26	0.15	59	64
Sb	0.01	0.01	0.01	0.00	53	0.54	0.50	0.52	0.03	5.9	63
Cs	0.62	0.64	0.63	0.01	2.3	0.06	<lod	0.06			2.1
Hf	3.44	3.55	3.49	0.08	2.2	0.11	0.00	0.05	0.07	132	1.8
Ta	0.31	0.35	0.33	0.02	6.9	0.004	<lod	0.004			12
W	0.08	0.10	0.09	0.01	14	0.07	0.00	0.04	0.05	133	16
Bi	0.01	0.01	0.01	0.00	5.1	<lod	<lod				32
Th	11.5	9.7	10.6	1.3	12	<lod	<lod				26
Ba						11		11			3.4

[1] Duplicate analyses are multiple digestions of a single powdered sample.

[2] Average %RSD of samples 71072, 71078, & 71128.

[3] Analysis a from 100 mg and b from 150 mg.

<lod = Below detection limit

Appendix VI: Trace element abundances for USGS reference materials (G-2 and DTS-2)

Material	G-2 (Granite)												
Source	PCIGR - this study						PCIGR - Pretorius (in press)	Govindaraju (1994)	Robinson et al. (1986)	Totland et al. (1992)	Meisel et al. (2001)		Liang et al. (2000)
Method	HR-ICP-MS							INAA	XRF	ICP-MS	ICP-MS		ICP-MS
Sampe No.[1]	RM06	RM06r	RM25	average	2σ	%RSD		1	2	3	HP4500	2σ (n=34)	5
Weight (mg)[2]	100	100	100										
Cs (ppm)	1.25	1.26	1.28	1.26	0.03	1.3	1.36						
Rb	156	159	153	156	5.7	1.8	201						
Ba													
Th	23	14	19	19	9.0	23.7	27	24.7		23	24.4	3.3	24.9
U	1.6	1.7	2.1	1.8	0.52	14.8							
Ta	0.63	0.68	0.69	0.67	0.063	4.7	0.63	0.88			0.78	0.10	0.89
Nb	9	10	10	10	1.4	7.0	11.6	12		11	11.9	2.1	11.2
La	82	81	78	80	4.3	2.7	91	89	86	91.3	89.6	6.1	87.1
Ce	150	144	137	143	13.1	4.6	165	160	165.5	166	164	12.1	155
Pr	16	16	15	15	1.1	3.6	17	18	15.2	15.6	16.7	1.3	17.1
Nd	51	51	48	50	3.5	3.5	54	55	52.4	53.7	54.9	4.3	52.6
Pb	24	25	24	24	1.5	3.1							
Sr	439	414	456	437	41.7	4.8							
Zr	260	268	260	263	9.1	1.7	365	309		313	300	51.6	262
Hf	6.9	7.1	7.1	7.0	0.19	1.3	8.5	7.9			8.1	1.5	6.95
Sm	6.7	6.8	6.1	6.5	0.78	6.0	7.3	7.2	7.54	6.32	7.48	0.6	7.22
Eu	1.21	1.23	1.19	1.21	0.04	1.7	1.4	1.4	1.63	1.43	1.48	0.1	1.46
Gd	3.6	3.7	3.5	3.6	0.25	3.5	3.8	4.3	4.13	4.23	4	0.3	4.13
Tb	0.41	0.41	0.40	0.41	0.01	1.2	0.46	0.48	0.55	0.55	0.49	0.0	0.45
Dy	2.0	2.1	2.0	2.1	0.12	2.8	2.2	2.4	2.15	2.07	2.32	0.2	2.29
Ho	0.33	0.34	0.32	0.33	0.021	3.1	0.37	0.4		0.38	0.38	0.0	0.31
Er	0.82	0.85	0.78	0.82	0.073	4.5	0.93	0.92	1		0.97	0.1	0.87
Yb	0.70	0.73	0.71	0.71	0.033	2.3	0.76	0.8	0.81		0.74	0.1	0.72
Y	8.1	8.4	8.5	8.3	0.36	2.1	9.2	11	10.8	8.9	10	0.8	10.2
Lu	0.096	0.094	0.099	0.096	0.004	2.3	0.11	0.11	0.15		0.108	0.0	0.1

[1] "r" denotes a replicate analysis from one digestion.

[2] Weight of sample powder in milligrams.

Appendix VI (continued): Trace element abundances for USGS reference materials (G-2 and DTS-2)

Material	DTS-2 (Dunite)							
Source	PCIGR - this study						Raczek et al. 2000	Raczek et al. 2000
Method	HR-ICP-MS	HR-ICP-MS	HR-ICP-MS					
Sampe No.[1]	RM01	RM16	RM16r	average	2σ	%RSD	DTS-2 (1)	DTS-2 (2)
Weight (mg)[2]	100	150	150					
Cs (ppm)	0.06	<lod	0.00	0.0304	0.0838	138		
Rb	0.9	<lod	0.0	0.46	1.3	138		
Ba	10.99			10.99				
Th	<lod	0.0032	0.0033	0.0032	0.0002	3		
U	<lod	0.0016	0.0016	0.0016	0.0001	2		
Ta	0.0045	<lod	<lod	0.0045				
Nb	0.08	0.04	0.03	0.05	0.056	55		
La	0.009	0.012	0.013	0.011	0.0039	17	0.0136	0.0117
Ce	0.028	0.024	0.025	0.026	0.0042	8	0.0275	0.0232
Pr	<lod	0.0032	0.0031	0.0032	0.0001	2		
Nd	0.014	0.011	0.011	0.012	0.004	15	0.014	0.0122
Pb	3.0	2.7	2.7	2.8	0.31	5		
Sr	0.7	0.4	0.4	0.5	0.33	31		
Zr	0.11	0.12	0.12	0.12	0.015	6		
Hf	0.11	0.00	0.00	0.04	0.12	157		
Sm	0.005	0.003	0.003	0.004	0.0018	25	0.0032	0.00284
Eu	<lod	<lod	<lod				0.00092	0.00081
Gd	0.00	0.02	0.02	0.02	0.019	61	0.00313	0.00294
Tb	<lod	0.0008	0.0008	0.0008	0.00002	2		
Dy	0.005	0.004	0.004	0.004	0.0010	12	0.00436	0.00401
Ho	<lod	0.0016	0.0016	0.0016	0.0001	2		
Er	0.0047	0.0040	0.0048	0.0045	0.0008	9	0.00471	0.00458
Yb	0.0093	0.0088	0.0087	0.0089	0.0006	4	0.00996	0.0093
Y	0.01	0.03	0.03	0.02	0.018	36		
Lu	<lod	0.0024	0.0023	0.0024	0.0001	2		0.002

[1] "r" denotes a replicate analysis from one digestion.

[2] Weight of sample powder in milligrams.

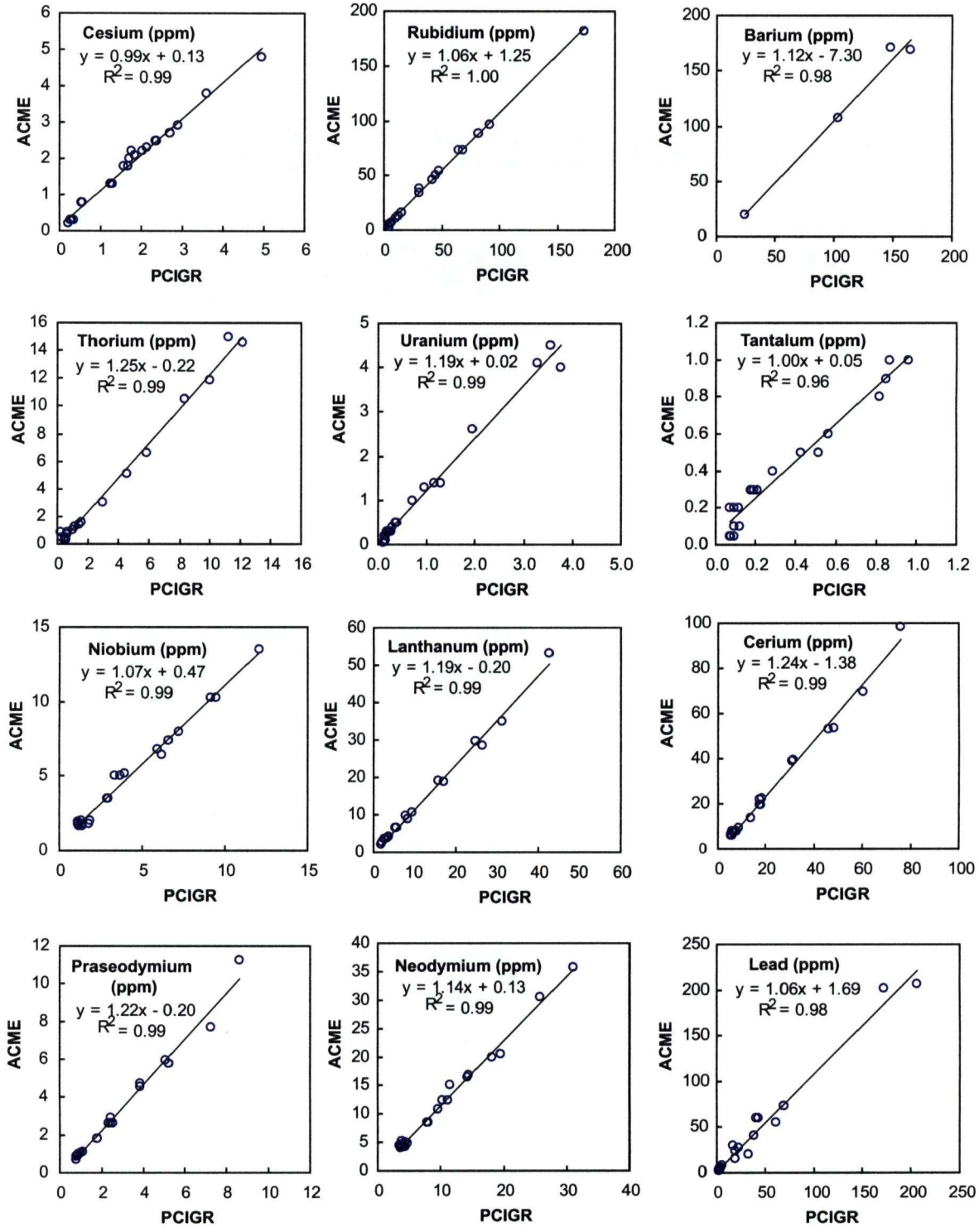

Appendix VII: Comparison of trace element results from PCIGR (HR-ICP-MS) and ACME Analytical Laboratories, Vancouver (ICP-MS and ICP-ES). ACME analytical methods summarized in Appendix I. All samples are included in Table 3.3 (PCIGR) and Table 2.1 (ACME). R2 values are >0.98 with the exception of Tantalum.

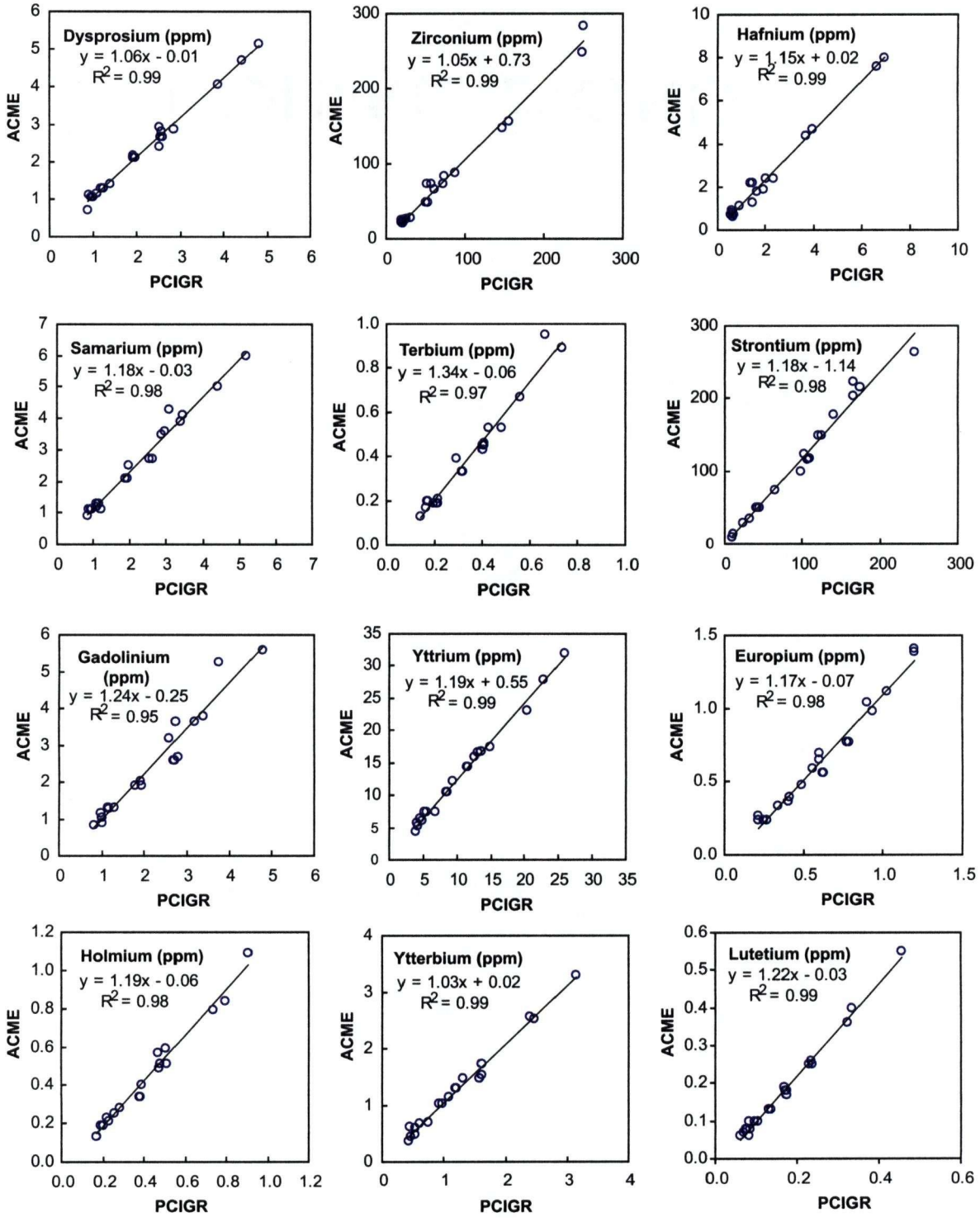

Appendix VII (continued): Comparision of trace element results from PCIGR and ACME Analytical Laboratories, Vancouver. R2 values are >0.98 with the exception of gadolinium and terbium.